UNIVERSITAT DE VALÈNCIA

DEPARTAMENT DE FÍSICA ATÒMICA, MOLECULAR I NUCLEAR
INSTITUT DE FÍSICA CORPUSCULAR

DOCTORAT EN FÍSICA

Development of the quality test protocol for the DEPFET pixel detectors and top-quark mass measurement at high energy e^+e^- colliders

---

PhD thesis dissertation by:
Març Josep Boronat Arévalo

under the supervision of :
Prof. Juan A. Fuster Verdú and Dr. Carlos Lacasta Llácer

València - June 2017

Marçà Josep Boronat Arévalo: *Development of the quality test protocol for the DEPFET pixel detectors and top-quark mass measurement at high energy* e^+e^- *colliders* - June 2017

Declaración

Prof. Juan A. Fuster Verdú
Profesor Investigación del CSIC, y

Dr. Carlos Lacasta Llácer
Investigador titular del CSIC

CERTIFICAN:

Que la presente memoria que tiene por título **"Development of the quality test protocol for the DEPFET pixel detectors and top-quark mass measurement at high energy e^+e^- colliders"** ha sido realizada bajo su dirección, en el Instituto de Física Corpuscular (Centro Mixto Universitat de València - CSIC) por D. Marçà Josep Boronat Arévalo y que constituye su trabajo de tesis doctoral en el Departamento de Física Atómica, Molecular y Nuclear para optar al grado de Doctor en Física por la Universidad de Valencia.

Y para que conste, en cumplimiento de la legislación vigente, firman el presente certificado en *València* a *Junio* 2017.

Prof. Juan A. Fuster Verdú
22 de Junio, 2017

Dr. Carlos Lacasta Llácer
22 de Junio, 2017

El presente trabajo ha sido realizado en el **Instituto de Física Corpuscular (IFIC)** en Paterna (València), España.

Dentro del marco de la **Beca de Formación de Personal Investigador (FPI)** concedida por el Ministerio de Ciencia e Innovación (MICINN) junto con el grupo de Futuros Aceleradores del IFIC.

El IFIC es un centro mixto del Consejo Superior de Investigaciones Científicas (CSIC) y de la Universitat de València (UV). En Julio de 2015 recibió la acreditación **Severo Ochoa (SEV-2014-0398)** que le distingue como Centro de Excelencia. Dicha acreditación reconoce la excelencia y las contribuciones científicas que realizan los centros y unidades a nivel nacional e internacional, su impacto empresarial y social y su capacidad para atraer talento.

. . . "If you knew Time as well as I do," said the Hatter, *"you wouldn't talk about wasting it. It's him"*

". . . Now if you only kept on good term with him, he'd do almost anything you like with the clock. For instance, suppose it were nine o'clock in the morning, just time to begin lessons: you'd only have to whisper a hint to Time, and round goes the clock in a twinkling! Half-past one, time for dinner!"

. . . "That would be grand, certainly," said Alice troughtfully: *"but then - I shouldn't be hungry for it, you know."*

"Not at first, perhaps," said the Hatter: *"but you could keep it to half-past one as long as you liked."*

— Alice's Adventures in Wonderland – Lewis Carroll

". . . Listen, then, you poor thing. Listen well. You have need of it. And now you hear not only a Händel who, disfigured by radio, is, all the same, in this most ghastly of disguises still divine; you hear as well and you observe, most worthy sir, a most admirable symbol of all life. . . . Better learn to listen first! Learn what is to be taken seriously and laugh at the rest!"

". . . Hören Sie gut zu, Männlein, es tut Ihnen not! Also, Ohren auf! So. Und nun hören Sie ja nicht blo¸ einen durch das Radio vergewaltigten Händel, der dennoch auch in dieser scheu¸lichsten Erscheinungsform noch göttlich ist; Sie hören und sehen, Wertester, zugleich ein vortreffliches Gleichnis alles Lebens. . . . Lernen Sie lieber erst zuhören! Lernen Sie ernst nehmen, was des Ernstnehmens wert ist, und lachen über das andre!"

— Der Steppenwolf – Hermann Hesse

Unity is variety and variety in unity is the supreme law of the universe.

— Isaac Newton

Acknowledgements

Sin lugar a duda, ningún logro personal es 100% propio, probablemente, sólo seamos dueños de una pequeñísima fracción del mérito que pueda haber en cada uno de esos logros. Siguiendo con esta idea, profesionalmente somos un cúmulo de contribuciones que, en cierto modo, nos ha tocado guardar. Es una pena que tendamos a olvidar esto tan fácilmente, por eso, una buena idea es dejarlo por escrito.

En primer lugar, agradecer a Juan Fuster, quien ha sido guía y mentor en cada paso del camino, siempre con la solución exacta cuando las dudas no te dejaban continuar y con la habilidad para crear las dudas precisas que te marcan el camino a seguir. A Marcel Vos y Carlos Lacasta que han sido parte de los cimientos de cada paso de este trabajo. Agradecer a Daniel Esperante y a Carlos Mariñas, porque sin su ayuda y sin su consejo, nada de esto hubiera sido posible. A Pablo Gomis, por compartir todos esos momentos duros lejos de nuestro Instituto y además por tomar el relevo, no hubiera podido elegir a nadie mejor. A Nacho, Miguel Angel, Jose, Martí, que conseguís hacer de un largo día de trabajo, algo divertido. A Carlos, Pablo R., Victor, las cervezas, sin vosotros, no son lo mismo.

Gracias a todas la personas de la secretaría del IFIC: Paqui, Luis, Amparo, Ana, Jose, Pilar, Sole... sois la maquinaria que hace funcionar todo esto.

I would like to thank Hans-Günther Moser, who was my host at the MPP, always willing to help and making much easier my long stay in Munich. Also, thanks to all people from the MPP-HLL, Edi, Felix, Jakob, Manfred, Paola, Philipp and especially Christian, Laci and Rainer, I have learnt a lot from your extensive experience.

Finalmente mi familia, a mis padres, Remei y Boro, a mi hermano Jordi, los imprescindibles, mis hooligans. Y muy especialmente a mi Bea, ya que decidió emprender este camino conmigo y que ha sido mi fuente de alegría en este largo proceso. Mil gracias, os quiero.

Abstract

The Standard Model is the most accurate theoretical framework, capable to include all particles discovered and their interactions. It is the result of more than 100 years of research on particle physics, starting with the observation, by J.J. Thompson, of the so called "corpuscles", using a small *Cathode Ray Tube*; to the recent discovery of the Higgs boson, which required the collaboration of thousands of researches from all around the world and the largest and more sophisticated machine ever constructed by the human kind (the LHC).

The need of an explanation to the nature phenomena is unstoppable and likewise the necessity of new machines to continue discovering them. On this context, several projects, with different approaches, are being developed. The discoveries performed by the LHC need to be complemented with high precision studies, which can be provided by the clean environment of an e^+e^- collider, such the International Linear Collider (ILC) and the Compact Linear Collider (CLIC), These machines will cover the energy range from hundreds of GeV to the multi-TeV scale. On the other hand, the SuperKEKB, which uses e^+e^- interaction at intermediate energies, will generate unprecedented luminosities to study the $B\bar{B}$ processes with very high accuracy.

The work presented here, entered on this context to perform a tiny contribution. The thesis was divided in two main topics. First part is dedicated to the study and development of a DEPFET-based pixel detector for e^+e^- collides. DEPFET is an active pixel technology, characterized by its excellent position reconstruction, its low material budget and low power consumption, which is capable to cope with all the requirement of the future e^+e^- colliders. For this reason, DEPFET is one of the candidates for the (ILC) and the baseline technology for the Belle II Pixel Detector (PXD) at the new Japanese Superflavour Factory SuperKEKB.

On this content, the DEPFET prototypes for Belle II PXD will be presented, likewise, the process of construction of the PXD shell, to contextualize and motivated the development of a quality control protocol using a needles card. The process of design and test of the distinct needle card prototypes will be described, together with a proposed testing protocol. This work resulted in a complete setup, with all the mechanical parts, the electronic boards and software, mounted and prepared to be used during the PXD production.

The second study is focused on the measurement of the top-quark mass. On this part a new observable, $B(m_t, \zeta_{S'})$, will be introduced, which uses the cross section of the $t\bar{t}$ radiative events to obtain the mass of the top-quark in the continuum. The study

has been performed on a high-energy e^+e^- collider scenario, to take advantage of this new environment and, potentially, reach unprecedented sensitivities. A partonic level study was done in order to obtain the maximum potential sensitivity achievable on the ILC-500 GeV physics scenario. The calculations were performed, independently, using the ISR and FSR particles and then, combining them. Afterwards, to approach towards a realistic study, the hadronization and the basic detector effects were included. Moreover, the study was extended to CLIC-380 GeV and ILC-1000 GeV.

$B(m_t, \zeta_{S'})$ does not require a specific interaction energy, for this reason, the calculation of the mass can be done not only over the production threshold but in the continuum. Therefore, the mass parameter can be defined on a good renormalization system, being sensitive to its running. On this context, the sensitivity to the running of the top-quark mass was probed. Finally, the study of the systematic errors were performed and a method to minimize their effects was proposed. The results obtained proved that the resolution of $B(m_t, \zeta_{S'})$ are way below the methods currently used in hadron colliders and in the same order of the threshold measurement on the ILC.

Contents

Acronyms

SM Standard Model

BNL Brookhaven National Laboratory

MC Monte Carlo

QED Quantum Electrodynamics

QCD Quantum Chromodynamics

DESY Deutsches Elektronen-Synchrotron

CERN European Organization for Nuclear Research

SPS Super Proton Synchrotron

LHC Large Hadron Collider

ATLAS A Toroidal LHC ApparatuS

CMS Compact Muon Solenoid

ISR Initial State Radiation

FSR Final State Radiation

MSSM Minimal Supersymmetric Standard Model

MC Monte Carlo Tool

ILC International Linear Collider

CLIC Compact Linear Collider

LCIO Linear Collider I/O

PFA Particle Flow Algorithm

SiD Silicon Detector

ECAL Electromagnetic calorimeter

HCAL Hadronic calorimeter

TPC Time Projection Chamber

SFF Super Flavor Factories

LER Low Energy Ring

HER High Energy Ring

VXD Vertex Detector

CDC Central Drift Chamber

PID Particle Identification Device

RPC Resistive Plate Chambers

RICH Ring-imaging Cherenkov detector

DCD Drain Current Digitizer

DHP Data Handling Processor

QFT Quantum Filed Theory

RMS Root Mean Square

CoG Center of Gravity

DUT Device Under Test

PXD Pixel Detector

SVD Silicon Vertex Detector

DHE Data Handler Engine

DHC Data Handling Concentrator

ONSEN ONline SElection Node

ROI Region of Interest

EVB EVent Builder

IF Inner-Forward

IB Inner-Backward

OF Outer-Forward

OB Outer-Backward

BSC Boundary-Scan Register Cell

TDI Test Data In

TDO Test Data Out

TMS Test Mode Select

TCK Test Clock

EMCM Electrically active Multi-Chip Module

LVDS Low Voltage Differential Signaling

Part I

Introduction

1 An Overview of the Physics Framework

The history of physics is very long, 3000 years of curiosity and work, from the Ancient Greeks theories, to the Gravitational Waves, thousands of scientists which have constructed our comprehension of Nature. This chapter intends to describe, briefly, the physics framework to introduce some of the theoretical aspects required to contextualize and motivate the results of this thesis. The main discoveries, of the last century, from the electron to the Higgs boson, will be quickly covered, to describe the process of construction of the present particle physics knowledge. Finally, the Standard Model (SM) will be introduced and some theoretical aspects will be briefly described.

1.1 *Historical Overview*

At the end of 19th century, physics could explain accurately Nature. The elementary particles were defined as the 92 known atoms, from Hydrogen to Uranium, classified on the D. Mendeleev's Periodic Table [1]. Classical mechanics could solve complex problems like thermodynamics, fluid mechanics and kinematics. The J. C. Maxwell's equations were widely accepted, together with the electromagnetic waves interpretation of optics.

New observations, coming from the studies of the cathode rays, started to create the necessity to change completely the point of view, arising the corpuscular explanation of the light. In 1887, H. Hertz, while testing the Maxwell's hypothesis with a spark-gap generator, noticed that illuminating the electrodes, with certain ultraviolet light, the sensitivity was increased [2]. This phenomenon was called Photoelectric Effect and was explained by A. Einstein 18 years later [3], under the assumption that light was not just a propagating wave through the space but discrete wave packages, called photons.

In 1897, J. J. Thomson studied the cathode rays and concluded that they were steams of particles, much smaller than atoms. He called them "corpuscles" and measured its charge/mass ratio (q/m) [4]. These particles became the known "electrons"[1]. Their charge was measured, precisely, by R. Millikan and H. Fletcher in 1909 [5]. The discovery of the electron opened the door to understand the internal structure of the matter[2]. Thomson postulated his atomic model named *Plum Pudding Model*, where atoms became spheres of positively charged matter with the electrons embedded inside [3], like plums in a pudding.

This model was abandoned when E. Rutherford discovered the atomic nucleus in 1911 [6]. He was studying the α and β radiation going through thin metal plates when he noticed that almost all of the impinging particles passed straight through the metal, but some got deflected and a small quantity moved backwards, like they would have hit a hardy part of the atom. This part was described as the nucleus. Rutherford postulated his atomic model, considering the atom as a central positive charge, concentrated in a very small volume [4], containing the bulk of the atomic mass, and surrounded, far away, by electrons, which neutralize the overall nuclear charge.

The protons were observed by E Rutherford (1919) [8] and by P. M. S. Blackett (1925) [9] using a Wilson chamber to study the elastic collisions between α particles and different gases (Fig. 1).

In 1932, J. Chadwick, found an explanation to the Beryllium rays generated on the nuclear reaction $\alpha + {}^{9}\mathrm{Be} \rightarrow {}^{12}\mathrm{C} + {}^{1}\mathrm{n}$. He postulated the neutron rays hypothesis [10].

Notice that in early 19th century, cosmic rays were the only source of high energy particles. The new technics and tools, like the Wilson chamber (1911) and the Geiger Detector (1908) made easier the study of these sources. First evidences of the cosmic rays were published in 1912 by V. F. Hess [11]. He observed that the level of radiation increases with the height. He took measurements, up to 5.3 km, using an electroscope in a balloon. First direct measurements of the cosmic rays were performed by W. Bothe and W. Kolhörster in 1929, developing a coincidence method across a metal blocks and measuring their penetration capability [12].

In 1926, E. Schrödinger postulated the probabilistic interpretation of the mechanics [13], introducing his famous equation (Eq. 1). This theory defines the position of one particle, at a given time, as a probability function that covers everywhere. But this assumption was not compatible with the relativity theory, postulated by A. Einstein in 1905 [14]. This theory fixed the maximum travel speed of information to the speed of the light (c), therefore, this rule is broken if a particle has a probability to be every-

1 Name introduced by G. J. Stoney in 1894.
2 With the ultimate goal of simplify the number of known elementary particles.
3 The total charge become neutral.
4 The electric repulsion must be overcome by a mysterious and strong force $\rightarrow$ Yukawa interaction (1935) [7].

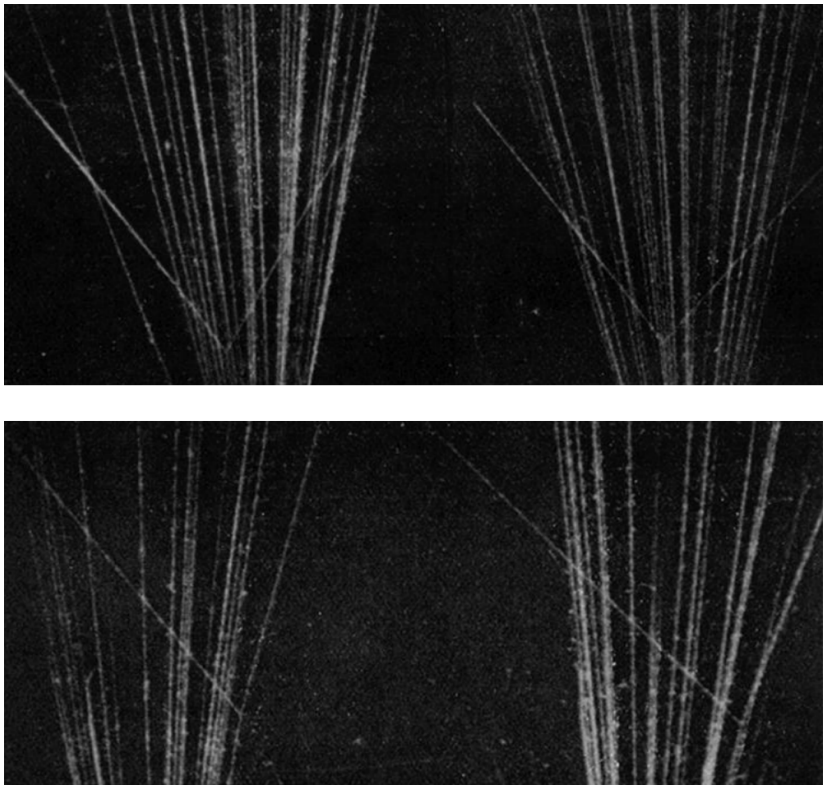

Figure 1: Elastic collision $\alpha + {}^4\mathrm{He} \rightarrow \alpha + {}^4\mathrm{He}$ (upper) and $\alpha + {}^1\mathrm{H} \rightarrow \alpha + {}^1\mathrm{H}$ (bottom).

where in a given time (causality breaking).

$$\hat{H}\,|\Psi(t)\rangle = i\hbar\frac{\partial}{\partial t}\,|\Psi(t)\rangle \tag{1}$$

A relativistic version of the quantum mechanics was postulated by P. A. M. Dirac in 1928 [15] [5]. He introduced the formula $(i\gamma^\mu\partial_\mu - m)\Psi(x) = 0$, which describes 1/2-Spin massive particles, such as electrons. Moreover, adding the correct electromagnetic potentials, this theory describes, with fine details, the hydrogen spectrum. However, the solution also includes states of negative energy. It entails that an electron, in a fundamental state of one hydrogen atom, could jump to negative energy state ($E < -m_e$), emitting a photon with energy $E_\gamma > 2m_e$ and the atom would become unstable. To solve this problem, in 1930, Dirac formulated his "holes theory" [16], which uses the Pauli exclusion principle to define the vacuum state as a configuration where all the negative states are full of electrons (the Dirac see) and all the positive states are empty.

5 Following up the quantum mechanics version introduced by O. Klein and W. Gordon in 1926 with the formula $(\partial^\mu\partial_\mu + m^2)\phi(x) = 0$.

If one electron is added, necessarily will take a positive energy state. This hypothesis has important consequences. For instance, if an electron, from the Dirac see, absorbs a photon with energy $E_\gamma > 2m_e$, it would jump to a positive energy state, generating a hole. This idea explains the electron-position pair creation $\gamma \to e^+e^-$ and the opposite process $e^+e^- \to \gamma$ (annihilation), when the hole is filled up again. But most important, the theory predicted the existence of an electron with positive charge (positron).

The positron was discovered by C. Anderson in 1932 [17] meanwhile he was studying the cosmic rays in a magnetic field, using a Wilson chamber inside of a magnet (Fig. 2).

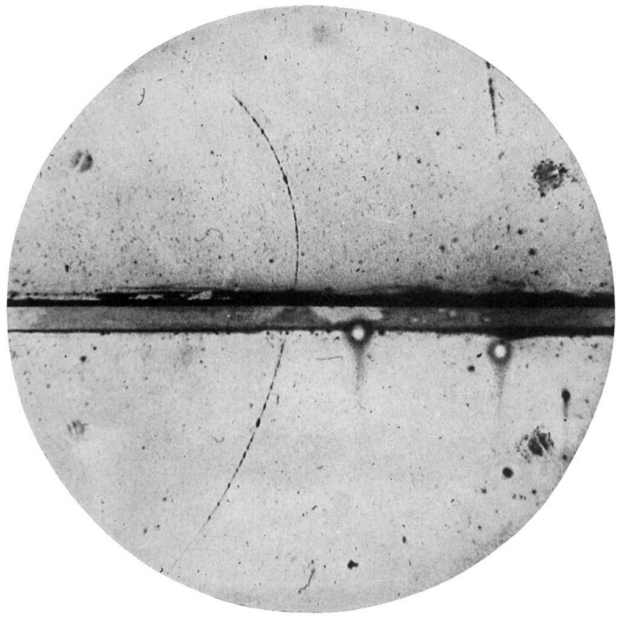

Figure 2: "A 63 million volt positron passing through a 6 mm lead plate and emerging as a 23 million volts positron ..." [18]. Image of the track left by a positron in a Wilson chamber, by C. Anderson (1932).

In 1930, W. Pauli introduced the idea of the neutrino, he explained the β-decay continuous spectrum ($A \to B + e^-$, i.e. ${}^{40}_{20}K \to {}^{40}_{19}Ca + e^-$) introducing a third particle, which he called "neutron". Three years later, E. Fermi postulated his β-decay theory [19] and concluded that the Pauli's particle had to be very light or massless and changed the name to "neutrino".

H. Yukawa, in 1935, published his theory about the nuclear force [7]. This theory described the interaction between a scalar field and a Dirac field and explained why the nucleus stick together against the $p - p$ electromagnetic repulsion. This happens due

to the exchange of scalar particles between nucleons, called "meson", later renamed as pion (π).

The π postulated by Yukawa and the photon (γ) were known as the scalar interaction particles and together with the known constituent particles $\binom{e}{\nu}\binom{p}{n}$, the matter was thought to be completely described.

Everything changed when, in 1937, S. Nedermeyer and C. Anderson discovered the muon (μ) [20]. They were studying the cosmic rays with the same Wilson chamber that was used to discover the positron. At first, they thought that it was the Yukawa "meson" but then realized that it behaved as an electron but heavier. It was the first particle of the second generation.

The Yukawa's π was discovered by C. Powell in 1947 [21], using nuclear emulsion plates. These plates were placed for long periods at high altitude on a mountain, to receive large doses of cosmic radiation. Same year, C. C. Butler and G. Rochester discovered a new particle (K_s^0), that behaved very unusually [22], this observation was the first evidence of one "strange" [6] particle. The rate of generation of these particles was really low and required long time of exposition to catch them. The construction of the first accelerators, made much easier these studies.

The Cosmotron, at Brookhaven National Laboratory (BNL), was the first proton synchroton constructed. The machine reached its full energy of 3.3 GeV in 1953. It was designed to reproduce cosmic rays interactions in a controlled environment. This machine enabled the massive production of particles [7], included the"strange" particles discovered by C. C. Butler and G. Rochester, allowing detailed studies of their interactions and properties. In 1952, A. Pais postulated that "strange" particles were produced via a strong interaction but decay via a weak interaction [23].

In 1953, F. Reines and C. L. Cowan made the first direct observation of a neutrino using β inverse decay reaction $\bar{\nu} + p \rightarrow n + e^+$ and the $\bar{\nu}$ produced in a nuclear reactor [24].

C. N. Yang and R. Mills, in 1954, applied the local gauge invariance theory[8] to higher dimension groups SU(N) [25]. In case of the weak isospin group SU(2), the lagrangian became that shown in equation 2, where $\vec{W}^\mu = (W_1^\mu, W_2^\mu, W_3^\mu)$ are the three gauge fields. It describes the interaction between a Dirac field and the three massless gauge bosons[9].

6 Particles composed by, at least, one strange-quark.

7 **Hundreds of new particles were discovered in two decades.**

8 $\mathcal{L}_{Dirac}$(Free)$\rightarrow$ $\mathcal{L}_{QED}$ (local gauge invariant), $\mathcal{L}_{QED} = \bar{\psi}(i\gamma^\mu \mathcal{D}_\mu - m)\psi = \bar{\psi}(i\gamma^\mu \partial_\mu - m)\psi - q\bar{\psi}\gamma^\mu\psi.\mathcal{A}_\mu = \mathcal{L}_{Dirac} - q\bar{\psi}\gamma^\mu\psi.\mathcal{A}_\mu$ (Appendix A).

9 Particles generated after requiring the local gauge invariance (Appendix A).

$$\begin{aligned}\mathcal{L}_{YM} &= \bar{\psi}(i\gamma^{\mu}\mathcal{D}_{\mu} - m)\psi - \frac{1}{16\pi}\vec{W}^{\mu\nu}\vec{W}_{\mu\nu} \\ &= \bar{\psi}(i\gamma^{\mu}\partial_{\mu} - m)\psi - g\bar{\psi}\gamma^{\mu}\frac{\vec{\sigma}}{2}\psi\vec{W}_{\mu} - \frac{1}{16\pi}\vec{W}^{\mu\nu}\vec{W}_{\mu\nu} \\ &= \mathcal{L}_{Dirac} - g\bar{\psi}\gamma^{\mu}\frac{\vec{\sigma}}{2}\psi\vec{W}_{\mu} - \frac{1}{16\pi}\vec{W}^{\mu\nu}\vec{W}_{\mu\nu}\end{aligned} \tag{2}$$

In 1956, M. Gell-Mann extended the idea of isospin (I_3) and introduced a new symmetry, the strangeness ($\mathcal{S}$) [10] [26]. This symmetry is conserved in strong interactions, but broken in weak interactions, following the explanation of A. Pais. Five years later, M. Gell-Mann [27] and Y. Ne'eman [28] proposed a sorting structure of the known hadrons, based on the representation of the SU(3) group (Fig. 3). The diagrams predicted particles not discovered yet and also an estimation of their masses, such as Ω^- particle, which was discovered, in 1964, at the Brookhaven National Laboratory (Fig. 4)[29].

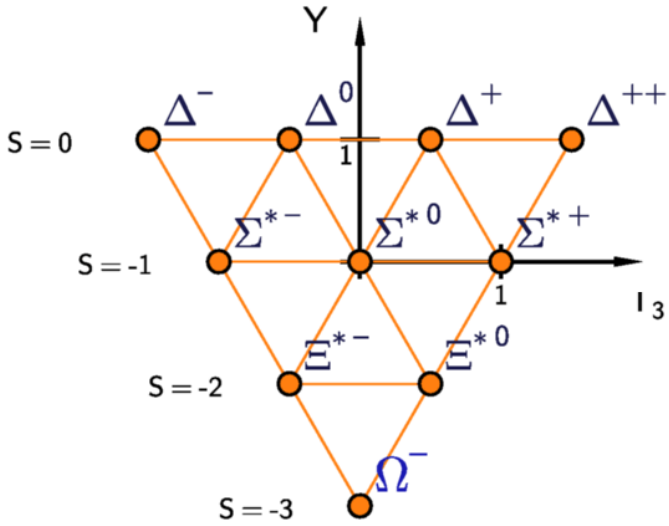

Figure 3: SU(3) decuplet of baryons. In black, known baryons, in blue, the missing particle (Ω^-) predicted by M. Gell-Mann and Y. Ne'eman.

In 1962, using the inverse decay reactions $\bar{\nu}_{\mu} + p \rightarrow n + \mu^+$, the muonic neutrino ($\nu_{\mu}$) was discovered, at BNL AGS, by L. M. Lederman, M. Schwartz and J. Steinberger [30].

In 1964, M. Gell-Mann [31] and G. Zweig introduced, independently, the quark model, which asserts that the particles, ordered as a representations of SU(3) (eightfold

10 Defining the charge relation $Q = I_3 + Y/2$ where the hipercharge was defined as $Y = \mathcal{B} + \mathcal{S}$, with the baryonic number ($\mathcal{B}$) and strangeness ($\mathcal{S}$).

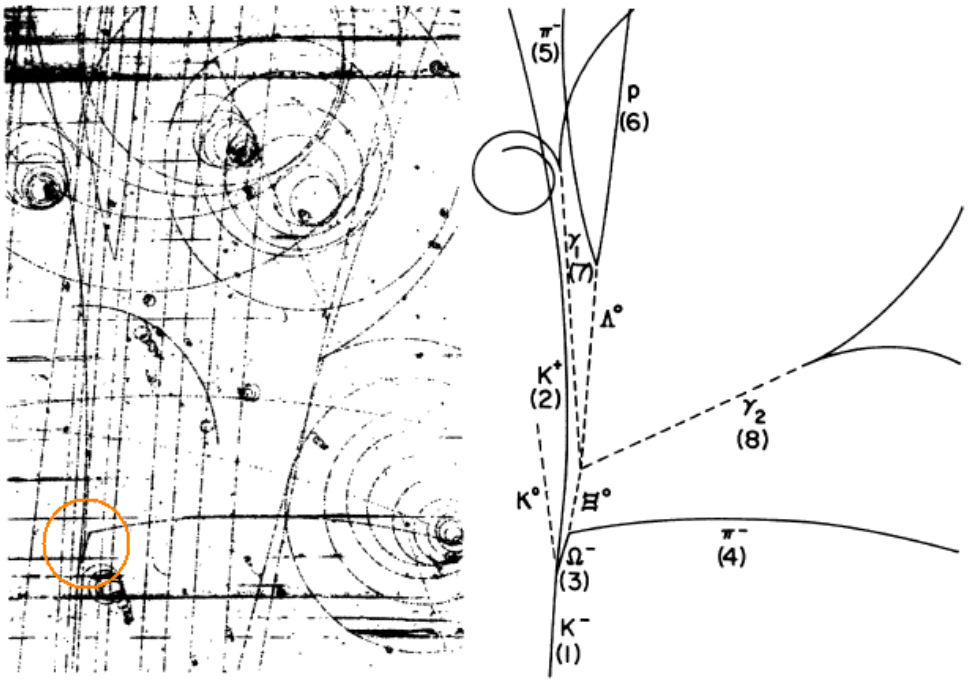

Figure 4: Discovery of Ω^- in a bubble chamber [29].

way), are composite objects that can be generated from the fundamental representations of this group ($SU(3)_F$ flavor). These fundamental particles were called "quarks" (u, d, s) and "antiquarks" $(\bar{u}, \bar{d}, \bar{s})$ [11]. Their fractional quantum numbers were defined as table 1 shown. This idea reduced the "jungle" of hadrons to three fundamental particles, but generated a couple of controversies. These constituent particles had never been observed free. Moreover, considering the case of the decuplet of baryons shown in figure 3, the Ω^- should be composed by $s \uparrow s \uparrow s \uparrow$, becoming a completely symmetric wave function and therefore breaking the Pauli exclusion principle. These issues were solved with the introduction of a new quantum number, the "color" [12]. The concept was based on the idea of M. Y. Han and Y. Nambu (1965) [32]. It postulated that all hadrons should be singlets of color, mesons $M = \frac{1}{\sqrt{3}}\delta_{ab}\left|q^a\bar{q}^b\right\rangle$ and baryons $B = \frac{1}{\sqrt{6}}\epsilon_{abc}\left|q^a q^b q^c\right\rangle$, making impossible the existence of a free quark (confinement). This idea turned the hadrons color antisymmetric, which solved the problem with the Pauli exclusion principle in all cases (Ω^-, Δ^{++}).

In 1961, S. L. Glashow, applied the results of C. N. Yang and R. Mills to weak isospin doublets $SU(2)_L$ and weak hypercharge group $U(1)_Y$ ($G \equiv SU(2)_L \otimes U(1)_Y$). And they

11 Antiquarks: the conjugated representation.
12 Quark color $\rightarrow q^a$ where $a = 1(R), 2(G), 3(B)$.

Quarks	Q	B	S	I_3	I	Y
u	2/3	1/3	0	1/2	1/2	1/3
d	-1/3	1/3	0	-1/2	1/2	1/3
s	-1/3	1/3	-1	0	0	-2/3

Table 1: Fractional quantum numbers of the constituent quarks.

achieved the unification of the weak and electromagnetic interactions and predicted the existence of a new weak neutral current [33]. However, only massless fields appear on the Lagrangian, even the fermions. The problem arose when these mass terms were included on the Lagrangian because gauge symmetry was broken. In 1964, P. W. Higgs, F. Englert and R. Brout proved that a new term can be added to the Glashow Lagrangian ($\mathcal{L}_{SBS}$), which preserve the gauge symmetry, but create a degenerated ground state. When one of these ground states is selected, the symmetry became spontaneously broken (Higgs Mechanism), providing mass to bosons and fermions and also predicting the existence of a new boson, called Higgs Boson [34].

In 1970, S. L. Glashow, J. Iliopoulos and L. Maiani introduced the GIM mechanism, which predicted the existence of a new quark (quark-charm - c), required to preserve the gauge invariance under $SU(2)_L \otimes U(1)_Y$ symmetry [35]. In 1974, the $J/\Psi = c\bar{c}$ meson was discovered, simultaneously, at the Stanford Linear Accelerator Center (SLAC) by B. Richter team and the Brookhaven National Laboratory (BNL) by S. Ting team, filling out the second family of quarks [13].

First attempt to apply the local gauge invariance to $SU(3)_c$ (strong interaction) was made by M. Gell-Mann, H. Leutwyler and H. Fritzsch in 1973 [36]. Same year, J. Gross, F. Wilczek and H. D. Politzer proved, theoretically, the concept of confinement on QCD. This theory evolved together with the electro-weak unification, constructing the currently known as Standard Model (SM) [14].

In 1975, the τ particle was discovered at SLAC, breaking the two families symmetry. This discovery opened the thirds family of leptons. It was detected indirectly via strange events that required its existence. They observed forbidden processes $e^+ + e^- \rightarrow e^{+-} + \mu^{+-}$, which break the leptonic symmetry. However, this symmetry can be recovered if the τ particle is included, $e^+ + e^- \rightarrow \tau^+ + \tau^- \rightarrow e^{+-} + \mu^{+-} + 4\nu$.

In 1977, in Fermilab, a new meson was discovered by the L. Lederman team [37]. It was very heavy and was recognized as the bounded state of a new quark ($\Upsilon = b\bar{b}$),

13 First family: $\begin{pmatrix} \nu_e & u \\ e^- & d \end{pmatrix}$ and second family: $\begin{pmatrix} \nu_\mu & c \\ \mu^- & s \end{pmatrix}$, plus the corresponding antiparticles.

14 Theory based on the gauge symmetry group $SU(3)_c \otimes SU(2)_L \otimes U(1)_Y$,

called "bottom" or "beauty".

First direct observation of the strong interaction mediator particles (gluons) were made by TASSO collaboration in 1979 [38][39], on the PETRA accelerator at Deutsches Elektronen-Synchrotron (DESY). They were detected studying events which included three jets on the final state ($e^+e^- \rightarrow q\bar{q} + g$).

In 1983, C. Rubbia and S. van der Meer, discovered and measured the mass of the $W^{\pm}$ and Z^0 bosons, in the UA1 and UA2 experiments [15], at CERN [40].

The massive production of Z^0 bosons at LEP (CERN), allowed to experimentally count, in 1990, the expected number of lepton families, measuring the cross section of the $e^+e^- \rightarrow \nu\bar{\nu} + \gamma$ [16]. The combined result from the four LEP experiments was $N_\nu = 2.984 \pm 0.008$ [41]. Furthermore, all data obtained during LEP and LEP2 periods were used to study the SM processes. This stablished its validity, including radiative corrections, which allowed to set bounds on the top-quark mass within the SM and constrain the expected mass of the Higgs boson.

The last quark was discovered at Tevatron (Fermilab) in 1993. It was named "top" and was observed in $p\bar{p}$ collisions with 1.8 TeV of energy [42]. This discovery, together with the direct observation of the ν_τ at DONuT (FNAL), in 2000 [43], closed the third family of leptons.

In 2012, a new particle, compatible with the Standard Model Higgs, was discovered at LHC (CERN), by the ATLAS and CMS experiments, with a mass of $M_H \sim 125$ GeV (Fig. 5) [44]. Being the last particle, predicted by the Standard Model, that was observed.

1.2 *The complete picture*

The most accurate theoretical framework capable to include all the particles and their interactions is the Standard Model. It is a gauge theory, based on the symmetry group $SU(3)_C \otimes SU(2)_L \otimes U(1)_Y$, that describes [17] the interactions between the constituent particles (fermions) and the interaction mediators (bosons). It includes, three families of fermions (Eq. 3), three massive bosons ($W^{\pm}$ and Z^0) from weak interaction, one massless photon (γ) from electromagnetic interaction, eight massless gluons (g) from strong interaction and the Higgs boson ($\mathcal{H}$), which generates the mass of the rest of elementary particles.

15 First evidences of the neutral currents, observed in Gargamelle in 1973 at CERN.
16 Using the realtion $N_\nu = \frac{\Gamma_{inv}}{\Gamma_l} \left(\frac{\Gamma_l}{\Gamma_\nu}\right)_{SM}$.
17 Excluding gravitational interaction.

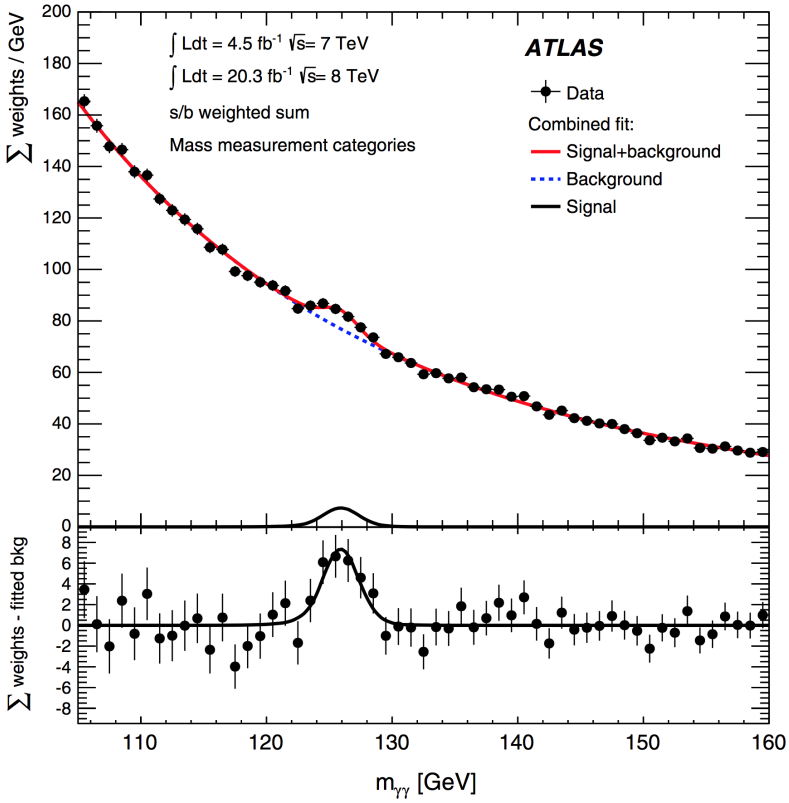

Figure 5: Invariant mass distribution for $h \to \gamma\gamma$, showing the peak corresponding to the Higgs boson [44]

$$\text{Fermion Families: } \begin{bmatrix} \nu_e & u \\ e^- & d \end{bmatrix} \begin{bmatrix} \nu_\mu & c \\ \mu^- & s \end{bmatrix} \begin{bmatrix} \nu_\tau & t \\ \tau^- & b \end{bmatrix}$$
$$\text{(plus its corresponding antiparticles)} \tag{3}$$

$$\text{Bosons: } \quad W^\pm, Z^0, \gamma, h$$

All these particles have been included or predicted by the Standard Model, and all of them have been experimentally observed. This proves the soundness of this theoretical framework. However, there are many phenomena to be understood and to be included to develop a complete theory of everything. The Standard Model does not provide a candidate for dark matter, does not include gravity and does not provide a satisfactory answer to the unbalance between matter and anti-matter. Alternative models, which incorporated good answers to these questions, need, for instance, the Higgs to be com-

posite or a larger number of Higgs particles or quarks. Because of that, there is a need of new searches. This searches can be done by increasing the energy threshold or by providing very high precision measurements of the properties of the Higgs and other particles. These goals will be the key of the high energy physics in the following years.

1.2.1 *Particles and more*

In the Standard Model, particles are divided in:

- Fermions (constituent particles): Characterized with the spin value $\frac{1}{2}$, they are divided in three families (Eq. 3), with same properties but different color numbers and masses. Each family is composed by two quarks (fractional charge) and two leptons. Quarks have an extra quantum number (color). Colored particles are not seen free in Nature, therefore, the quarks are confined in colorless structures called hadrons [18]. Ordinary matter is composed just with fermions from the first family. Hadrons created of fermions from other families will decay rapidly.

- Bosons (mediator particles of interactions): Characterized with an integer spin, they are the mediators of the interaction. In the Standard Model, the forces are described as the exchange of this spin-1 bosons. The electromagnetic interaction exchanges one massless photon (γ), the weak interaction three massive bosons ($W^{\pm}$ and Z^0), and the strong interaction eight colored, massless gluons (g).

- The Higgs boson (mass provider): h mediates the interaction with the Higgs field and the particles, the strength of this interaction determines the mass of the particle involved.

The interaction processes of these particles are described on the Standard Model via its theoretical formulation based on the gauge symmetry group $SU(3)_C \otimes SU(2)_L \otimes U(1)_Y$ of unitary gauge transformation [19]. The strong interaction, so called Quantum Chromodynamics (QCD), is based on the $SU(3)_C$ group of color. The eight gluons are the corresponding gauge bosons [36]. The electro-weak interaction, known as Glashow-Salam-Weinberg theory, is based on $SU(2)_L \otimes U(1)_Y$ group and the γ, $W^{\pm}$ and Z^0 are

18 All hadrons should be singlets of color, mesons $M = \frac{1}{\sqrt{3}}\delta_{ab}\left|q^a\bar{q}^b\right\rangle$ and baryons $B = \frac{1}{\sqrt{6}}\epsilon_{abc}\left|q^a q^b q^c\right\rangle$.

19 U(1) is the group of complex numbers with unit modulus.
SU(2) is the group of 2x2 unitary matrices, i.e $U^+U = UU^+ = 1$, with $detU = 1$. Any element of SU(2) can be written in terms of 3 generators ($\vec{\sigma}/2$) and 3 real parameters ($\vec{\theta}$), as $U = e^{i\vec{\theta}\vec{\sigma}/2}$, where $\vec{\sigma}$ are the Pauli matrices, which are traceless and satisfy $[\sigma_i, \sigma_j] = 2i\epsilon_{ijk}\sigma^k$, where ϵ_{ijk} is totally antisymmetric and its elements are the structure constants of SU(2).
SU(3) is the group 3x3 unitary matrices, i.e $U^+U = UU^+ = 1$, with $detU = 1$. Any element of SU(3) can be written in terms of 8 generators ($\lambda_\alpha/2$) and a set of 8 real parameters (θ_α) as $U = e^{i\theta^\alpha\lambda_\alpha/2}$. The generators are 3x3 hermitian matrices and are given by the so-called Gell-Mann matrices (λ_α), and satisfy $[\lambda_\alpha, \lambda_\beta] = if_{\alpha\beta\gamma}\lambda^\gamma$, where $f_{\alpha\beta\gamma}$ is totally antisymmetric and its elements are the structure constants of SU(3) [46].

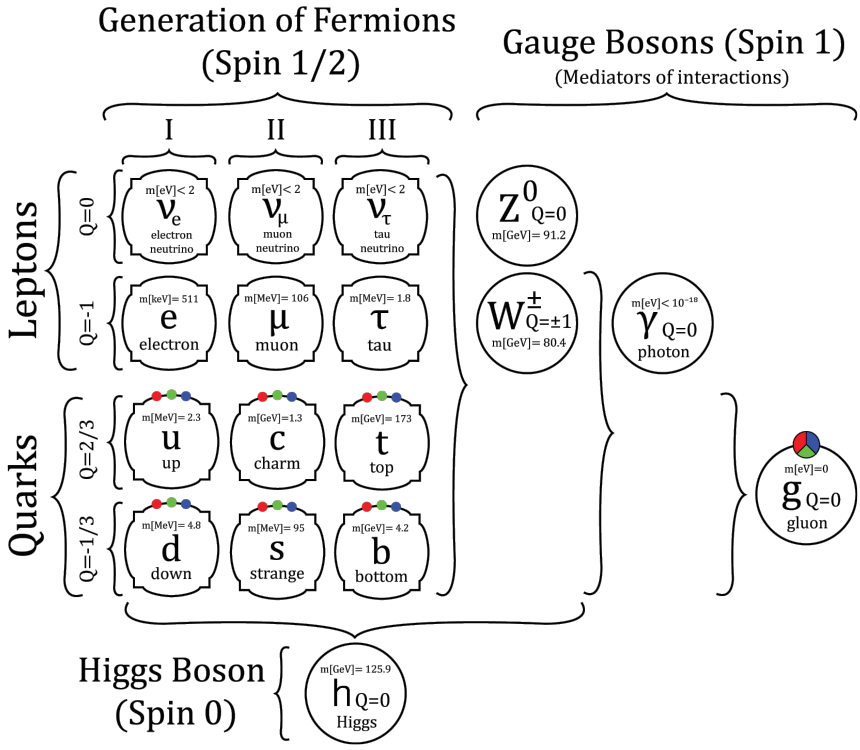

Figure 6: Particles table of the Standard Model. Left, the constituent particles of the matter (fermions), ordered by families. Right, the gauge bosons, ordered according the particles that are affected by the interaction. Bottom, the Higgs boson. The colored particles are shown with color dots around the box [45].

the corresponding gauge bosons [33]. This theory does not include, by default, mass terms for the $W^{\pm}$ and Z^0 bosons and other fermions. To include them, the so called Spontaneous Symmetry Breaking (SSB) has to be implemented via the Higgs Mechanism [34]. In order to understand the theoretical formulation of SM, basic theoretical aspects will be introduced (See Appendix A).

1.2.2 *Brush Strokes of Quantum Chromodynamics*

In the sixties, the number of hadrons discovered raised dramatically, inferring hints to reconsider the definition of the fundamental particles. M. Gell-Mann and G. Zweig [31] proposed the existence of quarks as a fundamental components of all the known particles (considering them as a composite structures). This description was called the SU(3) quark model.

However, the quark model does not satisfy the Pauli exclusion principle in every case. The most famous case was the Δ^{++} paradox. This particle is made of three quarks with identical quantum numbers. Therefore, it has a totally symmetric wave function. This issue was solve by the introduction of the color quantum number. Each quark type may have $N_C = 3$ different colors, q^α where $\alpha = 1, 2, 3$ (red, green, blue). In order to solve the problem of non-observed colored states, the asymptotic states must be defined as colorless. This assumption is known as the confinement hypothesis [20] (Eq. 4).

$$\text{Mesons: } M = \frac{1}{\sqrt{3}}\delta_{ab}\left|q^a\bar{q}^b\right\rangle;\ \text{Baryons: } B = \frac{1}{\sqrt{6}}\epsilon_{abc}\left|q^a q^b q^c\right\rangle \tag{4}$$

The existence of the color can be tested, experimentally, using the ratio $R_{e^+e^-}$ (Eq. 5). Considering energies bellow the Z peak, the cross-section is dominated by the γ - exchange amplitude and the ratio $R_{e^+e^-}$ can be approximated as the squared sum of the electric charge of the quarks involved and proportional to the number of colors (N_C). The creation of quarks depends on the interaction energy, if the available energy is enough to create them, the ratio $R_{e^+e^-}$ will change. Therefore, $R_{e^+e^-}$ representation, as a function of the energy, will include steps where energy become enough to create a new pair of quarks[21] (Fig. 7).

$$R_{e^+e^-} \equiv \frac{\sigma(e^+e^- \to \text{hadrons})}{\sigma(e^+e^- \to \mu^+\mu^-)} \approx N_C \sum_{k=1}^{N_f} Q_f^2 \tag{5}$$

Quantum Chromodynamics (QCD) is the gauge theory for the strong interactions. It is based on the $SU(3)_C$ color gauge symmetry. Starting with a free Lagrangian $\mathcal{L}_0 = \sum_f \bar{q}_f(i\gamma^\mu\partial_\mu - m_f)q_f$, which describes free colored particles [22]. It is invariant under global arbitrary transformations of $SU(3)_C$. The global transformation can be written as $U = e^{i(\lambda^a/2)\theta_a}$, where $\lambda^a (a = 1, 2, ..., 8)$ are the generators of the fundamental representation of the $SU(3)_C$, known as the Gell-Mann matrices[23].

Analogously to QED (See Section A.1), the gauge principle requires the invariance under local gauge transformations $U = e^{i(\lambda^a/2)\theta_a(x)}$, which parameter ($\theta_a(x)$) depends on space-time coordinates. Therefore, the derivative should be redefined as a covariant derivative (Eq. 6).

20 It purport the non-existence of free quarks, because they carry color, which lock them within color-singlet bound states.

21 i.e. $N_f = 3 : u, d, s \to R_{e^+e^-} = 2$, $N_f = 4 : u, d, s, c \to R_{e^+e^-} = \frac{10}{3}$, $N_f = 5 : u, d, s, c, b \to R_{e^+e^-} = \frac{11}{3}$

22 Vector notation: $q_f^\alpha = \vec{q}_f = (q_f^1, q_f^2, q_f^3)$, where q_f^α denotes a quark field of color α and flavor f.

23 The commutation relation of the $SU(3)_C$ matrices is $[t^a, t^b] = if^{abc}t^c$, where $t^a = \lambda^a/2$ and f^{abc} are the structure constants.

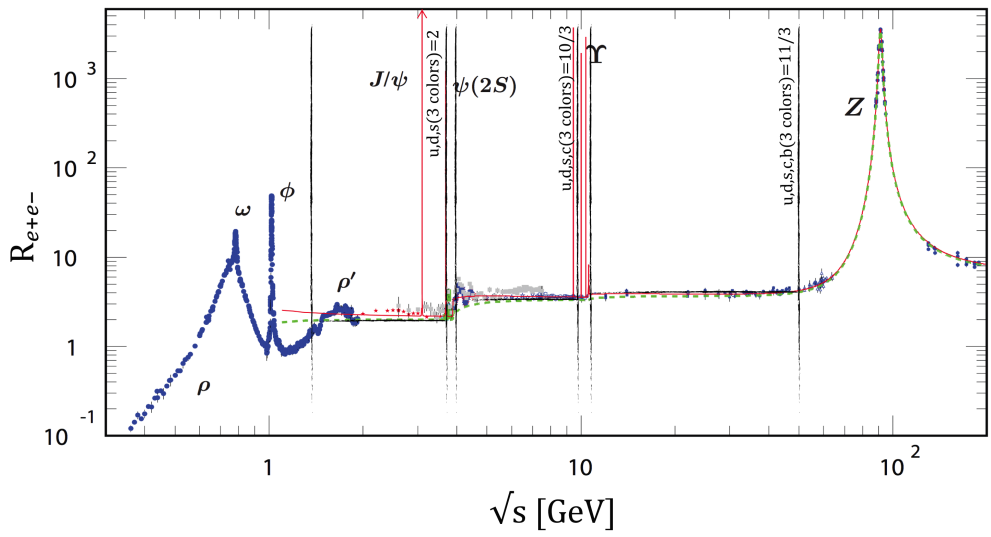

Figure 7: World data $R_{e^+e^-}$ ratio[45] as a function of the center-of-mass energy. The center-of-mass energy regions are separated, with vertical lines, in terms of the quarks that the processes are capable to generated, the $R_{e^+e^-}$ ratio changes when new quarks can be produces.

$$D^\mu q_f \equiv \left(\partial^\mu + i g_s \frac{\lambda^a}{2} G_a^\mu(x)\right) q_f \tag{6}$$

This process will create eight massless gauge bosons (gluons), corresponding to the $SU(3)_C$ generators, which require a kinetic term to be included, $G_a^{\mu\nu} = \partial^\mu G_a^\nu - \partial^\nu G_a^\mu + g_s f^{abc} G_b^\mu G_c^\nu$, where f^{abc} are the structure constants of $SU(3)_C$. The resulting Lagrangian is shown in equation 7.

$$\begin{aligned}
\mathcal{L} &= \sum_f \bar{q}_f (i\gamma^\mu D_\mu - m_f) q_f - \frac{1}{4} G_a^{\mu\nu} G^a_{\mu\nu} \\
&= \mathcal{L}_0 - \frac{1}{4}(\partial^\mu G_a^\nu - \partial^\nu G_a^\mu)(\partial_\mu G_\nu^a - \partial_\nu G_\mu^a) \\
&+ g_s G_a^\mu \sum_f \bar{q}_f^\alpha \gamma_\mu \left(\frac{\lambda^a}{2}\right)_{\alpha\beta} q_f^\beta \\
&- \frac{g_s}{2} f^{abc} (\partial^\mu G_a^\nu - \partial^\nu G_a^\mu) G_\mu^b G_\nu^c \\
&- \frac{g_s^2}{4} f^{abc} f_{ade} G_b^\mu G_c^\nu G_\mu^d G_\nu^e
\end{aligned} \tag{7}$$

The Lagrangian shows the propagator terms and the interactions between quarks and gluons, which involves the $SU(3)_C$ matrices λ^a. Also, the $G_a^{\mu\nu} G^a_{\mu\nu}$ term gen-

erates cubic and quartic gluon self-interactions, which is a consequence of the non-commutativity of the $SU(3)_C$ group. The self-interaction is a new concept that does not appear in QED and could explain properties like asymptotic freedom [24] or the confinement [25]. Another important consequence is that quarks can emit gluons. The interactions are given in terms of g_s and the strong coupling constant is defined as $\alpha_s = g_s^2/4\pi$.

First evidences of the gluon existence were obtained at PETRA (DESY), in 1979 [38][39]. Gluon emission was studied in e^+e^- annihilation ($e^+e^- \rightarrow q\bar{q}g$). In this processes, the colored quarks create many $q - \bar{q}$ pairs, which, finally, were arranged in colorless hadrons with same direction as the original quark. This process is called *hadronization* and the particles are grouped in entities called *jets*. However, one quark, before starting the hadronization process, can radiate gluons, which having enough angular separation from the original quark, will become an extra *jet*. The study of the three final jet topologies were used to measure the strong coupling constant and the spin of the gluon.

Analogously to QED, the $SU(3)_C$ gauge symmetry forbids to add a mass term for the gluon fields ($\frac{1}{2}m_G^2 G_a^\mu G_\mu^a$), due to the invariance conservation. The gauge fields will be massless, but since there are no evidences that suggest mass for the gluon, mass terms are not required.

1.2.3 *Electroweak Interaction theory.*

The construction of the electroweak gauge group is based on the experimental observations of β decays, such $\mu^- \rightarrow e^-\bar{\nu}_e\nu_\mu$, and the study of data from neutral currents interactions (Z^0), which observed that [47]:

- Only left-handed (right-handed) fermions (antifermions) chiralities [26] participate on weak transitions.
- The neutral current interaction are flavor conserving, only coupling to fermion-antifermion pairs appear [27].
- Photons (γ) interact equally for both chiralities and right-handed neutrinos do not interact in any case.

All these features have to be included on a group theory. For this, the left-handed fermion interactions were described as $SU(2)_L$ group (weak isospin). On the other hand,

24 Sort distances $\rightarrow$ the interaction became weaker.
25 Large distances $\rightarrow$ the interaction became stronger
26 Left-handed and right-handed fields are defined using the chirality operator $\gamma_5 = i\gamma_0\gamma_1\gamma_2\gamma_3$ as $\phi_L = \frac{1}{2}(1-\gamma_5)$ and $\phi_R = \frac{1}{2}(1+\gamma_5)$.
27 Always observed $\gamma \rightarrow f\bar{f}$ and $Z^0 \rightarrow f\bar{f}$ and never transition such $\mu \not\rightarrow e\gamma$ or $Z \not\rightarrow e^\pm, \mu^\pm$.

Q (charge) was not a good quantum number, because the doublets $\binom{u_L}{d_L}$ do not share the same Q (charge) value. A solution was to use the hipercharge quantum number Y, defined as $Y = Q - I_3$. To include the rigth-handed fermions, the $U(1)_Y$ group is used. The final gauge group were defined as $G = SU(2)_L \otimes U(1)_Y$ [28], which has four generators, three from $SU(2)_L$ ($T_i = \sigma_i/2$) and one from $U(1)_Y$ ($Y/2$) [46].

A free Lagrangian of G can be represented as $\mathcal{L} \equiv \sum_{j=1}^{3} \bar{\psi}_j(x)\gamma^\mu \partial_\mu \psi_j(x)$, where the fields will be defined such $\psi_1(x) = \binom{u}{d}_L, \psi_2(x) = u_R, \psi_3(x) = d_R$. Analogously to QED (See Section A.1), the gauge principle requires the invariance under local gauge transformations. To do this, the Lagrangian will be transformed to equation 8, including the covariant derivative and the kinetic terms $\mathcal{L}_K$.

$$\begin{aligned} \mathcal{L}_f &\equiv \sum_{j=1}^{3} \bar{\psi}_j(x)\gamma^\mu D_\mu \psi_j(x) + \mathcal{L}_K \\ \mathcal{L}_K &\equiv -\frac{1}{4} W^i_{\mu\nu} W^{\mu\nu}_i - \frac{1}{4} B_{\mu\nu} B^{\mu\nu} \end{aligned} \tag{8}$$

Developing the Lagrangian, the charged-currents part ($\mathcal{L}_{CC}$) is shown in equation 12, which defines the interaction between fermion and charged gauge bosons (Fig. 8).

$$\mathcal{L}_{CC} = \frac{g}{2\sqrt{2}} (W^+_\mu [\bar{u}\gamma^\mu(1-\gamma_5)d + \bar{\nu}_l \gamma^\mu (1-\gamma_5) l] + \text{h.c.}) \tag{9}$$

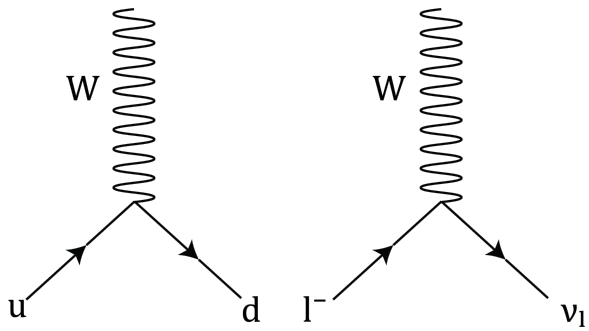

Figure 8: Interaction vertices of *W* (charged current) with quarks and leptons.

On the other hand, the *physical gauge bosons* from the neutral current (Z_μ and A_μ) should be defined as an arbitrary combination of the gauge bosons introduced on the

28 i.e. first family $\rightarrow \begin{bmatrix} \nu_l & u \\ l^- & d \end{bmatrix} \equiv \binom{\nu_l}{l^-}_L, \binom{u}{d}_L, l^-_R, u_R, d_R$.

theory, W^3_μ and B_μ [29]. The definition is shown in equation 10 in terms of the Weinberg angle (θ_w).

$$\begin{pmatrix} W^3_\mu \\ B_\mu \end{pmatrix} = \begin{pmatrix} cos\theta_w & sin\theta_w \\ -sin\theta_w & cos\theta_w \end{pmatrix} \begin{pmatrix} Z_\mu \\ A_\mu \end{pmatrix} \tag{10}$$

$$\begin{aligned} Z_\mu &= cos\theta_w W^3_\mu - sin\theta_w B_\mu \\ A_\mu &= cos\theta_w W^3_\mu + sin\theta_w B_\mu \end{aligned} \tag{11}$$

The neutral-current interaction Lagrangian, in terms of the *physical gauge bosons* is shown in equation 12, which defines the interactions with fermions (Fig. 9).

$$\begin{aligned} \mathcal{L}_{NC} &= \mathcal{L}^A_{NC} + \mathcal{L}^Z_{NC} \\ &= \sum_j \bar{\psi}_j \gamma^\mu (A_\mu [g T_3 sin\theta_w + g' Y cos\theta_w] \\ &+ Z_\mu [g T_3 cos\theta_w - g' sin\theta_w]) \psi_j \end{aligned} \tag{12}$$

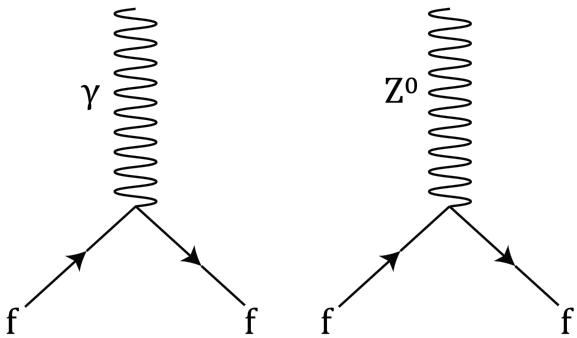

Figure 9: Interaction vertices of Z (neutral current) with fermions.

The comparison between the neutral-current term $\mathcal{L}^A_{NC}$ and the QED Lagrangian, $\mathcal{L}_{QED} = \mathcal{L}_0 - eqA_\mu(x)\bar{\psi}(x)\gamma^\mu\psi(x) - \frac{1}{4}F^{\mu\nu}F_{\mu\nu}$, generate the relations $e = g' cos\theta_w = g sin\theta_w$, which can be written as show equation 13.

$$g = \frac{e}{sin\theta_w};\ g' = \frac{e}{cos\theta_w};\ Q = T_3 + Y \tag{13}$$

These relations provide the unification of the weak and electromagnetic interactions, besides, the final Lagrangian only contains massless fields, for the gauge bosons and

29 Considering the previous definition of hipercharge: $Q(A_\mu) = Y(B_\mu) + T_3(W^3_\mu)$.

even for the fermions. The inclusion of the mass terms must be done preserving the gauge symmetry. The solution was to use the spontaneous symmetry breaking (SSB) of the $SU(2)_L \otimes U(1)_Y$ and the Higgs mechanism [47].

1.2.4 *The missing masses and the Higgs boson*

As Appendix A introduced, the method to include mass terms on a local gauge symmetric Lagrangian is based on adding a term ($\mathcal{L}_{SSB}$), which keeps the invariance of the Lagrangian under G $=SU(2)_L \otimes U(1)_Y$ and transforms the ground state (vacuum), in such way that has a degenerated set of states with minimal energy. This means that ground state does not posses the gauge symmetry anymore. When one of these degenerated states is arbitrarily selected, the symmetry is spontaneously broken [30] and the mass terms appear, together with a new boson (Higgs Boson)[46].

Likewise Goldstone model postulates, the easiest choice is to define the Lagrangian extra term as show equation 14 (Fig. 129).

$$\begin{aligned} &\mathcal{L}_{SSB} = (D_\mu \phi)^\dagger (D^\mu \phi) - V(\phi) \\ &V(\phi) = -\mu^2 \phi^\dagger \phi + \lambda (\phi^\dagger \phi)^2 \\ &\text{where } \lambda > 0 \text{ and } -\mu^2 < 0 \end{aligned} \tag{14}$$

The $SU(2)_L$ doublet of complex scalar fields and the covariant derivative under G are defined in the equation 15.

$$\phi(x) = \begin{pmatrix} \phi^+ \\ \phi 0 \end{pmatrix}; \; D_\mu \phi = (\partial_\mu - \frac{1}{2} i g \vec{\sigma} \vec{W}_\mu - \frac{1}{2} i g' B_\mu)\phi \tag{15}$$

The parameter values chosen, on the potential (Eq. 14), will generate a set of degenerated states with the energy minimum that equation 16 shown.

$$|\langle 0||\phi||0\rangle| = \sqrt{\frac{-\mu^2}{2\lambda}} \equiv \frac{v}{\sqrt{2}} \tag{16}$$

To spontaneously break the $SU(2)_L \otimes U(1)_Y$ symmetry, the vacuum has to be fixed by choosing arbitrarily one ground state. The $SU(2)_L$ scalar field can be parametrized as show equation 17 where $\vec{\theta}(x)$ and $h(x)$ are four real fields (Section A.3).

$$\phi(x) = e^{i \frac{\theta^i(x)\sigma_u}{2}} \frac{1}{2} \begin{pmatrix} 0 \\ v + h(x) \end{pmatrix} \tag{17}$$

30 The SSB mechanism will appear when there is a symmetric Lagrangian, but a non-symmetric vacuum.

The $SU(2)_L$ allows to rotate any dependence on $\theta^i(x)$ to the unitary (physical) gauge $\theta^i(x) = 0$. The derivative term of the scalar Lagrangian will change to the equation 18.

$$\begin{aligned}(D_\mu\phi)^\dagger(D^\mu\phi) &= \frac{1}{2}\partial_\mu h\partial^\mu h + \\ &(v+h)^2\left(\frac{g^2}{4}W_\mu^\dagger W^\mu + \frac{g^2}{8\cos^2\theta_W}Z_\mu Z^\mu\right) \\ &= \frac{1}{2}\partial_\mu h\partial^\mu h + \frac{1}{2}(2\mu^2)h^2 \\ &+ \frac{1}{2}\left(\frac{g^2v^2}{2}\right)W_\mu^\dagger W^\mu \\ &+ \frac{1}{2}\left(\frac{g^2v^2}{4\cos^2\theta_w}\right)Z_\mu Z^\mu + \text{interactions}\end{aligned} \tag{18}$$

The $W^\pm$ and the Z^0 (not the γ, because $U(1)_{QED}$ is an unbroken symmetry) have acquired masses and the Higgs boson is generated (Eq. 19).

$$\begin{aligned}M_W &= \frac{gv}{2} \\ M_Z &= \frac{gv}{2\cos\theta_w} = \frac{M_W}{\cos\theta_w} \\ M_H &= \sqrt{2}\mu\end{aligned} \tag{19}$$

The masses of the $W^\pm$ and the Z^0 bosons were measured at CERN SPS collider, in 1985 [40]. The charged vector boson mass was $m_{W^\pm} = 81 \pm 2$ GeV/c^2 and the neutral boson mass $m_{Z^0} = 93 \pm 3$ GeV/c^2 . Currently the most accurate values obtained are $m_{W^\pm} = 80.339 \pm 0.023$ GeV/c^2 and $m_{Z^0} = 91.1875 \pm 0.0021$ GeV/c^2 , which allows to obtain a precise estimation of the electroweak mixing angle $\sin^2\theta_w = 1 - M_W^2/M_Z^2 = 0.223$ [48] [45].

The Higgs Boson was discovered, in 2012, by two experiments of the Large Hadron Collider (LHC) , ATLAS and CMS, the mass obtained was $m_H = 125.09 \pm 0.21$ (stat.) $\pm$ 0.11 (syst.) [49].

In order to provide mass to the fermions, without breaking the gauge symmetry, an additional piece needs to be added to the Lagrangian, which is called the Yukawa Lagrangian [31] [50] (Eq. 20).

31 This Lagrangian only includes the first family of fermions, but can be extrapolated to all of them.

$$\begin{aligned}&\mathcal{L}_Y = \lambda_e \vec{l}_L \phi e_R + \lambda_u \vec{q}_L \tilde{\phi} u_R + \lambda_d \vec{q}_L \phi d_R + \text{h.c.}\\&\text{where } \vec{l}_L = \begin{pmatrix}\nu_L\\ e_L\end{pmatrix};\ \vec{q}_L = \begin{pmatrix}u_L\\ d_L\end{pmatrix};\ \tilde{\phi} = i\sigma_2\phi^* = \begin{pmatrix}\phi_0^*\\ -\phi^-\end{pmatrix}\end{aligned} \tag{20}$$

In the unitary gauge, the Yukawa Lagrangian became the equation 21 and includes the mass terms for the fermions, proving that the SSB also generates the fermion masses.

$$\begin{aligned}&\mathcal{L}_Y = -\frac{1}{\sqrt{2}}(v+h)\left(\lambda_e e\bar{e} + \lambda_u u\bar{u} + \lambda_d d\bar{d}\right)\\&m_e = \lambda_e \frac{v}{\sqrt{2}};\ m_u = \lambda_u \frac{v}{\sqrt{2}};\ m_u = \lambda_u \frac{v}{\sqrt{2}}\\&\mathcal{L}_Y = -\left(1+\frac{h}{v}\right)\left(m_e e\bar{e} + m_u u\bar{u} + m_d d\bar{d}\right)\end{aligned} \tag{21}$$

The Higgs mechanism provides masses to the gauge bosons ($W_\pm$ and Z^0) and the fermions. It is important to notice that all fermion masses depend on λ_i parameter and since this parameter is not known, the masses are completely arbitrary. Furthermore, the interaction coupling constants of the Higgs boson and the other particles are proportional to the particle mass itself (Eq. 22).

$$\begin{aligned}&f\bar{f} \propto -\frac{igm_f}{2M_W};\\&W_\mu^\dagger W_\nu h \propto igM_W g_{\mu\nu};\\&Z_\mu Z_\nu h \propto \frac{ig}{\cos\theta_w} M_Z g_{\mu\nu}\end{aligned} \tag{22}$$

As is shown in equation 22, the mass of the fermions and bosons are basic input parameters on the Standard Model. It means that to perform accurate predictions, it is crucial to have a very precise measurements of the fermion and boson masses. On the other hand, the discovery of the Higgs boson concluded the first stage of this lengthy quest, proving that Higgs mechanism is not just a mathematical solution to the problem of the Standard Model masses, but a real mechanism that, in fact, provides mass to the elementary particles. The Higgs boson is the cornerstone of the Standard Model, therefore, it becomes fundamental to develop new method and new tools to measure, as precisely as possible all the Higgs boson properties.

2 Future e^+e^- Colliders

The discovery of the Higgs boson, with the ATLAS and CMS experiments, was a crucial event that moved, as a priority, the measurement with high precision of all properties of this new particle and its couplings. Moreover, the need for new searches, to confirm or deny alternative theories to the Standard Model requires new collider strategies to be successfully applied. In this chapter, some of these future projects will be, briefly, introduced. First, the e^+e^- linear colliders, which intend to reach unprecedented collision energies. The International Linear Collider (ILC) with an energy range of $\sqrt{s} = 250 - 500$ GeV (extendable to 1 TeV) [51] and the Compact Linear Collider (CLIC) [52], capable to cover a range between $\sqrt{s} = 380$ GeV $- 3$ TeV. On the other hand, the Super Flavor Factory (SFF), SuperKEKB, which will generate unprecedented luminosities, in a circular e^+e^- machine, using asymmetric beams (4 GeV, 7 GeV) to study with high accuracy the $\Upsilon(4S)$ resonance decay [53].

2.1 *High energy physics at linear e^+e^- colliders*

Hadron colliders can reach much higher energies than e^+e^- colliders, however, the latter option presents many advantages in terms of precision. In hadron collisions, the energy transferred to the processes is not well defined since hadrons are composite particles. Electrons (e^-) and positrons (e^+) are point-like particles, therefore, the interaction energy is very close to the nominal energy (there are other effects can change this value, like beam energy spread, initial state radiation...). Moreover, the environment on electron-positron collisions is much more benign, as for example the LHC where about 30 proton-proton collisions occur every 50 ns, producing hundreds of energetic particles. These differences will have a large implication on the detectors design. Hadrons colliders require radiation-hard materials to handle the background, thicker calorimeters to contain the outgoing particles and a very complex trigger system. The e^+e^- interactions are pretty clean, therefore, the design of the detectors can be focused on improving the precision of the different sub-detectors. Likewise, the cross-section cal-

culations, relying on QCD, include corrections, at NLO, around $30-50\%$. On the other hand, e^+e^- interactions only include couplings through the electroweak interactions, which, at first order, have corrections at a few-percent level. In general, the simplicity of e^+e^- interactions environment opens the door to perform, with unprecedented precision, new physic studies.

The discovery of the Higgs boson with a mass around 125 GeV, confirmed that interaction energies greater than 250 GeV are not required to produce Higgs bosons [1]. However, the future linear collider projects go further in term of energy of interaction (ILC up to 1 TeV and CLIC up to 3 TeV), allowing a precise estimation of many Standard Model parameters and perform searches of exotic particles in a very large mass range (Tab. 2) [54].

Energy	Reaction	Physics Goal
91 GeV	$e^+e^- \to Z$	precise electroweak studies
160 GeV	$e^+e^- \to WW$	precise W mass measurement
250 GeV	$e^+e^- \to Zh$	precise Higgs coupling studies
$350-400$ GeV	$e^+e^- \to t\bar{t}$	precise quark mass and coupling studies
	$e^+e^- \to WW$	precise W coupling studies
	$e^+e^- \to \nu\bar{\nu}h$	precise Higgs coupling studies
500 GeV	$e^+e^- \to f\bar{f}$	precise searches for Z'
	$e^+e^- \to t\bar{t}h$	Higgs coupling to top-quark studies
	$e^+e^- \to Zhh$	Higgs self-coupling studies
	$e^+e^- \to \tilde{\chi}\tilde{\chi}$	search for supersymmetry
	$e^+e^- \to AH, H^+H^-$	search for extended Higgs states
700 GeV and more	$e^+e^- \to \nu\bar{\nu}hh$	Higgs self-coupling studies
	$e^+e^- \to \nu\bar{\nu}VV$	composite Higgs sector studies
	$e^+e^- \to \nu\bar{\nu}t\bar{t}$	composite Higgs and top-quark studies
	$e^+e^- \to \tilde{t}\tilde{t}*$	search for supersymmetry

Table 2: Processes to be studied, at e^+e^- colliders, in terms of the interaction energy range [54].

Table 2 shows the main studies that can be performed on e^+e^- colliders at different interaction energies. In general, the measurement of the Standard Model basic parameters (masses, coupling ...) will be performed on the first energy ranges. But the

1 Higgsstrahlung: Higgs production in association with Z boson $\to e^+e^- \to Zh$.

capability of cover much higher energies, opens the door to perform searches of new physic phenomena and exotic particles with unique precision.

2.2 *The International Linear Collider (ILC)*

The International Linear Collider will be constructed using two linear accelerators facing each other. The electrons (e^-) and positrons (e^+) will be accelerated on their corresponding branches to be smashed on the halfway point, where the detectors will be located. Since the particles will go through the accelerators only one time, a huge gradients and a long acceleration stage are required. The accelerator technology is based on 1.3 GHz superconducting radio-frequency (SCRF) cavities, working at 2 K with an average accelerating gradient of 31.5 MV/m. The nominal interaction energy spans a range between $250 - 500$ GeV, upgradable to 1 TeV in a second phase. The expected nominal luminosity will be 1.8×10^{34} cm^{-2}s^{-1} [2].

This design is the results of almost twenty years of development. Since 2005 the ILC has become a worldwide international collaboration, where more than 300 national laboratories, universities and institutes have participated. This effort has been reflected on the technical design report published on 2013 [51]. The machine operation will be done at different interaction energies to cover various region of interest. The possible running stages are summarized in table 3.

Scenario	$\sqrt{s}$ [GeV]	500	350	250	L-500	L-350	L-250
G-20	$\mathcal{L}$ [fb^{-1}]	1000	200	500	4000	—	—
	time [years]	5.5	1.3	3.1	8.3	—	—
H-20	$\mathcal{L}$ [fb^{-1}]	500	200	500	3500	—	1500
	time [years]	3.7	1.3	3.1	7.5	—	3.1
I-20	$\mathcal{L}$ [fb^{-1}]	500	200	500	3500	1500	—
	time [years]	3.7	1.3	3.1	7.5	3.4	—
Scenario	$\sqrt{s}$[GeV]	250	500	350	L-250	L-500	L-350
Snow	$\mathcal{L}$ [fb^{-1}]	250	500	250	900	1100	—
	time [years]	4.1	1.8	1.3	3.3	1.9	—

Table 3: Accumulated luminosity and running-time stages in the proposed energy scenarios, up to 500 GeV. The table is divided by a vertical line: the columns on the left represent the stages on a first phase, the columns on the right shows possible stages in a second phase [55].

2 Nominal energy of 500 GeV.

2.2.1 *Accelerator*

The total length of ILC will be 31 km, divided in two branches (Fig. 10). Each branch will host one linac (based on SCRF cavities) of 11 km. Both linacs will be placed with 5 km separation, this region is reserved to the different subsystems (damping rings, e^+e^- sources...) and the detectors.

The acceleration process can be described, briefly, as follows. First, the particles generated on the electron and positron sources will be stored and pre-accelerated on the damping rings, then, the conformed bunches will be injected on the main linacs, afterwards, the bunches will be accelerated to the nominal energy. Finally, the bunches will collide on a single interaction point on the center of the detector. The main subsystems involved are the followings [55]:

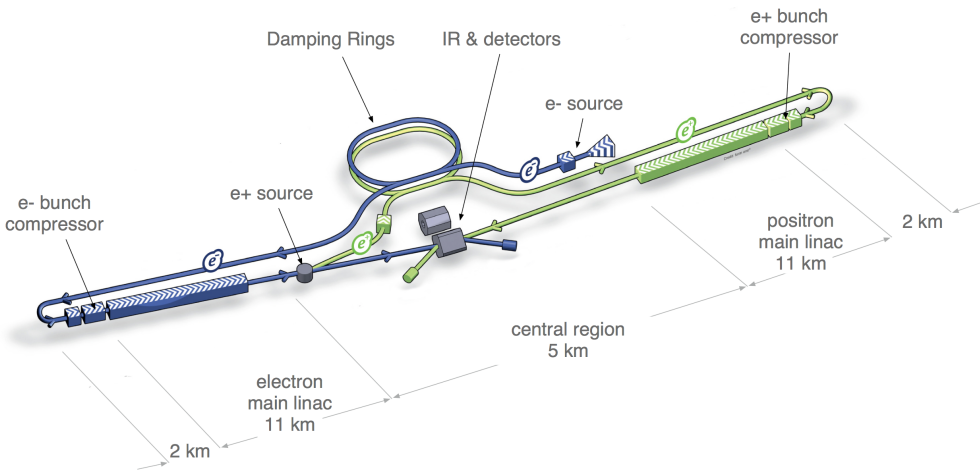

Figure 10: Schematic layout of the ILC (not to scale) [56]

- **Electron Source (DC gun):** Two lasers (DC gun), pointed on a photocathode generate bunches of polarized electrons (expected polarization over 80%). Afterwards, the bunches are pre-accelerated up to 5 GeV to be injected on its corresponding damping ring.
- **Positron Generator:** The polarized positron bunches (expected polarization around 30%) have to be created by pair production. To produce this process, the electron bunches from main linac are deflected to pass through an undulator. Here, a high energetic photon beam is generated, afterwards, the electron bunches are sent back to the main linac. The photon beam generated hits thin metal layers to create electron-positron pairs. The positrons are selected, pre-accelerated up to 5 GeV and stored on its damping ring.

- **Damping Rings:** The 3.2 km damping rings, located in the same tunnels, are meant to store and stabilize the incoming bunches from the sources. At first, the injected bunches (5 GeV of energy) will have a large transverse and longitudinal emittance, but the rings are designed to reduce the emittance using a combination of oscillators and SCRF chambers.

- **Ring to Main Linac (RTML):** Identical subsystem for electrons and positrons, meant to transport the 5 GeV fermions to the main linacs. It also includes collimators and the capability to orient the beam polarization to the desired direction. Before the injection, the bunches go through the **bunch compressor**, which reduces, in two stages, the size of the bunch trains from mm to few hundreds of μm, increasing the energy up to 15 GeV.

- **Superconducting RF Main Linacs:** The ILC main linacs accelerate the beam from 15 GeV to a maximum energy of 250 GeV. They are 11 km-long, based on 1.3 GHz superconducting radio-frequency (RF) accelerating cavities.

- **Beam delivery system (BDS):** Each linac includes a BDS of 2.2 km-long, which transport the e^+e^- beams from the high-energy linacs to the interaction point. The beams will be focused to the sizes required to meet the ILC luminosity goals, bringing them into collision with a 14 mrad crossing angle. Then, the spent beams are transported to the main beam dumps [51].

The beam structure is defined as follows. The repetition rate will be 5 Hz (bunch train separation of 200 ms), every bunch train (with 727 μs length) will contain 1312 bunches with a 554 ns between them. Table 4 and 5 summarize the beams and accelerator parameters.

Beam Parameters:	Interaction energy:	500 GeV(250 GeV + 250 GeV)
	Luminosity:	1.8×10^{34} cm^{-2}s^{-1}
	Accelerating gradient:	31.5 MV/m
	Number of bunches:	1312
	Bunch spacing:	554 ns
	Repetition rate:	5 Hz
	Beam current:	5.8 mA
	Final beam width:	474 nm
	Final beam thickness:	5.9 nm

Table 4: Summary of main beam parameters [51][56].

Accelerator units:	Number of cryomodules:	14742
	Cryomodules diameter:	1 m
	Cryomodules length:	12 m
	Cryomodules pulse:	1.3 GHz
	Cryomodules temperature:	2 K
	Cryomodules power:	190 kW/cavity
	Damping Ring length:	3.2 km
	Main Linac lenght:	11 km

Table 5: Summary of main accelerator parameters [51][56].

2.2.2 *The ILC detector concepts*

The interactions at high energy e^+e^- colliders present a completely new scenario to be exploited with suitable detectors. The discoveries performed by the LHC determine the starting point of the future experiments and define the design strategy to successfully complete the required physics program. The detectors of the future high energy e^+e^- colliders will measure, precisely, the Standard Model parameters, like bosons and quarks masses or the Higgs couplings. Moreover, they must be prepared to be sensitive to new physics phenomena, like dark matter or extra-dimensions. Also, their overall precision has to be enough to be sensitive to any deviation from the theory and open the door to explain unknown processes. Consequently, these machines will require vertex detectors with very low material budget and unprecedented granularity to tag the displaced vertices from b, c, and τ decays. The calorimeters will need high segmented technologies and will use the strategy of Particle Flow to reduce the uncertainty in calorimetric di-jet mass measurements. The angular coverage will be large. The magnetic field will be increased and the muon detector will be optimized to identify and measure (together with the tracker) the muons momentum [57].

The ILC has two detector proposals. Currently they are planed to be constructed simultaneously, sharing the interaction region in a pull-push operation scheme [3]. In the following sections the main characteristics of these detectors will be introduced.

2.2.3 *The SiD detector*

The Silicon Detector (SiD) is a compact detector, constructed under the Particle Flow Algorithm (PFA) requirements, to separate both charged and neutral particles, using a combination of tracking and calorimetry. It is based on a silicon pixel vertex detec-

3 One detector would take data, while the other is waiting in the close-by maintenance position.

tor, silicon tracking, silicon-tungsten electromagnetic calorimeter (ECAL) and a highly segmented hadronic calorimeter (HCAL), enabling an integrated tracking system, optimized for a high precision Particle Flow identification. Also includes a high-field solenoid, covering the complete tracking and calorimeter sub-detector, which will generate a 5 T magnetic field. Finally, it is surrounded by a muon identification system [57]. Figure 11 shows a schematic view of the structure.

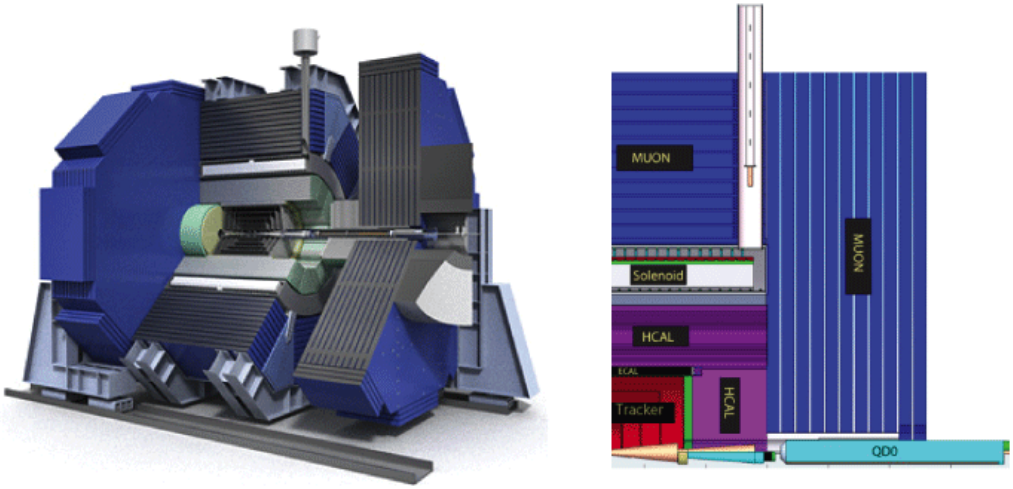

Figure 11: SiD schematic view (left) and quadrant section (right) [57]

- **Tracking system:** The tracking system has been designed to provide a point resolution on the scale of μm, with a very low material budget to minimize the multiple Coulomb scattering. One of the main goals is the identification of heavy flavor decay vertices. With this purpose, the barrel section will include five silicon pixel layers with a pixel size of 20×20 μm^2. The forward and backward regions have four silicon pixel disks each. Moreover, three silicon pixel disks at a larger distance will provide uniform coverage for the transition region between the vertex detector and the outer tracker. The outer tracker will be constructed using silicon strip sensors arrayed in five cylinders in the central region and four disks in the forward and backward regions. The detectors will be single-sided silicon sensors with a readout strip pitch of 50 μm and placed for small angle stereo measurements.

- **ECAL & HCAL:** The calorimeter will be contained inside the solenoid magnet in order to make easier relate the tracks and the deposits of energy. The combined ECAL and HCAL systems consist of a central barrel and two endcaps, nested inside the barrel. The ECAL will be constructed with silicon active layers (5×5 mm^2 silicon pixels) between tungsten absorbers. The total depth of the electromagnetic

calorimeter is 26 radiation lengths (X_0) and one nuclear interaction length. The HCAL will have a depth of 4.5 nuclear interaction lengths, it will consist on steel plates alternated with active layers [4]. Moreover, two forward calorimeters will be placed on the very forward region, the Lumical, to obtain a precise measurement of the luminosity and the BeamCal for a fast estimation.

- **Magnet & Muon detector:** The SiD superconducting solenoid will have 3.4 m radius covering all the tracker and calorimeter with 5 T magnetic field. Surrounding the magnet, the flux-return yoke will be instrumented with position sensitive detectors to be used as a muon detector and tail catcher [5]. The baseline design will include scintillator technology, with RPCs as an alternative.

The main characteristics of the SiD are presented on table 6 and 7.

SiD Barrel	Tech	In R [cm]	Out R [cm]	Z [cm]
Vertex detector	Si pixels	1.4	6.0	±6.25
Tracker	Si strips	21.7	122.1	±152.2
ECAL	Si pixels-W	126.5	140.9	±176.5
HCAL	RPC-steel	141.7	249.3	±301.8
Solenoid	5 T SC	259.1	339.2	±298.3
Flux Return	Scint-Steel	340.2	604.2	±303.3

Table 6: Summary SiD Barrel characteristics [57].

SiD EndCap	Tech	In Z [cm]	Out Z [cm]	Out R[cm]
Vertex detector	Si pixels	7.3	83.4	16.6
Tracker	Si strips	77.0	164.3	125.5
ECAL	Si pixels-W	165.7	180.0	125.0
HCAL	RPC-steel	180.5	302.8	140.2
Flux Return	Scint-Steel	303.3	567.3	604.2
LumiCal	Si-W	155.7	170.0	20.0
BeamCal	Diamond/GaAs-W	277.5	300.7	13.5

Table 7: Summary SiD EndCap characteristics [57].

4 Glass resistive plate chamber, GEM or Micromegas.
5 Particle showers that scape from the HCAL.

2.2.4 *The ILD detector*

The International Large Detector (ILD) concept has been optimized for good energy and momentum resolution, with flexibility for operation at energies up to the TeV range. The design strategy has followed the Particle Flow requirements, with especial effort on b tagging capabilities and detection of secondary vertices. A hermertic structure has been implemented to ensure the solid-angle coverage, but also to avoid cracks and non-uniformities in response. With this purpose, the detector will employ a multilayer silicon vertex detector, surrounded by a TPC. Outside the tracker a highly segmented electromagnetic calorimeter (ECAL) and hadronic calorimeter (HCAL) will be installed. A large volume superconducting coil, surrounding the calorimeters, will create a magnetic field of 3.5 Tesla. Finally, the iron yoke will be equipped with scintillator strips or resistive plate chambers (RPCs), to serve as a muon detector and tail catcher calorimeter [57]. Figure 12 shows a schematic view of the structure.

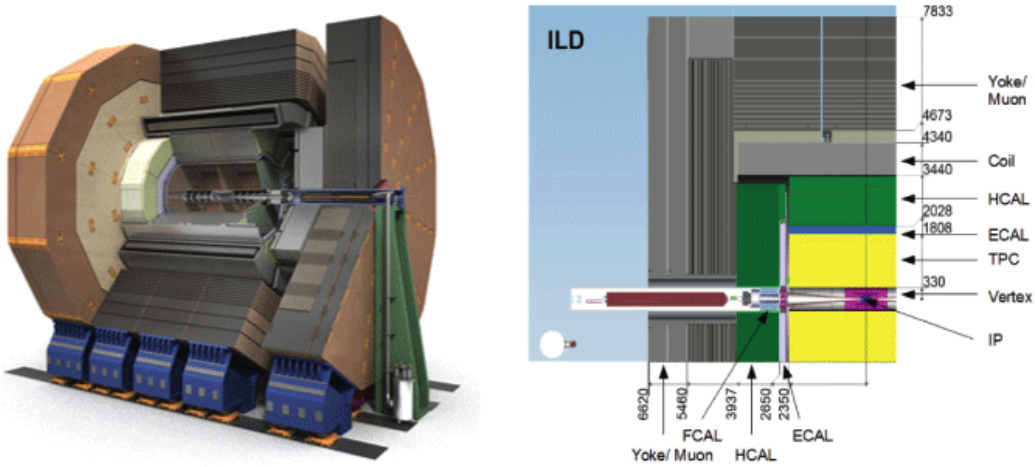

Figure 12: ILD schematic view (left) and quadrant section (right) [57]

- **Tracking system:** In the baseline design, the interaction point will be surrounded with three layers of double-sided pixel ladders or five layers of single single-sided pixel ladders [6], followed by the tracking system composed by: the Silicon Inner Tracker (SIT), the Time Projection Chamber (TPC) and the Silicon External Tracker (SET). One EndCap component will be placed behind the Endplate of the TPC (ETD) (Fig. 13). The SIT, SET and ETD will be constructed with two single-sided strip layers tilted for small angle stereo measurements. The forward tracker (FTD)

6 Several technologies are being developed. Some candidates are DEPFET (Chapter 3), CMOS Pixel Sensor or Fine Pixel CCD.

will be designed with the first two discs of silicon pixels, followed by five silicon micro-strips discs. The central tracker will be a Time Projection Chamber (TPC), optimized for a excellent three dimensional point resolution, with a minimum material budget on the field cage. It also has the capability to identify particles, based on the energy loss (dE/dx).

- **ECAL & HCAL:** The calorimeter has been designed to be a very hermetic cylinder composed by the barrel and two large EndCaps. The ECAL was conceived to optimize the separation between photons from near-by particles. To do this, highly granular sensitive plates have been alternated with passive tungsten absorbers. The baseline technology will be 5×5 mm^2 silicon pin diodes, but scintillator strips with 5×45 mm^2 arranged in alternative directions or a combination of both technologies are also being considered. The system will be constructed with 30 readout layers and a thickness of 24 X_0. The HCAL is optimized to separate the deposits of charged and neutral hadrons and to precisely measure their energy. It is conceived as a sampling calorimeter with steel absorber and 3×3 cm^2 scintillator tiles (analogue HCAL) or 1×1 cm^2 gaseous devices (semi-digital HCAL) as active plates. This design has been performed following the directives of the Particle Flow Algorithm, making easier to relate the tracks and their corresponding energy deposits. On the very forward region, three systems are proposed. The luminosity monitor (LCAL), beamstrahlungs monitor (BeamCal) and the LHCAL, closing down the coverage to a very small angles, also for neutral hadrons.

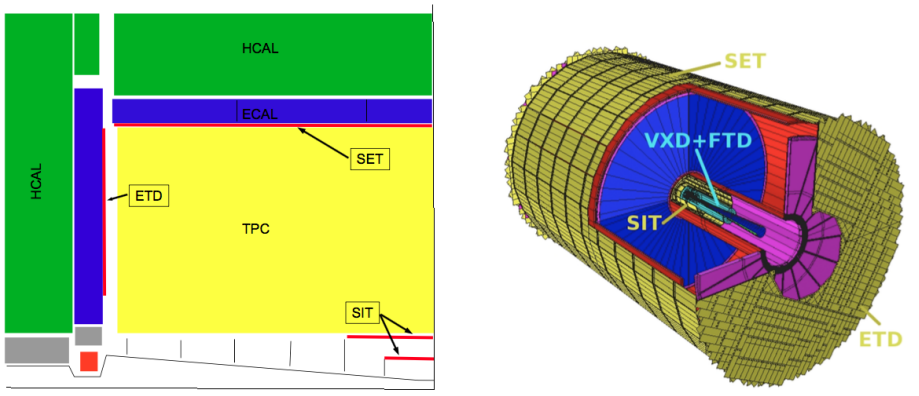

Figure 13: ILD Tracking system schematic view (right) and quadrant section (left) [57]

- **Magnet & Muon detector:** The calorimeter region is placed inside of the superconducting solenoid coil, which will generate a nominal magnetic field of 3.5 T (maximum 4 T). Moreover, an anti-DID (Detector-Integrated-Dipole) will be installed, in order to suppress background from beamstrahlung incoherent pairs. Finally, the iron yoke will be equipped to detect muons and measure showers

that escape the hadron calorimeter (tail catcher). The muon detector technology options are scintillator strips equipped with wave-length shifting fibers and read out with silicon photomultipliers (SiPM) or resistive plate chambers (RPC)

The main characteristics of the ILD are showed on table 8 and 9.

ILD Barrel	**Tech**	**In R [cm]**	**Out R [cm]**	**Z [cm]**
Vertex detector	Si pixels	1.6	6.0	±12.5
SIT	Si strips	15.3	30.0	±64.4
SET	Si strips	181.1	—	±230.0
TPC	MPDG readout	33.0	180.8	±235.0
ECAL	Sc, Si pixels-W	184.3	202.8	±235.0
HCAL	Sc, RPC-steel	205.8	342.0	±235.0
Solenoid	3.5 T SC	344.0	440.0	±395.0
Muon	Scint-Steel	445.0	775.5	±280.0

Table 8: Summary ILD Barrel characteristics [57].

ILD EndCap	**Tech**	**In Z [cm]**	**Out Z [cm]**	**Out R[cm]**
FTD	Si pix-strip	22.0	37.1	—
ETD	Si strips	242.0	244.5	41.9 — 182.2
ECAL	Sc, Si pixels-W	245.0	263.5	—
HCAL	Sc, RPC-steel	265.0	393.7	33.5 — 319.0
BeamCal	GaAs-W	359.5	371.5	2.0 — 15.0
LumiCal	Si-W	250.0	263.4	7.6 — 28.0
LHCAL	W abso	268.0	320.5	9.3 — 33.1
Muon	Scint-Steel	256.0	—	30.0 — 775.5

Table 9: Summary ILD EndCap characteristics [57].

2.3 *The Compact Linear Collider (CLIC)*

The design and construction of a multi-TeV e^+e^- collider is a very challenging process. The characteristics of the electrons make them very hard to be accelerated up to such scale, in a circular machine. They are strongly affected by the synchrotron radiation. For this reason, only linacs are capable to do this. To achieve such collision energies,

huge acceleration gradients will be necessary, avoiding untenable accelerator lengths and costs. The Compact Linear Collider (CLIC) is a multi-TeV linear e^+e^- collider, based on a novel two-beam acceleration technique, capable to achieve accelerating gradients up to 100 MV/m. The two-beam accelerator scheme consists of producing RF power for the main beams by extracting energy from a secondary beams, running in parallel (drive beams). The drive beams will be of much higher current and much lower energy, therefore, can be generated by a "short" accelerator. The principle is based on the transformer idea; the low voltage seen by the high current drive beam is converted into high voltage seen by the low current main beam [58]. The CLIC physics program covers the center of mass energies from 380 GeV to 3 TeV, divided in several stages (Tab. 10 and Fig. 14), covering all the studies at low energy and exploring the multi-TeV energy frontier.

Stage	$\sqrt{s}$ [GeV]	$\mathcal{L}$ [fb^{-1}]
1	380	500
	350	100
2	1500	1500
3	3000	3000

Table 10: CLIC center of mass energy stages and its corresponding accumulated luminosity [59].

2.3.1 *Accelerator*

The CLIC accelerator will be a combination of many linacs and rings, precisely arranged to achieve, in a very compact size, energies in the multi-TeV scale. The total facility length (with nominal energy 3 TeV) will be 50 km-long, divided in two branches. Each branch will include a main linac, with 21 km, and its corresponding drive beam system (including the drive beam accelerators, delay loops and the decelerators). The injection system will be constructed adjacent. The electrons and positrons bunches will be generated using the corresponding DC-gun and a converter. The bunches will be stored and cooled down in its corresponding damping rings before being pre-accelerated up to 9 GeV to be finally injected on the main linacs (Fig. 15). The main subsystems involved are the followings [60]:

- **Electrons source:** The polarized electrons will be generated using a DC-photon gun, working at 1 GHz. Then, the bunches will be accelerated up to 200 MeV and rotated to the desired spin direction. These bunches will be injected on the damping ring, which stores and cools them down. Finally, a common accelerator

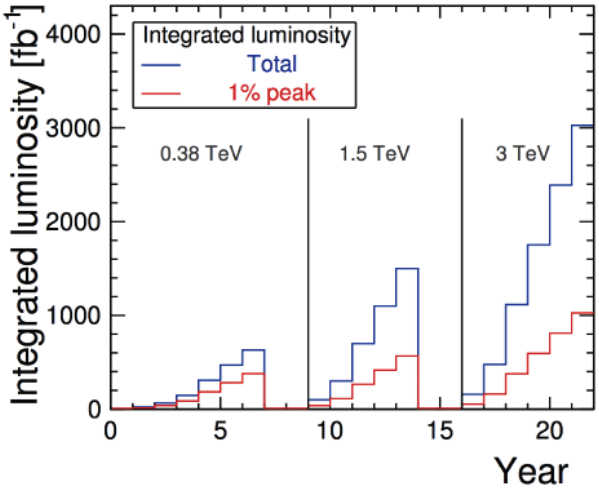

Figure 14: CLIC Stages: Left: Integral luminosity. Right: Luminosity per year [59]

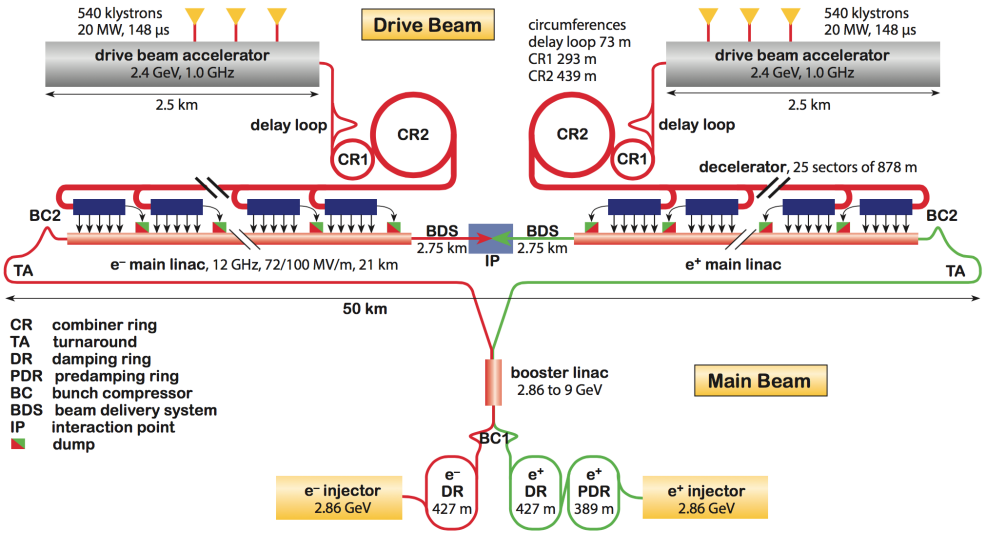

Figure 15: Schematic layout of CLIC-3 TeV [60].

(same for the e^+e^--bunches) is used to pre-accelerate the particles up to 9 GeV and then deliver them to the RTML.

- **Positrons source:** The positron source will use a primary electron beam linac (energy of 5 GeV), followed by two parallel target stations, each constructed with two layers of tungsten targets, a positron capture section, and a pre-injector linac

to accelerate the positrons to 200 MeV. Then, the bunches generated in parallel will be compressed and injected on the positron damping ring. Finally, they will be send through the common accelerator, reaching 9 GeV, to be delivered on the RTML.

- **Ring to Main Linac (RTML):** The Ring to Main Linac (RTML) connects the damping rings and the main linacs. The beam lines transport the bunches from the injection systems (near to the surface) to the main linac entrance, which is about 100 m underground. The total length is around 27 km. It also includes the subsystems necessary to match the beam properties to the values required by the main linacs.

- **Main Linac:** The Main Linacs are identical for electrons and positrons, with a total length of 21 km, they are meant to accelerate the beams from an initial energy of 9 GeV up to 1.5 TeV. They use normal conducting accelerator structures with a gradient of 100 MV/m and a RF frequency of 12 GHz. To obtain this huge gradients, the energy is transferred from a secondary beam, which runs in parallel. The energy is obtained using the so called decelerators, where the high current beam, in a low voltage, is converted in low current beam, in a high voltage.

- **Drive beam accelerator (DBA):** The two Drive-Beam Accelerators (DBAs) generate a 4.2 A, 142 μs-long drive-beam pulses. They use electrons bunches and accelerate them to a final energy of ~ 2.4 GeV, using normal conducting structures with an RF frequency of 999.5 MHz. The DBAs have a total length of 2.6 km, including injectors and bunch compressors. They provide the main linac with the pulses required to create its accelerating gradients.

- **Beam Delivery System (BDS):** The BDS guide the e^+e^- bunches, from the exit of the main linac to the interaction point (IP). The main task is to prepare and bring the bunches into collision, for this, the bunches are oriented and focused up to the nominal size ($\sigma_x = 45$ nm, $\sigma_y = 1$ nm). In addition, some critical functions are also performed on this region, such measuring the energy and the polarization.

The difficulty to achieve these huge accelerator gradients makes the design and construction of this facility a very complex procedure. For this reason, the CLIC accelerator will be built as each energy stage requires, re-using the existing equipment on the subsequent stage. The construction is planed to be divided in three steps, as shown in table 10. The first and second stage will use a single drive-beam accelerator system, to feed both linacs, while in the third stage, each linac will be fed by a separated facilities [55]. Table 11 shows the main parameters in each stage.

Parameter	**Stage 1**	**Stage 2**	**Stage 3**
E_{CM} [GeV]	380	1500	3000
Rep. Freq. [Hz]	50	50	50
Num. Bunches	352	312	312
Bunch Sep. [ns]	0.5	0.5	0.5
Pulse Length. [ns]	244	244	244
Gradient [MV/m]	72	72/100	72/100
$\mathcal{L}$ $[10^{34}cm^{-2}s^{-1}]$	1.5	3.7	5.9
Tunnel lenght km	11.4	29.0	50.1
Part./Bunch 10^9	5.2	3.7	3.7
Bunch length σ_z[µm]	70	44	44
IP beam size σ_x/σ_y[nm]	149/2.9	$\sim$ 60/1.5	$\sim$ 40/1

Table 11: Main CLIC accelerator parameters in the different stages [61].

2.3.2 *The CLIC detector concept*

The detectors introduced on Section 2.2.2 can be considered as a general purpose detectors, designed for e^+e^- colliders. Therefore, they can be used as a baseline proposal and then be modified accordingly to the CLIC interaction environment. The CLIC detector concepts are called CLIC_SiD and CLIC_ILD and maintains the structure of the ILC detectors concept. Main changes performed have been done on the vertex detector and the very forward region to mitigate the impact of the background and the enlargement of the calorimeter considering the energy increment of the out-going particles. The main CLIC_SiD and CLIC_ILD parameters are shown in table 12 and 13.

2.4 ***Super Flavor Factories (SFF)***

Section 2.1 has introduced e^+e^- colliders capable to explore the multi-TeV region with unprecedented precision. However, it is possible to be sensitive to new physics without requiring such scale of energies. This is the approach followed by the Super Flavor Factories (SFF). The SFF are design to use intermediate interaction energies, maximizing the luminosity peak and focusing the detectors construction on specific physical processes to optimize the measurement precision. The SFF strategy, to be sensitive to new physics, is based on measuring with high precision parameters from the Standard Model and look for small deviations (due to new physics) on the expected values. As example, figure 16 shows the one loop diagrams of the process $b \to \gamma s$. On the experi-

	CLIC_ILD	CLIC_SiD
Vertex Detector:		
Inner radius [cm]	3.1	2.7
Outer radius [cm]	6.0	7.7 (barrel), 16.9 (disks)
Max. Z [cm]	12.5 (barrel), 25.7 (disks)	9.9 (barrel), 83.0 (disks)
Barrel layers	6 (3 double)	5
Forward disks	6 (3 double)	7
Barrel Tracker:		
Technology	TCP (Si-strips)	Si-strips
Inner radius [cm]	32.9(16.5)	23.0
Outer radius [cm]	180.8(183.5)	123.9
Max. Z [cm]	225.0	57.8 to 153.6
Max. samples	2 (Si),224 (TCP),1 (Si)	5
Forward Tracker:		
Technology	Si-strips	Si-strips
Inner radius [cm]	4.7 to 21.8	20.7 to 116.2
Outer radius [cm]	32.0	125.2
Max. Z [cm]	186.8	155.6
Max. samples	5	4
Coil + Cryostat:		
Field	4T	5T
Outer radius [cm]	429.0	371.0
Max Z. [cm]	417.5	324.5
Yoke & Muon D.: Barrel		
Material	Steel	Steel
Inner radius [cm]	440.4	391.4
Outer radius [cm]	699.0	700.0
Number of layers	9	9
Yoke & Muon D.: EndCap		
Material	Steel	Steel
Inner radius [cm]	69.0	69.0
Outer radius [cm]	699.0	700.0
Max. Z [cm]	620.0	620.0
Num. layers	9	9

Table 12: Summary of CLIC detector concept parameters [61].

ment, the cross section measurement includes the contribution of all possible loops. In a situation, strictly under the Standard Model, only diagrams from the Standard Model theory (Fig. 16 - above) will contribute. However, if a new physics theory is considered, for example a charged Higgs model, also these diagrams will be included (Fig. 16 - below). These diagrams will generate changes on the parameters measured [62].

	CLIC_ILD	CLIC_SiD		CLIC_ILD	CLIC_SiD
ECAL: Barrel			**ECAL: EndCap**		
Absorber	Tungsten	Tungsten	Absorber	Tungsten	Tungsten
Active layer	Si-pads	Si-pads	Active layer	Si-pads	Si-pads
Sampling layers	30	30	Sampling layers	30	30
Cell Size [mm]	5.1×5.1	3.5×3.5	Cell Size [mm]	5.1×5.1	13mm^2 hexagons
X_0 & λ_I	23 & 1	26 & 1	X_0 & λ_I	23 & 1	26 & 1
Inner radius [cm]	184.7	129.0	Inner radius [cm]	27.0	22.2
Outer radius [cm]	202.0	143.0	Outer radius [cm]	227.0	126.9
Max. Z [cm]	235.0	176.5	Min. Z [cm]	245.0	165.7
			Max. Z [cm]	262.2	180.0
HCAL: Barrel			**HCAL: EndCap**		
Absorber	Tungsten	Tungsten	Absorber	Steel	Steel
Sampling layers	75×10 [mm]	75×10 [mm]	Sampling layers	60×20 [mm]	60×20 [mm]
Cell Size [mm]	30×30	30×30	Cell Size [mm]	30×30	30×30
λ_I	7.5	7.5	λ_I	7.5	7.5
Inner radius [cm]	205.8	144.7	Inner radius [cm]	40	50.9
Outer radius [cm]	329.6	262.4	Outer radius [cm]	305.9	262.4
Max. Z [cm]	235.0	176.5	Min. Z [cm]	265.0	180.0
			Max. Z [cm]	424.0	339.5

Table 13: Summary of CLIC detector concept parameters [61].

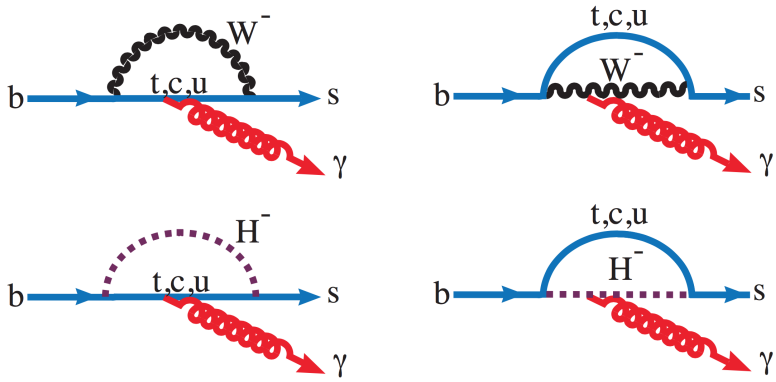

Figure 16: Above: SM diagrams for $b \to \gamma s$. Below: Charged higgs model diagram contribution [62].

2.5 *SuperKEKB*

The SuperKEKB SFF (the upgrade of KEKB) is being constructed on Tsukuba (Japan). It is a superB-Factory with an instantaneous luminosity target of 8×10^{35} $\text{cm}^{-2}\text{s}^{-1}$. The e^+e^- circular accelerator has been constructed on the same tunnel of its predecessor,

the total length is 3 km and includes one crossing point. The nominal interaction energies are set to the range of the $\Upsilon(1S)$ to $\Upsilon(6S)$ resonances. The detector placed on the interaction point (Belle II) has been designed to fully reconstruct the $B\bar{B}$-pairs generated and their daughters. To be able to distinguish the decay vertex from B meson and $\bar{B}$ meson, the positron accelerator or low energy ring (LER) and the electron accelerator or high energy ring (HER), use asymmetric energies to infer a boost on the particles produced. The beam energy of the positron beam (LER) is 4 GeV with a current of 2.6 A and the electron beam (HER) is 7 GeV with 3.6 A. To achieve these energies and to compensate the loses due to the synchrotron radiation, the ring includes stages with RF cavities working at 508.89 MHz, combined with dipoles to curve the beam trajectories and quadrupoles to stabilize and cool down the bunches [63]. Bunches are created in a facility aside, the electron bunches are generated using a low emittance gun, and positrons are created using a converter target. Bunches are injected continuously, with a frequency of 50 Hz in each ring. These new bunches injected ("noisy bunches") are further away from expected parameters of the corresponding main bunches. The cooling down process takes $\sim$ 4 ms and during this time, these noisy bunches will cross the IP every 10 μs, generating additional background. This will force the detectors involved to become blind during the passing through [64] (Section 3.5). Table 14 shows the main parameters of SuperKEKB.

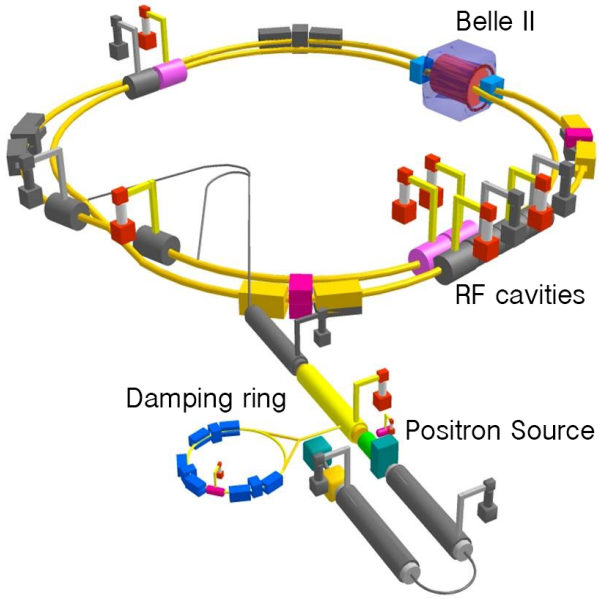

Figure 17: Schematic layout of SuperKEKB.

	LER (e^+)	HER (e^-)
Beam energy [GeV]	4	7
Horizontal Beam Size [μm]	10.2(10.1)	7.75(7.58)
Vertical Beam Size [nm]	59	50
Beam Current [A]	3.60	2.62
Number of bunches/ring	2503	2503
Energy lost/turn [MeV]	2.15	2.50
Bunch length [mm]	6.0(4.9)	5.0(4.9)

Table 14: Main SuperKEKB accelerator parameters [53].

2.5.1 *The Belle II detector*

The Belle II detector design has been optimized to fully reconstruct the $B\bar{B}$-pairs generated and distinguish their decay vertices. Accordingly to the accelerator strategy, Belle II structure has been constructed asymmetrically relocating the interaction point slightly to the backward region and hence increasing the forward coverage (Fig. 18).

- **Vertex Detector (VXD):** The VXD has been design with two layers of pixelated silicon sensors (PXD) at 1.4 & 2.2 cm, and four layers of double-sided silicon strip sensors (SVD), at 3.8, 8, 11.5 & 14 cm. The e^+e^- interaction will generate outgoing particles with a low momentum (range from 50 MeV to few GeV), which will add a constrain to the maximum material budget allowed near to the interaction point. Moreover, the requirement to determine the particles trajectory, with high precision (to reconstruct the secondary vertices), makes necessary a very precise and granular PXD. For these reasons, DEPFET (Chapter 3) has been chosen as a PXD technology baseline. This technology provides a very granular thin sensors (75 μm with a 0.1% X_0 contribution) and the capabilities to locate their readout electronics outside the acceptance region, minimizing, even more, the contribution to the material budget.
- **Central Drift Chamber (CDC):** The VXD is surrounded by a drift chamber ($r = 16 \rightarrow 112$ cm), meant to measure the trajectories, the momentum and the energy losses (dE/dx) of charged particles.
- **Particle Identification Device (PID):** The PID is located around the CDC, over the barrel and at the EndCap regions. It is design, specifically, to discriminate K/π, but also is capable to distinguish electrons with energy below 1 GeV. The system uses, on the barrel, a Ring-Imaging CHerenkov detector (RICH) with Time of Propagation counters (TOP) to measure the Cherenkov radiation light emitted

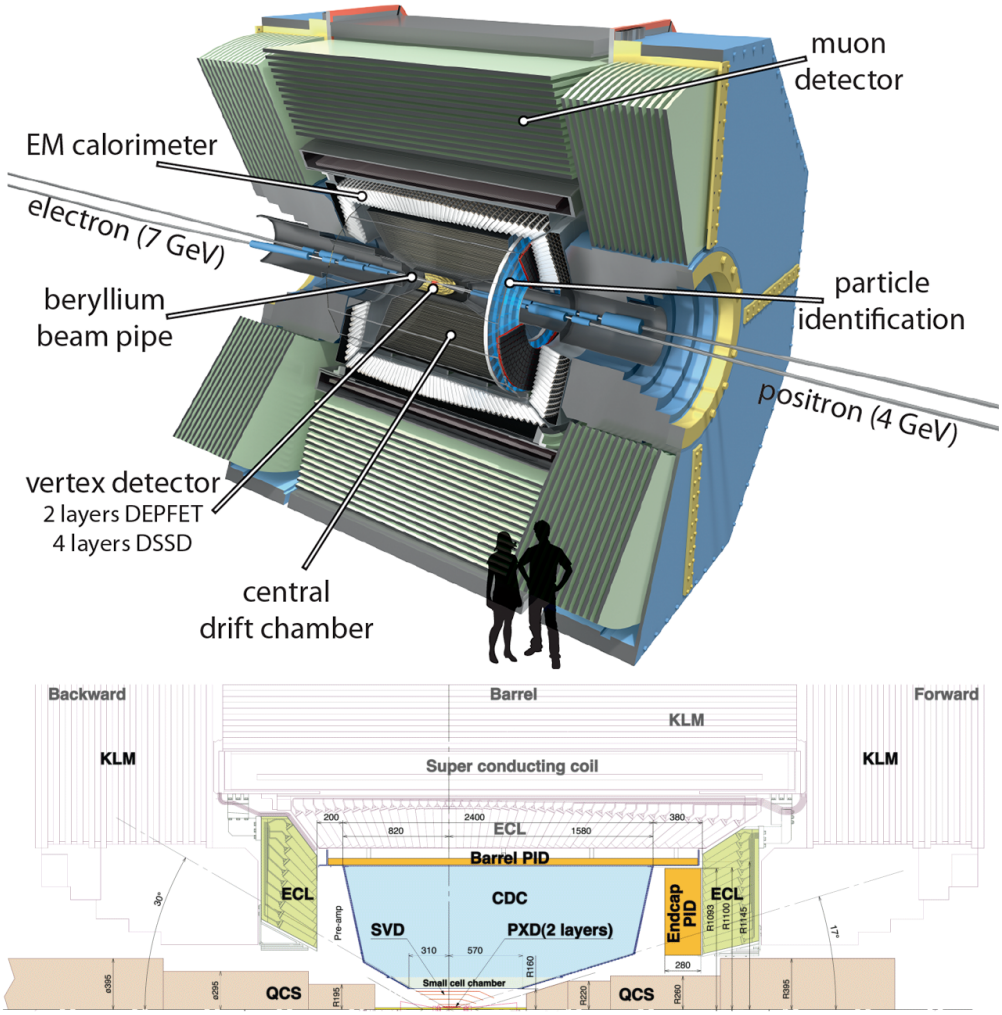

Figure 18: Belle II schematic view (top) and half section (bottom) [53].

from charged particles passing through quartz radiation bars. At the endcaps, the TOP is replaced by aerogel radiators (ARICH).

- **Calorimeter (ECL):** The ECL consists of a 3 m long barrel section with an inner radius of 1.25 m and EndCaps located at $z = 1.96$ m (forward) and $z = -1.02$ m (backward) from the interaction point. The barrel part has a tower structure that projects to a region near the vicinity of the interaction point. It is constructed with CsI(Tl) crystals. Each crystal is a truncated pyramid of an average size about 6×6 cm^2. The total thickness is 16.1 X_0.

- **Maget and K_L/Muon Detector (KLM):** A superconducting solenoid, covering the ECL, provides a magnetic field of 1.5 T in a cylindrical volume 3.4 m in diameter and 4.4 m in length. The coil is surrounded by a multi-layer structure consisting of iron plates, which is integrated into a magnetic return circuit. This structure is instrumented with resistive plate chambers (RPC). On the end-cap region, the RPCs are replaced by scintillators with silicon photomultiplier. The KLM is meant to detect the K_L^0 mesons and the outgoing muons.

The main characteristics of the Belle II are summarized on table 15.

Component	Type	Configuration
Beam Pipe	Beryllium double-wall	In-R: 10 mm
PXD	DEPFET	2 layers: 8/12 ladders
SVD	double-sided Si-strips	4 layers: 16/30/56/85 ladders
CDC	Drift chamber	$r = 16 - 112$ cm
		$-83 < z < 159$ cm
TOP	RICH with quartz radiator	Barrel: $r \sim 120$ cm
ARICH	RICH with aerogel radiator	End-Caps
ECL	CsI(Tl)	Barrel: $r = 125 - 162$ cm
KLM	Barrel: RPCs	
	End-Caps: Scintillator strips	

Table 15: Summary of Belle II parameters [53].

2.6 *Summary*

New machines are necessary to continue improving the measurements and open the door to new discoveries. This chapter has shown different approaches to continue searching new physics and increasing the measurement precision of the Standard Model parameters. ILC and CLIC will explore the limits of e^+e^- interactions energies, to complete the Standard Model picture and search for new phenomenons, contributing with its unprecedented precision measurements. On the other hand, SuperKEKB presents other approach, focusing the effort on maximizing the luminosity and optimizing the detector structure to study the $\Upsilon(nS)$ resonance decay. In general, the study and the development of these machines is a complex and an important task to be done and it is carried on by a huge team. On this thesis, a tiny contribution to these projects will be presented.

Part II

Development of the quality test protocol for DEPFET pixel detectors

3 The DEPFET Technology

Future e^+e^- accelerators provide a new collision environment, which allows to measure, with unprecedented precision, the Standard Model parameters and search for new physic phenomena. Accordingly, to explode this new scenario, it is required the development of ”cutting edge“ detectors. Particularly important is the innermost subsystem, which must keep, as low as possible, the material budget and the power consumption, without renouncing to provide a high spatial resolution and high readout speed. One technology, capable to fulfill all these requirements, is the **DEP**leted **F**ield **E**ffect **T**ransistor structure (DEPFET), which is the baseline technology for the Belle II PXD and one of the candidates for the International Linear Collider (ILC). This chapter enters on this context to introduce the DEPFET technology principle. Then, it will summarize the data analysis strategies and the debugging of the distinct DEPFET prototypes, including some studies performed on these topics.

3.1 *Introduction to Semiconductor Technology*

First researches on semiconductor materials started on the early 19th century, studying their unusual conductivity [1]. However, it took a century to find the first practical applications [2]. Currently, the use of devices that require semiconductor components are widely extended, even on high energy physics, where particles detectors based on semiconductor are extensively used.

1 J. Davy (1821) found a decrease of the conductivity in metals. M. Faraday (1833) observed a strong increase with temperature in a number of binary chemical compounds.

2 In 1904, the development of the Cat's-whisker detector (a primitive semiconductor diode) by Henry H. C. Dunwoody, G. W. Pickard and others.

Materials can be classified by their capability to conduct electricity. The conductors, like copper or silver, let pass the electric current easily. On the other hand, the insulators, such rubber or glass, generate resistance to the passing of an electric current. The semiconductor conductivity lies between those of conductors and insulators. The differences on the conductivity can be explained using quantum mechanics. Without going into a detailed explanation [3], the conductivity depends on the energy level of the electrons and the lattice structure of the crystal. A schematic explanation is shown on figure 19, the valence band (red) represents the energy region, for the electrons, that keep them fixed on the lattice structure. The conduction band (blue) represents the energy region that allows them to move freely along the crystal, these electrons are responsible of the current conduction. In case of metals (conductors) the valence band and conduction band are overlapped, this means that some electrons are so lightly fixed to the lattice structure that can move almost freely from one atom to another. In the opposite case, the insulators have a huge gap between the valence band and the conduction band, this means that the electrons cannot jump to the conduction band in any case, and therefore the conductivity is almost zero.

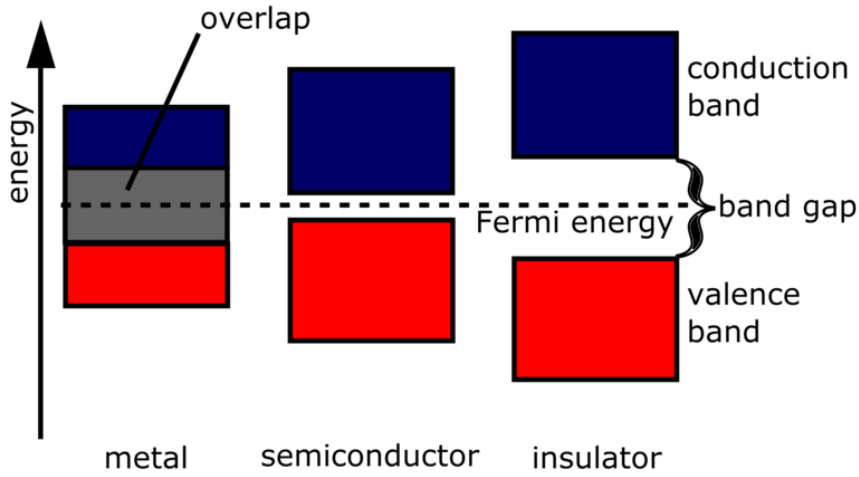

Figure 19: Schematic view of the bands structure in metals, semiconductors and insulators.

On the other hand, the semiconductors have a small band gap, which confers their special conductivity features. In principle, all the electrons are located on the valence band, in this case, the semiconductor behaves as an insulator, however, the electrons can jump to the conduction band (i.e. due to thermal excitation), increasing the conductivity. This conductivity value depends on the temperature and the purity of the crystal.

3 More details on Ref. [65]

There are several semiconductor materials: Silicon, Germanium, Selenium, Carbon, etc. However, Silicon is the most important semiconductor material used in building electrical devices. In pure form, Silicon has an atomic structure with its four valence electrons locked up into the covalent bonds between neighboring atoms (Fig. 20). In this case, since there are none free charge carriers available, the pure Silicon lattice will act more as an insulator than a conductor. The basic process to play around with the conductivity parameter is called *doping*.

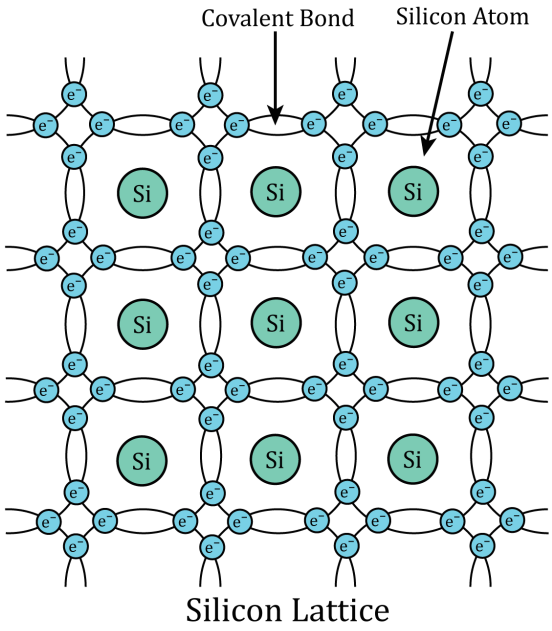

Figure 20: Scheme of the pure Silicon lattice structure, which does not contain any free charge carriers, all electrons are fixed on the covalent bonds between Si atoms.

Basically, the doping refers to the process of adding other atoms (impurities) to the Silicon lattice in such way that conductivity parameter changes at will. The two most important atoms used are Phosphorus (n-type) and Boron (p-type). When these atoms are added to the Silicon lattice, its electrical conductivity is altered dramatically.

- **n-type:** Unlike Silicon, Phosphorus has five valence electrons instead of four. On a Silicon lattice, four of the Phosphorus valence electrons will form covalent bonds with the valence electrons of four neighboring Silicon atoms (Fig. 21 - left). The fifth valence electron will not have a binding site and will loosely float around the atoms. If a voltage is applied, these extra electrons will migrate through the crystal. This doped Silicon is referred to as *n-type* .

- **p-type:** Other option is to add Boron. Boron, unlike Silicon or Phosphorus, contains only three valence electrons. When it is added to a Silicon lattice, all three electrons will bind with neighboring Silicon atoms (Fig. 21 - right), however, there will be a empty spot (*hole*), which will act as a positive charge carrier. If a voltage is applied, the holes will move towards the negative voltage end. This doped Silicon is referred to as *p-type* .

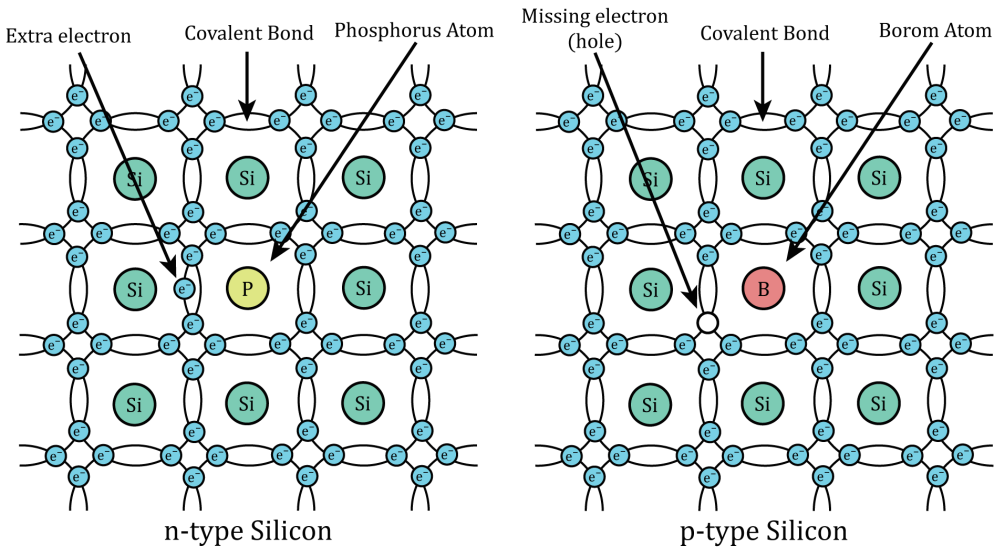

Figure 21: Scheme of a doped Silicon lattice structure. Left: n-type Silicon with negative charge carrier. Right: p-type Silicon with positive charge carrier

Essentially, the doped Silicon behaves now like a conductor material, however, these two new conductors have two unique and distinct way of transporting electrical charge, one does it with holes (p-type), the other with electrons (n-type). The combination of these doped semiconductors can be used to construct several electronic devices, such diodes, transistors or even particle detectors.

3.1.1 *Diodes*

A junction diode is formed by attaching together n-type (cathode) and p-type (anode) Silicon. This combination of crystals will create a device where current will flow in only one direction. The behavior depends on how charge carriers interact which each other and with the electrical field, the two possible polarization are the following:

- **Forward-Biased:** Electrons from the n-side and holes from the p-side are forced toward the pn-interface by the electrical field. The electrons and holes combine and the current passes through the diode (Fig. 22 - left).
- **Reverse-Biased:** Holes and electrons are forced on the opposite direction of the pn-interface. This results in an empty zone around the pn-junction that is free of charge carriers, known as the *depletion region*. This region has an insulative quality that prevents current from flowing trough the diode (Fig. 22 - right).

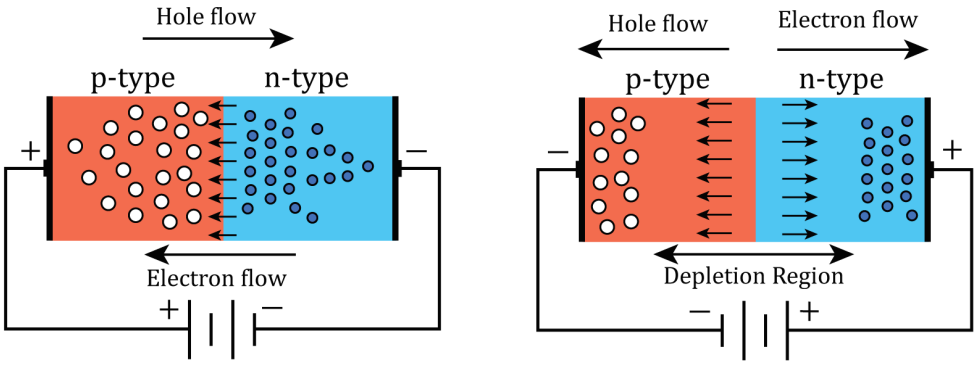

Figure 22: Schematic diode operation. Left: Forward-Biased diode ("Open Door"). Right: Reverse-Biased diode ("Closed Door")

3.1.2 *JFET and MOSFET transistors*

Several transistor concepts have been developed. In general, the transistor operation consists in generate an output signal, responding to an input signal. Most transistors have a variable current control feature, but a few, do not. The two major families of transistors are the *bipolar transistors* and *field-effect transistors* (FET). The main difference between these two families is that bipolar transistors require a input current, whereas FETs require only a voltage (practically not current). This section will describe only the FET family, which will be used to construct DEPFET sensors. As a brief explanation, the FET transistors work as a current flow modulator, there are three main transistor connectors to be introduced (See Fig. 23):

- **Source:** The source current, which will be modulated, is connected through the *source* input.
- **Drain:** The output current modulated by the transistor is obtained through the *drain* output.
- **Gate:** The input voltage, which is used to modulate the source current, is applied through the *gate* connector.

Junction Field-Effect Transistors (JFET): Figure 23 shows a n-channel JFET, which is made with an n-type Silicon bulk that contains two p-type Silicon implants placed on either sides. The gate contact is connected to the p-type implants, and the drain and the source contacts are connected to the n-type channel. When no voltage is applied through the gate, the current flows freely though the central n-channel (Fig. 23 - left). However, if the gate is set to a negative voltage a depletion region is formed expanding from the p-type implants into the channel. The more negative the gate voltage is applied, the larger the depletion region is created, and hence, the harder is for the electrons to make it through the channel (Fig. 23 - right).

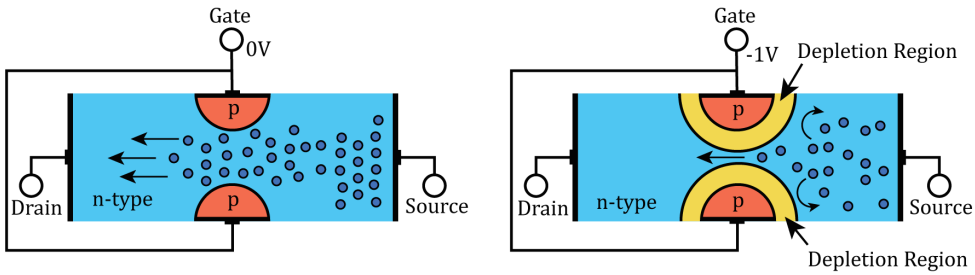

Figure 23: Schematic JFET transistor operation. Left: Since no voltage is applied through the gate contact, the current flows freely. Right: Gate contact is set to a negative voltage, the p-type Silicon "bumps" will generate depletion region that extends into the channel. Increasing the resistivity of the channel.

Metal Oxide Semiconductor Field-Effect Transistors (MOSFET): The two major families of MOSFETs are the *enhancement-type MOSFET* and the *depletion-type MOSFET*. A depletion-type MOSFET is normally *on* (maximum current flows) when no voltage is applied on the gate contact and the channel becomes more resistive as higher is the voltage applied [4]. On the other hand, an enhancement-type MOSFET is normally *off* (minimum current flows) and if a voltage is applied to the gate contact, the channel becomes less resistive. Figure 24 shows an schematic view of enhancement-type MOSFET operation. Enhancement-type MOSFETs have, normally, a high resistive channel (there are few charge carriers within it). Assuming a n-channel enhancement-type MOSFET, if a positive voltage is applied to the gate contact, electrons migrate into the channel and thereby the conductivity is increased (Fig. 24 - left). For the p-channel enhancement-type MOSFET, a negative voltage applied on the gate contact draws holes into the channel to increase the conductivity (Fig. 24 - right). The p-channel enhancement-type MOSFET transistor will be used to construct the DEPFET pixels.

4 The depletion-type MOSFET operation is very similar to the JFET operation.

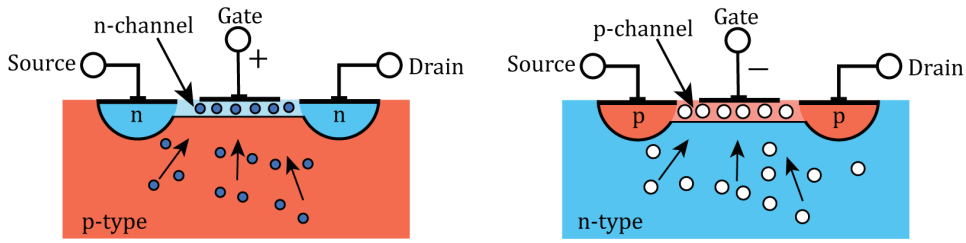

Figure 24: Schematic view of enhancement-type MOSFET operation. Left: n-channel enhancement -type MOSFET. Right: p-channel enhancement-type MOSFET.

3.1.3 *Basic Semiconductor Detectors Concept*

Doped semiconductor crystals can also be used to detect ionizing particle. As mentioned on the previous section, if an inverse voltage is applied to a pn-juntion, a depletion region is generated (Fig. 22). This depletion region is emptied of free charge carries, and therefore it behaves as an insulator. When an ionizing particle passes through the depleted region, electron-hole pairs are generated along the path (electrons are ripped out from the bindings). They will be separated by the electric field, the holes will move towards the p^+ junction, while electrons will drift to the n^+ electrode. This movement of charge carriers will generate a signal, on the collecting nodes, that can be detected and amplified. A schematic view of basic Silicon detector bulk is shown in figure 25.

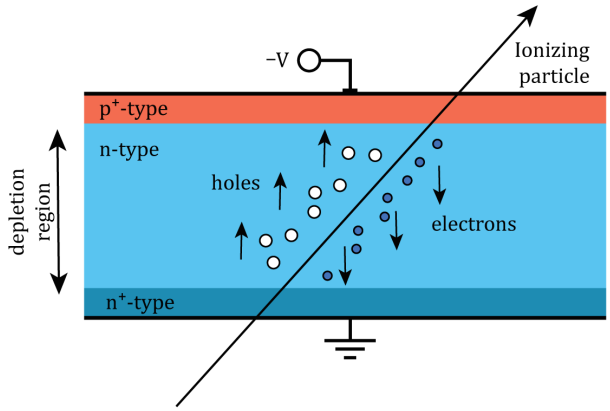

Figure 25: Schematic view of a basic semiconductor detectors, the passing through of an ionizing particle creates electron-hole pairs.

3.2 DEPFET Technology

The **DEP**leted **F**ield **E**ffect **T**ransistor structure (DEPFET) is an active pixel technology which uses the combination of detection and amplification on the same structure. The idea was proposed, in 1987 [66], by J. Kemmer and G. Lutz and finally developed on 1990 [67].

A DEPFET pixel is constructed with a MOS field effect transistor (MOSFET) integrated onto the surface of a n-doped Silicon bulk, with p^+ contacts [65]. As was mentioned on Section 3.1.1, if a negative voltage in applied though the contacts, the electrons will be forced to move away from the pn-interfaces, creating the depletion region. If the depletion region is generated from both sides (Fig. 26), a minimum of potential plane, for the electrons, is created [5]. If voltage applied on both sides of the bulk are equal, the minimum of potential will be created at the center of the bulk (Fig. 26, b). However, varying the voltage ratio between both sides, the minimum of potential can be vertically shifted. On a DEPFET pixel, the voltages will be fixed in order to place minimum of potential plane near the MOSFET transistor, around ~ 1µm below (Fig. 26, c) [68].

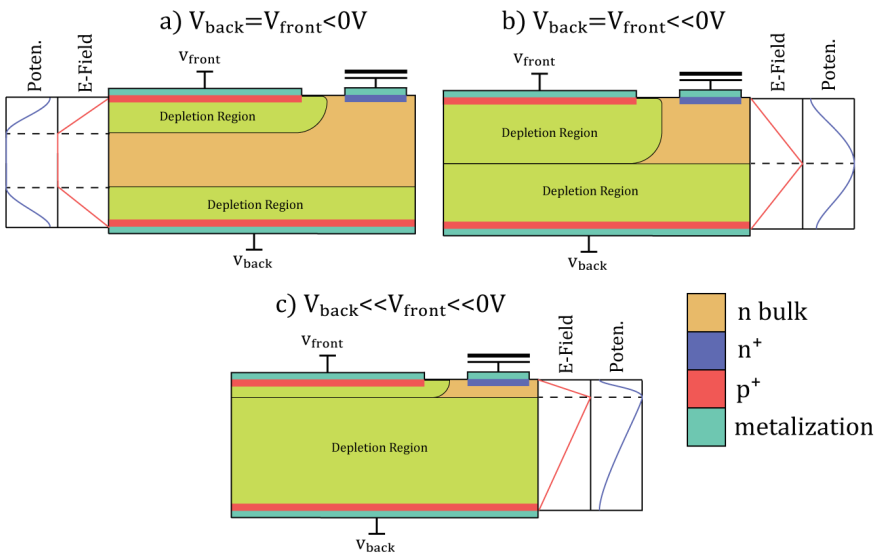

Figure 26: Schematic view of the sideward depletion concept. Depending on the voltage balance between both sides, the minimum of potential plane, for the electrons, can be moved upwards or downwards [69].

5 The electrons generated by an impinging particle will tend to move as far as possible from the pn-juntion on both sides, finding an equilibrium plane (minimum of potential).

An additional deep n-doping implantation, under each MOSFET gate, is performed. This creates an attractive region, for the electrons, called *internal gate* [6].The DEPFET structure makes the internal gate the most attractive region for the electrons. Therefore, when an incident particle goes through the detector, the electrons generated will be stored on the internal gate (holes will be drift to the backside plane). The charge accumulated on this region will leads to a change on its potential, the internal gate is capacitive coupled to the transistor's channel and therefore resulting in a modulation of the channel current (Fig. 27) [70].

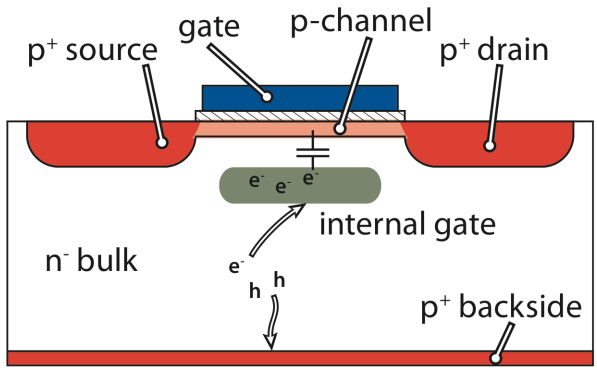

Figure 27: DEPFET lateral section. The MOSFET is integrated on the top of the fully depleted Silicon bulk. The deep n-doping implantation creates the internal gate under the transistor channel [71].

The DEPFET structure generates a drain current proportional to the charge located on the internal gate, the proportion between these two quantities is know as *internal amplification* (g_q), which can be defined as a function of the transistor's design parameters (Eq. 23, see Appendix B) [69], such the gate length (L), transistor's width (W), oxide thickness (d_{ox}) and the transistor's current (I_{DS}). In the present devices, which use a $L = 5\ \mu m$ and a $I_{DS} \sim 100$ nA/LSB, the internal amplification is about 750 pA/e^-.

$$g_q \propto L^{-3/2},\ W^{-1/2},\ d_{ox}^{1/2},\ I_{DS}^{1/2} \tag{23}$$

One of main characteristics of DEPFET structure is its low noise, even at room temperature, due to small capacitance of the internal gate. Moreover, on the first stage of amplification, non external connection circuitry is necessary, since each DEPFET pixel delivers, by themselves, a readable current signal. The electrons stored on the internal gate are stored permanently, because the signal readout does not affect them. However, the internal gate has a limited storage capacity and therefore it must be emptied

6 The electrons that reached the minimum of potential plane will be attracted (lateral diffusion) by this n^+ doped region, generating a lateral confinement.

to avoid the full filling and consequently to become insensitive to new charge. Since, charge generated on the bulk, can be originated by an impinging particle, but also due to the thermal electrons (leakage current), the cleaning process must be done periodically.

The *clear process* is performed by using another deep n-doping implantation (n^+) close by the internal gate, called *clear* contact (Fig. 29). To induce the electrons to flow from the internal gate to the clear contact, a positive voltage is applied, which turns this contact in the most attractive region. However, to prevent the electrons from drifting to the clear contact when it is not required, the clear implantation is shielded by a deep p^+-implantation, called p-well. During the charge collection process [7], a negative voltage is applied to the clear contact and consequently, the p-well shields it from the internal gate. Another structure, called *cleargate*, has been added to mediate and help during the clear process (Fig. 28) [72].

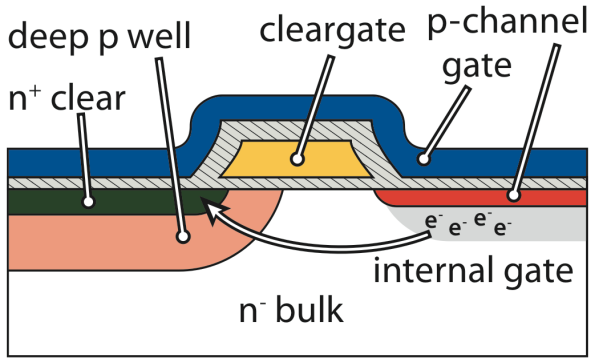

Figure 28: Lateral section of the DEPFET *Clear* implantation and *Cleargate* structure [71]. The electrons are extracted from the internal gate via punch through over the p-well.

3.2.1 *DEPFET Pixel Matrices*

One of the main features of the DEPFET pixel technology is the ability to perform a readout process independently from the sampling or charge collection period. This allows to modify the integration time or the readout scheme to accommodate them to the requirements of the experiment. Moreover, the clear process is also independent and can also be adapted, depending on the necessities. For these reasons, DEPFET is an adaptable technology, capable to cope with the requirement of many detector

7 Charge collection process only requires the static voltages to guide the electrons to the internal gate. It does not require the readout mechanism (which is completely independent). Therefore, the power consumption, even having a sensitive module, is very low.

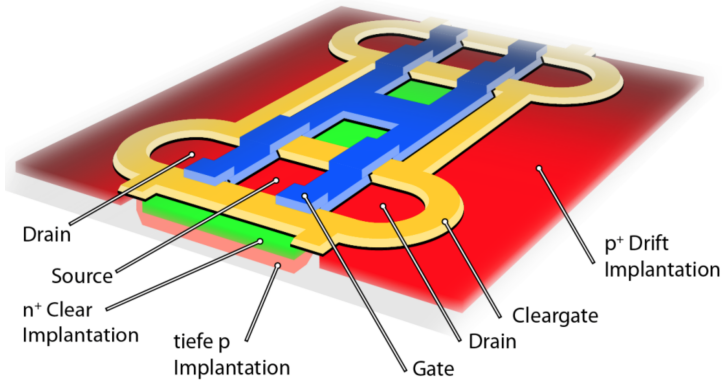

Figure 29: Top view of the DEPFET four-pixels structure [71].

schemes. However, a typical operation method can be described as the following iterative loop [70]:

- **Sampling or charge collection period:** This period only requires the static voltages to guide the electrons to the internal gate, the transistors are switched off. Therefore, the power consumption is almost zero but the pixel still remains sensitive to new charge. The collection time is very short (~ 10 ns), since the Silicon bulk is fully depleted.
- **Readout:** A voltage is applied to the gate contact and the channel is formed, therefore the source-drain current starts to flow, modulated by the charge located on the internal gate. This current contains the *pedestal* [8] and the *signal* contribution. The current will flow through the drain line to the subsequent signal processing steps.
- **Clear and Reset:** A voltage pulse is applied to the clear contact, removing all the charge located on the internal gate. At this stage, the DEPFET technology allows to measure again the drain current (internal gate completely empty), obtaining an online measurement of the pedestals (correlated double sampling method). However, the readout scheme depends on the experiment timing requirements. For this reason, pedestals can be also subtracted offline (they are stable in a constant temperature). Finally, the external gate voltage is set back, switching off the transistor and bringing back the DEPFET pixel to the sampling state.

DEPFET pixels can be arranged in a two-dimensional matrix structure, which allows to place all required ASICs [9] (Fig. 30) outside of the acceptance region. Since DEPFET

8 The pedestal is defined as the baseline source-drain current, produced even having a completely emptied internal gate. It is an intrinsic characteristic of transistors.

9 Electronics necessary to readout and operate the matrix.

pixels have a very high amplification and a very low intrinsic noise, the matrices can be implemented in a very thin Silicon wafer, reducing the intrinsic material budget. In addition, during the sampling period, the matrix remain sensitive with a very low power consumption and producing negligible heat, which, in terms of mechanics and cooling, reduces also the material budget.

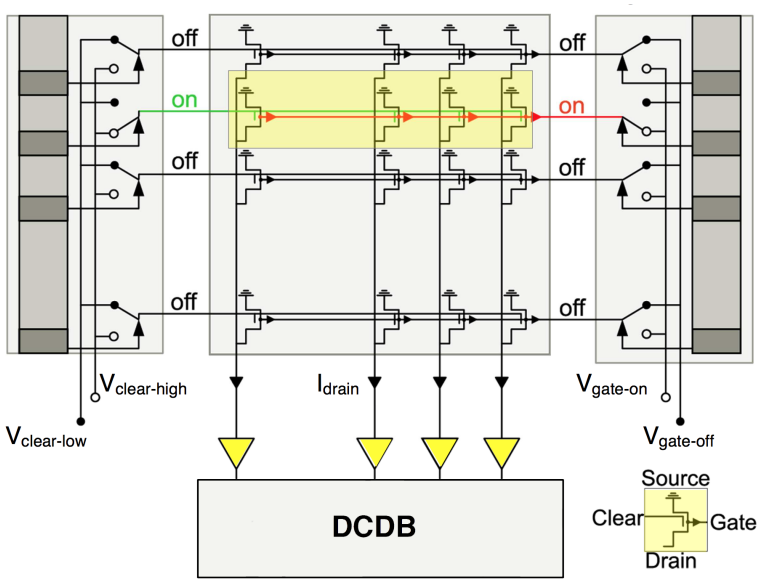

Figure 30: DEPFET matrix scheme. The gate and clear voltages are controlled by the peripheral chips. The drain currents are digitized on the DCD (Drain Current Digitizer) [64].

The operation of a DEPFET matrix requires a steering chip to manage the control signals, such as gate voltage and clear pulses (Switcher). Also, the drain current has to be digitized to, subsequently, be processed. The digitalization is performed by another chip, called Drain Current Digitizer (DCD).

The chips are placed aside of the matrix and determine the distribution of interconnections between pixels and also the readout scheme. The typical readout process is known as *rolling shutter mode* and is based on the idea of reading sequentially the matrix row by row. In this scheme, all pixels on the same column share the drain line, and all pixels on the same row share the control lines (gate and clear). Figure 30 represents, schematically, the connections between DEPFET pixels and the ASICs. To perform this readout, the switcher will control which row is activated, the transistors involved will provide the drain current to the DCD through the drain lines. The DCD will sample, on the precise moment, and will extract and digitize the corresponding value [10]. Then,

10 The drain current is digitized by the DCD, which provides the current value in ADUs

the switcher will disconnect this row a will repeat the process on the next one. The readout speed depends on the swiftness of the ASICs internal clock and the response speed of the different parts [11]. However, one strategy to accelerate this process is to readout, simultaneously, multiple rows, implementing several parallel drain lines. For example, on Belle II prototypes, 4 rows are activated and readout simultaneously, allowing a readout time of 20 μs for a 768×250 pixels matrix.

3.3 *Data Analysis Strategies*

One of the main tasks performed during this thesis, was the development of software tools for the analysis of the data from Belle II DEPFET prototypes. In this section, the general analysis chain will be described and also some of the studies performed .

The analysis process can be divided in two main steps:

- **Distinguish the primary signal data:** Obtain the primary signal data, distinguishing it from the other contributions, such pedestal contribution.
- **Studies over the primary signal data:** The primary data can be analyzed to extract the desired information

All the studies presented have been performed on small DEPFET matrices, designed to test the characteristic of the pixels prototypes for Belle II, with a typical matrix size of 32×64 pixels. These matrices were integrated on hybrid boards to perform the configuration and readout. The output data obtained was a list of frames [12], ordered by the acquisition time (time stamp).

The raw signal (S_{ij}^{raw}) from a pixel ij (considering a matrix where i represents the rows and j the columns) can be divided in four contributions (Eq. 24): P_{ij} is the pedestal contribution, N_{ij} is the noise contribution, N_{ij}^{CM} is the common mode contribution and S_{ij}^{pure} denotes the primary signal proportional to the charge on the internal gate. To obtain S_{ij}^{pure}, the other contributions have to be calculated and then subtracted from S_{ij}^{raw}. The following sections will introduce the standard methods to obtain each contribution.

$$S_{ij}^{raw} = P_{ij} + N_{ij} + N_{ij}^{CM} + S_{ij}^{pure} \tag{24}$$

3.3.1 *Pedestal Calculation*

The pedestal contribution can be described as the pixel drain current response when no charge is located on the internal gate. The impossibility to construct identical pixels

11 This response can be limited by the intrinsic and parasitic capacitances.
12 Data frames which includes the signal contribution, the pedestal contribution and the noise contribution.

on the same matrix, creates variation between DEPFET pixels, in terms of geometrical dimensions, doping concentration, etc. These small differences generate considerable changes on the pedestal currents between them. Therefore, the pedestal value is intrinsic to each pixel and has to be calculated individually. For this, different approaches can be followed to obtain these values:

- **Correlated double sampling:** It requires of two sampling steps foreach readout loop, therefore, this method can be used when the readout speed is not an issue (Fig. 31). First sample is taken before the clear process and a second sample is obtained immediately after (with the internal gate completely empty). Then, the differences between these currents can be considered as the pedestal cleaned signal.

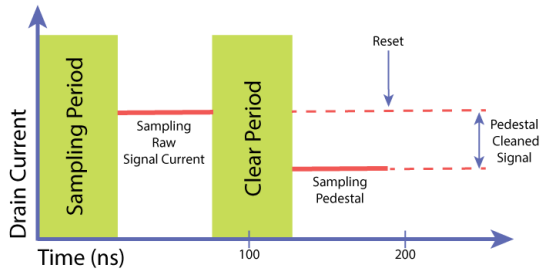

Figure 31: Correlated double sampling: Schematic view of the double sampling method.

- **Offline Correction:** The offline method assumes the correlated pedestals do not change over time, in a constant temperature. The pedestal frame is calculated as the mean value, per pixel, over a large number of consecutive frames. Finally, this frame can be subtracted, offline, to the raw frames.

Usually, the pedestal map is calculated offline, using an iterative method. The pedestal map has to be updated periodically to include the small variations due to temperature changes. The iteration has to be applied to reduce the deviations produced by the impinging particles. To use this method, the frame occupancy has to be low, to ensure that almost all pixel data is obtained with an empty internal gate. The pedestal calculation is performed twice:

- On the first iteration, the mean value, per pixel, is calculated and used to define a baseline charge.
- The cut is defined (the baseline charge with a small tolerance) to exclude, from the next calculation, the pixels which include charge on the internal gate. The second iteration calculates the mean value, per pixel, using the frame data which are below the cut.

3.3.2 *Common Mode Correction (CMC)*

The common mode noise is caused by the row-wise readout scheme. It is a constant offset to all pixel drain currents which have been sampled and processed at the same time. It is produced due to instabilities of the power supply or due to electromagnetic pickup. The CMC fluctuates heavily in time but it is the same for all pixels involved. Therefore, it can be isolated, offline, by obtaining the mean value, as it is shown equation 25, where N_{CM} is the number of pixels readout a time, S_k^{raw} is the raw signal on the pixel k and P_k its pedestal value.

$$N^{CM} = \frac{1}{N_{CM}} \sum_{k=0}^{N_{CM}} (S_k^{raw} - P_k) \tag{25}$$

N_{CM} depends on the readout scheme, for instance, in Belle II prototypes, four rows are sampled simultaneously [13], hence the CMC is calculated averaging the pixels from all of them. To obtain a precise N^{CM} value, it is also important to take into account the random particle hits, that can affect the calculation. Accordingly, these hits have to be excluded following the criteria defined on the pedestal calculations, which exclude the pixels with charge over the defined cut.

3.3.3 *Noise Distribution*

The noise produced by the DEPFET pixel itself is negligible compared to the noise generated by the electronics. Mainly, it is produced on the DCD as a resistor noise and thermal noise. The noise signal values are randomly distributed and can be approximated to a Gaussian distribution. It cannot be removed as the pedestal and common mode contribution, but can be used to identify noisy pixels and omit them from the further calculations [14]. The noise value is calculated with the root-mean-square (RMS) per pixel over n frames, as it is shown in equation 26, where $S_{ij}^{k,Cor}$ is the signal corrected by pedestal and common mode, $\overline{S_{ij}^{Cor}}$ represents the mean corrected signal value of the ij pixel over n frames.

$$N_{ij} = \sqrt{\frac{1}{n} \sum_{k=0}^{n} (S_{ij}^{k,Cor} - \overline{S_{ij}^{Cor}})^2} \tag{26}$$

13 The four rows share same gate connection.
14 Noisy pixels: pixels with a noise level higher than the expected value in an specific DEPFET prototype.

3.3.4 *Clustering*

Once the contributions to the raw signal (S_{ij}^{raw}) are isolated, the primary data signal (S_{ij}^{pure}) can be obtained as equation 27.

$$S_{ij}^{pure} = S_{ij}^{raw} - P_{ij} - N_{ij}^{CM} \tag{27}$$

DEPFET matrices provide analog information about the charge deposited by the impinging particles. The analog information can help in improving the binary single point resolution via charge sharing. To be able to distinguish the clusters, two cuts are applied:

- **Seed Cut:** It is used to search for the pixels with the highest signal values (seed pixels), assuming that, normally, almost all charge deposited by an impinging particle will be found in one pixel (on perpendicular incidence). The cut should be high but not excessively to include hits with large charge sharing. If two adjacent pixels exceed the cut, they will be considered as one cluster and the pixel with higher value will be defined as seed pixel (Fig. 32).

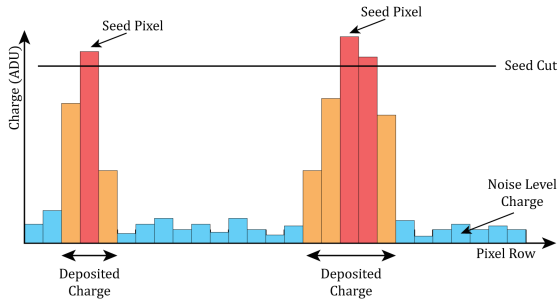

Figure 32: Charge deposited by two impinging particles in one row. The blue bars represent the baseline charge level due to the pixel noise. The seed cut is fixed to a high value to distinguish the pixels with higher charge.

- **Neighbor Cut:** It is used to search around the seed pixels and construct the final cluster. The process starts from the seed pixel, if any neighbor pixel exceeds this cut, it will be considered part of the cluster. Then, iteratively the search is extended to the neighbor pixels, which are included on the cluster (Fig. 33), the aim is to follow the shape of the cluster and even include δ-electrons [15]. This cut should be high enough to exclude noisy pixels but has to remain as low as possible to maximize the cluster information.

15 δ-electrons are recoil electrons generated by a secondary ionization process. They are produced by the impinging particle and generate a parallel (to the suffice) ionization track on the sensor matrix.

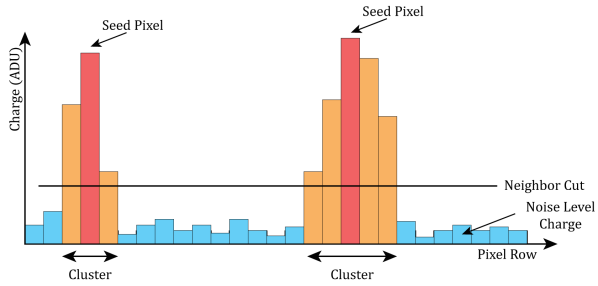

Figure 33: Charge deposited by two impinging particles in one row. The neighbor cut should be high to exclude noisy pixels but has to include all the cluster information.

These cuts are used to identify, offline, the cluster on the *primary signal map*. But, on large matrices, due to the huge amount of data generated (i.e. DEPFET Matrix Belle II design: ~ 80Gb/s), the *neighbor Cut* has to be applied online, to reduce the volume of readout information. In that case it will be called *Zero suppression cut*.

Once the clusters are identified, the next step is to use the cluster algorithms to calculate the hit position. The easiest approximation is the Center-of-Gravity method (CoG), which considers a linear charge sharing between pixels. The formula used is shown in equation 28, where x_{reco} is the reconstructed hit position on the x axis, Q_i is the charge deposited on the i pixel and x_i represents the center position of the i pixel. Analogously, same formula can be applied to the y axis.

$$x_{reco} = \frac{\sum_i Q_i x_i}{\sum_i Q_i} \tag{28}$$

In reality, the charge sharing between DEPFET pixels is not linear, therefore the hit position has to be corrected for this effect. One option is to use the η-correction. This method has been used, extensively, but won't be covered on this thesis, for more detailed information see Ref. [73].

3.4 *DEPFET Resolution*

The DEPFET technology has been widely studied in several test beam campaigns. The following study intends to measure the spatial resolution achievable with a DEPFET prototype. The idea was to find the optimal *neighbor cut* (*zero suppression cut*) to reach the maximum spatial resolution. Then, the study of the resolution was generalized to prove the existence of limits on the maximum resolution achievable with solid-state devices that rely on charge sharing between neighboring cells.

The resolution can be obtained comparing position reconstructed by the DEPFET sensor (Device Under Test - DUT) and the real hit position. For this, the exact position of the incident particle should be known. The information is provided by the so called telescope, which consist in six planes of pixel sensors, placed in parallel, allowing the extrapolation of the track over the DUT (Fig. 34). Using this data, it is possible to obtain the residuals distribution ($r = x_{reco} - x_{real}$) [16]. The resolution is calculated with the RMS of the residuals distributions.

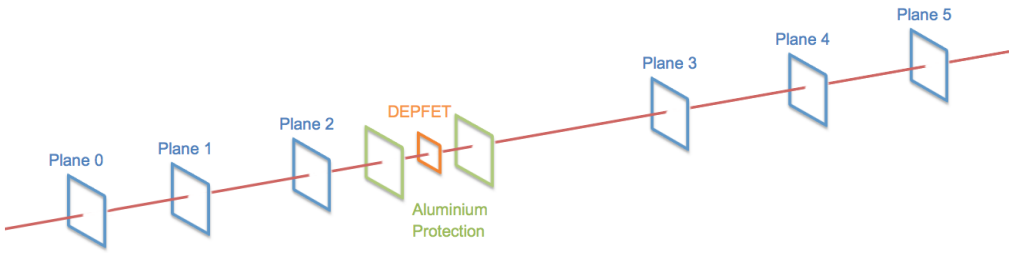

Figure 34: Schematic geometry of a telescope with the DUT placed in the center of the 6 telescope planes.

The study has been performed with small DEPFET matrices (32×64 pixels), with a thickness of 50 μm and a pixel size of 50×75 μm^2, the expected signal to noise ratio (S/N) is around 20. These modules have been tested on the SPS-CERN facilities, using 120 GeV pions (π).

Since DEPFET technology provides analog information about the charge deposited by the impinging particle, the *neighbor cut* or *zero suppression cut* is a crucial parameter, which defines the maximum resolution. The *zero suppression cut* should be as small as possible to include the maximum cluster information, but high enough to reject noisy pixels. A scan of the zero suppression cut (defined in terms of multiples of the intrinsic noise) is shown in figure 35.

The sensor resolution increases as the zero suppression cut decreases, up to a limit where the noisy pixels begin to blur the real signal. On the other hand, when increasing the cut, the resolution approaches to a limit corresponding to the binary resolution, in this situation, the sensor is behaving as a binary sensor, which resolution limit is defined as show in equation 29. This study gives an idea of the minimum *zero suppression cut* that can be used to ensure that noisy pixels will be omitted from the hit reconstruction.

16 Residual Distribution represents, in a histogram, the difference between the track extrapolated by the telescope and the hit position reconstructed by the DUT. The x and y axis are calculated independently.

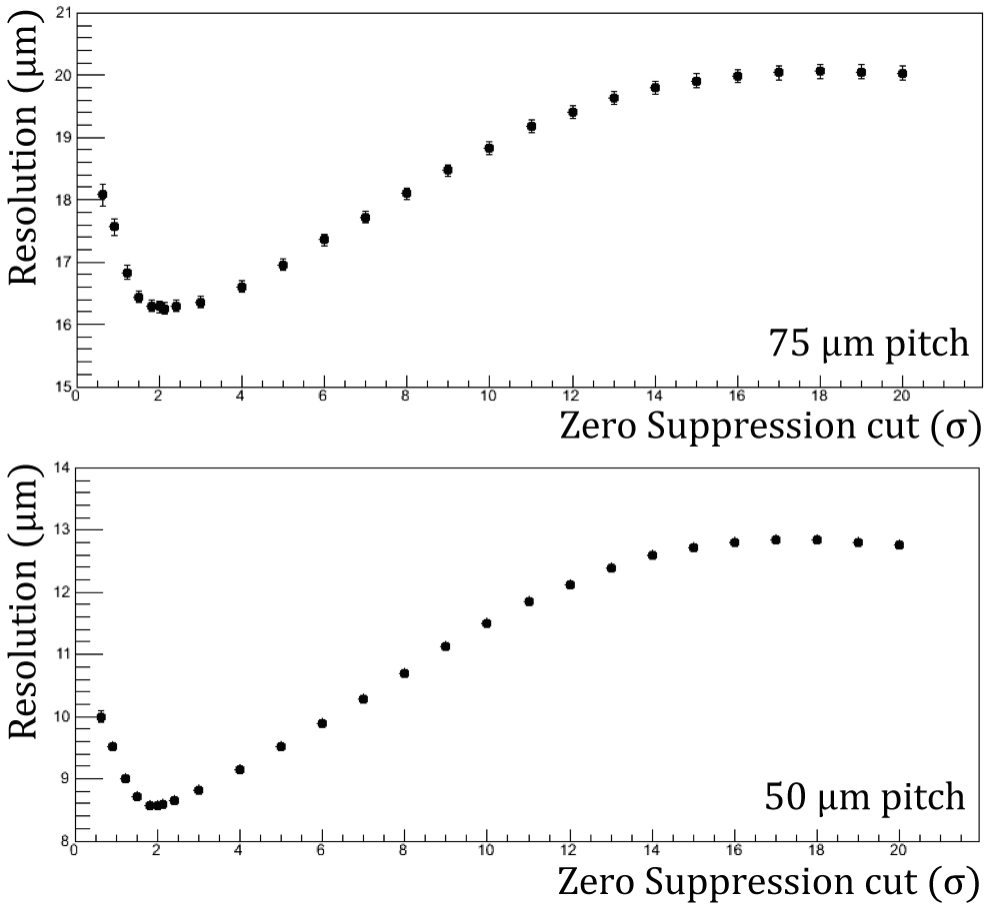

Figure 35: DEPFET sensor resolution as a function of the zero suppression cut. Upper plot shows the results on the rows direction (pitch 75 μm) and the bottom plot on the columns direction (pitch 50 μm) [73].

$$R = \frac{\text{Pitch}}{\sqrt{12}} \tag{29}$$

These DEPFET prototypes (50 μm thick), achieve resolutions up to 8.5 μm. However, with thicker prototypes (higher signal-to-noise ratio) and with smaller pixel sizes (~ 20 μm), it has been proved that DEPFET technology is capable to reach a spatial resolution that approaches to a single μm [74].

At this level of thickness and pitch size, there are effects, such Landau fluctuations or δ-electrons, that can blur the expected resolution. The study was extended to see if these effects can limit the maximum resolution achievable with solid-state devices

that rely on charge sharing between neighboring cells. The results were published at Ref. [75].

Ideally, the resolution should scale with the signal-to-noise ratio (S/N) and the *pitch* size as show equation 30 (See Ref. [76]). Considering the resolution achieved with the DEPFET prototypes, on the order of few microns. If Silicon-based devices continue with the fine segmentation and improving the S/N, it is expected to obtain resolution well below 1 μm in a near future. At this level of resolution, the effects, previously mentioned, have to be considered. The aim of this work was to study the impact of these effects on the maximum resolution:

$$R \propto \frac{\text{Pitch}}{S/N} \tag{30}$$

- **Straggling Functions (Landau distribution of charge deposition):** The energy deposited by a charged particle in a thin layer of Silicon can be described by a straggling function (also called *Landau distribution*). The predictions performed with the H. Bichsel model [77] are shown in figure 36, where the expected distributions for 450 μm, 50 μm, 5 μm and 1 μm thin Silicon detectors are shown. The figures on the left are compared with the charge distribution collected by a DEPFET prototype with the corresponding thickness. Notice that fluctuations on the energy deposition become much more conspicuous as the sensor become thinner.

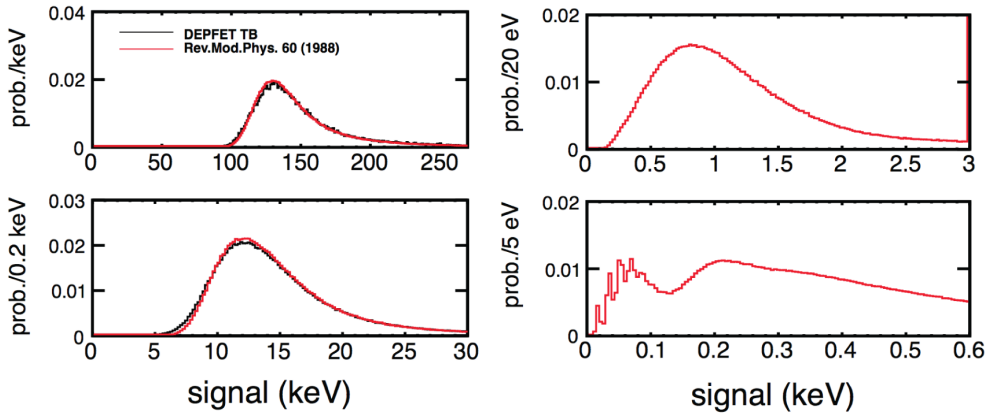

Figure 36: Energy deposition distribution in Silicon sensors with different thickness (450 μm - top-left, 50 μm - bottom-left, 5 μm - top-right, 1 μm - bottom-right). The plots on the left contains a comparison to the charge distribution collected by a DEPFET prototype whit the corresponding thinness [75].

- **δ-electrons:** Charged particles traversing material ionize atoms along the trajectory. Sometimes, the momentum transferred to an electron is high enough to generate a secondary track (δ-electron). This electron can travel along the Silicon, carrying away energy from the primary impact and modifying the charge distribution of the primary cluster. Figure 37 (right) shows a δ-electron candidate detected with a DEPFET pixel detector. Figure 37 (left) presents the probability that 120 GeV pion generates a δ-electron traversing 450 μm of Silicon sensor in a perpendicular direction. Solid black points are data from a DEPFET test beam and the dashed line represents the GEANT4 simulation. Notice that long range δ-electrons are relatively rare (5.4% with a track longer than 100 μm), however, shorter range δ-electron are common.

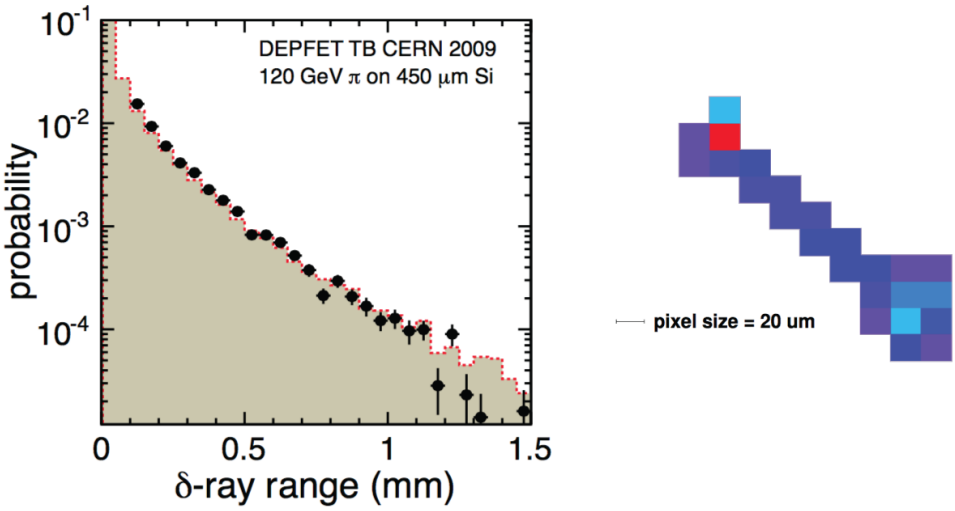

Figure 37: Left: Probability of δ-electron emission by a 120 GeV pion traveling perpendicularly on a 450 μm thick Silicon sensor. The black points are data from DEPFET test beam data and the dashed line represents the GEANT4 simulation. Right: δ-electron candidate detected with a DEPFET pixel detector [75].

To evaluate the δ-electrons and the Landau distribution impact, two possible incidence scenarios have to be distinguished:

- **Perpendicular incidence:** In this case, the effect of Landau fluctuation will be negligible since the charge will be generated on a linear track inside of the same cell. On the other hand, eventually a δ-electron can be generated. This electron creates a track outside of the primary cell and therefore it will carry part of deposited charge, modifying the distribution of the cluster. GEANT4 simulations

with a detailed model of the DEPFET detector [78] response have been used [17]. Figure 38 shows the resolution/pitch as a function of the S/N ratio. The solid red curve represents the GEANT4 simulation, including δ-electrons, the dashed red curve shows the same but excluding δ-electrons. They are compared with the data obtained with a DEPFET detector (solid black line), which has been smeared to include the behavior of detector with higher noise. The expected curve, following the equation 30, has been also included (dashed black line). The differences within the curves confirm that δ-electrons play an important role, limiting the resolution for the detectors with very high S/N ratio.

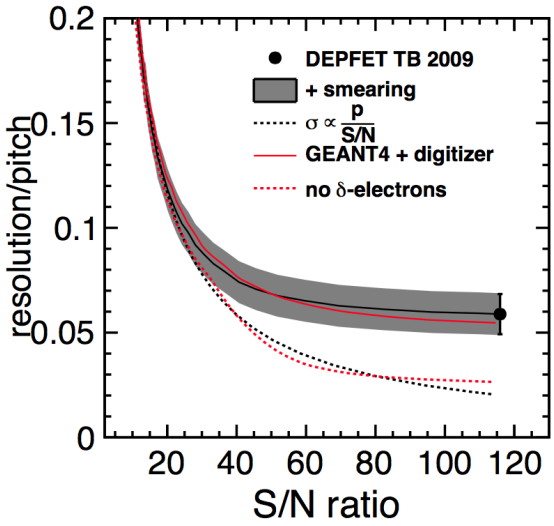

Figure 38: Spatial resolution divided by the pixel size versus S/N ratio, using pions of 120 GeV perpendicularly impinging a 450 μm thick DEPFET device (black solid line), compared to the GEANT4 simulation with δ-electrons (red solid line) and without δ-electrons (red dashed line). The ideal situation have been also included (black dashed line) [75].

- **Incidence under an angle:** For a non-perpendicular incidence, the additional influence of the Landau fluctuations must be considered. In an ideal situation, the charge deposited by an impinging particle would be proportional to the length of the track inside every traversed pixel. However, this is not true. A particle crossing a bulk will have a probability of deposit a certain amount of charge described by the Landau distribution. Figure 39 (left) shows the impact of these fluctuations simulated with a Monte Carlo tool [18]. The dashed line represents the ideal situation where the charge deposited is proportional to the track length. On the

17 Simulation performed by Benjamin Schwenker [78].
18 This calculation does no include a realistic DEPFET detector, neither the δ-electrons effect.

other hand, the solid lines represent the same curve including the Landau fluctuation, considering a sensor with 50 μm thick (red) and 450 μm thick (black). The ideal detector achieves a resolution of 6% of the pitch (five times better than the binary limit), however the more realistic scenarios reach a 9% resolution for the 450 μm thick device and 12% resolution for the 50 μm thick. This result proves that, considering a high S/N ratio, an increment on the S/N ratio does not contact to improvements on the spatial resolution. Figure 39 (right) shows the behavior of several devices in a non-perpendicular incidence angle. To compare these three devices with different thicknesses on a equal scale, the result of thicker devices have been multiplied by a factor 1.5, obtained from the Monte Carlo simulation. The resolution/pitch obtained is ~ 7%, which is in good agreement with the simulation.

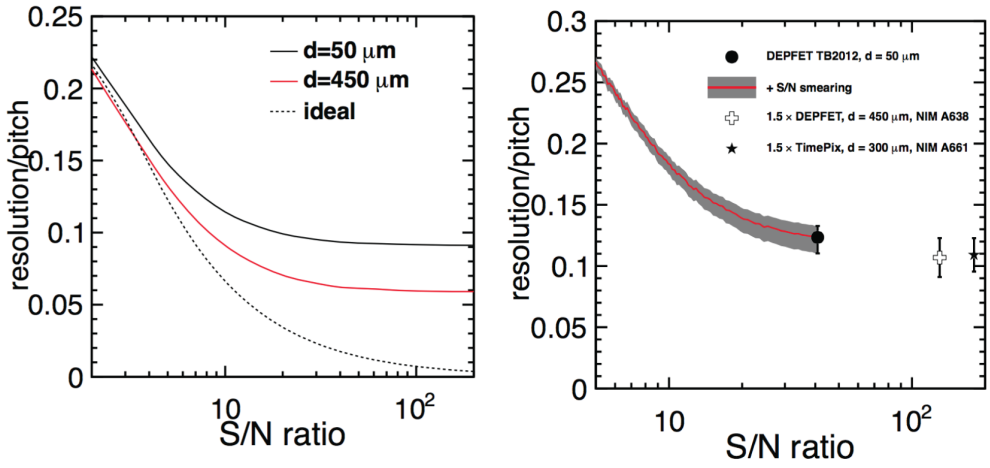

Figure 39: Left: Monte Carlo simulation of the spatial resolution divided by the pitch versus S/N ratio. The dashed line represents the situation where charge deposited is proportional to the track length, solid lines include the Landau fluctuation effect, considering a 50 μm (red) and 450 μm (black) device thickness. Right: Spatial resolution divided by the pitch versus S/N ratio for multiple devices [75].

This study proved that the maximum resolution of solid-state devices that rely in charge sharing between neighboring cells, is limited by the impact of the δ-electrons and the Landau fluctuations. Therefore, increasing the S/N ratio, reducing the pixel size or the thickness, will generate a negligible improvement on the spatial resolution. Also important is to notice that the current DEPFET technology is capable to reach these resolution limits.

3.5 *Gated Mode*

As was mentioned on Section 2.5, SuperKEKB will inject periodically new bunches, alternating HER and LER with frequency of 50 Hz (Fig. 40). The cooling down process of the injected bunches will take ~ 4 ms, therefore, during this time, noisy bunches will pass through the inner detectors every 10 µs, generating additional background and spoiling the information already stored on the DEPFET matrix.

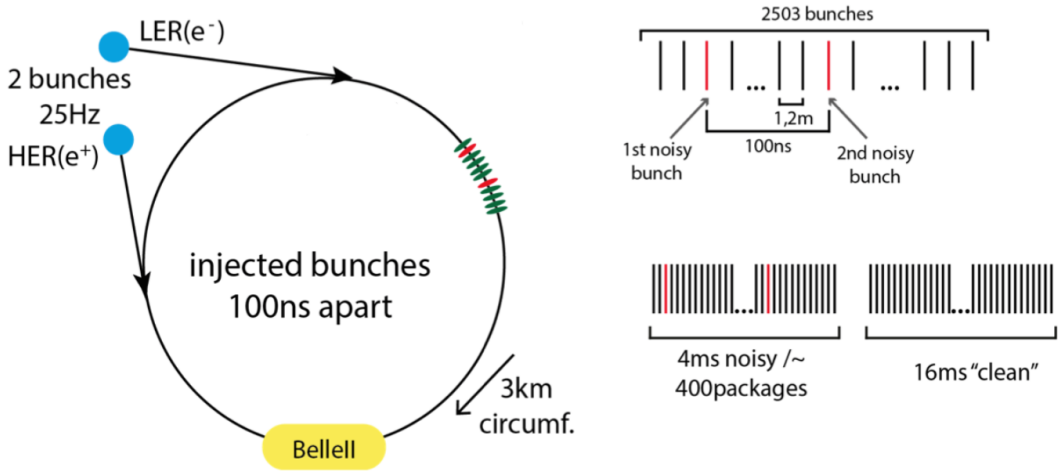

Figure 40: SuperKEKB injection scheme.

DEPFET collaboration has developed a method to coexist with the injection period, which requires to remove all charge coming from the passing through of the new bunches but preserving the charge already stored inside the pixel. This method is called *Gated Mode* and consists on shielding the charge located on the internal gate and then enabling the clear contact to remove all new charge generated. Figure 41 shows, schematically, the three operational modes.

During the charge collection operation (Fig. 41 - left), the internal gate is the most attractive region for the electrons, the p-well hide the clear implantation, avoiding charge losses during this period. The electrons generated by an impinging particle will drift and will be stored on the internal gate. When a positive voltage is applied to the clear contact this region becomes the most attractive (Fig. 41 - center), the potential barrier between clear implantation and the internal gate is small (~ 0.5 V), therefore, the electrons stored will overcome the barrier and will drift to the clear region. On the other hand, by changing the *gate* voltage, since it is capacitive coupling to the internal gate, this will effectively increase the potential barrier between the internal gate and the clear implantation (~ 2 V), suppressing the cleaning process and precluding the extraction of charge. In this scenario, all new charge generated will drift directly to the clear con-

tact (Fig. 41 - right). Consequently, the charge already collected will be shielded and available to be readout afterwards.

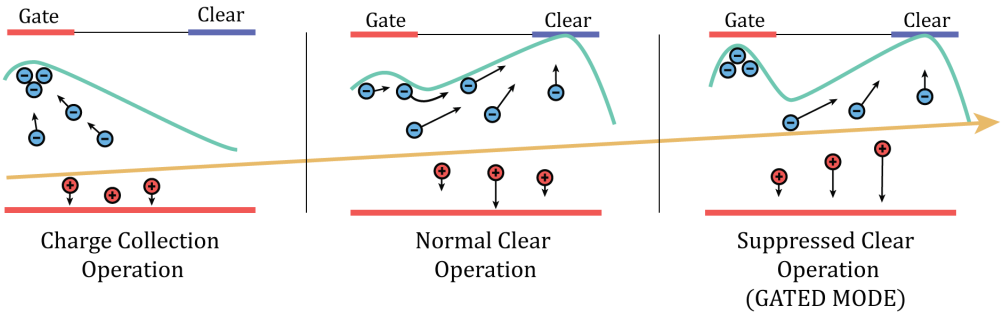

Figure 41: Schematic view of the three DEPFET operational modes. The blue line represents, schematically, the potential for the electrons. Left: during the charge collection operation, the clear contact is hidden, therefore, the internal gate is the most attractive region. Center: a voltage is applied to the clear contact, therefore all charge is attracted and removed. The barrier between clear and internal gate is small, allowing the charge to escape. Right: the internal gate is shielded, only new charge generated drift to the clear contact.

The gated mode performance was tested on the laboratory, using a small DEPFET matrix (32×64 pixels) placed on a hybrid board especially designed to perform these studies [64]. Two experiments were proposed to test the signal charge preservation and the shielding in front the junk charge generated.

- **Signal charge preservation:** The aim of this test was to check if all signal charge stored on the internal gate remained after the gated mode period. Also, it intended to optimize the *clear*, *gate* and *cleargate* voltages, to maximize the charge preservation. To perform this test, the system was programed to take *eight frames* consecutively. By default, the normal clear process was disabled and only was applied on the last frame. To generate the charge, a laser pulse was used. On figure 42 the schematic idea of the test is shown. Starting from left side, the two first frames remained empty to check if standard clear process worked normally, the laser pulse was applied on the third frame. The charge was completely collected of the fourth frame. Then, the gated mode was enabled during two frames. If the signal charge was preserved, the spot should appear, again, on the last two frames. Finally, the charge accumulated on the laser spot (frame 4) is measured and compared with the charge remaining on the last frame (frame 8).

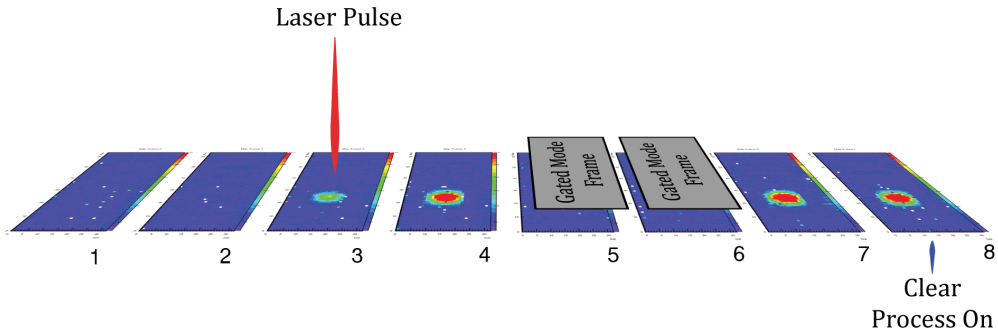

Figure 42: Schematic view of the signal charge preservation test.

To optimize the *clear*, *gate* and *cleargate* [19] voltages a scan was performed. Considering a fixed *cleargate* voltage of 4.5 V, the results are shown on figure 43. The region in red represents the combination of voltages where the charge is completely preserved. As expected, if *clear* voltage is increased, to keep the preservation, the *gate* voltage must be higher to shield the charge stored. If *clear* voltage is too high and *gate* voltage is kept low, the charge is completely lost.

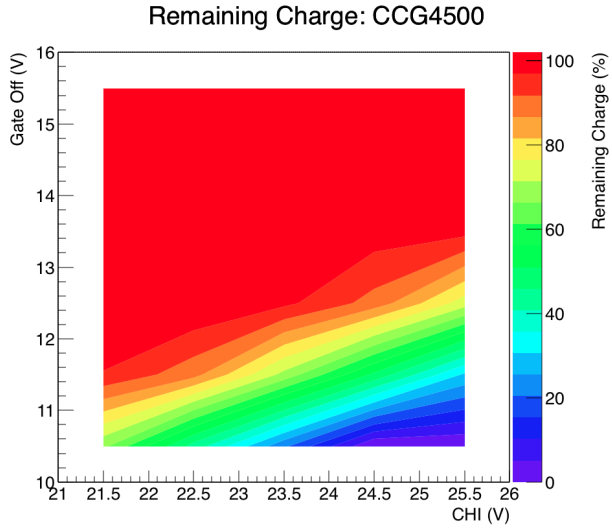

Figure 43: *Clear* and *gate* voltage scan to define the regions where charge is completely preserved. *Cleargate* voltage has been fixed to 4.5 V.

19 The aim of cleargate is to help, during the clear period, increasing the efficiency of the internal gate emptying process.

- **Shutter performance:** This test was designed to check the efficiency of the internal gate shielding and prove that the junk charge generated during the gated mode is completely removed. To perform this test, the system was programed to take *eight frames* consecutively, the normal clear process was disabled and only applied on the third and the last frame. On figure 44 schematic idea of the test is shown. Starting from the left side, a laser pulse is applied on the first frame to check if the sensor is sensitive, the laser spot remains until third frame, where is cleaned. Then, the gated mode is enabled during three frames and a laser pulse is applied during this period. After gated mode, if shielding worked, no spot should appear on the last two frames. A perfect shielding was observed in all test performed.

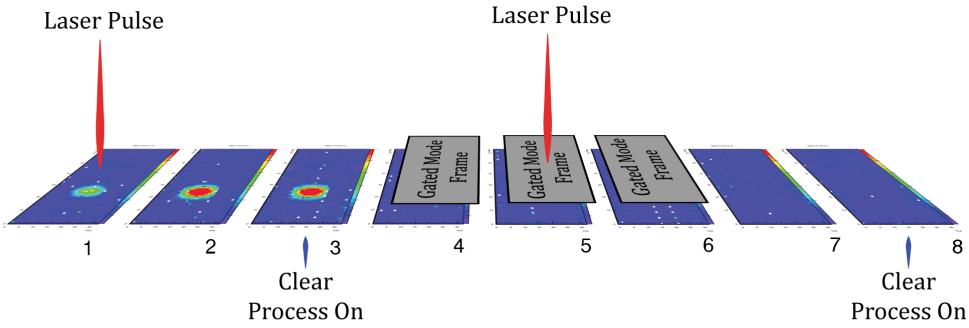

Figure 44: Schematic view of the signal charge shielding test.

In this section, a brief introduction of the results obtained during the gated mode test has been done. However, the gated mode operation is a very complex process that requires a fine tuning of all voltages involved and have shades on the operational modalities, which have not been covered here. The aim of this section was to prove the feasibility of the gated mode concept and introduce the analysis performed. For a more detailed description see Ref. [64].

3.6 *Summary*

This chapter has explained the basics of the semiconductor technology and the semiconductor detectors to introduce the necessary parts to construct a DEPFET sensor. Then, it has described the main characteristics of the DEPFET technology, emphasizing on the versatility in terms of internal pixel design, as well as the matrix operation flexibility. The internal amplification, low material budget, low power consumption, high spatial resolution, are some of the features that make DEPFET a perfect candidate as a pixel technology, capable to cope the requirement of the future e^+e^- colliders.

The main contribution of this work was the development of software tools to study and characterize the DEPFET prototypes, therefore, the main analysis techniques have been introduced. Moreover, the study of the DEPFET resolution has been presented, to describe the analysis performed on this topic, flowing into the study of the maximum resolution limits achievable with solid-state devices that rely in charge sharing between neighboring cells. Finally, the Gated Mode analysis contribution has been briefly introduced, describing the feasibility on this concept on the Belle II detector framework.

4 Belle II PXD Production

DEPFET is the used technology for the Belle II PXD. Over the last years, the DEPFET collaboration was focused on the design and construction of this detector. Part of this thesis enters on this context to participate on the production process, designing and preparing a quality control test with a specifically constructed needle card. This chapter intends to introduce the DEPFET prototypes for the Belle II experiment, briefly describing the main characteristics of these modules and their design an operation. Then, the process of production and assembly of the Belle II PXD detector will be summarized and finally, the boundary-scan operation will be introduced, since it is a crucial step during the sanity control test.

4.1 *DEPFET Sensor for Belle II*

The Vertex Detector (VXD) is the innermost sub-system of Belle II. It must be capable to measure the track of the outgoing particles with enough precision to be able to distinguish the interaction or decay vertices. By the fact of being placed nearby the beam pipe, the detectors must be radiation hard to survive the high radiation doses. Furthermore, the readout speed has to be high enough to minimize the event pile-up. The interaction energy of SuperKEKB will be in the range of the $\gamma(1S)$ to $\gamma(6S)$ resonances, therefore, low energy tracks are expected, for this reason, the low material budget will be a crucial parameter to be minimized [1]. In Belle II, the vertex detector consists os several silicon detector layers in a cylindrical structure surrounding the beam pipe. The two VXD sub-systems are shown in figure 45.

1 Material budget optimization involves the sensor supporting structure, cooling system, readout electronics...

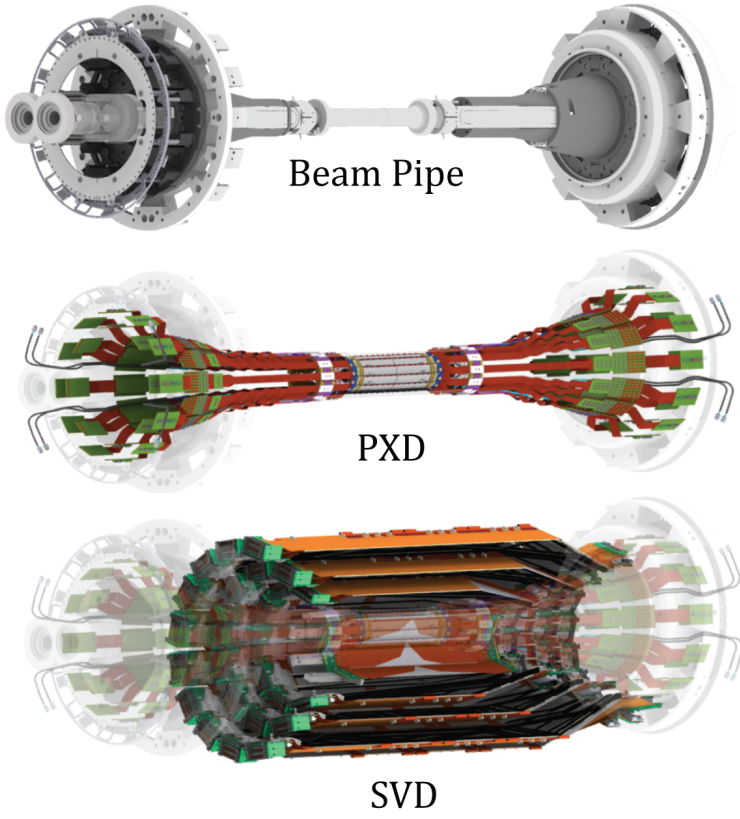

Figure 45: Belle II vertex detector sub-systems. From the top picture, the beryllium beam pipe, the PXD detector with DEPFET technology and the SVD detector designed with double sided Si strip detectors.

The Be-Ti beam pipe [2] will have a radius of 10 mm, surrounded by the pixel detector, which consists in 2 layers of DEPFET pixel modules at radius of 1.4 & 2.2 cm from the interaction point. The outermost subsystem of the VXD volume is the Silicon Vertex Detector (SVD), designed with 4 layers of double sided silicon strip modules at 3.8, 8.0, 11.5 & 14 cm. This thesis will be focused on the PXD detector, the requirements that the DEPFET modules must cope are shown in table 16.

The design of the PXD modules have been done accordingly to the environment that must confront. Table 17 shows the main characteristics of the DEPFET modules in each layer.

2 Beam pipe: central region constructed with beryllium and sides from titanium.

Occupancy	0.4 hits/μm^2/s($< 3\%$)
Radiation	2 Mrad/year
Duty cycle	1
Frame time	20 μs (cont r.o. mode)
Acceptance	$17° - 155°$
Material budget	0.21% X_0 per layer
Resolution	15 μm (50×75 μm^2)

Table 16: Requirements for the Belle II PXD detector [53].

	Layer 1	Layer 2
Module	8	12
Radii	14 mm	22 mm
Ladder Size	15×136 mm^2	15×170 mm^2
Pixel Sizes	50×55 μm^2 50×60 μm^2	50×70 μm^2 50×85 μm^2
Pixels	250×1536	250×1536
Thickness	75 μm	75 μm

Table 17: Main characteristics of DEPFET modules in each layer [79].

The number of ladders will be 8 on the first layer and 12 on the second layer, the sensitive area is designed with 250×1536 pixels and a total thickness of 75 μm. Two different pixel sizes will be used on each ladder, to maximize the charge sharing between pixels, on the central region and keep the expected occupancy level, on the forward/backward region. The central region will include pixels with 50×55 μm^2, on the first layer, and 50×70 μm^2, on the second layer. The forward/backward region of the modules will be constructed with pixels of 50×60 μm^2, on the first layer, and 50×85 μm^2, on the second layer (Fig. 46).

Each DEPFET ladder is divided in two half-ladders (modules) that will be constructed and operated separately. To assemble the full-ladder, both parts have to be glued together. The operation of a module is done using three different ASIC. The steering control of the *gate* and *clear* voltages is performed by the *Switcher*, located at the lateral balcony, along the sensitive region. The digitalization of the drain currents is accomplished by the *Drain Current Digitizer (DCD)*, and the control operation and first step of digital processing is handled by the *Data Handling Processor (DHP)*, both located on the end-of-stave region. Figure 47 shows a module including the ASICs.

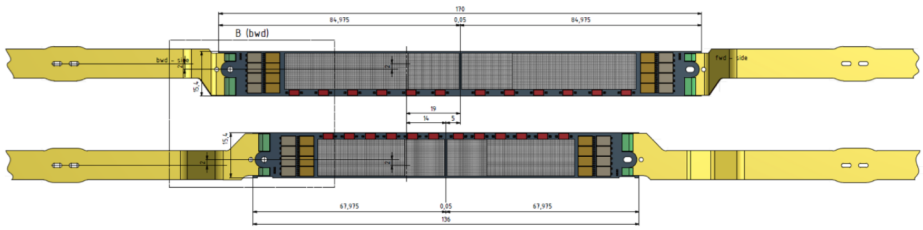

Figure 46: DEPFET ladder design picture (top: outer module, bottom: inner module). The size of the pixels on each ladder will vary to optimize the sharing of charge between pixels. On the central region the pixel density will be higher since more perpendicular tracks are expected [79].

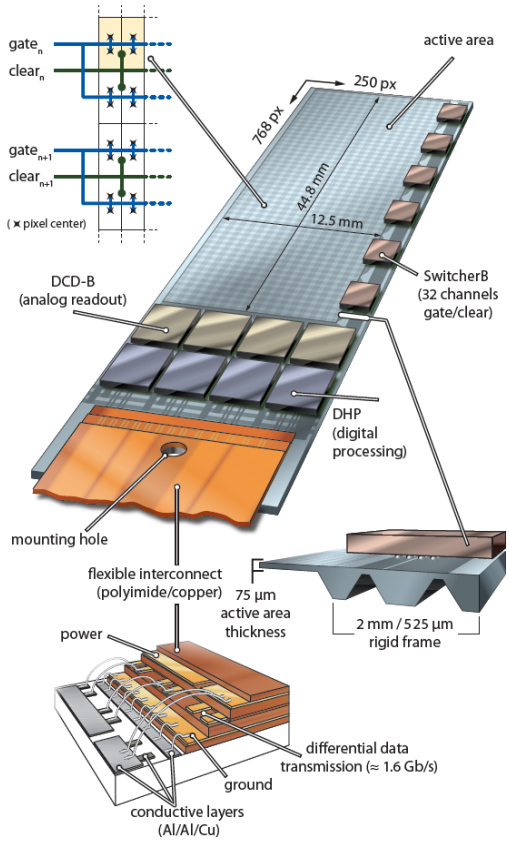

Figure 47: Module for Belle II PXD, where the three ASIC region can be identified. The Switchers are located on the balcony, reinforced with the silicon rigid frame. The DCDs and the DHPs are located on the end-of-stave. The kapton cable interconnects the module with control and readout external electronics [71].

- **Switcher:** It performs the steering of the *gate* and *clear* voltages generating fast high voltage pulses (up to 20 V in 10 ns rise time over ~ 100 pF [64]), which enables the readout and the clear processes. Six chips with 32 channels each (four rows connected per channel) are used to operate a module. They are mounted on the edge of the DEPFET module, along the sensitive part. The Switcher works as an electronic switch in order to jump between upper an lower voltage levels [79].
- **Drain Current Digitizer (DCD):** It is the analog front-end chip, meant to digitize the incoming DEPFET drain currents. Four chips with 256 analog-to-digital converters (ADCs) of eight bit resolution, working in parallel, are used to digitize all the drain currents. The digital output data is transmitted to the DHP for further processing [79].
- **Data Handling Processor (DHP):** It is the digital backend chip. Its main task is to control the other ASICs. It also preprocesses the data provided by the DCD chip and performs the first data reduction step. The DHP uses a zero-suppression (ZS) cut over the input data, storing the remaider information and only transmitting the data that has been triggered. However, before applying the zero suppression the data have to be preprocessed. First, the common mode offset is corrected. Then, the pedestal reduction is applied by subtracting a pedestal frame previously stored on the DHP. Finally, the zero-suppression is performed by discarding all data below a selected threshold. Furthermore, on each DEPFET module, one of the four DHPs controls the timing of the Switcher outputs [79].

The data generated by the DHP is transmitted to the Data Acquisition System (DAQ) via a kapton flex cable, wire-bonded to the small aluminum pads and located at the edge of the end-of-stave region (Fig. 48).

The kapton cable is connected to a patch panel. This PCB is responsible of routing the connectors for data and configuration signals and also the power supply (performing the filtering and the impedance matching). The power supply generates all the required voltages (24 voltages) to operate the DEPFET module. It also monitors them (with *sense lines*) to ensure that the proper voltage value reaches the destination. The Data Handling Engine (DHE) is designed to handle the readout and the configuration of the system. It controls the trigger (synchronized with the Belle II clock distribution system) and receives the data from the DHPs via 4 Low Voltage Differential Signaling (LVDS) high speed lines (1.6 Gbit/s). Moreover, the DHE generates the connection with the front-end configuration software and the ASICs via slow control (JTAG). Five DHEs are grouped and connected to the Data Handling Isolator (DHI) and Data Handling Concentrator (DHC), which serves as a sub-event builder and sends the pre-processed data to the computer nodes via optical links. The ONline SElection Node (ONSEN) receives the data and performs another data reduction process, using the information

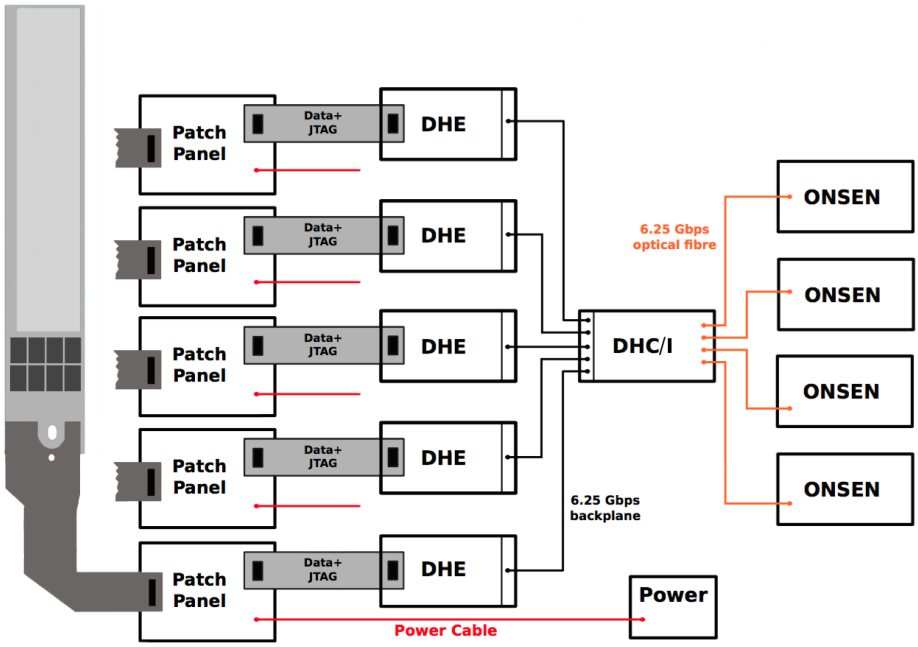

Figure 48: Scheme of the PXD DAQ system. The patch is responsible of routing the connectors for data and configuration signals (DHE) and also the power supply to the kapton cable. Five DHEs are grouped and connected to the DHI and DHC. The ONSEN receives the data and performs another data reduction process, using the information from the SVD and CDC and applying a ROI strategy.

from the SVD and CDC and applying a Region of Interest (ROI) strategy [3]. Afterwards, the data is sent to the EVent Builder (EVB) over a Gbit Ethernet. The estimated average data rate for the complete PXD will be ~ 58 Gbit/s (average occupancy of 1%), the maximum expected data rate (maximum occupancy 3%) will be ~ 170 Gbit/s [53].

4.2 *The PXD Mechanics and Cooling*

One of the main concerns, on the PXD design, was the minimization of the amount of material, which involved the mechanical structure and the cooling system. DEPFET modules are constructed including a small frame (525 µm thick), which works as a self-supporting structure and as a balcony where the Switchers are placed. Regarding the generation of heat per ladder, on the active area is very small, ~ 1 W in total, in

3 ONSEN uses the hits information obtained on the SVD detector (DATCON ROI) and SVD+CDC detectors (HLT ROI) to extrapolate backward the hit position over the PXD and select a small region around this position (ROI - Region of Interest).

addition, the total heat produced by the 6 Switchers is also around 1 W. The main sources of heat are the chips located at the end-of-stave (DCD 1.5 W each, DHP 0.5 W each). The DEPFET design allows to place the readout electronics outside of the acceptance region. Therefore, the solution was to take advantage of this feature, integrating the cooling system and the supporting structure in the same block, placed below the end-of-stave, outside of the acceptance region. Figure 49 shows half cooling block, constructed with stainless steel. The total power consumption is 18 W per ladder, becoming 360 W on the full PXD [68].

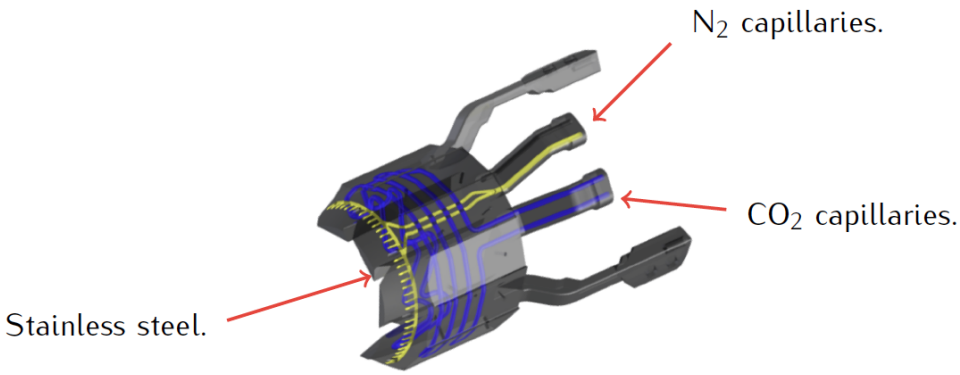

Figure 49: Support and cooling block (SCB). The CO_2 at -30 °C flows through the blue circuit and the N_2 at 0 °C through the yellow circuit [80].

The ladders will be screwed to these blocks from both sides and the readout electronics will be placed over them, therefore, keeping the blocks in a low temperature will be enough to absorb the heat generated. In order to do this, CO_2 at -30 °C will flow inside the blocks (Fig. 49, blue circuit). On the other hand, the temperature over the sensitive regions, in between both layers, will be homogenized by blowing N_2 at 0 °C to the central region, using small holes located on the cooling blocks (Fig. 49, yellow circuit). Moreover, carbon fibers, including small holes which are pointing to the Switchers [80], have been added to blow N_2 directly to these chips (Fig. 50).

4.3 *Belle II PXD Production*

DEPFET modules are all-silicon units, which integrating the active material and the high density electronic components on a self-supporting structure. The construction of these modules is a complex process which involves several steps. This section aims to summarize the basic actions to introduce the assembly process and contextualize the sanity check test, designed during this thesis.

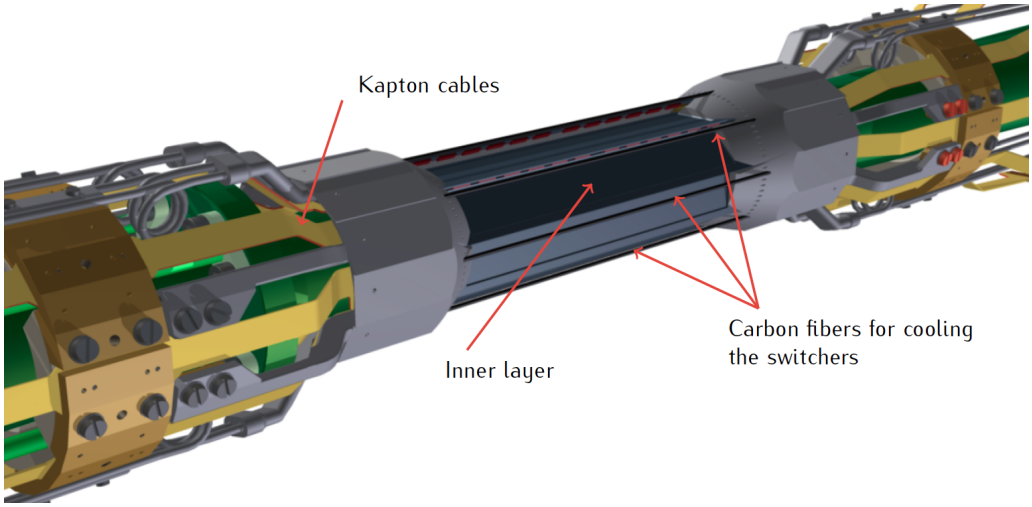

Figure 50: Simulation of the inner layer final structure including the carbon fibers. The cooling system and the supporting structure have been integrated on the same block. Carbon fibers have been added to blow N_2 directly to the Switchers.

The construction process starts with two wafers. First, the backside implants are placed on the *top wafer* and the oxidation is performed (Fig. 51 - a). Second, the top wafer is bonded to a thick *handle wafer* and then, the top wafer is thinned down to the desired thickness (75 µm for Belle II), Fig. 51 - b. In the third step, the processing of the DEPFET structures are performed on the front side (Fig. 51 - c). Finally, a photolithographic process (deep anisotropic etching) opens windows on the handle wafer, below the sensitive region of the sensor (Fig. 51 - d). The thicker silicon around the edges forms a support frame.

After cutting the wafer and separating the modules, the next step is the ASICs bump-bonding (Switchers, DCDs, DHPs) and the placement of all the passive components (resistors, capacitors ...). After this step, four distinct DEPFET modules have been produced, with different pixel pitch and pads distribution [4], two for the inner layer (inner-forward - IF and inner-backward - IB) and two for the outer layer (outer-forward - OF and outer-backward - OB).

At this point, the modules (half-ladders) are completely assembled and ready to be attached to the kapton flex cable. However, they have to be tested before. The importance of performing a sanity check before attaching the kapton cable lies on the difficulty to repair the modules once it is soldered. Since the kapton cable is not attached yet, to perform the connection a *needle card* is required. The needle card design depends on the pad distribution, however only two different pad distributions have been implemented,

4 The pads are located on the edge of the end-of-stave region. It is the region where the kapton flex will be attached and wire bonded (See next section).

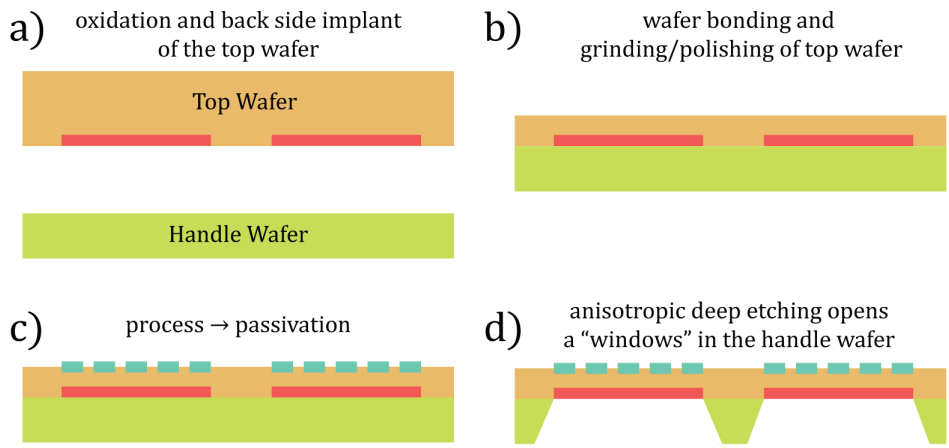

Figure 51: Thinning process flow to produce the DEPFET modules [81].

one for IF and OB modules and a second type for IB and OF modules. Therefore, two needle cards geometries will be constructed. The aim of this step is to perform a fast quality check to test the performance of the modules and, in case of malfunction, locate the error and repair it. If the module passes the test, the kapton cable will be attached (Fig. 52 - b). Afterwards, two half-ladders are glued together to construct a full-ladder (Fig. 52 - c), the junction is done using Araldite and reinforced with ceramic mini-rods. Finally, the PXD is assembled in two separated parts (half shells, Fig. 52 - d) to be joined together becoming the complete PXD detector (Fig. 52 - e).

4.4 *JTAG Boundary Scan*

Due to the small size of the components, and the huge amount of connections required, the chips are soldered using a technique called bump bonding and flip chip mounting. The process starts placing small solder balls (bumps) on the pads of an ASIC, then, the chip is turned upside down (flipped) and aligned, in contact, with the footprint of the module. Finally, temperature cycles are applied to melt the solder balls and electrically connect both parts. The size of the bumps and the distance between them (on the scale of 100 μm) difficult the soldering process and eventually some faults can occur, which can generate malfunction of the chips. Since the connections are not accessible from outside, there is not an easy way to externally test the quality of the soldering. The solution is to implement on the chips JTAG Boundary-Scan architecture which allows to test the logic (digital) part of the chips.

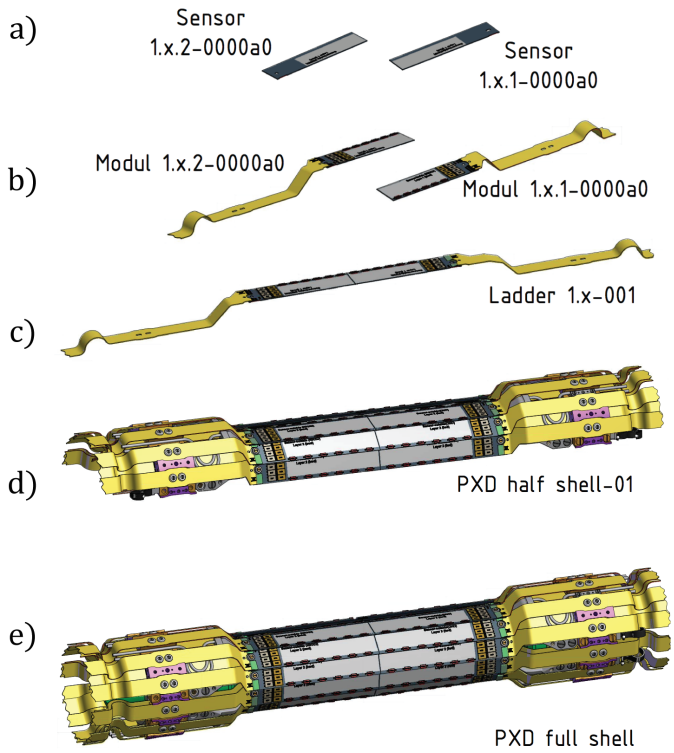

Figure 52: PXD full-shell assembly process [79].

The JTAG Boundary-Scan architecture is applied during the design and development of the chip, by implementing additional logic into the system. It is added around the system logic (Fig. 53) and should be invisible when the chip is operating and performing its task. This section will summarize the boundary scan system. For more detailed information see Ref. [82].

Basically, the idea is to implement a small electronic circuitry (called *Boundary-Scan Register Cell* - BSC) in every digital connection of the chip. They are capable to shift digital levels when is required and become invisible when the internal logic of the chip is working normally. In every chip all BSCs are connected creating a chain (called register) where the digital levels shift one to another, entering through *TDI (Test Data In)* connection and going out through *TDO (Test Data Out)* connection. The shift speed is driven by the *TCK (Test Clock)*, preforming the transition at the falling edge of the pulse. The *TAP Controller* is the system that manages the operation mode of the chip and can

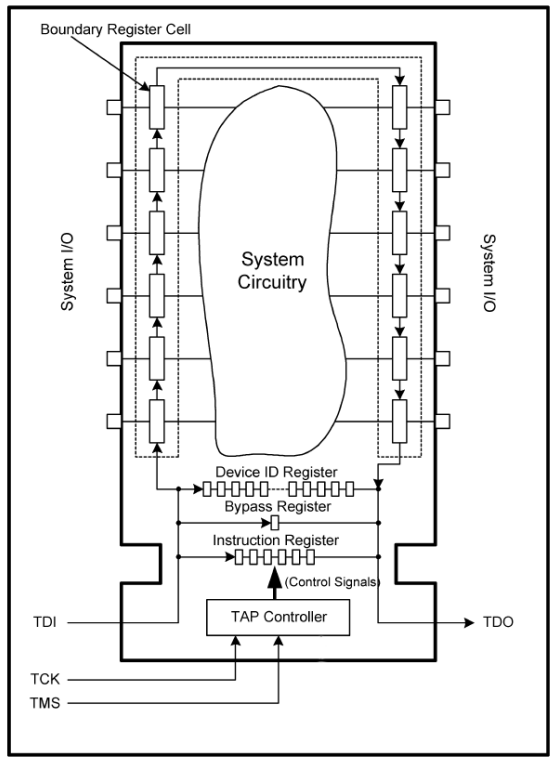

Figure 53: Simplified scheme of the Boundary-Scan architecture [83].

select the register [5]. The register selection is driven by the *TMS (Test Mode Select)* input. In summary, the BSC chain is a group of small cells that store a digital level and can be readout through the TDO by shifting all the cell values (Fig. 54).

However, the aim of the JTAG boundary scan test relies on the interconnections between ASICs. For instance, considering a situation as is shown in figure 55, where several chips are connected via *nets*. The cells are designed to share the same digital level with other cell that shares the same net, therefore if a digital level is shifted on this cell, this value has to be seen on the other cell. The key of the boundary scan test is to shift values on different BSC and check the response on the corresponding BSC. If the values are as expected, this would result in a good net connection. Noticing that these cells are connected through the bumps, if there is a faulty bump, the test will fail.

5 Every register can be described as a group of logic cells (a cell can "store" a digital level and shift it when it is required by the TCK). For instance, the chain of BSCs is the register that stores the present digital state of the BSCs. However, several registers can be implemented, for example a register to store the "Device ID" (Fig. 53).

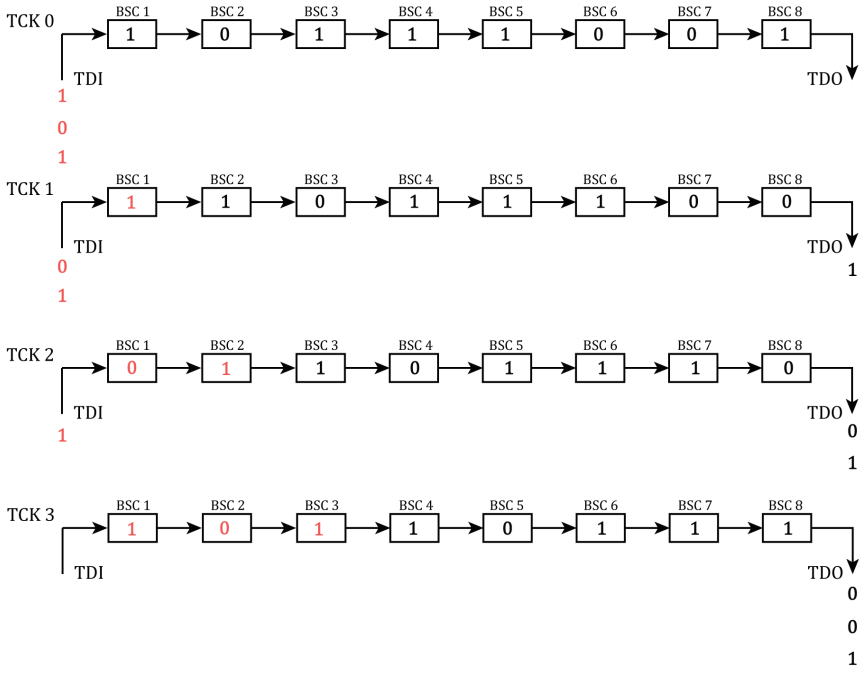

Figure 54: Example of shifting mechanism, when a new bit is introduced through the TDI, all the BSC chain shifts one position and the last bit is extracted through TDO.

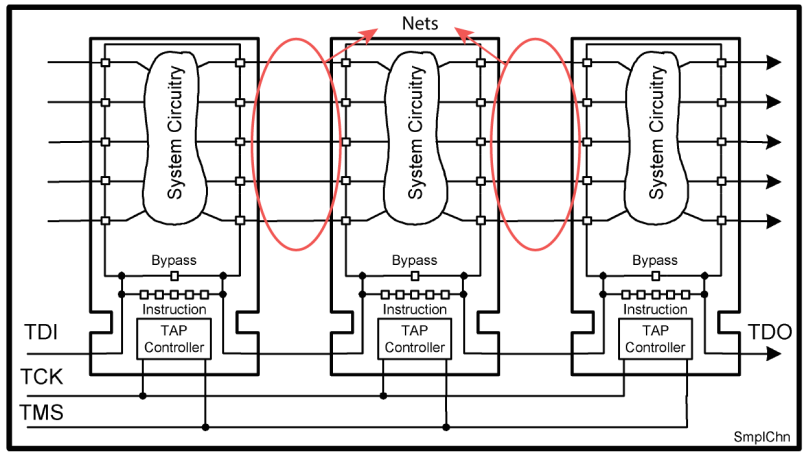

Figure 55: Scheme of the Boundary-Scan chain [83].

Figure 56 shows an schematic example. The connection between ASIC 1 and ASIC 2 is okay, therefore the values shifted on BSC-2, on ASIC 1, will be seen on BSC-1, on

ASIC 2, and vice versa. On the other hand, since ASIC 3 has a faulty bump, the communication between ASIC 2 and ASIC 3 will fail and the test will reveal the issue.

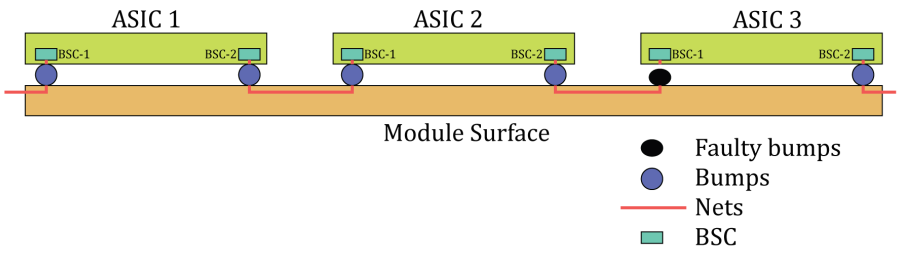

Figure 56: Schematic example of the Boundary-Scan detection method.

JTAG Boundary Scan test is a very useful method to check the quality of the ASICs assembly. However, this method can be only implemented on the logic part of the chips. DEPFET ASICs include several analog connections, therefore, the total coverage of this test method is ~ 27.6% [82] of the bumps. The rest of them have to be checked with indirect measurement that involve the normal operation of the module.

4.5 *Summary*

The production of the DEPFET modules for the PXD Belle II is a complex process that requires several steps of quality assurance. The work presented on this thesis is focused on the design and development of the first sanity check performed after complete assembly of the modules, using a *needle card*. This chapter has introduced the characteristics of the DEPFET prototypes for Belle II and has described the distinct parts of the system, including cooling and mechanics. It also summarized the production process, to put in context the *needle card* test. Finally, the boundary-scan architecture has been explained as an important tool that will be used during the test.

5 Needle Card Test

The construction of the Belle II PXD is a delicate process which requires an accurate planning and several stages of precise quality control. The work presented on this thesis includes the preparation of a needle card to perform a sanity check, on each module, once it is assembled and before the attachment of the connection cable (kapton cable). This chapter summarizes the process of design and improvement of the different needle card prototypes, to finally reach a fully functional needle card setup, to be used during the PXD production, likewise, the testing protocol proposed.

5.1 *Needle Card Test*

On a DEPFET module for Belle II, the cables to communicate the DAQ and the power supply has to be attached directly to the module. The solution is to use a kapton flex cable, integrating all lines; the high and low current lines, slow control (TDI, TDO, etc), high speed connections (to transfer the data), etc. This cable is soldered on a specific region, located at the edge of the end-of-stave (Fig. 57). The connection region includes 4 big copper pads (Cu), for the high current connections [1], and the rest of the connections that are implemented with small aluminum pads (Al), using different sizes, depending on the connection requirements.

The kapton cable is soldered or glued to the big copper pads, lining up the outlying edge to the aluminum pads. Then, the pads integrated on the kapton cable are wire-bonded to the aluminum pads of the module (Fig. 58). Once the kapton cable is attached, the module can be operated through the patch panel [79].

1 Analog and digital ground (AGND and DGND) and the AMPLOW and AVDD for the DCD.

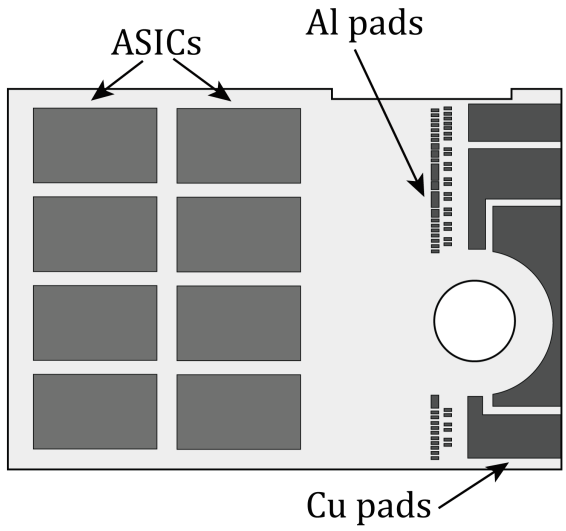

Figure 57: Schematic view of the end-of-stave region, including the aluminum pads and the copper pads.

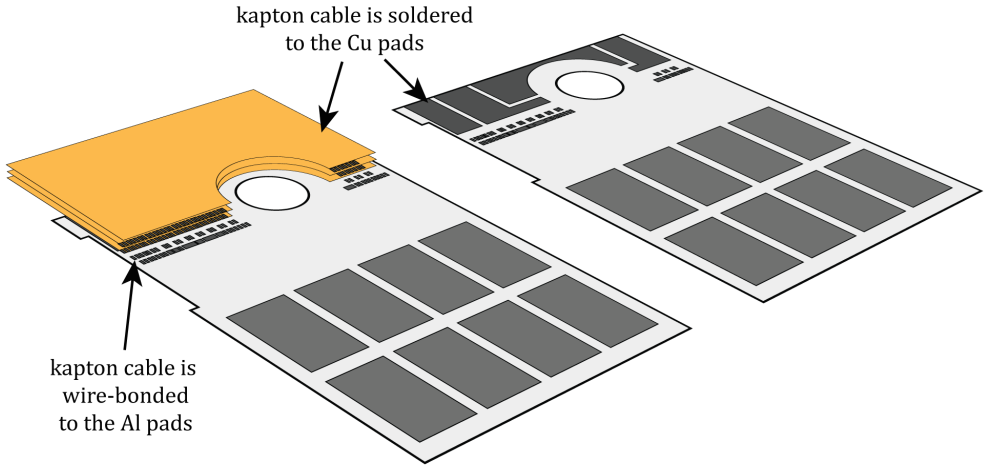

Figure 58: Schematic view of the kapton cable attachment.

As was introduced in Chapter 4, the bump-bonding and flip-chip of the ASICs are a delicate processes, which eventually can generate faults. Since these faulty bumps are hidden below the chips, the only method to test the quality of the assembly is to apply the boundary-scan protocol and operate the module externally.

The problem arises when one of these faults occur, because the faulty chip must be removed and replaced. The fact of having the kapton cable attached hinders the handling. Moreover, during the repair process, the kapton connection can be damaged. One option is to detach the kapton cable to repeat the bump-bonding process, however, this involves a high risk of damaging the module pads and the difficulty of removing the remainders from the previous soldering and wire bonding. The natural solution is to test the modules before attaching the kapton cable. This can be performed using a *needle card*.

The use of needles to perform quality control tests is widely extended. On the production of the DEPFET PXD several quality control steps involve the use of this method (such the ATG machine). The aim of the test presented on this thesis is to design a sanity check of the full assembled modules, before attaching the kapton cable, using a specifically designed needle card.

The needle card replaces the kapton cable and the patch panel. The power cables and the DAQ and control cables are, therefore, connected directly to the PCB. The needles will perform the contact with the module pads, accordingly, the needle distribution has to be implemented with a precision of tens of microns to match perfectly with the footprint of the pads. The needles must be constructed with a low impedance material, they should be flexible and, at the same time, stable to perform a good contact. For this reason, they are designed with different metal composition[2] depending the tip size and the requirements of each connection. The maximum current that a needle can carry is $\sim$ 150 mA, requiring multiple needles in some connections. The maximum vertical bending is around 100 µm and the expected planarity of the needles, to ensure a homogeneous contact along the surface of the pad footprint, should be $\sim$ 10 µm.

The contact is performed in two steps. First, the module and needle spider approach each other gradually until the first needle [3] slightly touches the surface of the pads (Fig. 59 - a). This process has to be followed closely with a microscope to guarantee the alignment of the needles with the pads and controls the contact process. When the touchdown is performed, the pressure over to pad is incremented (*overtravel*) to drive all the needle to contact them. This will bend faintly the needles and force them to lightly scratch the surface of the pads (Fig. 59 - b). Once the electrical contact is guaranteed, the DEPFET module can be operated and all tests can be performed. However, getting a good contact is not obvious and sometimes requires the repetition of the process.

During the production of the DEPFET PXD for Belle II, several prototypes of the needle card have been constructed and tested, adapting the design to the availability

2 Tungsten, Gold Plated, Tungsten Carbide, BeCu.

3 First needle is referred to the needle that, due to the differences on the planarity, is located by default closest to the pads surface and touch first the corresponding pad.

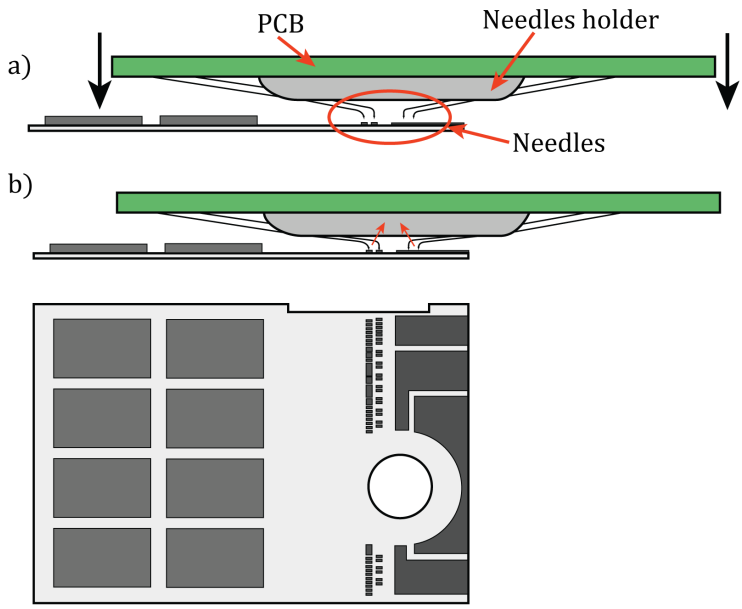

Figure 59: Touchdown of needles and overtravel procedure (top). The increment of pressure will bend faintly the needles and force them to lightly scratch the surface of the pads. The lower plot shows a top view of the end-of-stave region from a DEPFET module.

of the DEPFET modules and the demands of each module type. In this chapter, these prototypes will be described and also the tests performed on them.

5.2 *EMCM Prototype*

The first prototype of needle card was designed for the Electrically active Multi-Chip Module (EMCM), with the purpose of proving the feasibility of this testing method. The EMCM is a electrical prototype from the Belle II PXD, which includes all the circuitry and chips but does not integrate a sensitive region (Fig. 60). Therefore, these modules are fully operational electrical prototypes, which can be configured and operated normally, but without reading out any DEPFET matrix.

The connection pads are located, as was mentioned, at the edge of the end-of-stave region. The EMCM includes 73 small aluminum pads, with a typical size of 100×300 μm[4] and 4 big copper pads (AGND, DGND and the AMPLOW and AVDD for the DCD).

4 Some of the aluminum pads are bigger to accommodate additional wires to cope with the high current required on these connections.

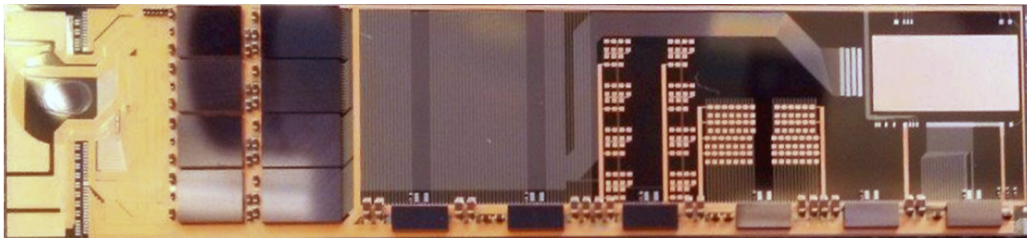

Figure 60: EMCM prototype picture.

The 8 pads for the LVDS high speed lines are really important (red pads on Fig. 61) since they transport the readout data at 1.6 Gbit/s and therefore, the signal integrity is crucial. The pads related with the JTAG configuration are colored in blue on figure 61. The rest of the pads are the necessary connections to power up the DEPFET matrix and the different ASICs.

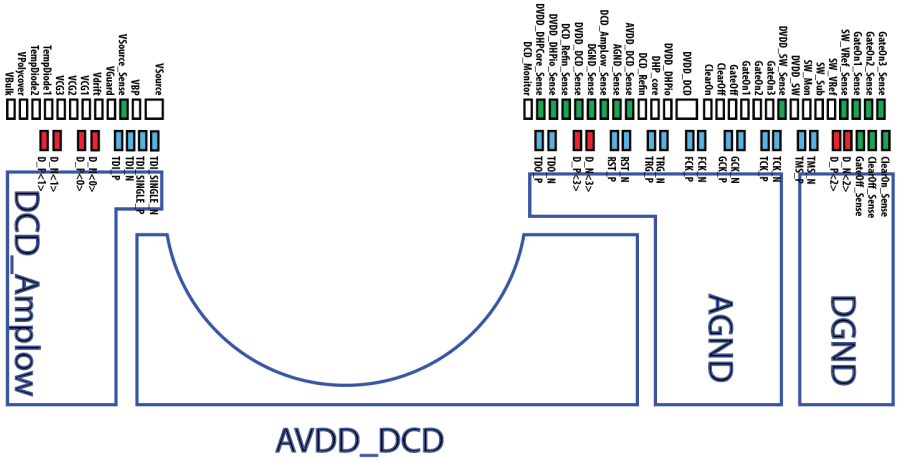

Figure 61: EMCM Pads layout, with 73 Al pads and 4 Cu pads. In red, the 8 pads of the LVDS high speed lines. In blue, the pads related with JTAG configuration. In green, the pads corresponding to the sense lines.

The performance of the DEPFET module is very sensitive to the voltages applied, therefore, it is mandatory to ensure that the specified voltages (on the Power Supply) reach the destination correctly. The long cables and the intermediate components will induce resistances, for this reason, the voltages have to be monitored. The solution is to use *sense lines* connected on the destination point, to feedback the power supply and, accordingly, compensate for the looses. Figure 62 shows a schematic view of the sense line connection. The circuit is designed to ensure that the specified voltages will reach the *sampling point*. On the DEPFET modules, these sampling points are routed on the

module itself, consequently, the number of voltage pads are duplicated (green pads on Fig. 61).

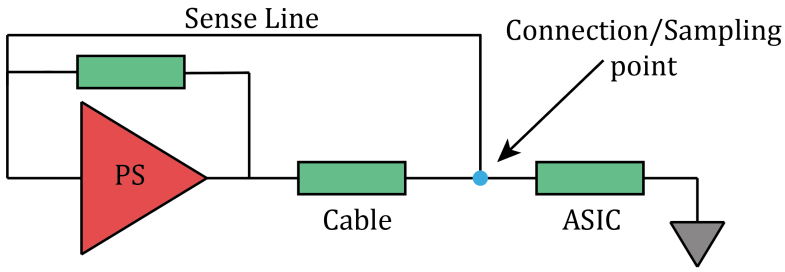

Figure 62: Schematic view of the sense line connection.

The design of the needle card has been done considering all the special requirements of each connection. The contribution to this process during the thesis was the design of the needles contact distribution and the corresponding PCB component. The PCB routing and design have been performed by Dr. Daniel Esperante. On Appendix C the design of the needles contact distribution and the PCB is summarized.

5.2.1 *EMCM Needle card Tests*

The goal of testing with the EMCM needle card was to prove the feasibility of this testing method. To achieve this, the needle card had to be capable to fully operate the EMCM and to establish the data HS links and readout dummy data. The test strategy was defined sequentially, divided on 3 parts:

- Powering of the EMCM.
- Configuration via JTAG and Boundary Scan.
- HS link stability and data extraction.

To perform the test, the setup included: a microscope to control the touchdown process and the DEPFET subsystems; the DHE, the power supply and the computer to configure the system and readout the data. Also, the mechanic structure, which included a specifically designed holder for the needle card (Fig. 63).

The EMCM under test, W17 – 4, was placed directly on the probe station chuck. Previously, the planarity of the needles was tested, and the tilt of the needle card was optimized to ensure a homogenous contact (Fig. 64).

Figure 63: Picture of EMCM needle card at the holder with all cables connected, the EMCM W17 − 4 is placed on the probe-station chuck.

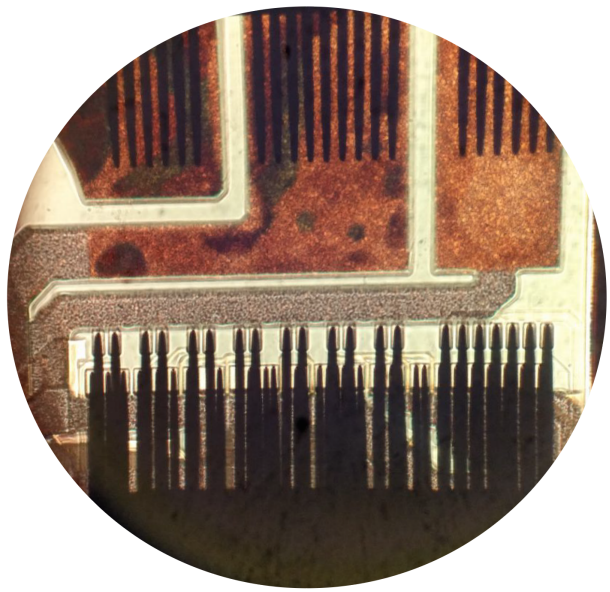

Figure 64: Picture of the needles aligned with the module pads.

The contact between the pads and the needles was performed slowly, following the progress with a microscope and a micrometer. Once the first needle touches the pad, the overtravel is applied. To get a stable contact, assuming a planarity $\sim$ 10 µm, the overtravel was in the range of $30 - 50$ µm and never exceeding 70 µm (for safety reasons). The overtravel must be as small as possible to minimize the inflicted damage, but enough to get a good connection. After finishing this process, the only way to see if the contact has been done correctly was to start the power up sequence.

Powering of the EMCM: The software used to configure and control the chips are the programs implemented by the DEPFET collaboration [5]. Using these programs, the aim of the test was to go over the power up sequence, step by step, verifying that the chip current consumptions were within the expected range. Figure 65 shows an example of the online voltages control panel used to perform this test.

min.	Set Voltage	max.	Reg.	Voltage at Regulator	Voltage at Load	Current	
0 mV	0 mV	0 mV		-130 mV	-139 mV	2 mA	sw-sub
0 mV	1800 mV	2000 mV		2296 mV	1799 mV	27 mA	sw-dvdd
0 mV	0 mV	0 mV		-918 mV	1399 mV	-2 mA	sw-refin
0 mV	400 mV	500 mV		545 mV	405 mV	0 mA	dcd-amplow
0 mV	1900 mV	2000 mV		2016 mV	1897 mV	41 mA	dcd-avdd
0 mV	1800 mV	2000 mV		2615 mV	1796 mV	303 mA	dcd-dvdd
0 mV	1200 mV	1300 mV		1262 mV	1202 mV	1 mA	dcd-refin
0 mV	1200 mV	1640 mV		2015 mV	1200 mV	252 mA	dhp-core
0 mV	1800 mV	2000 mV		2732 mV	1801 mV	180 mA	dhp-io
0 mV	0 mV	10000 mV		4 mV	-6 mV	-1 mA	bulk
0 mV	0 mV	22000 mV		-11 mV	28 mV	-1 mA	clear-on
0 mV	0 mV	20000 mV		-21 mV	27 mV	0 mA	clear-off
-4000 mV	0 mV	3000 mV		1 mV	4 mV	0 mA	gate-on1
-4000 mV	0 mV	3000 mV		-3 mV	1 mV	0 mA	gate-on2
-4000 mV	0 mV	3000 mV		0 mV	1 mV	0 mA	gate-on3
0 mV	0 mV	6000 mV		-244 mV	-2 mV	-1 mA	gate-off
0 mV	0 mV	7000 mV		375 mV	-38 mV	3 mA	source

Figure 65: Voltages control table. Starting from left, minimum voltage that can be applied, voltage selected, maximum voltage, green - enabled voltages, voltage provided by the PS, voltage applied on the sampling point, current consumption.

Configuration via JTAG and Boundary Scan: Once the necessary voltages are applied, the configuration scripts can be executed. This process will modify the current consumption of several voltages, pointing out a successful configuration. Furthermore, JTAG configuration allow to write and read back some parameters, therefore, if the configuration uploaded on the chips agree with the read back, means that JTAG chain is completed. Once the configuration is finished, the boundary-scan test can be accomplished. To perform the test, a specific software, provided by the JTAG company, is required and also break-out board, to bridge the JTAG connection [6]. The test is performed in two steps:

5 This thesis will not go into details on this part, however the debugging and optimization of the software consumed much part of the time.

6 For a detailed description see Ref. [82]

- **Infrastructure test:** To check if all boundary-scan cells, defined on the design files, are present and accessible. The typical output is shown in figure 66. The EMCM W17 – 4 passed the test.

```
================================================================================
6/15/2015 3:53:14 PM  UUT: EMCM-P6-1   Start Test: Infrastructure
================================================================================
Testing boundary register SWITCHER_5 ...Ok
Testing boundary register SWITCHER_4 ...Ok
Testing boundary register SWITCHER_3 ...Ok
Testing boundary register SWITCHER_2 ...Ok
Testing boundary register SWITCHER_1 ...Ok
Testing boundary register SWITCHER_0 ...Ok
Testing boundary register DCD3 ...Ok
Testing boundary register DHP3 ...Ok
Testing boundary register DCD2 ...Ok
Testing boundary register DHP2 ...Ok
Testing boundary register DCD1 ...Ok
Testing boundary register DHP1 ...Ok
Testing boundary register DCD0 ...Ok
Testing boundary register DHP0 ...Ok
================================================================================
3:53:14 PM  P A S S  Elapsed Time  00:00:00.111
================================================================================
```

Figure 66: Infrastructure test output for the EMCM W17 – 4.

- **Interconnection test:** On this step, the interconnection between the cells is checked, ascertaining the quality of the bumps connected on each line. It is important to remark that boundary-scan only checks the digital connections and it does not give information about the rest of the bumps. Figure 67 shows the output from the EMCM W17 – 4. The results revealed a massive failure in one of the ASICs pair (connection between the DCD and DHP). It is unlikely that all the bumps involved were faulty, therefore, the problem should come from another part of the chips that cannot be seen. However, the importance of this test is the ability to detect this kind of failures in advance and still having the chance to repair them.

HS link stability and data extraction: The High Speed link stability was the crucial step to prove the feasibility of the needle card testing concept. The data communication requires a high level of signal integrity. Keeping the communication with the module (HS links up) was not obvious since the lines routed on the PCB, the needle length and the contact point with the pads, were sources of distortion. The test was performed using the DHE software and configuring the transference speed to a half rate. Adjusting and debugging the connection parameters took several months to successfully achieve the final results, which proved that the needle card is not an impediment to keep the HS links up. To quantify the quality of the signal transferred, the so called, *eye diagram* or *eye pattern* was measured. This test overlaps several cycles of a bit chain transferred

```
================================================================================
6/15/2015 3:54:33 PM  UUT: EMCM-P6-1   Start Test: Interconnection
================================================================================
DHP2:DI0_0(#28)      EH ML
DHP2:DI0_1(#20)      EH ML
DHP2:DI0_2(#16)      EH ML
DHP2:DI0_3(#24)      EH ML
DHP2:DI0_4(#30)      EH ML
DHP2:DI0_5(#22)      EH ML
DHP2:DI0_6(#18)      EH ML
DHP2:DI0_7(#26)      EH ML
DHP2:DI1_0(#27)      EH ML
:::
:::
- 1- Line NET0141_0 defective:
-73-       1. pin <: OUT DCD2:DO7_7(#P79)     {BScan     } DCD_FOOTPRINT NET0141_0
-73-       2. pin >: In  DHP2:DI7_7(#99)      {BScan     } DHP10_FOOTPRINT NET0141_0
- 8-    Stuck at Low of the line

-24- Test step table of the line NET0141_0:
-25-        Expected                    H L L L H L H L H L L H H L H L H L H H
-28-        Measured <Stuck at low>
-30-      Output pin  DCD2:DO7_7(#P79)  H L L L H L H L H L L H H L H L H L H H
-31-       Input pin   DHP2:DI7_7(#99) >L L L L>L L>L L>L L L>L>L L>L L>L L>L>L
:::
:::

================================================================================
3:54:35 PM  F A I L  Elapsed Time  00:00:01.702
================================================================================
```

Figure 67: Interconnection test output for the EMCM W17 – 4.

through the monitored HS link. Figure 68 shows two sections of the bit chain, obtained from the DHP 0.

In summary, **the tests planed were completed successfully, proving that a fully-populated EMCM module can be operated, normally, using a needle card**. The only missing piece, to fully cover all parts of the module operation, was to readout of a DEPFET matrix.

The main handicap of the needle card testing method is that, eventually, the contact of one needle can fail (due to some movement or vibration) an disable the connection. The second set of tests performed was focused on checking all possible scenarios of contact failure and design and implement protection mechanism to ensure the safety of the modules, specially on the voltage related needles.

- **Voltage needle failure:** The failure of some of these needles can produce serious damage on the ASICs. It can be prevented only by using a large overtravel and handling carefully the setup. Moreover, to minimize the possibility of damage the ASICs, an automatic script can be designed, which monitors the current con-

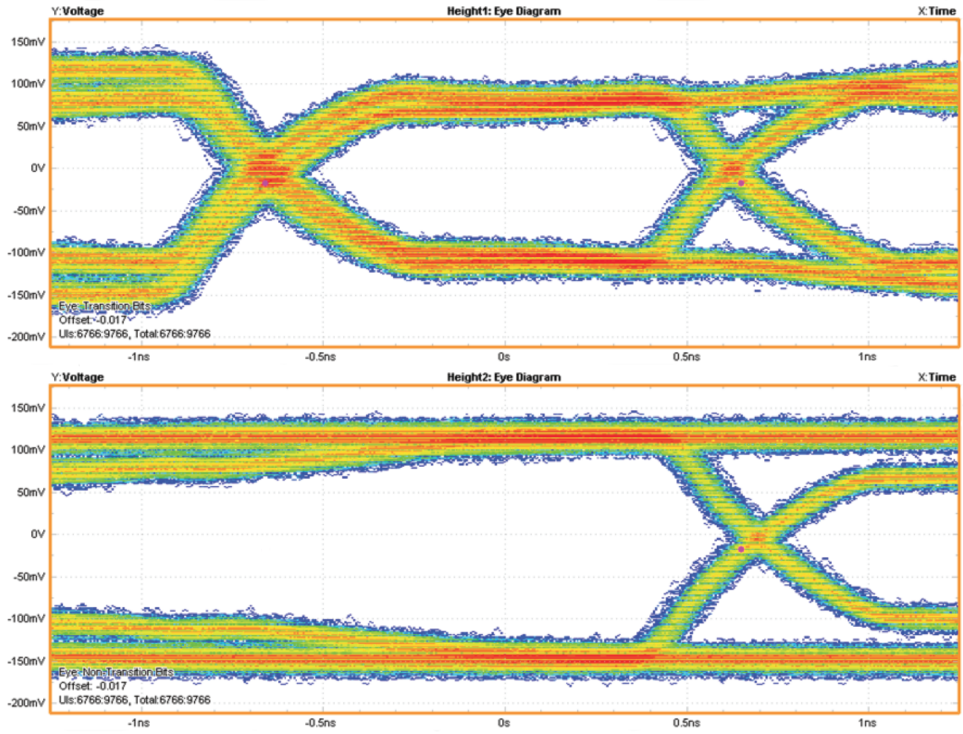

Figure 68: Eye diagrams, at half rate, of DHP 0.

sumptions and the voltage values and, in case some voltage needle fails [7], it will start the system emergency shutdown automatically.

- **Sense line needle failure:** Sense lines are important connections to ensure the stability of the module operation. In case some of these needles fails, the power supply will not receive a feed back and will presume that the voltage on the sampling point is very low. Consequently, the power supply would increase the voltage as high as possible, changing the operational equilibrium and even damaging the module. To simulate these situations, a dummy power cable, which allowed to connect and disconnect the sense lines, was used. The test was performed in several voltages, comparing the voltage value provided by the power supply in both cases. Table 18 summarizes the results obtained. The mechanism to avoid this problem can be implemented by moving the sampling point to the needle card PCB, near to the needle spider.

7 For instance: It will be reflected on a drop of the current consumption.

Name:	R_{val} (Ω)	V_{appl} (V)	V_{ASIC}^{Sensed} (V)	$V_{ASIC}^{NotSensed}$ (V)
DHP core	12	1.7	1.74	1.99
DHP io	12	1.8	1.9	2.2
DCD DVDD	2	1.8	1.77	1.94
Source	390	7	7.25	8.7
DCD AVDD	82	1.9	2.15	2.59

Table 18: Sense line failing test. Starting from the left: Resistor value applied to simulate the power consumption; voltage fixed on the configuration; voltage on the sampling point when sense line is connected; voltage on the sampling point when sense line is disconnected.

5.3 *Testing Protocol*

Based on the results obtained during the EMCM test, a baseline testing protocol, for the sanity check, has been proposed. The final goal of the protocol is to discover any big issue on the ASICs that must be repaired before attaching the kapton cable. The previous results determined the guidelines followed:

- **Minimize the number of touchdowns:** Each touchdown inflicts damage on the pads, therefore, the number of touchdowns required must be minimized. Since the boundary-scan needs a special break-out board [82], which is incompatible with obtaining HS links, a minimum of two touchdowns are recommended.
- **Maximize the test coverage in the minimum time:** The results obtained proved that the needle card is able to complete a full-coverage test, however, it is important to perform the test as quickly as possible to minimize the connection time and avoid unexpected needle contact failures.
- **Sequential test in order of safety:** The test has to be performed sequentially in order of safety. First the test involving only the digital part of the system, which in case of needle contact failure, the module can be recovered. If the systems behave stably, the following steps can be carried on.

The touchdown and overtravel protocol has to be defined. The overtravel steps would be 50 µm, 70 µm and 90 µm. It means that on the first touchdown, the overtravel applied will be 50 µm. Afterwards, all steps of the testing protocol will be carried on. In case the system behaves unstably, the overtravel will be incremented to the next step. After applying 90 µm, if the system continues failing, the problem will be reported and discussed by the experts. It is important to notice that after the boundary-scan, the break-out board has to be removed and the system reconnected. It is recommended

to start the testing with the break-out board connected and after the boundary-scan, shut-down the system to separate the needles. Then, repeat the touchdown with the same overtravel.

The test protocol has two differentiated parts: The digital region, which is very safe to perform since only requires the digital voltages. In this part, the testing coverage is limited because most of the bumps are related with the analog connection to the matrix. The second part has the aim to cover the analog region.

Digital Region:

1. **Voltage and Current consumption (digital):** The power up sequence of the digital region is followed, enabling the voltages one by one and observing the current consumptions in each step. In case any value goes out of range, the process should be stopped immediately. If all voltages behave as expected, it means that the voltage connections and the digital part of the ASICs are working properly. It is important to notice that the bumps are not being checked individually, however any critical failure has to be reflected on the values. Figure 69 shows the region covered on this test.

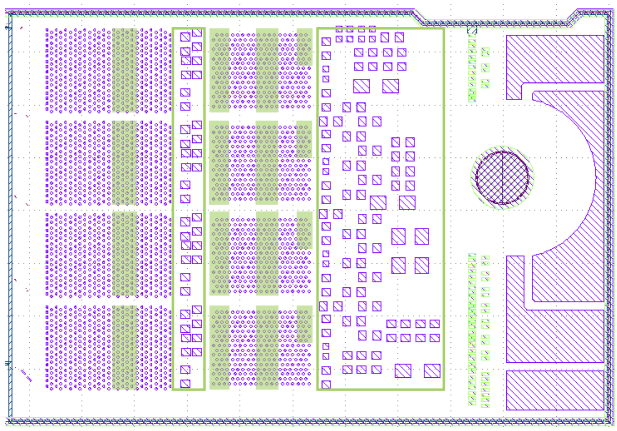

Figure 69: Voltages and current consumption (digital) test. Green: Bumps region under test.

2. **JTAG Chip Configuration:** Once the chips are powered, an automatic script can be executed to configure the ASICs. When finished, the current consumption is expected to change accordingly to the configuration implemented. If the values go to the design values, it means that the configuration was successful. Then, some specific parameters which have a direct impact on the current consumption, can be written and read back via JTAG observing the response. In this case, the JTAG chain (TDI, TDO, ...) is been tested, inferring a proper slow control connection. Figure 70 shows the region involved.

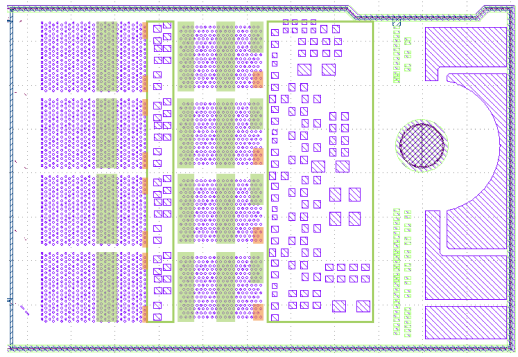

Figure 70: JTAG Chip Configuration test. Orange: Bumps region under test.

3. **Boundary-Scan:** As was mentioned, the boundary scan has two steps: The infrastructure test, which test the integrity of the boundary-scan cells and the size of the registers. It is followed by the interconnection test, which checks the communication between boundary-scan cells, involving the connection bumps. In this case, a dedicated software is used to check all possible problems on each individual bump. Figure 71 shows the region under test.

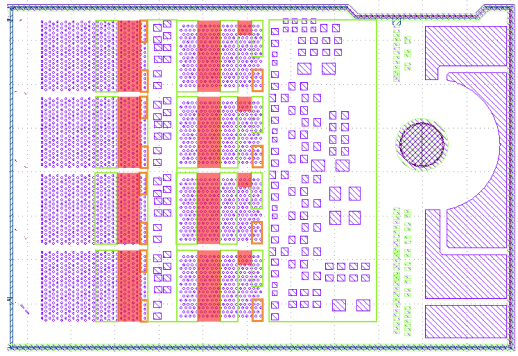

Figure 71: Boundary-Scan test. Red: Bumps region under test.

4. **High Speed Link Stability:** This step requires the fine tuning of the high speed link input/output parameters. In principle, it can be done using the DHE configuration software. The goal is to stably establish the four HS links. However, to really test the stability, readout data is necessary. It can be done by extracting the *test injection pattern*, which is a frame generated on the DCDs [8]. On this test, the quality of the data transfer connection is tested. Figure 72 shows the region involved.

8 Specific output frame, designed to test the HS links and the delays on the communication between the DCD-DHP.

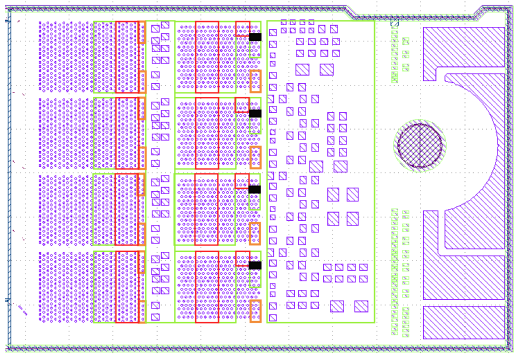

Figure 72: High Speed Link Stability test. Black: Bumps region under test.

This part of the protocol involves ~ 20% of the Switcher bumps, ~ 50% of the DCD bumps and ~ 90% of the DHP bumps. The untested bumps correspond to the analog connections with the matrix and to check them, the readout of a data frame is necessary. The second part of the test requires to power up completely the module and has to be performed carefully. The following steps will be carried on, only if the stability of the connection during the first part of the test was proved. The aim of this part is to read raw frames from the matrix and count the number of pixels which are responsive.

Analog Region:

5. **Voltages and Current consumption (analog):** The power up sequence, of the analog region is followed voltage by voltage, observing the current consumption in each step. In case any value goes out of design values, the process should be stopped immediately. Then, the analog part of the ASICs has to be enabled and the changes produced on the current consumptions must fit the expected values. In this step, the normal behavior of the ASICs is been tested. It is important to check the stability of the HS link again.

6. **DCD Pedestals:** The DCD baseline outputs can be readout, this is important as a crosscheck of the digital connections between DCD and DHP, which have been tested with the boundary-scan.

7. **Voltage and Current consumption (matrix):** The power up sequence of the matrix voltages is carried on, voltage by voltage, observing the current consumption in each step. In case any value goes out of expected range, the process should be stopped immediately. During this process the response of the matrix is being checked. Then, the automatic protection script can be enabled, to monitor the voltages and current consumptions, in case any of the values goes out of range, the emergency shutdown is triggered.

8. **Pedestals:** After finishing the power up sequence, the module is ready to perform the readout of raw frames from the matrix (*pedestal frame*). Since most of the

DCD and Switcher connections are related with the matrix analog lines, the only method to check the quality of the bump bonding is to analyze the extracted frames.

9. **Matrix Response:** Generate matrix response can be done with several methods. The options are: Use an external light or laser to inject charge on the matrix, however, since some matrix regions are shadowed by the metal layers and the passive components, these regions will not react. On the other hand, the switcher sequence can be modified to suppress the clear process, therefore, the internal gate will be filled up with junk charge and the matrix signal will saturate (*signal frame*). Figure 73 shows the region of bumps that are being tested and also all switcher analog connections.

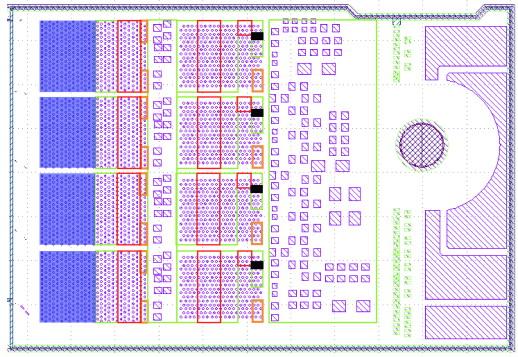

Figure 73: Pedestals and matrix response. Blue: Bumps region under test. Also all switcher analog connections are tested.

Once the two frames are obtained (*pedestal frame* and *signal frame*), the system must be shutdown and the needles disconnected. The analysis can be completed offline. The aim of these two final steps is to find out the matrix regions that do not behave normally. The idea is to compare both frames, searching for the pixels that do not respond as expected. When these pixels are identified, depending on the distribution, they can be related with some ASIC or bump bonding problems. For instance, if four consecutive rows saturate in all cases, this will hint to a problem in one clear channel of one Switcher [9]. This final analysis can be implemented in an automatic script, obtaining the total number of faulty pixels. The results obtained in the comparison of these frames can be use to classify the module, using a score proportional to the number of faulty pixels.

9 Assuming a good delay optimization.

5.4 *PXD9 Pre-production Modules*

PXD9 are the pre-production modules for the Belle II PXD. These modules (in contrast with the EMCM) include a DEPFET matrix (Fig. 74). The PXD9 pad distribution has been redesigned, compare to the EMCM, and two distinct pad distributions have been implemented, depending on the prototype. Accordingly, two needle cards have been constructed: one for the IF and OB modules (*design A*) and a second for the IB and OF modules (*design B*). The new pad layouts are shown in figure 75, which include 59 aluminum pads and 4 copper pads.

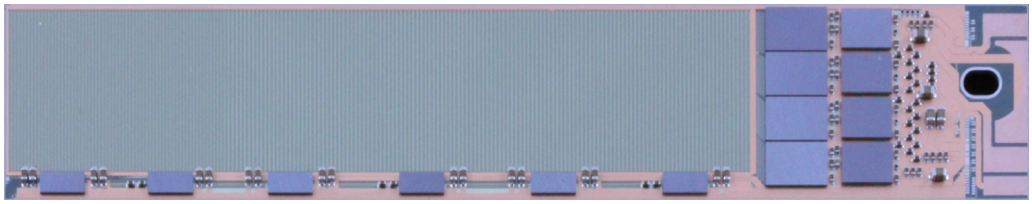

Figure 74: Picture of a PXD9 Pilot Run module.

The design of the new PCBs was based on the EMCM needle card adding the following modifications to improve the performance and the stability of the high speed links. For more detailed information see Appendix C.

- **Connectors modification:** The final DHE requires different connectors, therefore the needle card PCB has been adapted by replacing one infiniband connector with a RJ45.
- **Length minimization of the HS link needles:** The needle hole distribution has been modified to minimize the length of the HS link needles.
- **Length reduction of the HS link PCB paths:** All bends of the HS link PCB paths have been removed to reduce as much as possible the impedance of the lines.
- **Redesign of the needle contact distribution:** The damage on the module pads, due to the touchdowns, is inevitable. The needle contact distribution has been redesigned to minimize the spread of the scratches on the pad surface. Replacing a double row distribution to a linear distribution, which allow to perform the needle contact on the corner of the pads (Fig. 76).
- **Sampling point of the sense lines before the needle spider:** To avoid unexpected increments on the voltages applied, due to a disconnection of a sense line needle, another sampling point has been implemented on the PCB, near to the needle spider.

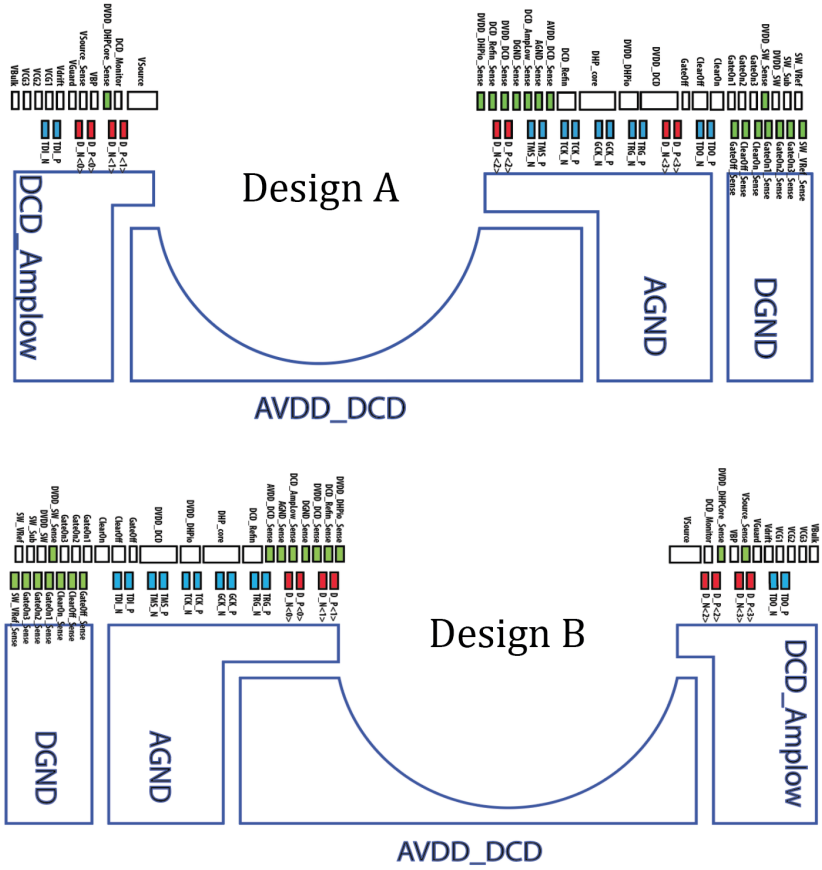

Figure 75: Pad distribution layout of the two PXD9 module flavor, with 59 Al pads and 4 Cu pads. In red, the 8 pads of the LVDS high speed lines. In blue, the pads related with JTAG configuration. In green, the pads corresponding to the sense lines.

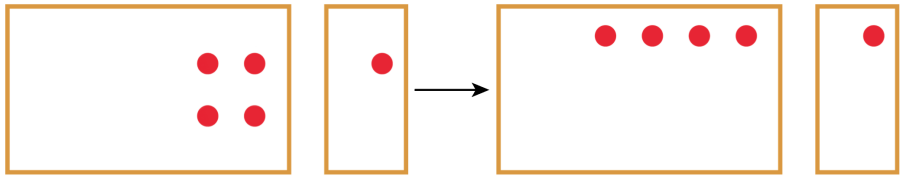

a) Double row distribution b) Single row distribution

Figure 76: Needle contact distribution. Left: double row strategy used on the EMCM needle card. Right: Single row distribution to minimize the spread of the damage on the PXD9 final modules.

5.4.1 *PXD9 Needle card test*

The missing step, to prove the feasibility of using a needle card and to fully apply the quality control protocol, was to obtain a frame of the matrix pedestal. Therefore, the ultimate goal of testing with a PXD9 module was to reach the last step on the quality control protocol. Notice that before being able to readout the pedestal frame, all the previous steps have to be carried out. Since the output obtained in every previous step is equivalent to the results shown on the EMCM test, they will be omitted on this section. However, all the results from PXD9 test are summarized of Appendix D.

Accordingly to the production plan, once a module is fully assembled, it will be placed on a custom designed transport box (transport jig and a cover). Before being attached to the PXD shell, the modules must be fully-optimized, and for this a cooling system has to be included to operate them safely. The solution was to design a cooling block with an internal liquid coolant circuit, where the jig will be fixed (Fig. 77).

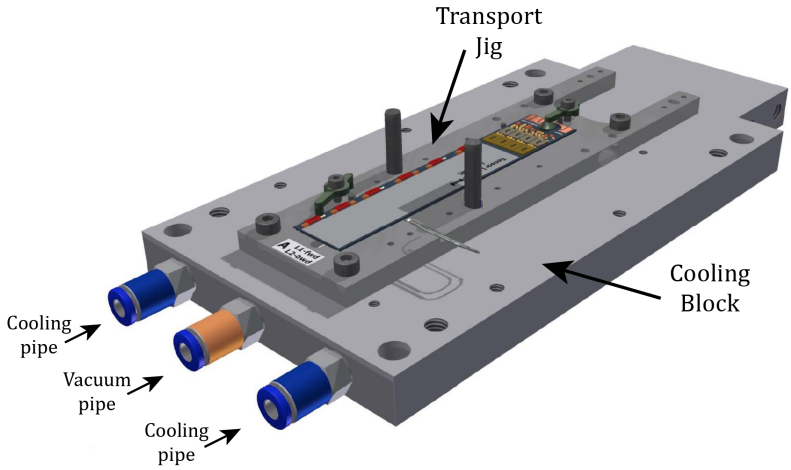

Figure 77: Cooling block and transport jig structure.

The needle card setup was modified to accommodate this cooling system, avoiding unnecessary and dangerous changes on the module storage box. For this, an specific plate was constructed to adapt the chuck of the probe station.

To check the new needles touchdown distribution a realistic double touchdown was done over a dummy pad distribution. This test was used to visualize the damage inflicted on the pads once a real quality control test is performed. The touchdown was done on the corner of the pads, minimizing the damage spread. The overtravel used was 50 µm, corresponding to the default value. Figure 78 shows an image of the pads

and the scratches due to the needle contact. The important point is that the new distributions allow to concentrate the damage on a small region of the pads, keeping the rest empty of scratches that could influence the wire bonding process.

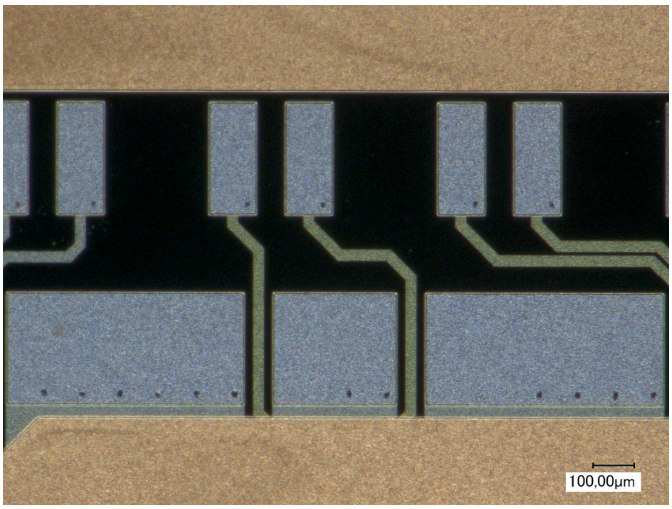

Figure 78: Picture of the PXD9 module pads. The scratches on the bottom-right side are due to the needles contact with an overtravel of 50 µm.

As was mentioned, the main goal of testing with the PXD9 prototype was to readout a pedestal frame. The testing protocol was followed, successfully, step by step. After completing the power up sequence, having all chips configured and the high speed communication enabled, a trigger can be sent to read a raw matrix frame. Figure 79 presents an image of the pedestal distribution (left) and a pedestal map (right). Notice that during this measurement, the room was not in complete darkness, for this reason, these shapes appear on the surface of the sensor and the distribution becomes wider than the nominal, moreover, this sanity check protocol has been applied before any optimization of the DEPFET parameters. **In any case, obtaining the pedestal frame is enough to conclude that the module is working and responding, and this is the ultimate aim of the testing protocol with the needle card.**

The frame shown in figure 79 concluded the process of design and characterization of the needle card: the design and construct the setup, with all the mechanical parts and the electronic boards, the software development and debugging, and the training hours with many failed attempts. At the end, a fully functional setup has been design and mounted and the testing protocol to cover all required aspects has been proposed and tested. Figure 79 was only the final touch that proved that all part of the sanity check, over the full-assembled DEPFET modules, are ready to be applied during the PXD production for Belle II.

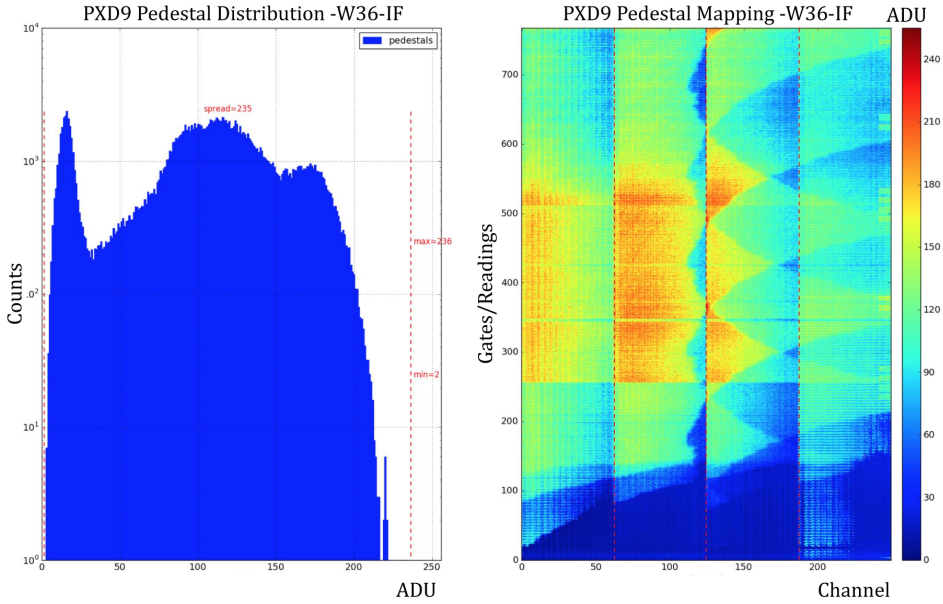

Figure 79: Pedestal frame obtained with the needle card design A and a IF module.

5.5 *Summary*

The work assigned during this thesis was the development of a sanity check for the full assembled DEPFET modules, during the production of the Belle II PXD. The solution was to construct a *needle card* to perform the connection with them. Several needle card prototypes were produced, adapted to the availability and the characteristics of each DEPFET prototypes. First, a needle card designed for the EMCM was constructed to prove the feasibility of testing with this method. Based on the results, a testing protocol was proposed to cover the test of all DEPFET module aspects. The experience gained during the previous test allowed to improve, substantially, the subsequent needle cards. The final prototypes were designed for the PXD9 modules. The test over these modules proved the capability of this system to readout data and therefore to fully apply the test protocol proposed.

At the end of this development period, the setup with all the mechanical parts, the electronic boards and the software, was mounted and prepared to be used during the production. Likewise, the *desing A* and *desing B* needle cards and also the testing protocol for the sanity check.

6 DEPFET: Summary and Future Work

The **DEP**leted **F**ield **E**ffect **T**ransistor structure (DEPFET) is an active pixel technology constructed with a MOS field effect transistor (MOSFET), integrated onto the surface of a fully depleted n-doped Silicon bulk. It has the capability to, internally, amplify the small charge created by an impinging particle and generate a readable signal. Chapter 3 has introduced the DEPFET technology structure and has presented the main characteristics of the DEPFET matrix operation. Moreover, the data analysis strategies have been explained to introduce some studies performed during this thesis, which intended to explore the parameters of the DEPFET technology and their implications.

First, the intrinsic resolution of the DEPFET matrices has been studied in terms of the *zero suppression cut*, concluding that the maximum resolution archivable with these DEPFET prototypes is ~ 8.5 μm. The data was obtained on the July-2012 DEPFET beam test campaign at SPS-CERN. At this level of resolution, there are observable physical phenomena that can blur the hit position reconstruction. On this line, these effects were studied to determine if a physical limitation to the spatial resolution exists, on solid-state devices that rely in charge sharing between neighboring cells [75]. In particular, the δ-electrons were studied for particles with perpendicular incidence[1] (Fig. 80), likewise the effect of the Landau distribution of the charge deposition for incidence under an angle (Fig. 81).

In both cases, the study concluded that **spatial resolution of such devices is limited by these effects and even increasing the S/N ratio, reducing the pixel size or the thickness, will generate a negligible improvement on the spatial resolution.** Also important is to notice that the current DEPFET technology is capable to reach the resolution limits.

Chapter 3 introduced the main characteristics of the DEPFET technology, emphasizing on the versatility in terms of internal pixel design, as well as the matrix operation flexibility. The internal amplification, the low material budget, the low power consumption, the high spatial resolution, are some of the features that make DEPFET a perfect candidate as a pixel technology, capable to cope all the requirement of the future e^+e^- colliders. For this reason, it is a candidate as a pixel detector technology for the ILC and the technology for the PXD of Belle II in SuperKEKB.

On this context and in order to fulfill all the SuperKEKB requirements, the PXD has to be designed to work with the injection scheme of the corresponding accelerator. For

1 Simulation performed by Benjamin Schwenker.

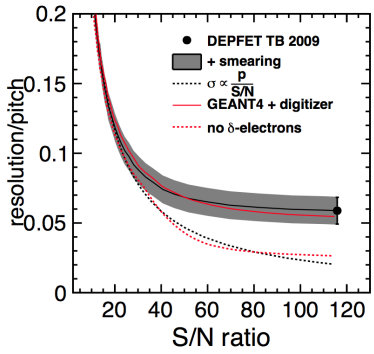

Figure 80: Spatial resolution divided by the pixel size versus S/N ratio, for 120 GeV pions with perpendicular incidence angle on a 450 µm thick DEPFET device (black solid line), compared to the GEANT4 simulation with δ-electrons (red solid line) and without δ-electrons (red dashed line). The ideal situation have been also included (black dashed line) [75].

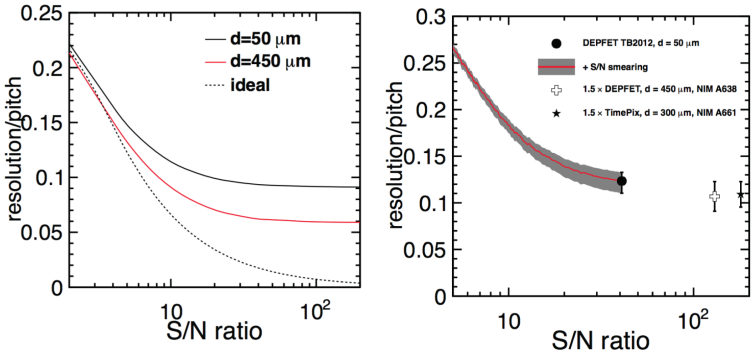

Figure 81: Left: Monte Carlo simulation of the spatial resolution divided by the pitch versus S/N ratio. The dashed line represents the situation where charge deposited is proportional to the track length, solid lines include the Landau fluctuation effect, considering a 50 µm (red) and 450 µm (black) thick device Right: Spatial resolution divided by the pitch versus S/N ratio for multiple devices [75].

this reason, DEPFET technology has developed a method to survive to the new injected bunches, called *Gated Mode*. Another study performed was the analysis and debugging of this operational mode to prove the efficiency of the signal charge preservation and the signal charge shielding. Figure 82 shows the voltage regions where the gated operational mode successfully preserve the charge on the internal gate.

Focused on the PXD for Belle II, Chapter 4 has introduced the main characteristics of the DEPFET prototypes for this experiment, likewise the description of the necessary ASICs and the DAQ system. Also, the mechanics and cooling system were summarized.

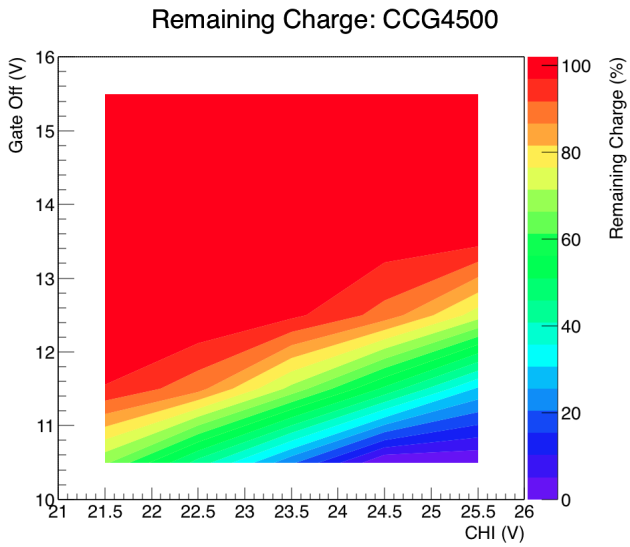

Figure 82: *Clear* and *gate* voltage scan to define the regions where charge is completely preserved. *Cleargate* voltage has been fixed to 4.5 V.

On this scenario, the work performed during this thesis was the design and development of a sanity control test to be applied to the fully assembled modules, using a *needle card*. This chapter described the Belle II PXD production process to contextualize the needle card test. Finally, the Boundary-Scan test were presented, since it is a crucial step on the testing process.

The PXD modules will be connected to the external components through a kapton cable, soldered directly to the end-of stave region. In case some problem on the ASICs occurs, the kapton cable will hiders the chip replacement. The solution proposed was to perform a sanity check before attaching the kapton cable and for this, a *needle card* is required. The development process of the sanity check has been summarized on Chapter 5. A **needle card prototype** was designed **for the EMCM**. **It was used to prove the feasibility of this testing concept** (Fig. 83).

All test over the EMCM were successfully performed, concluding that **if the contact between the needles and the module pads is good enough, there is no problem to operate the module, even to get stable high speed links**. Based of the results obtained, a baseline **testing protocol was proposed**. The ultimate goal of the testing protocol is to check the quality of the chips bump bonding and the chips operation performance. The test was divided into two parts, in order of safety. First part, only involves the digital region of the chips, using the Boundary-Scan. Second part includes the analog region with the aim of readout pedestal frames, covering all module operation aspects.

Figure 83: Picture of EMCM needle card at the holder. The EMCM W17 − 4 is placed on the probe-station chuck.

The experience gained with the EMCM needle card allowed to improve the final needle card prototypes, in terms of data links stability, safety on the operation and reducing the damage performed on the module pads. Since two pad layout are implemented, two needle card are necessary for the PXD production (*design A* and *design B*).

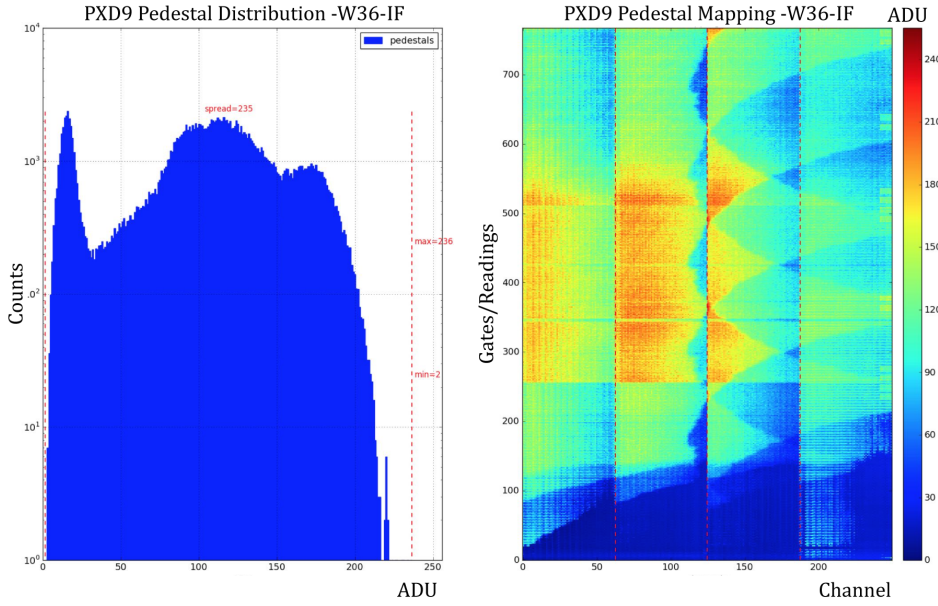

Figure 84: Pedestal frame obtained with the needle card design A and a IF module.

The final needle card prototypes were tested with a PXD9 module, the testing protocol proposed was completely applied with the aim of obtaining a pedestal frame. Figure 84 shows **this pedestal frame**, concluding the process of design and characterization. This picture **prove the capability of this system to readout data and therefore to fully apply the test protocol proposed**.

The setup, with all the mechanical parts, the electronic boards and the software, was mounted and prepared to be used during the production. Likewise, the *design A* and *design B* needle cards and also the test protocol for the sanity check.

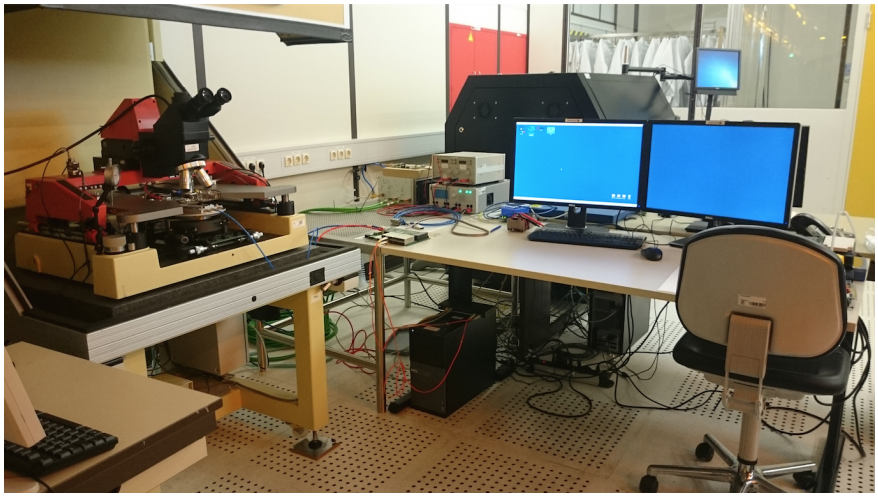

Figure 85: Picture of needle card setup at the HLL (Munich).

Part III

t-quark mass measurement at high energy e^+e^- colliders

7 The Physics Framework of Top Quark

This part of the thesis intends to summarize the development a new observable to measure the top quark mass with high precision in e^+e^- colliders. However, since the definition of the quarks mass is related with the strong interaction itself, understanding the basics of QCD is crucial to obtain meaningful results. For this reason, this chapter introduces, briefly, some concepts about QCD calculations, the ultraviolet and infrared divergencies and renormalization of couplings. Also, it describes, briefly, the Monte Carlo tools used to perform the study and the basics of the jet reconstruction methods. Finally, an overview of the top-quark physics is performed, with special emphasis on the current status of the top-quark mass measurements .

7.1 *Ultraviolet divergencies*

Quantum Filed Theory (QFT) is the theoretical framework used for constructing quantum mechanical models. Intrinsically, these theories lead to integrals, which, in some cases, are divergent when energy goes to infinite (ultra violet divergencies). To show an example, consider the gluon self-energy (Fig. 86) [46]. Using the Feyman Rules [1], the integral over the momentum space can be written as shows in equation 31 .

$$\int \frac{d^4p}{(2\pi)^4} \frac{p^\alpha (p-q)^\beta}{p^2 (p-q)^2} \tag{31}$$

This integral involves a divergence on the term $\int d^4p/(p^2)$. There are several methods to enclose this problem, the most common procedure is the dimensional *regulariza-*

1 The Feyman Rules are a set of prescriptions which describe pictorially and mathematically the interaction between particles, and let the transition between this two representations.

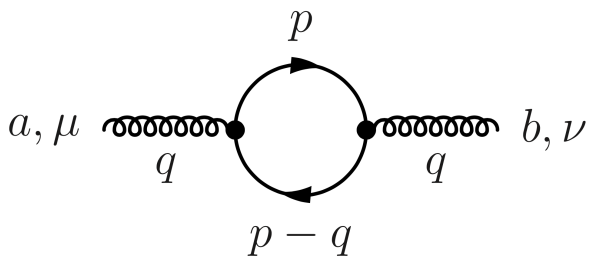

Figure 86: Gluon self energy diagram.

tion, which replaces the four-dimension integral by a D−dimension integral, where D is defined as $D = 4 - 2\epsilon$ and $\epsilon \neq 0$ (Eq. 32).

$$\int \frac{d^4p}{(2\pi)^4} \rightarrow \int \frac{d^Dp}{(2\pi)^D} \tag{32}$$

The resulting integral is shown in equation 33, where the divergence is enclosed on the gamma function ($\Gamma(-\epsilon)$). The γ_E represents the Euler−Mascheroni constant [84]. Noticing that the four-momentum (q^2) has dimensions, to keep the result dimensionless, the renormalization scale constant (μ) has been introduced. Then, the divergent terms can be isolated as show equation 34.

$$\begin{gathered}\int \frac{d^Dp}{(2\pi)^D} \frac{p^\alpha (p-q)^\beta}{p^2(p-q)^2} = \frac{-i\mu^{2\epsilon}}{6(4\pi)^2} \left(\frac{-q^2}{4\pi\mu^2}\right)^\epsilon \Gamma(-\epsilon) \left(1 - \frac{5}{3}\epsilon\right) \left(\frac{q^2 g^{\alpha\beta}}{2(1+\epsilon)} + q^\alpha q^\beta\right) \\ \text{where } \Gamma(-\epsilon) = -\frac{1}{\epsilon} - \gamma_E + \mathcal{O}(\epsilon)\end{gathered} \tag{33}$$

$$\mu^{2\epsilon} \left(\frac{-q^2}{4\pi\mu^2}\right)^\epsilon \Gamma(-\epsilon) = -\mu^{2\epsilon} \left(\frac{1}{\epsilon} + \gamma_E - \log 4\pi + \log\left(\frac{-q^2}{\mu^2}\right) + \mathcal{O}(\epsilon)\right) \tag{34}$$

The self-energy of the gluon can be divided in two parts. One enclosing the divergent terms and a second including all the q^2 dependences. The definition of these terms is called *scheme* and it is completely arbitrary. For instance, the MS scheme (Minimal Subtraction) only separates the term $1/\epsilon$ from the rest of the equation. The most used scheme is $\overline{MS}$ (Modified Minimal Subtraction) which subtracts $1/\bar{\epsilon} = 1/\epsilon + \gamma_E - \log(4\pi)$.

The regularization process have introduced extra parameters to the calculation: the scheme and the scale μ. The prediction obtained with these models should not depend on these parameters. Therefore, they have to be reabsorbed by redefining couplings and quark masses, this process is called *renormalization*.

To illustrate the renormalization process, consider the arbitrary observable [2] Q (Eq. 35), which, by definition, depends on the energy scale, q^2/μ^2, the renormalized coupling, $\alpha(\mu)$, and quark masses, $m(\mu)/q$.

$$\begin{aligned}&\mu\frac{d}{d\mu}Q(q^2/\mu^2,\alpha(\mu),m(\mu)/q)=0\\&=\left(\mu^2\frac{\partial}{\partial\mu^2}+\beta(\alpha)\frac{\partial}{\partial\alpha}-\gamma(\alpha)m\frac{\partial}{\partial m}\right)Q\end{aligned}\tag{35}$$

The renormalization is performed by defining two group of coefficients. The $\beta(\alpha)$ and the $\gamma(\alpha)$ [3], which can be written as a perturbative expansion (Eq. 36), where the perturbative expansion parameter β_j is referred to $j+1$ calculation order.

$$\begin{aligned}\beta(\alpha)&=\mu^2\frac{\partial\alpha}{\partial\mu^2}\\&=-\beta_0\alpha^2-\beta_1\alpha^3-\beta_2\alpha^4+\mathcal{O}(\alpha^5)\\\gamma(\alpha)&=-\mu^2\frac{1}{m}\frac{\partial m}{\partial\mu^2}\\&=-\gamma_0\alpha-\gamma_1\alpha^2-\gamma_2\alpha^3+\mathcal{O}(\alpha^4)\end{aligned}\tag{36}$$

The solution of these two differential equations is shown in equation 37, where β_0 is a first order calculation and corresponds to $\beta_0=(33-2n_f)/(12\pi)$ [4], and n_f is the number of active quark flavors. As long as $n_f<16$, α will be inversely proportional to the scale. This suggest the property of asymptotic freedom, because in short distances regimen (high energy), the coupling constant becomes very small, and when the energy decreases (long distances), the coupling constant grows, requiring colored objects to be confined in a colorless structures. Moreover, in the $\overline{\text{MS}}$ scheme, quark masses also depend on the scale, being smaller at higher energies, this mass definition is known as *running mass*.

$$\begin{aligned}\alpha(\mu^2)&=\frac{\alpha(\mu_0^2)}{1+\beta_0\alpha(\mu_0^2)\log(\mu^2/\mu_0^2)}\\m(\mu^2)&=m(\mu_0^2)\exp\left[-\int_{\alpha(\mu_0^2)}^{\alpha(\mu^2)}\frac{\gamma(\alpha)}{\beta(\alpha)}d\alpha\right]\end{aligned}\tag{37}$$

2 Observable: Experimental entity defined as the quantity that can be observed or measured. Subsequently used to extrapolate the parameter of interest.

3 Known as mass anomalous dimension.

4 Detailed calculations up to fourth order on [85] and [86].

To perform the calculations in a safe region of scales (far from the divergencies), it is important to introduce a cut-off. Usually the constant Λ_{QCD} is used to ensure the meaningfulness of the perturbative expansion [5]. Therefore, the scale must conform $\mu >> \Lambda_{QCD}$ ($\alpha << 1$). For this reason, the perturbative expansion cannot be applied on very small scales.

7.2 *Quark Mass Definition*

In order to define an observable to measure a quark mass, it is crucial to have a clear definition of the quark mass concept. In case of leptons, the mass can be measured directly [6] as the pole mass of the propagator. Things are different with the quarks, since they cannot be observed as free particles but in hadron structures. Therefore, their mass cannot be determined directly and needs to be defined in a chosen convention and be seen through the effects on the hadrons properties. The most common mass definitions are the *running mass* ($m_q(\mu)$) and the perturbative *pole mass* (m_0).

In the previous section, the concept of *running mass* was introduced. In this case, the mass of the quarks are considered couplings in the QCD Lagrangian. When the theory is being renormalized, the mass parameter gets dependencies with the scale (μ), this is why they are known as *running masses*, because they depend on the scale of the process.

The second definition is the perturbative *pole mass*, which can be derived by identifying the pole on the quark propagator $S(p)$, where m_0 is the bare mass and the self energy (Σ) [7] is given by the sum of the irreducible one-particle Feynman diagrams (Eq. 38) [87]. However, the pole mass cannot be given with arbitrarily high accuracy due to the non-perturbative infrared effects in QCD [88].

$$S(p) = \frac{1}{i\not{p} + m_0 - \Sigma(p)} \tag{38}$$

It is important to notice that both definitions are related via equation 39 at order α, and cannot be distinguish at first order (LO) [8].

$$m_0^{pole} = m_q(\mu)\left(1 + \frac{4}{3\pi}\alpha(\mu) + \right) + \mathcal{O}(\alpha^2) \tag{39}$$

5 The Λ_{QCD} is defined on each renormalization scheme.
6 i.e Curvature of a particle in a magnetic field.
7 Dyson Summation of the quark propagator self energy. It shifts the location of the pole in the propagator.
8 This relation has been computed at higher order in Ref. [45],[89].

7.3 *Infrared Divergences*

One consequence of QCD is the possibility of coupling between quarks and gluons. This coupling implies that quarks can radiate gluons. For example, consider the cross section $\sigma(e^+e^- \to \text{hadrons})$. At parton level, it can be written as $\sigma(e^+e^- \to q\bar{q} + q\bar{q}g + q\bar{q}gg + ...)$, including all gluon emissions. The cross section, at first order, $\sigma_{q\bar{q}g}$ (Fig. 87) is shown in equation 40 (assuming $m_q \sim 0$, see Ref. [90]), where $x_q \equiv 2E_q/\sqrt{s}$, $x_{\bar{q}} \equiv 2E_{\bar{q}}/\sqrt{s}$, $x_g \equiv 2E_g/\sqrt{s}$, being E_g the energy of the gluon, $E_{q,(\bar{q})}$ the energy of the quark (antiquark) and θ_{qg} or $\theta_{\bar{q}g}$ the gluon emission angle regarding of the quark or antiquark, respectively.

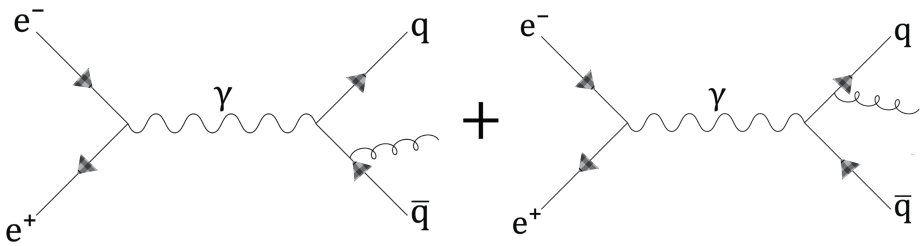

Figure 87: Feynman diagrams for the real gluon emission.

$$\frac{1}{\sigma_{q\bar{q}}}\frac{d^2\sigma_{q\bar{q}g}}{dx_q\,dx_{\bar{q}}} = 3\sum_j Q_j^2 C_F \frac{\alpha_s}{2\pi}\frac{x_q^2 + x_{\bar{q}}^2}{x_g^2(x_{\bar{q}}(1-\cos\theta_{\bar{q}g}))(x_q(1-\cos\theta_{qg}))} \tag{40}$$

When this differential cross section is integrated over the phase space, regions of singularities appear (*infrared divergences*). This happens when the gluon emitted is very soft, $E_g \to 0$, or when the gluon emitted is collinear to the quark involved, $\theta_{ig} \to 0$ $(i = q, \bar{q})$. To be able to absorb these divergences a higher order diagrams are added to the integral, including diagrams with virtual gluons (Fig. 88), which have infrared divergences that cancel the previous ones [91].

The infrared divergences are an important concept to consider when an observable is defined. One observable can be labeled as *infrared safe* if it is not sensitive to the collinear and soft emissions. For instance, the observable defined as the inclusive cross section $\sigma_{q\bar{q}}$, including all possible final states $e^+e^- \to q\bar{q} + q\bar{q}g + q\bar{q}gg + ...$ would be infrared safe, because all possible emissions have been considered. On the other hand, an observable, defined as the number of final partons on a specific process, would not be infrared safe because the emission of a soft/collinear gluon will change the final multiplicity. In this particular case, the observable can become infrared safe if, instead of be defined as the partons multiplicity, is defined as the *jets* multiplicity, which are objects non-sensitive to the soft/collinear emissions.

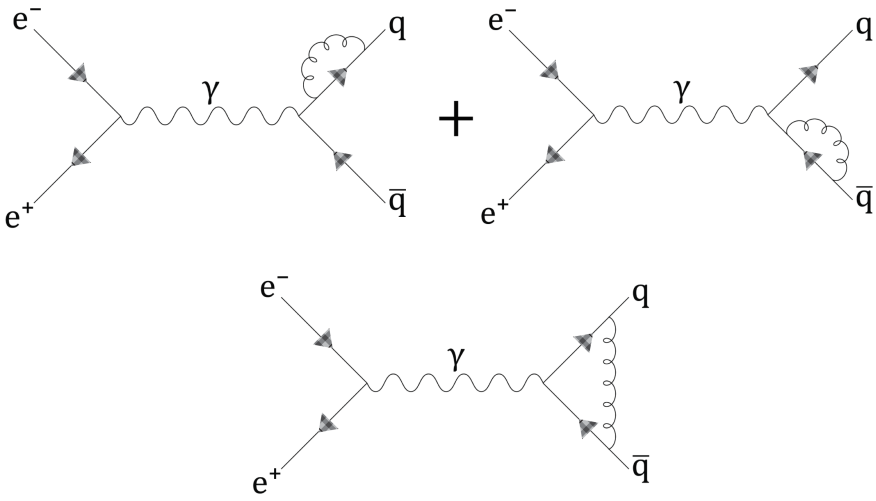

Figure 88: Feynman diagrams for 1-loop virtual gluonic corrections.

7.4 e^+e^- *annihilation and jets*

High energy physics experiments generate, simultaneously, a massive number of hadrons observed as streams of energy around the direction of the primary parton emission. These streams can be classified as *jets*.

In order to understand the generation of jets, the e^+e^- annihilation into hadrons have to be introduced, this process can be divided in the following steps (Fig. 89):

1. **Initial state radiation (ISR):** It refers to the emission, by the incoming particles, of photons through a higher order QED processes. The photons can be very hard and carry out a huge fraction of the particle energy.
2. e^+e^- **annihilation into** $q\bar{q}$ **pairs via** γ **or** Z^0 **exchange.**
3. **Parton shower:** The primary $q\bar{q}$ radiates gluons. These gluons will also radiate gluons, which, eventually, will split into $q\bar{q}$ again, which will also radiate gluons and so on. This process will continue until the remaining energy is not enough to continue ($Q \sim \Lambda_{QCD} \sim \alpha_S \sim 1$).
4. **Hadronization:** Quarks and gluons merge [9] to become hadrons.
5. **Decay:** The unstable hadrons and resonances decay into stable hadrons.

9 When the energy of the system is not high enough to keep the partons separated, due to the confinement requirement, they merge into hadrons.

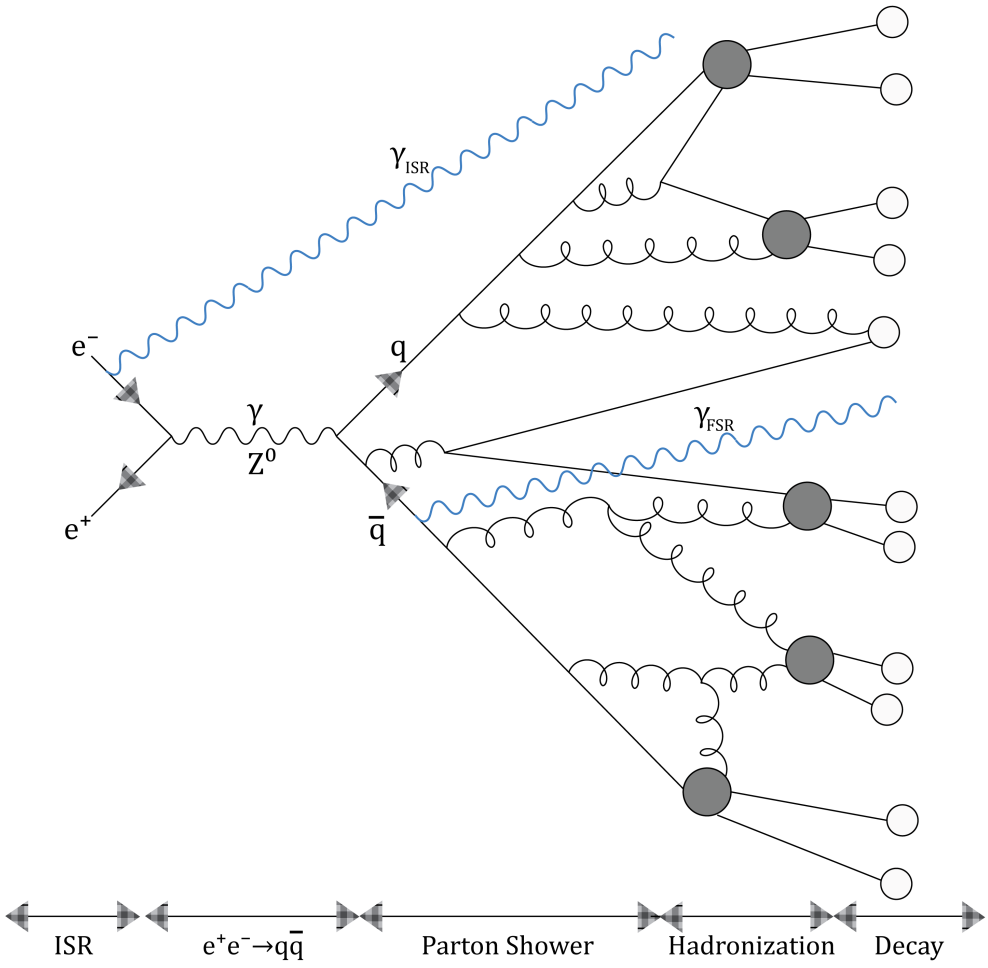

Figure 89: Annihilation e^+e^- into hadrons

To be able to perform calculations or define models over these processes, different strategies have to be used on each step. Usually, the e^+e^- annihilation can be calculated using Feyman diagrams (matrix element), the parton shower (including ISR) involves many difficult diagrams and are calculated via perturbative QCD, the hadronization is obtained via non-perturbative QCD and the decay process could be obtained, again, via the matrix element.

- **Feyman Rules (Matrix Elements):** They are a set of prescriptions which describe pictorially and mathematically the interaction between particles, taking in account the kinematics. The calculation become harder as the calculation order is increased (steps 2 and 5).

- **Parton Shower:** The process begins in the final state calculated by the matrix elements [10]. Each quark or gluon can radiate softer quarks or gluons and so on[11]. This process is called *partons split* and is described, step by step, with the equation 41, where p_T is the transverse momentum, $P_{i,jk}(z)$ is the splitting function and z is the fraction of momentum splitted (Fig. 90).

$$d\sigma_{n+1} \simeq d\sigma_n \frac{dp_T^2}{p_T^2} \frac{\alpha}{2\pi} P_{i,jk}(z) dz \tag{41}$$

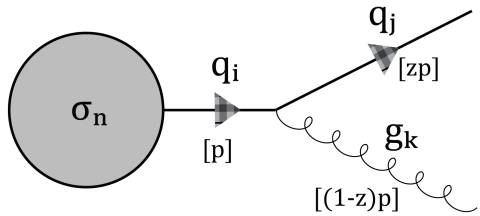

Figure 90: Quarks i, splits in quark j and gluon k.

The process is repeated sequently, dividing and reducing the remaining energy. Step by step the emissions approach to the collinear regime up to a predefined *infrared cuttoff*. In general, the equation which describes the parton shower evolution can be written as show equation 42, where $\Delta(t)$ is the Sudakov form factor (step 1 and 3). Detailed description on Ref. [92]

$$d\sigma_n \simeq d\sigma_0 \left[\Delta(t_0 + \Delta(t) \frac{\alpha}{2\pi} \frac{dt}{t} P(z)) \right] \tag{42}$$

- **Hadronization:** It is defined as the transition process from partons to hadrons. It takes place when energy becomes too small to keep the partons separated ($Q \sim \Lambda_{QCD}$). It happens at low energy and it is very difficult to describe with perturbative QCD (Lattice). Instead, phenomenological models are used. These models implement a probabilistic and iterative procedure, which depend on some parameters that need to be tuned. The most commonly used models are the *cluster fragmentation* and the *string fragmentation* (Step 4).

  - *Cluster fragmentation:* When the parton shower is over, each gluon breaks into a $q\bar{q}$ pair and then quarks and antiquarks are grouped into clusters (colorless objects). The hadrons are obtained from the clusters decay.

10 Parton shower is also used to compute the emission of photons by the incident particles, Initial State Radiation photons (ISR) [50].

11 Quarks can radiate also photons, known as Final State Radiation photons (FSR).

– *String fragmentation:* The model describes each parton as a color flux tube, called string, which is stretched until the final singlet state is obtained. If the stretching power is high enough to create a secondary $q\bar{q}$ pair from the vacuum, the string will split into two different pieces. This process is repeated until the energy is not enough to continue splitting the string. In that time, the hadrons are generated.

7.5 *Jet algorithm introduction*

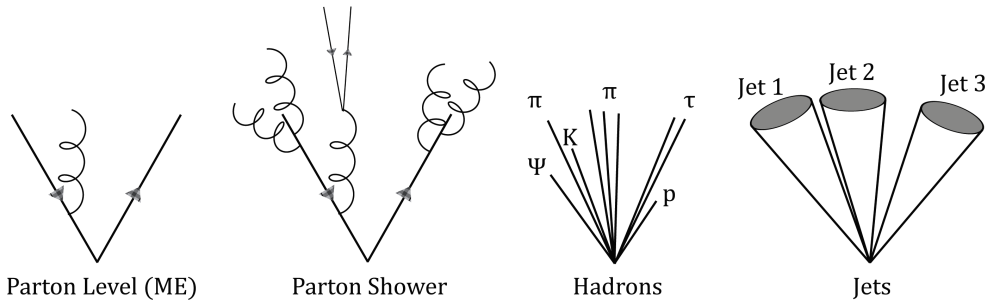

Figure 91: Jets algorithms have to provide a number of jets, insensitive the soft and collinear emissions.

A jet algorithm is a software tool which organizes the final particles in separated energy streams. It must be capable to distinguish multiple jets, coming from the distinct partons (Fig. 91). However, this is not easy to perform since hadrons are not perfectly collimated due to the quantum interference and, in some cases, the final hadrons can be constructed with parts coming from different partons. Moreover, jets can be produced close together, making very difficult the distinction.

The definition of a jet algorithm is performed in two steps. First, it is necessary a criteria to order the particles and choose which are the best candidates to be recombined and which order must be followed to perform this recombination. The second step is to define the recombination scheme, which describes the combination procedure inside the jet, for example adding the four-momentums of the particles (E-scheme).

Usually, the selection criteria is based on a parameter called d_{ij}, which defines the "distance" between the pseudo-jet [12] i and a pseudo-jet j. To start the process of recombination, the first step is to find the smallest d_{ij} between all possible combinations of particles. Then, the pseudo-jet i and pseudo-jet j are recombined using the E-scheme

12 Inside the algorithm, all particles and recombination of them are called pseudo-jets until the algorithm reach a point in which a pseudo-jet is defined as a jet.

to a new pseudo-jet. This process is repeated recursively until the smallest distance exceeds a cut value, d_{cut} (inclusive clustering), or the number of pseudo-jets reach a previously defined number of jets (exclusive clustering) [93]. The most extended algorithms are:

- **Jade:** It was the first clustering algorithm, developed in the middle of 1980's. The "distance" criteria (d_{ij}) is defined in equation 43, where E_α is the energy of the pseudo-jet, s is the corresponding interaction energy and θ_{ij} is the angular distance between the particles [94].

$$d_{ij} = \frac{E_i^2 E_j^2}{s^2}(1 - \cos\theta_{ij}) \tag{43}$$

- **Durham or k_t:** It was extensively used at LEP and SLC. The "distance" criteria (d_{ij}) was redefined as show equation 44, using instead, the smallest of the energies E_i or E_j[95].

$$d_{ij} = 2\min(E_i, E_j)(1 - \cos\theta_{ij}) \tag{44}$$

- **Generalized k_t algorithm:** Hadron colliders present different scenarios to perform the jet reconstruction. For instance, the incoming beams, usually, radiate gluons that can generate collinear jets to the direction of the incident particles. To adapt the jet algorithms to this new scenario, the *beam jets* parameter [96] was introduced, defined as $d_{iB} = p_{Ti}^{2n}$ [13]. If the d_{iB} of one pseudo-jet becomes smaller than any "distance" d_{ij}, this pseudo-jet is removed and considered part the beam-jet. The "distance" criteria was redefined as equation 45, where $p_{T\alpha}$ is the transverse momentum, R is a radius parameter (usually $R < 1$), and $\Delta R_{ij} = \sqrt{(\phi_i - \phi_j)^2 + (\eta_i - \eta_j)^2}$ represents the angular distance [14].

$$d_{ij} = \min(p_{Ti}^{2n}, p_{Tj}^{2n})\frac{\Delta R_{ij}^2}{R^2} \tag{45}$$

  The n parameter decides the type of k_t algorithm to be used. If $n = 1$ the algoritm is called *invariant* k_t and $n = -1$ correspond to the *anti*-k_t algorithm, which is the default jet reconstruction method used at LHC.

- **The VLC algorithm:** VLC algorithm aims to cope the requirement of the future high energy e^+e^- colliders, including the managing of the background levels on the LHC. It maintains the Durham-like distance criterion based on energy and the polar angle. However, it redefines the "distance" d_{ij} and the *beam jets*

13 d_{iB}: Distance parameter between the pseudo-jet i and the beam (B).

14 The η variable is defined as the pseudorapidity $\eta = -\ln[\tan(\theta/2)]$, being θ the angle between the pseudo-jet four-momentum and the incoming beam direction. The angle ϕ is the azimuthal angle.

(d_{iB}) parameter. Equation 46 shows the redefined criterions, where β and α are arbitrary parameters, which generalize the algorithm and provide independent handles on the clustering order and the background resilience [15] [97].

$$\begin{aligned} d_{ij} &= 2\min(E_i^{2\beta}, E_j^{2\beta})(1-\cos\theta_{ij})/R^2 \\ d_{iB} &= E^{2\beta}\sin^{2\gamma}\theta_{iB} \end{aligned} \tag{46}$$

7.6 *Monte Carlo tools*

In the previous section, an overview of the jet algorithms have been done. Also, the physics processes behind these final entities have been covered. These concepts provide an idea how the data is generated using *Monte Carlo tools*. Monte Carlo tools implement the physical processes, to simulate the final state particles expected in a real event. The study presented in this thesis requires data from colliders that will not be available in many years, therefore the calculations have been carried out using simulations. This section will introduce, briefly, the MC tools used to obtain this data:

- **Pythia8:** Pythia8 is the C++ version of Pythia6, it is a Monte Carlo tool, specifically developed to generate high-energy collisions, starting at LO hard process calculation to multi-hadronic final states. The hard process calculation is done with pp, $p\bar{p}$, e^+e^- and $\mu^+\mu^-$ incoming beams, which does not include detailed machine effects (like the smearing of the interaction energy). The parton shower, including initial and final state radiation, are $p_\perp$-ordered, interleaved with multiple interaction and dipole recoil. The hadronization is based solely on the Lund string fragmentation. The program flow starts with the generation of a "process", which determines the nature of the event (hard process). The second step is the calculation of the partonic level, involving initial and final state radiation, multiple parton-parton interaction and the structure of the beam remnants, which include non-perturbative physics aspects. Finally, the hadronization is performed via string fragmentation and followed by the decays of the unstable particles. These calculations are almost completely non-perturbative, requiring extensive modelling and tuning. At the end, a realistic event is generated. Afterwards, this simulated data can be processed to include detector effects [98].

- **Whizard:** Developed to compute automatically complete tree-level matrix elements, integrated over the phase space and generate unweighted partonic event samples. The parton shower and hadronization of the samples can be implemented by calling external codes (i.e. Pythia6). Matrix elements are computed as helicity amplitudes, so spin and color correlations are retained. The standard

15 For $\alpha = \beta$ the method is called *Valencia* algorithm, $\alpha = 1$ and $\beta = 0$ define the *VLC-angular* and $\alpha = \beta = -1$ yield to the *anti-VLC* [93].

model, the MSSM, and models such as Little Higgs or effects of extra dimensions have been implemented, covering hadron, lepton and photon colliders. The calculation also includes detailed machine effects, like the smearing of the interaction energy, which is calculated online using "circe" or via external input files. In contrast to programs such as Pythia, it does not contain a fixed library of physics processes. Instead, for any process that is possible at tree level, the matrix element is computed as needed [99].

These programs have being used extensively on present and future experiments, like LHC or ILC. They are necessary to predict and study the behavior of some observables and to understand the backgrounds involved on the measurements. In the present study, since it is focus on future e^+e^- colliders, Monte Carlo tools were used to perform every step, from studies at partonic level to the particle level including detector effects. The detailed description is performed in Chapter 8, where the observable to measure of the top-quark mass will be presented.

7.7 *The Top-quark*

The top quark is the last and the heaviest quark discovered. It was first observed at Fermilab in 1995 [42], on the Tevatron experiments CDF and D0. On the standard model, it composes the isospin doublet together with the b-quark. Its electric charge is $Q = -2/3$ and its mass and its CKM (Cabibbo-Kobayashi-Maskawa) matrix elements are free parameters that should be determined experimentally.

The particle data booklet [45] presents the combined measurements [16] of the top-quark main properties ($I(J^P) = 0(\frac{1}{2}^+)$). The mass value using a direct measurement is $m_t = 173.21 \pm 0.51 \pm 0.71$ GeV. The mass difference between the top-quark and the top-antiquark correspond to $m_t - m_{\bar{t}} = -0.2 \pm 0.5$ GeV. The top-quark decay width are $\Gamma = 1.41^{+0.19}_{-0.15}$ GeV and the width ratio $\Gamma(Wb)/\Gamma(Wq(q = b, s, d)) = 0.957 \pm 0.034$. The EW couplings obtained from the measurement of the W helicity fraction can be summarized as: $F_0 = 0.690 \pm 0.030$ (longitudinal fraction), $F_- = 0.314 \pm 0.025$ (left-handed fraction), $F_+ = 0.008 \pm 0.016$ (right-handed fraction) and $F_{V+A} < 0.29, CL = 95\%$ (vector plus axial couplings fraction).

The top-quark decays via weak interaction mostly to Wb. Due to its large mass, its lifetime becomes very short ($\sim 0.5 \times 10^{-24}$ s), decaying before any hadronization and offering the unique feature to study this particle as a quasi-free quark [17]. The identification of the top-quark, experimentally, is performed by picking out the decay products. The b-quark produces a characteristic jet, and the W boson can decay via two channels, lepton-neutrino or two quarks (two jets). Considering the events in which the top-quark

16 Combined measurements until summer 2016.

17 i.e. it is possible to study the top quark polarization, since the hadronization does not remove the spin information.

is produced in pairs, three decay modes can be differentiated:

- **Full-Hadronic:** The *W* bosons decay hadronically. The event is identified by two pairs of jets produced by the light quarks from the *W* bosons and two jets produced by the b-quarks (Fig. 92).

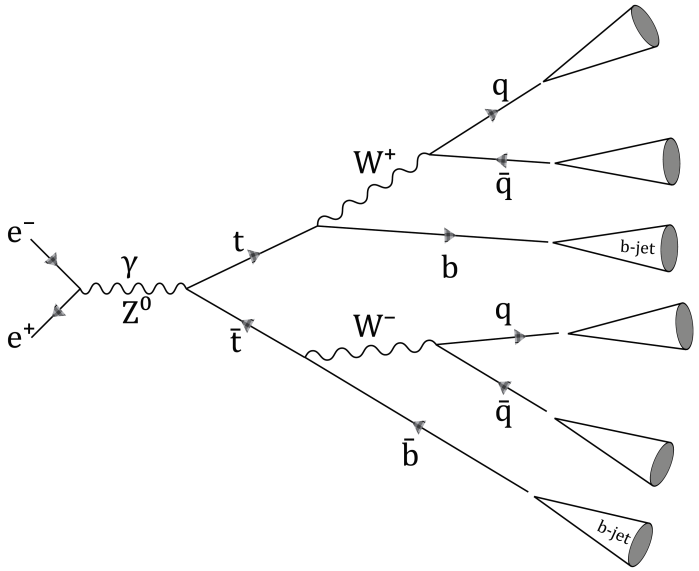

Figure 92: $t\bar{t}$ full-hadronic decay mode. The final state has 6 jets.

- **Semi-Leptonic:** One *W* decay leptonically and the other hadronically. The signature is two jets from the light quarks produced in the hadronic decay of the *W* boson, two jets produced by the b-quarks and one energetic lepton [18] plus missing energy (neutrino) coming form the other *W* boson (Fig. 93).
- **Full-Leptonic:** Both *W* bosons decay leptonically, producing two energetic leptons, missing energy due to the neutrinos and the two corresponding jets coming from the b-quarks (Fig. 94).

In general, the decay of the top-quark pair generates scenarios where a precise determination of jets is needed. Also, it requires a good identification of the leptons produce by the *W* boson decay and estimations of the missing energy carried by the neutrinos. Jet algorithm and identification software are used to perform these identifications. The $t\bar{t}$ decays ratios are shown in figure 95.

18 τ-lepton decay mode, produce a hadronic jet or a electromagnetic cascade. μ-lepton decay mode, produce a μ that can be detected. *e*-lepton decay mode, produce a electromagnetic cascade

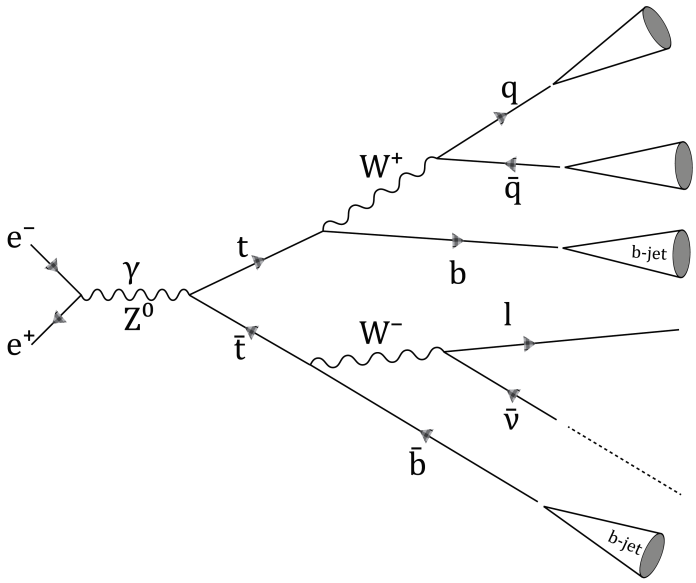

Figure 93: $t\bar{t}$ semi-leptonic decay mode. The final state has 4 jets, one energetic lepton and missing energy due to the neutrino (dashed line).

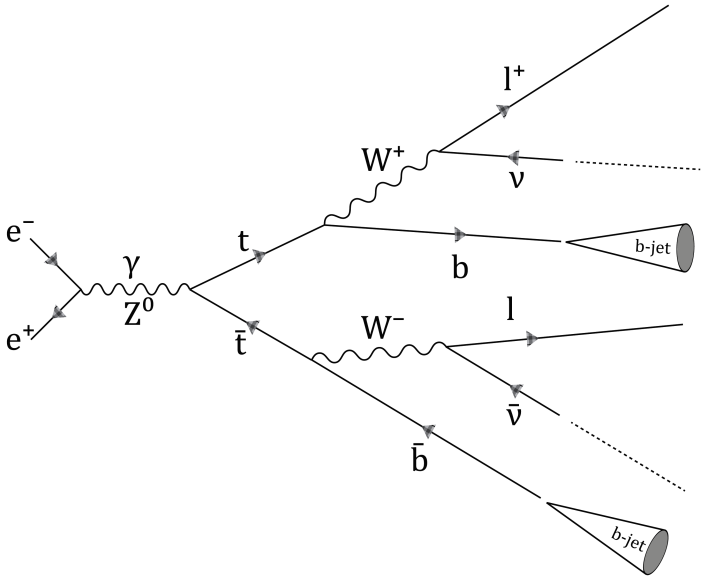

Figure 94: $t\bar{t}$ full-leptonic decay mode. The final state has 2 jets, two energetic leptons and missing energy due to the neutrinos (dashed line).

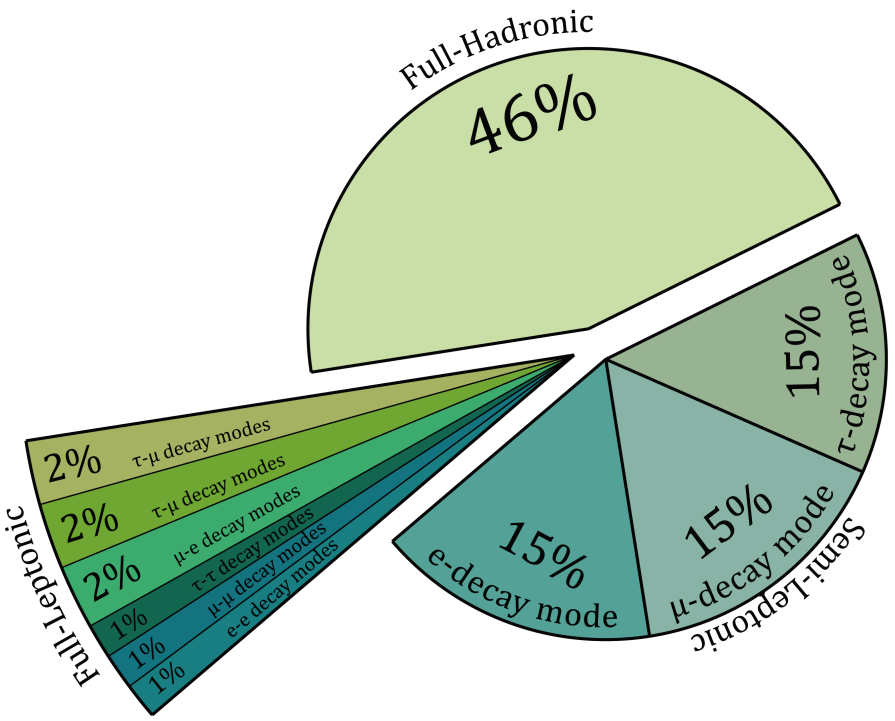

Figure 95: $t\bar{t}$ decay channels ratios.

The production cross section of top pairs, in e^+e^- colliders, depends on the polarization of the incoming beams. For example, on the ILC at 500 GeV [19], the extreme cases are [100]:

- Beams completely unpolarized $\rightarrow \sigma_{unpol} = 572$ fb.
- A 100% left-handed polarised electron beam $(-)$ and 100% right-handed polarised positron beam $(+) \rightarrow \sigma_{-+} = 1564$ fb.
- A 100% right-handed polarised electron beam $(+)$ and 100% left-handed polarised positron beam $(-) \rightarrow \sigma_{+-} = 724$ fb.

The σ in a particular polarization [20] can be calculated using the equation 47.

$$\sigma_{p_{e^-}p_{e^+}} = \frac{1}{4}\left[(1 - p_{e^-}p_{e^+})(\sigma_{-+} + \sigma_{+-}) + (p_{e^-} - p_{e^+})(\sigma_{+-} - \sigma_{-+})\right] \tag{47}$$

19 CLIC-380 GeV $\rightarrow \sigma_{unpol} = 520$ fb and ILC-1000 GeV $\rightarrow \sigma_{unpol} = 210$ fb.

20 For the ILC the polarization will be $p_{e^-} = \pm 80\%$ $p_{e^+} = \mp 30$.

7.7.1 *The Top-quark mass measurements*

The most extended methods to measure the top-quark mass are:

- **Direct measurement:** The mass is reconstructed from a kinematic fit of the decay products. This method is applied to $t\bar{t}$ pairs decaying semileptonically requiring events that contain a single isolated electron (e) or muon (μ), at least 4 jets, and exactly 2 b-tags (b-jets) [101].
- **Extraction from inclusive cross section:** The top-quark mass is obtained from its dependency with the inclusive $t\bar{t}$ cross section.

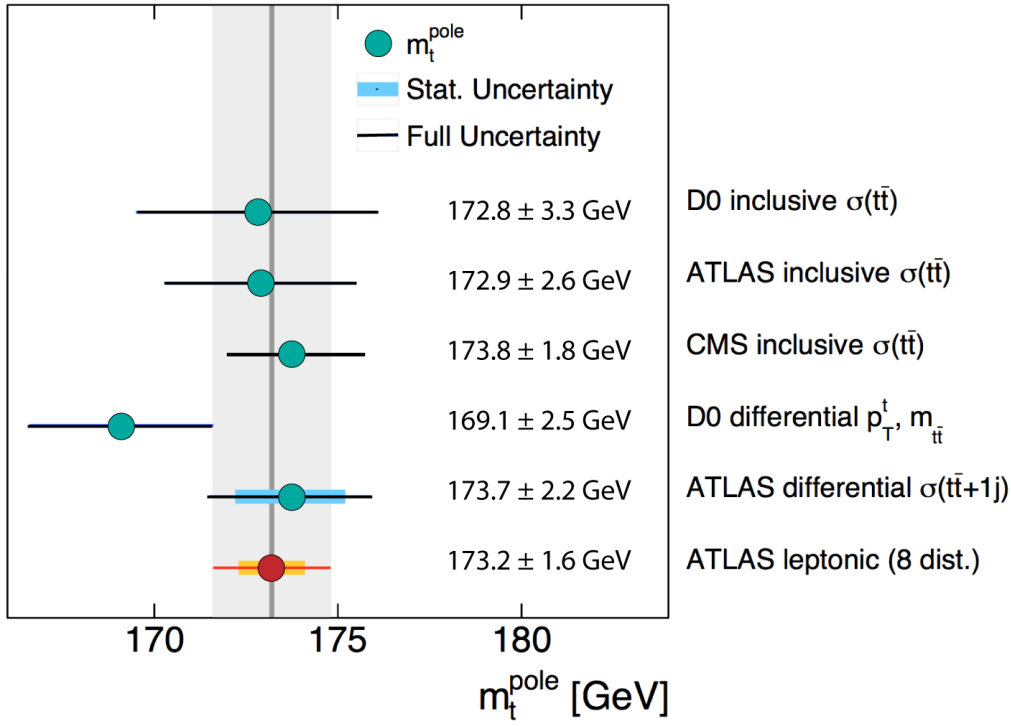

Figure 96: Top quark mass measurements at Tevatron and LHC.

Recently, a new method has been developed, which explodes the dependence of gluon radiation processes and the mass of the radiating top-quark (Eq. 48).

$$\sigma_{q\bar{q}g} \propto A(\alpha, \sqrt{s}) + B(\alpha, \sqrt{s}, m_q)\frac{m_q^2}{s} + \ldots \tag{48}$$

The method uses the so called $\mathcal{R}$ **distribution**, defined as shown equation 49 [102] ($m_0 = 170$ GeV is an arbitrary constant required to get a dimensionless ρ_s).

$$\mathcal{R}(m_t^{pole}, \rho_s) = \frac{1}{\sigma_{t\bar{t}+1jet}} \frac{d\sigma_{t\bar{t}+1jet}}{d\rho_s}(m_t^{pole}, \rho_s)$$
$$\text{where } \rho_s = \frac{2m_0}{\sqrt{s_{t\bar{t}j}}} \tag{49}$$

This method has been applied on ATLAS experiment at 7 GeV, obtaining unprecedented precision on the top quark mass measurement. Equation 50 shows the last results, presented on Ref. [50].

$$m_t^{pole} = 173.71 \pm 1.50(\text{stat.}) \pm 1.43(\text{syst.})^{+0.95}_{-0.49}(\text{theo.}) \text{ GeV} \tag{50}$$

7.8 *Summary*

This chapter has introduced the basic concepts of QCD to motivate the definitions of top-quark mass. Then, the processes involved on the e^+e^- annihilation into hadrons have been summarized, likewise the strategies used to model them into the Monte Carlo tools. The definition of the infrared divergencies motivated the introduction of jets, describing the basic algorithms and the new available methods. After getting over these concepts, the top-quarks basics have been presents and also the current methods to measure top-quark mass, which exploit the limits of the present machines, like $\mathcal{R}$ distribution measurement. This thesis, enters on this context to introduce the definition of a new observable to measure the top-quark mass, meant for the future e^+e^- colliders.

8

The Top-quark Mass Measurement at High Energy e^+e^- Colliders using Radiative Events in the Continuum

The top-quark is the last quark that has been observed. It owns a high mass and therefore a short life-span, decaying before any hadronization. This large mass, also undergoes the highest coupling strength to the Higgs boson. For this reason, the top-quark has special importance on the Standard Model and, in like manner, its mass. The measurement of the top-quark mass has become a crucial target for the present and future high energy physic experiments. This thesis propose a new observable, using the cross section of the $t\bar{t}$ radiative events to obtain the mass of the top-quark in the continuum. The study has been performed on e^+e^- collider scenario to take advantage of this new environment and, potentially, reach unprecedented sensitivities. This chapter is devoted to introduce this new observable and its dependency with the initial (ISR) and final (FSR) state radiation. Then, the maximum potential resolution combining both effects will be presented.

8.1 *A new observable*

The cross section of the $e^+e^- \to t\bar{t} + \gamma$ (ISR and FSR) and $e^+e^- \to t\bar{t} + g$ (FSR) radiative events are dynamically related with the top-quark mass since they imply a reduction on the phase space of the subsequent process. The ISR photon emission reduces the probability of the top-quark production, which, at the same time, depends on the quark-mass itself [1], likewise, the top-quark mass reduces the phase space of the gluon emission.

1 With greater masses, production rates are reduced, because, more energy is required to produce the $t\bar{t}$ pair.

The strategy proposed is to experimentally measure the energy of the radiated particle, assuming a fixed energy of interaction. The production of the $t\bar{t}$-pair will constrain the maximum energy that the radiated particle can carry and this limit will depends, directly, on the mass of the top-quark. One advantage of this method is that no specific interaction energy is required [2], being sensitive to the top-quark mass over a large range of production energies. This allows the study the mass not only over the production threshold but in the continuum, and therefore, the mass can be defined on a good renormalization system and even being sensitive to its running.

In order to estimate the potential of the observable, the realism of the study was introduced sequentially. As a first approach, the study only considered the ISR photons. The monte carlo (MC) tool used was PYTHIA8. The events were generated at partonic level, avoiding to simulate any effect coming from the detector or the accelerator. The $e^+e^- \to t\bar{t}$ events were generated at 500 GeV (ILC physics program scenario) with several top-quark masses, to study the energy of the photons emitted. As was mentioned, when an ISR photon is emitted, the remaining interaction energy will be reduced, becoming S_{rem}<S. The remaining interaction energy is inversely proportional to the energy that the ISR photon is carrying. This emission will reduce the phase space of $t\bar{t}$ pair production, which at the same time, depends on the top-quark mass. Demanding a $t\bar{t}$-pair final state, a limit will appear on the maximum energy that can be extracted by the ISR photon. This dependency is illustrated on figure 97.

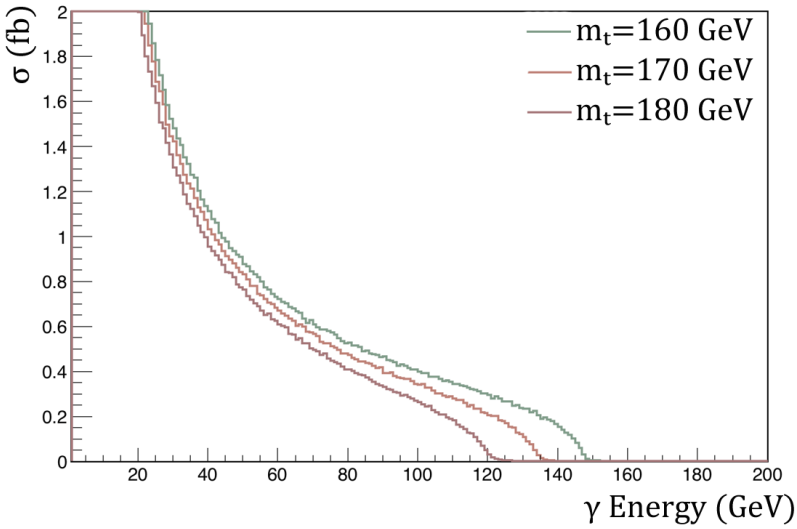

Figure 97: Energy distribution on the ISR Photons, in $e^+e^- \to t\bar{t}$ events with a Monte Carlo mass $m_t = 160$ GeV, 170 GeV, 180 GeV

2 In contrast to the top-quark mass measurement on the threshold.

The energy distribution of the ISR photon would be sensitive to the top-quark mass. However, the definition of a robust observable requires to use an invariant parameter. Considering $e^+e^- \rightarrow t\bar{t}$ events in a center-of-mass reference system, the four-momentum of the incident particles, on the interaction point, can be written as $p_- = (E_B, \vec{p})$ (electron) and $p_+ = (E_B, -\vec{p})$ (positron) and the center-of-mass energy will be the invariant $S = (p_- + p_+) = 4E_B$, where E_B is the energy of each beam. In general, if an arbitrary number of ISR emission are produced (by the electron and the positron), the energy of the incident particles, on the interaction point, will change to $p'_- = (E_B - \sum_i E_{\gamma_i}, \vec{p} - \sum_i \vec{p}_{\gamma_i})$ and $p'_+ = (E_B - \sum_j E_{\gamma_j}, -\vec{p} - \sum_j \vec{p}_{\gamma_j})$ and the invariant S will become $S'_\gamma = (p'_- + p'_+) = \left(2E_B - \sum_k E_{\gamma_k}, -\sum_k \vec{p}_{\gamma_k}\right)^2$. The development of the parenthesis is shown in equation 51.

$$\begin{aligned} S'_\gamma &= \left(2E_B - \sum_k E_{\gamma_k}\right)^2 - \left(\sum_k \vec{p}_{\gamma_k}\right)^2 \\ &= 4E_B^2 - 4E_B \sum_k E_{\gamma_k} + \left(\sum_k E_{\gamma_k}\right)^2 - \left(\sum_k \vec{p}_{\gamma_k}\right)^2 \\ &= S\left(1 - \frac{2\sum_k E_{\gamma_k}}{\sqrt{S}}\right) + \left(\sum_k E_{\gamma_k}\right)^2 - \left(\sum_k \vec{p}_{\gamma_k}\right)^2 \end{aligned} \tag{51}$$

For simplicity, only the radiation of one ISR will be considered (Fig. 98), therefore, since $E_\gamma^2 = \vec{p}^2$ the invariant can be written as equation 52.

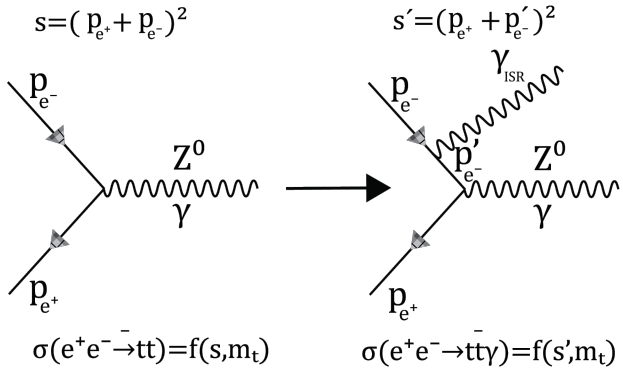

Figure 98: Invariant S before and after emission of a ISR photon. The available energy on the interaction point is reduced due to this emission.

$$S'_\gamma = S\left(1 - \frac{2E_\gamma}{\sqrt{S}}\right) \tag{52}$$

Given that the cross section of the process $e^+e^- \to t\bar{t}+\gamma$ also depends on the top-quark mass, the observable can be defined as show equation 53. Figure 99 represent the $B_\gamma(m_t, \zeta_{S'_\gamma})$ using distinct top-quark masses.

$$B_\gamma(m_t, \zeta_{S'_\gamma}) = \frac{d\sigma_{t\bar{t}\gamma}}{d\zeta_{S'_\gamma}} \to \zeta_{S'_\gamma} = \sqrt{S'_\gamma} \tag{53}$$

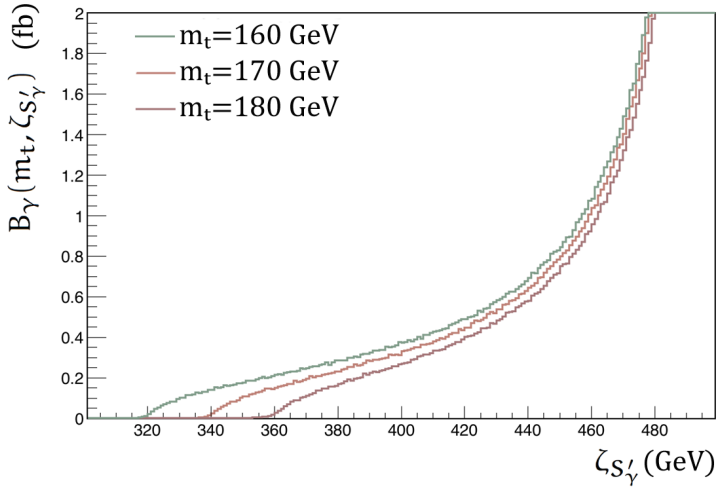

Figure 99: Photon ISR $B_\gamma(m_t, \zeta_{S'_\gamma})$ distribution with $m_t = 160$ GeV, 170 GeV, 180 GeV

8.2 $B_\gamma(m_t, \zeta_{S'_\gamma})$ *potential sensitivity - Parton Level*

The dependence of $B_\gamma(m_t, \zeta_{S'_\gamma})$ with the top-quark mass has been illustrated on figure 99, still, an estimation of the potential sensitivity will depend on the experimental available statistics. For this, a rough study has been performed using the ILC at 500 GeV scenarios. The expected accumulated luminosity, on each stage, is shown in table 19, based on the ILC schedule, presented, in 2013, by Howard E. Haber, during the LCWS13 in Tokio (Japan) [103].

Since the main parameter to obtain the $B_\gamma(m_t, \zeta_{S'_\gamma})$ is the energy of the photon, for simplicity, to construct the binning, the energy steps represents the energy resolution of the ILD electromagnetic calorimeter E-CAL ($\sigma/E = 0.16/\sqrt{E} \oplus 1\%$). Then, these energy steps have been converted to the $\zeta_{S'_\gamma}$ scale using the corresponding formula (Eq. 52). At this stage, all the reconstruction efficiencies have been considered 100%, to focus only on the statistical uncertainty.

Stage	1	2	3	4
$\mathcal{L}$ at 250 GeV(fb^{-1})	250	250	250	1150
$\mathcal{L}$ at 500 GeV(fb^{-1})		500	500	1600
$\mathcal{L}$ at 1000 GeV(fb^{-1})			1000	2500

Table 19: Integral luminosities obtained on the different stages of the ILC [103].

As a first approximation to obtain the $B_\gamma(m_t, \zeta_{S'_\gamma})$ sensitivity, assuming a linear dependency with the top-quark mass, the relation 54 can be used to evaluate a dependency parameter α. Several samples with high statistics [3] have been generated with PYTHIA8. One of these samples has been taken as a reference ($m_{t_{ref}} \rightarrow B_{ref}$). Afterwards, the distances to the other samples ($\Delta m_t = m_t - m_{t_{ref}} \rightarrow \Delta B = B_{m_t} - B_{ref}$) can be calculated, bin by bin. Finally, the dependency parameters, per bin (α), have been obtained.

$$\frac{\Delta B}{B_{ref}} = \alpha \frac{\Delta m_t}{m_{t_{ref}}} \tag{54}$$

On the other hand, B_{ref} can be also calculated through the $\sigma_{t\bar{t}\gamma}$. The cross-section is provided by the MC tool, using as a Monte Carlo input mass the $m_{t_{ref}}$. The relation $B_{ref} = \sigma_{t\bar{t}\gamma}\mathcal{L}$ provides the total number of expected events, where $\mathcal{L}$ represents the expected luminosity shown on table 19. The observable uncertainty ΔB is defined as the B statistical uncertainty ($\Delta B = \sqrt{B}$). Finally, the top-quark mass uncertainty (Δm_t) can be extrapolated using the equation 55.

$$\Delta m_t = \frac{\Delta B}{B_{ref}} \frac{m_{t_{ref}}}{\alpha} \tag{55}$$

The stages shown in table 19 represent the different energy steps that ILC will go over [4]. The sensitivity (Δm_t) has been evaluated for all ILC stages , considering integral luminosities ($\mathcal{L}$) of $500 fb^{-1}$, $1000 fb^{-1}$ and $2600 fb^{-1}$. On figure 104 the reference mass used was $m_t = 170$ GeV, the other masses were compared, independently, to the reference. The sensitivity values have been obtained bin by bin. As expected, the region with maximum resolution is located near the threshold region. It is important to notice that, in the MC tools, top-quark mass is not represented as a delta function, but a Breit-Wigner function. Therefore, for each mass, there is a small tail beyond the expected cut-off.

3 To obtain the dependency parameter α, the statistical fluctuations have to be minimized

4 Stage 1: up to 250 GeV. Stage 2: up to 500 GeV. Stage 3: up to 1000 GeV. Stage 4: To increase the accumulated luminosity in all energies.

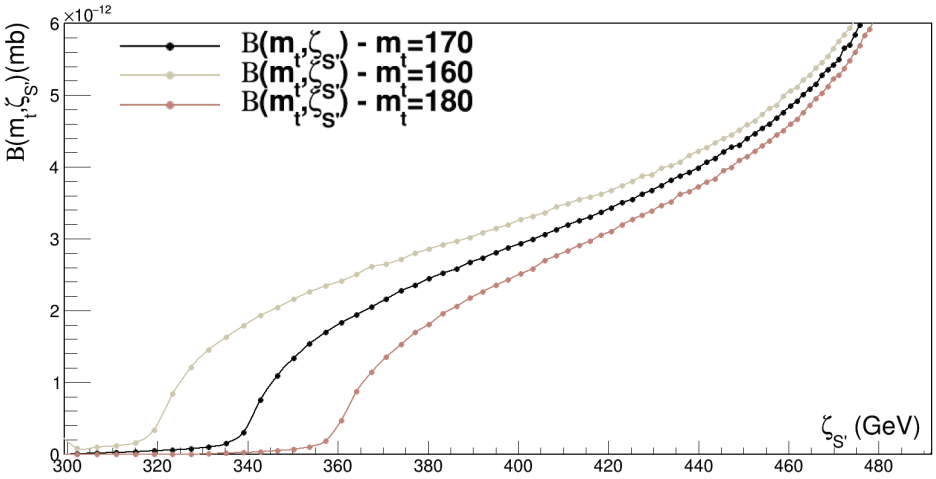

Figure 100: $B_\gamma(m_t, \zeta_{S'_\gamma})$ comparison using different top-quark masses (upper plot). Lower plot shows the sensitivity per bin, using as reference $m_t = 170$ GeV.

Since the resolution obtained is bin by bin independent, the total potential sensitivity can be calculated using the weighted average of all bin values. Moreover, each distribution compared to the reference will provide the same estimation of the sensitivity, which can be slightly different from one mass to another, therefore, several masses were evaluated and the final value was obtained averaging all of them. The results are presented in table 20.

	500 fb^{-1}	1000 fb^{-1}	2600 fb^{-1}
Number of Events:	295.000	589.000	1.532.000
$B_\gamma(m_t, \zeta_{S'_\gamma})$ Sensitivity:	0.14 GeV	0.10 GeV	0.062 GeV

Table 20: $B_\gamma(m_t, \zeta_{S'_\gamma})$ potential sensitivity considering only the statistical fluctuation effects and the total number of useful events expected, using the maximum luminosity expected on the ILC stages at 500 GeV.

The maximum resolution achievable with $B_\gamma(m_t, \zeta_{S'_\gamma})$ goes up to 60 MeV, way below the methods currently used in hadron colliders and in the same order of the threshold measurements on the ILC, however, this estimation is very unrealistic and no detector or particles level effects are included, but shows that the study is worth and the physics potential high. Moreover, the FSR radiation has not been considered and its inclusion will increase, even more, the expected sensitivity when combine them.

The inclusion of the FSR gluon, also at parton level, will require the implementation of a more robust method to obtain the potential sensitivity. The solution was to use a fit calculation. Nevertheless, since a theoretical distribution was not available yet, an approximation, as exact as possible, had to be implemented. To do this, a template fit was applied.

To prove the feasibility of this method, expecting to obtain same results as the previous study, first, only the ISR radiation was included. To construct the template, a set of distributions with high statistics were simulated, at partonic level. These pseudo-theoretical distributions were generated with a top-quark masses from 160 GeV to 180 GeV in steps of 1 GeV (Fig. 101).

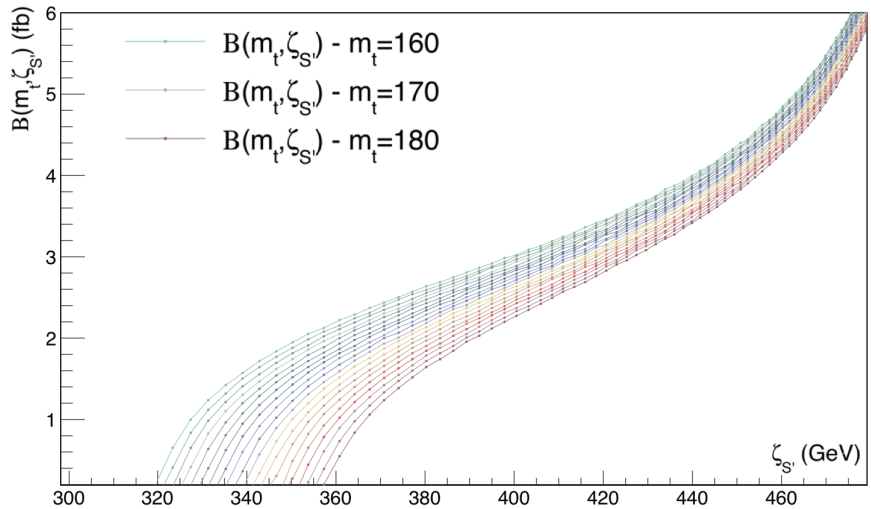

Figure 101: $B_\gamma(m_t, \zeta_{S'_\gamma})$ pseudo-theoretical distributions. m_t steps from 160 GeV to 180 GeV in steps of 1 GeV

To perform the template fit, an extrapolation of the intermediate top-quark mass positions were required. In order to do this, in each bin, $B(m_t, \zeta_{S'})$ has been considered as a function of the top-quark mass. Then, a "spline" extrapolation method has been implemented.

The data sets were generated using a Monte Carlo top-quark mass of 173.1 GeV and including the maximum accumulated luminosity expected on each ILC stage (Tab. 19). Several data-sets were fitted using TMinuit [104]. The minimized parameter (fitted mass) from each data-set was plotted on a histogram. The $B_\gamma(m_t, \zeta_{S'_\gamma})$ sensitivity was obtain via the RMS (root mean square) of this distribution. An example of these fits is shown on figure 102 (left) together with the corresponding final histogram (right).

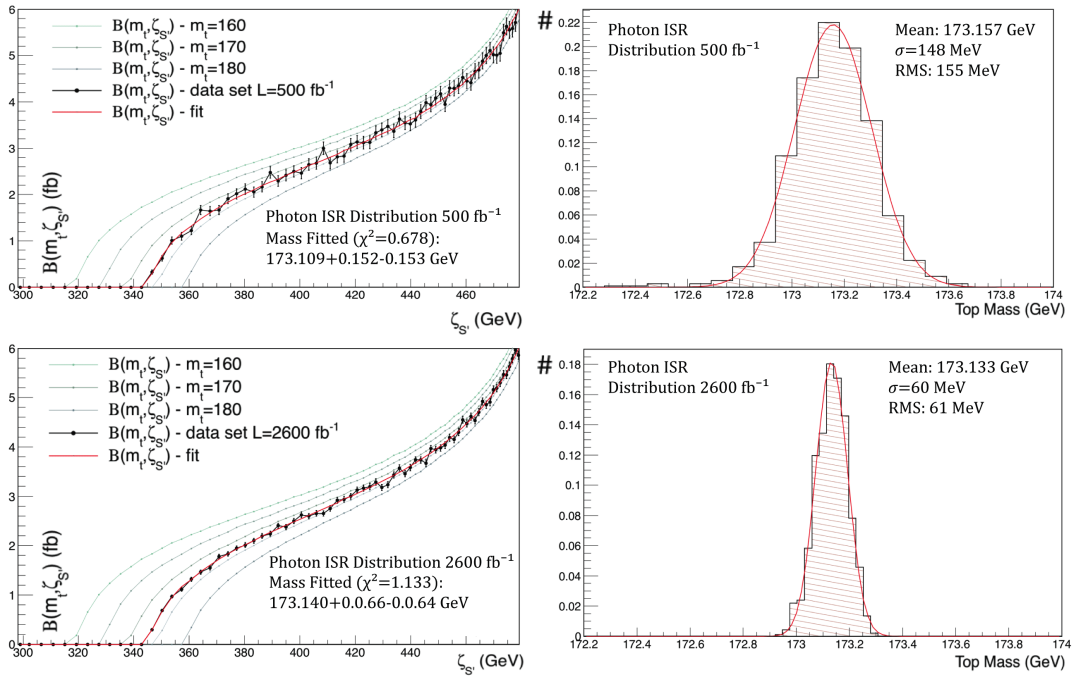

Figure 102: Examples of $B_\gamma(m_t, \zeta_{S'_\gamma})$ fit. Right: Fit at 500 fb^{-1} (above) and 2600 fb^{-1} (below). Left: Resulting m_t dispersion distribution of the minimized masses, at 500 fb^{-1} (above) and 2600 fb^{-1} (below). The uncertainty on the masses measurement correspond the width of the distribution.

Table 21 shows the resulting sensitivity (right column) on the different ILC stages. The results are equivalent to the values shown in table 20. The m_t (GeV) is given by the mean value of the distribution of the fitted masses.

Stage	$\mathcal{L}$ (fb^{-1})	m_t (GeV)	Δm_t (GeV)
2	500	173.15	0.15
3	1000	173.14	0.10
4	2600	173.133	0.061

Table 21: $B_\gamma(m_t, \zeta_{S'_\gamma})$ fit results considering the possible stages of the ILC. The m_t is the mean value of the top-quark mass fitted. The uncertainty or sensitivity is the RMS of all fitted masses obtained.

8.3 *FSR gluon inclusion*

After implementing the fit method, an analogous study to ISR has been performed to include the FSR radiation. The top-quark pair, can emit gluons or photons. However, the gluon emission (strong interaction) is much more common than the photon emission (electromagnetic interaction), therefore, at this step only the FSR gluon will be considered.

The aim of this study was to obtain a rough estimation of the potential sensitivity. Considering that the experimental identification of the gluon is much more challenging and requires the use of jet algorithms, the first study will be carried on, at parton level, using the gluon energy defined by the Monte Carlo, as an approximation.

The definition of the observable $B_g(m_t, \zeta_{S'_g})$ has been done in terms of an invariant variable and analogously to $B_\gamma(m_t, \zeta_{S'_\gamma})$ (Fig. 103). The invariant S'_g is adapted by using the energy of the gluon (E_g) (Eq. 56) and the observable $B_g(m_t, \zeta_{S'_g})$ has been wrote, as a function of the S'_g, as show equation 57.

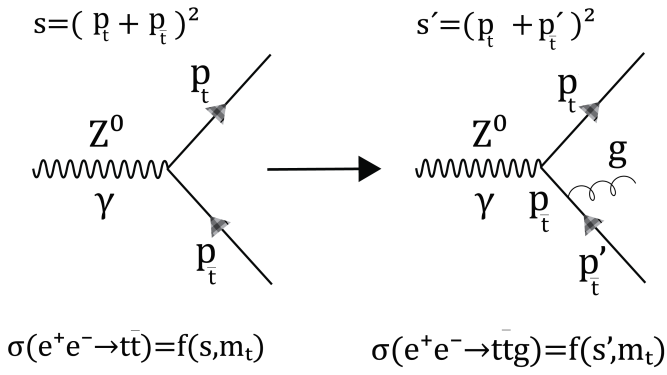

Figure 103: FSR gluon emission diagram.

$$S'_g = S\left(1 - \frac{2E_g}{\sqrt{S}}\right) \tag{56}$$

$$B_g(m_t, \zeta_{S'_g}) = \frac{d\sigma_{t\bar{t}g}}{d\zeta_{S'_g}} \rightarrow \zeta_{S'_g} = \sqrt{S'_g} \tag{57}$$

8.3.1 $B_g(m_t, \zeta_{S'_g})$ *potential sensitivity - Parton Level*

The template fit method was also applied only to the FSR gluon. The pseudo-theoretical distributions matrix was created (template), from 160 GeV to 180 GeV in steps of 1 GeV

(Fig. 104). Then, sets of data, with the expected statistics (Tab. 19) were generated, using a Monte Carlo top-quark mass of 173.1 GeV. Finally, the data-sets were fitted with the pseudo-theoretical distributions. The $B_g(m_t, \zeta_{S'_g})$ sensitivity was obtained using the RMS of the distribution of minimized masses. An example of these fits is shown on figure 105 (left) and its corresponding histogram (right).

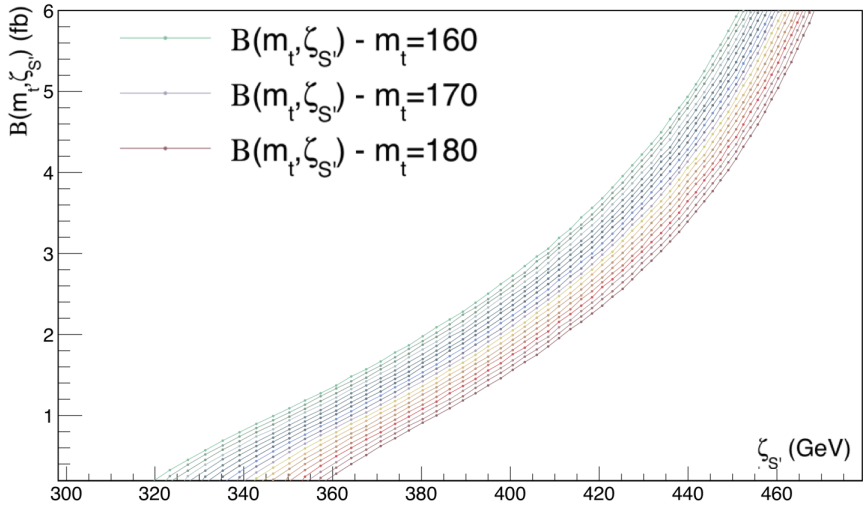

Figure 104: $B_g(m_t, \zeta_{S'_g})$ pseudo-theoretical distributions. m_t steps from 160 GeV to 180 GeV in steps of 1 GeV

Table 22 summarize the results obtained with $B_g(m_t, \zeta_{S'_g})$, which sensitivity is slightly better than $B_\gamma(m_t, \zeta_{S'_\gamma})$. Notice that both measurements, $B_\gamma(m_t, \zeta_{S'_\gamma})$ and $B_g(m_t, \zeta_{S'_g})$, are performed independently, therefore, the sensitivity can be better if both observable are combined.

Stage	$\mathcal{L}$ (fb^{-1})	m_t (GeV)	Δm_t (GeV)
2	500	173.15	0.13
3	1000	173.127	0.092
4	2600	173.114	0.057

Table 22: $B_g(m_t, \zeta_{S'_g})$ fit results considering the possible stages of the ILC. The m_t is the mean value of the top-quark mass fitted. The uncertainty or sensitivity is the RMS of all fitted masses obtained.

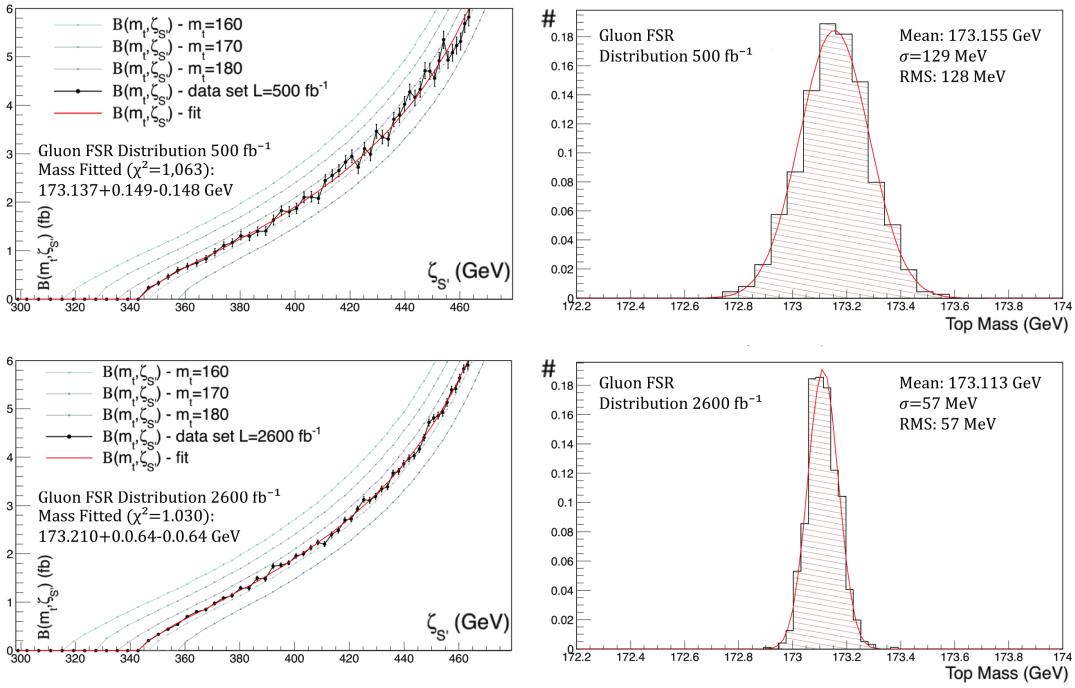

Figure 105: Examples of $B_g(m_t, \zeta_{S'_g})$ fit. Right: Fit at 500 fb^{-1} (above) and 2600 fb^{-1} (below). Left: Resulting m_t dispersion distribution of the minimized masses, at 500 fb^{-1} (above) and 2600 fb^{-1} (below). The uncertainty on the masses measurement correspond the width of the distribution.

8.3.2 *Combined potential sensitivity*

The combined measurement has been performed by extracting both distributions from the same data-sets. In this case, the fit has been done using on both distributions the same parameter to minimize (the top-quark mass). Then, analogously to the previous test, the final sensitivity has been obtain as the RMS of the distribution of minimized masses. Table 23 shows a summary of the results.

The combined observable is much more sensitive to the top-quark mass, resulting in a maximum resolution achievable around 40 MeV. As was mentioned, the value obtain is very unrealistic, but the aim of the study was to show the potential resolution archivable in an ideal situation were only the statistical limitations are considered.

Stage	$\mathcal{L}$ (fb^{-1})	m_t (GeV)	Δm_t (GeV)
2	500	173.15	0.10
3	1000	173.136	0.069
4	2600	173.124	**0.042**

Table 23: Combined results performing a simultaneous fits of $B_\gamma(m_t, \zeta_{S'_\gamma})$ and $B_g(m_t, \zeta_{S'_g})$, considering the possible stages of the ILC. The m_t is the mean value of the top-quark mass fitted. The uncertainty or sensitivity is the RMS of all fitted masses obtained.

8.3.3 *Beam Polarization Contribution*

An important feature of the ILC, is the possibility to use polarized beams. The cross section of $e^+e^- \to t\bar{t}$ production depends on this polarization. In the previous studies, the beams have been considered unpolarized, expecting a cross section $\sigma_{unpol} = 572$ fb. But, in reality, the ILC will use polarized beams (i.e. $p_{e^-} = +80\%$, $p_{e^+} = -30\%$) [100], which will increase the production rates:

- Unpolarized $\to \sigma_{unpol} = 572$ fb.
- $p_{e^-} = -80\%$, $p_{e^+} = +30\% \to \sigma_{-80+30} = 940$ fb.

The polarized beams scenario will be advantageous for $B(m_t, \zeta_{S'})$ observable since it will increase the available statistics. However, to prove that the polarization does not have any effect on the distribution shape, as a cross check, the $B_\gamma(m_t, \zeta_{S'_\gamma})$ distribution was generated with Whizard Monte Carlo tool on these polarization scenarios. Figure 106 shows the comparison of both scenarios. Both distributions are equivalent, therefore, the polarization of the beams can only be considered as an increment on the production cross section. Table 24 shows a summary of the maximum resolutions expected using polarized beam.

Stage	$\mathcal{L}$ (fb^{-1})	Δm_t (GeV)
2	500	~ 0.080
3	1000	~ 0.055
4	2600	$\sim$ **0.035**

Table 24: Combined results ISR/FSR at partonic level. It considers polarized beams ($p_{e^-} = +80\%$, $p_{e^+} = -30\%$) in a possible stages of the ILC.

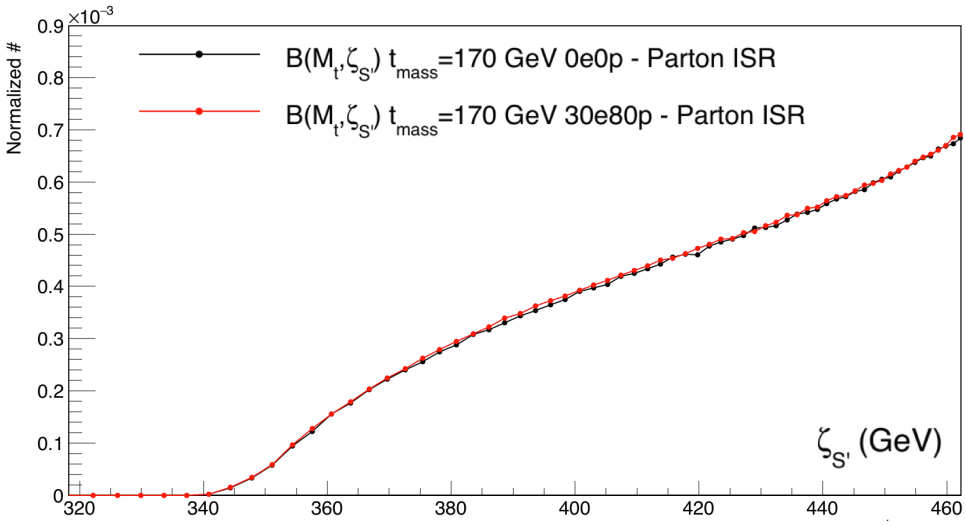

Figure 106: Comparison of $B_\gamma(m_t, \zeta_{S'_\gamma})$ in two polarization scenarios. $p_{e^-} = +80\%$, $p_{e^+} = -30\%$ (red) and unpolarized (black)

8.4 *Running mass of the top quark*

The definition of running mass has been introduced on Section 7.1. In summary, the mass is considered as a couplings on the QCD Lagrangian. Therefore, when the theory is being renormalized, the mass gets dependencies with the energy scale.

Since the observable $B(m_t, \zeta_{S'})$ does not require a specific interaction energy to be applied, the top-quark pairs are generated on a range of energy scales. For this reason, enclosing the energy of the radiated particle, the $t\bar{t}$ production energy (S') will be also enclosed on a scale range. To do this, the $B(m_t, \zeta_{S'})$ distribution can be divided in several regions (See Fig. 107 - left). The available interaction energy (S') will be confined on these range of energies and hence the energy of the top-quark pair created. In this case, the sensitivity of the $B_\gamma(m_t, \zeta_{S'_\gamma})$ can be propagated to the measure of the running mass, fitting only these specific section of energies. The *scale*, to calculate the running mass, is defined as the weighted average of S' in the range. To obtain the running mass values, the package used was C++ CRunDec [105].

Figure 107 shows the ISR distribution divided in regions, were independent template fits have been performed. The method applied to obtain the sensitivity is the same as Section 8.3. In this case, the fit is applied independently on the regions of interest. The plot on the right, in figure 107, shows the expected running mass (black dots) on each section and its error bar, which represents the sensitivity. The fits were performed considering an accumulated luminosity of 2600 fb^{-1}. The final results are shown in table 25, where "Run. m_t" represents the mean value of the distribution of minimized

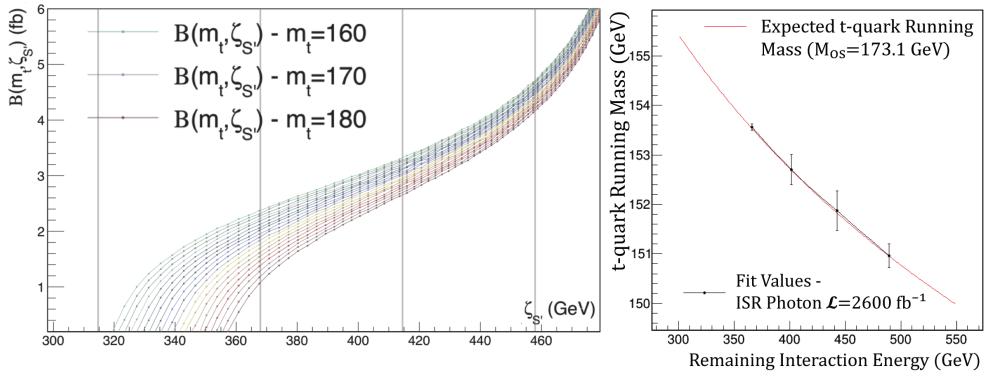

Figure 107: Left: Pseudo-theoretical distributions of $B_\gamma(m_t, \zeta_{S'_\gamma})$. The vertical lines are the division of the $B_\gamma(m_t, \zeta_{S'_\gamma})$ regions used to perform the fit. Right: the corresponding running mass obtained at $2600 fb^{-1}$. The black dots represent the mean mass obtained on the fits, considering the selected $B_\gamma(m_t, \zeta_{S'_\gamma})$ regions and the sensitivity is represented with the error bars. They have been plotted over the expected top-quark running mass calculated in the range of scales with a $m_{t_{OS}} = 173.1 GeV$ (red line).

masses, on the corresponding range, "Run. Δm_t" is the RMS of all fitted masses obtained on the same region, and "Sigma" represents the distance in $\sigma = \Delta m_t$ to the reference mass.

Scale S′(GeV)	Run. m_t (GeV)	Run. Δm_t (GeV)	Sigma
~ 360	153.7	0.062	Ref.
~ 400	152.7	0.30	3.3σ
~ 440	151.9	0.39	4.5σ
~ 490	150.9	0.24	11.6σ

Table 25: Resulting $B_\gamma(m_t, \zeta_{S'_\gamma})$ running mass sensitivity on the selected regions. The remaining interaction energy is the weighted average of S′, the running m_t, is the running mass obtained on the corresponding scale and the running Δm_t is the sensitivity on the selected region.

The study was repeated with the FSR gluon ($B_g(m_t, \zeta_{S'_g})$), using the same method (Fig. 108). The resulting sensitivities, considering an accumulated luminosity of 2600 fb^{-1}, are show in table 26.

This section has proved the capacity of $B(m_t, \zeta_{S'})$ to obtain the top-quark mass in a full range of energies, that can be translated in a multiple scales to obtain the top-quark

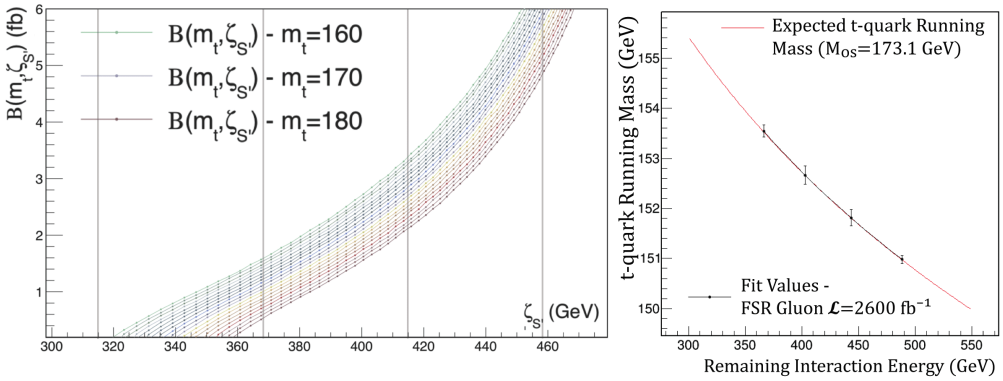

Figure 108: Left: Pseudo-theoretical distributions of $B_g(m_t, \zeta_{S'_g})$. The vertical lines are the division of the $B_g(m_t, \zeta_{S'_g})$ regions uses to perform the fit. Right: the corresponding running mass obtained at $2600 fb^{-1}$. The black dots represent the mean mass obtained on the fits,considering the selected $B_g(m_t, \zeta_{S'_g})$ regions and the sensitivity is represented with the error bars. They have been plotted over the expected top-quark running mass calculated in the range of scales with a $m_{t_{OS}} = 173.1 GeV$ (red line)

Scale S'(GeV)	Run. m_t (GeV)	Run. Δm_t (GeV)	Sigma
~ 360	153.5	0.11	Ref.
~ 400	152.7	0.18	4.4σ
~ 440	151.8	0.16	10.4σ
~ 490	150.9	0.077	33.6σ

Table 26: Resulting $B_g(m_t, \zeta_{S'_g})$ running mass sensitivity on the selected regions. The remaining interaction energy is the weighted average of S', the running m_t, is the running mass obtained on the corresponding scale and the running Δm_t is the sensitivity on the selected region.

running mass. It has been proved that $B(m_t, \zeta_{S'})$ has the potential to be sensitive to these changes, even performing the two studies separately for ISR and FSR gluon. In both cases, the sensitivity is enough to distinguish the variation of the running mass in different scales.

8.5 *Summary*

This chapter has introduced a new observable, $B(m_t, \zeta_{S'})$ to measure the mass of the top-quark using the cross section of the $e^+e^- \to t\bar{t}+\gamma$ (ISR and FSR) and $e^+e^- \to t\bar{t}+g$

(FSR) radiative events. $B(m_t, \zeta_{S'})$ **provides sensitivity to the top-quark mass in a large range of production energies, which allows a mass definition in a good renormalization system.** The template fits performed, at partonic level, using PYTHIA8 Monte Carlo tool, proved its high physics potential, achieving **resolutions up to 40** MeV **(35** MeV **considering polarized beams)**, well below the methods currently used in hadron colliders and in the same order of the threshold measurements on the ILC. Moreover, Section 8.4 proved the $B(m_t, \zeta_{S'})$ capacity to be sensitive to the running of the top-quark mass. Next steps consist in increasing, sequentially the realism of the studies, including simulations at particle level and detector and accelerator effects.

9 Towards a realistic study: $B_\gamma(m_t, \zeta_{S'_\gamma})$ at particle level

The studies at parton level presented in Chapter 8 have evaluated the physics potential of the $B(m_t, \zeta_{S'})$ observable to measure the top-quark mass. The results obtained, encouraged the study to be pursued increasing its realism and complexity. To approach a more realistic study, next steps required the inclusion of the hadronization and the basic detector effects. In this chapter, the ISR photon will be studied at particle level, and likewise the influence of the selection process. Some detector and accelerator induced effects will also be evaluated. Moreover, the study will be extended to several operation energies and luminosities, considering the CLIC and ILC physics program.

9.1 *ISR at Particle Level - Photon Selection*

The study presented in this section intends to explore the $B(m_t, \zeta_{S'})$ resolution, only considering the ISR photon, in a more realistic approach. The simulations have been performed at particle level, to include the effects of the selection process and the detector acceptance. The samples have been generated using PYTHIA8, considering, at first, the ILC program at 500 GeV, and then extending the study to CLIC - 380 GeV and ILC - 1000 GeV.

As was introduced on Section 7.3, the photon emission is collinear to the emitter particle. Hence, it is expected that majority of photons emitted, by the incident beams, will have a very low polar angle and, probably, will not be detected. Therefore, the coverage of the forward and backward photon detectors is of crucial importance for this analysis, with a considerable impact on the final resolution.

A simulation was performed to quantify the number of photons going out of the detectors acceptance. In order to do this, a scan over the coverage angle (θ_{min} [1]) was done, obtaining the percentage of ISR photons accepted as a function of this angle. Figure 109 shows the percentage of photons emitted that can be observed by the detector. Notice, that a high percentage of the photons will be lost. Therefore, to include this limitation on the study, an acceptance cut has to be defined. Considering that the ILD coverage angle is in the order of 7° [57], the θ_{min} defined and applied, from now on, will be 7°, which results on a percentage of photons lost around ~ 75% [2].

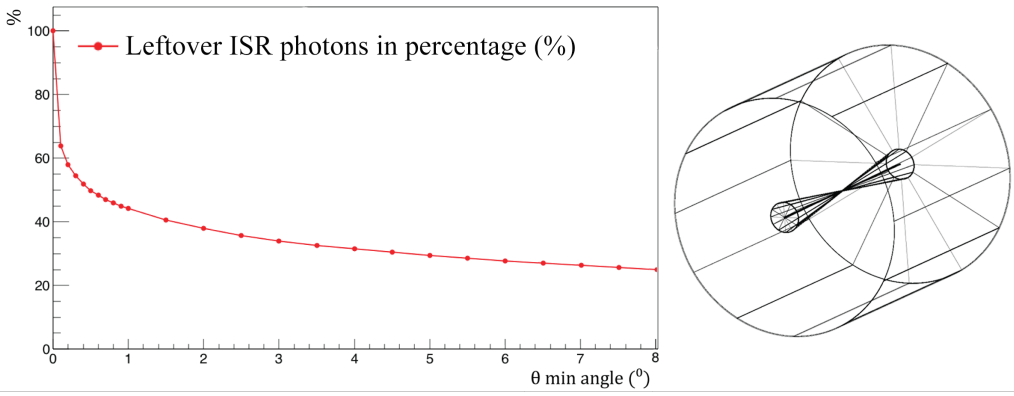

Figure 109: Rigth: remaining ISR photons on the sample as a function of the angle to the center of the beam-pipe (θ). Left: scheme of a general detector coverage, where particles flowing inside the internal cones are excluded.

The process followed to obtain the $B_\gamma(m_t, \zeta_{S'_\gamma})$ resolution started with the simulation, at particle level, of $e^+e^- \to t\bar{t} + \gamma$. In this case, the efficiency of $t\bar{t}$ reconstruction has not been considered, the goal of this study was to determine if it is possible to perform an efficient selection process. After generating the samples, all out-of-coverage particles were removed from the list.

The selection criteria implemented to select the final ISR photons had to consider the emission characteristics. As was mentioned on Section 8.4, the most sensitive part of the distribution corresponds to the most energetic photons, therefore, a requirement on the minimum energy will not affect significantly the sensitivity, but will reduce the background substantially. Moreover, the ISR photon emission happens alone and, usually, only a single photon is emitted. It is not expected to have ISR photons included in a jet of particles, therefore, the photon isolation angle will be a good criteria to exclude

1 θ is the polar angle between center of the beam-pipe and the line segment on the direction of the outgoing particle.

2 This percentage depends on the interaction energy: CLIC-380 ~ 71%, ILC-500 ~ 75% and ILC-1000 ~ 79%.

photons generated on an electromagnetic cascade [3]. However, some other photons will get over the cuts, the origin of these background photons are multiple, they can be produced on the beam-beam interaction; coming from the final state radiation of the top quark; or maybe photon emitted by top decay products (This will be covered later). To choose the optimum values for the selection criteria, scans have been performed (Fig. 110), evaluating the background photons reduction efficiency (black) and the percentage of ISR outlasting the cut (red).

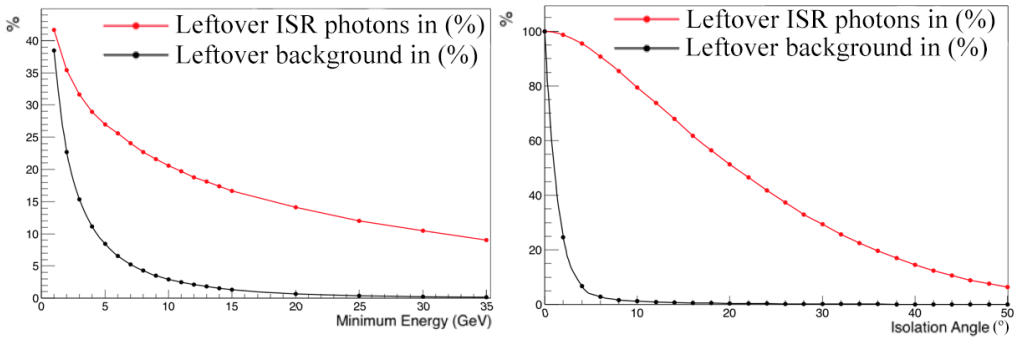

Figure 110: ILC 500 GeV scans. In red, leftover photons after applying the cut, in black, remaining background. Rigth: Scan over the minimum energy of the photons. Left: Scan over the isolation angles of the photons.

The selection criteria are applied sequentially. Considering only the particles inside the detector coverage:

- **First Step (energy cut):** It has been fixed at 10 GeV. The background reduction will be ~ 97%. The ISR photons rejected will go up to ~ 79% [4]
- **Second step (selection via isolation angle):** It is applied to the remaining photons from first cut. The isolation angle has been fixed on 8^{o} [5]. This will reduce the remaining background up to ~ 98% and will reject around 15% of ISR photons.

The calculation of the $B_{\gamma}(m_t, \zeta_{S'_{\gamma}})$ sensitivity, at particle level, has been carried out using the fit method presented on Section 8.3. Data-sets with a top-quark Monte Carlo mass of 173.1 GeV were generated. The selection criteria have been applied over these samples. The photons outlasting the cuts were used to construct the $B_{\gamma}(m_t, \zeta_{S'_{\gamma}})$ distribution. Finally, the pseudo-theoretical curves were used to perform the fits. Table 27 shows the mean mass obtained and its uncertainties, considering the ILC schedule presented, in 2013, by Howard E. Haber during the LCWS13 in Tokio (Japan) [103]. Table 28 presents the same results but considering the ILC schedule presented, in 2015,

3 The isolation angle is taken as the minimum angle between the photon and the closest particle

4 The ISR photons rejected belong to the $B_{\gamma}(m_t, \zeta_{S'_{\gamma}})$ region with minimum sensitivity, therefore, the consequences over the resolution are not such big.

5 It means that any other particle should appear inside the solid angle with radius 8^{o}.

by J. Brau during PAC Meeting in Osay (Japan) [106] .

Stage	$\mathcal{L}$ (fb^{-1})	m_t (GeV)	Δm_t (GeV)
2	500	173.327	0.29
3	1000	173.223	0.21
4	2600	173.143	0.12

Table 27: ILC 500 GeV results, obtained with the ISR photons selected. The m_t is the mean value of the top-quark mass fitted. The uncertainty or sensitivity is the RMS of all fitted masses. ILC schedule presented, in 2013, by Howard E. Haber during the LCWS13 in Tokio (Japan)

Stage	$\mathcal{L}$ (fb^{-1})	m_t (GeV)	Δm_t (GeV)
2	500	173.327	0.29
3	4000	173.122	0.10

Table 28: ILC 500 GeV results, obtained with the ISR photons selected. The m_t is the mean value of the top-quark mass fitted. The uncertainty or sensitivity is the RMS of all fitted masses. ILC schedule presented, in 2015, by J. Brau during PAC Meeting in Osay (Japan)

The results show that $B_\gamma(m_t, \zeta_{S'_\gamma})$ is still very sensitive, considering that only the ISR photons were used.

9.1.1 *CLIC physics program and ILC extended physics program*

The interaction energy is another parameter that influences on the $B_\gamma(m_t, \zeta_{S'_\gamma})$ sensitivity. Equivalent analysis have been performed considering the CLIC conditions with an interaction energy of 380 GeV. Also, a higher energy scenario has been included with the ILC at 1000 GeV physics program. The studies have been done analogously to ILC 500 GeV scenario. First, an optimization of the selection parameters was carried out (Fig. 111 and Fig. 112). Then, the pseudo-theoretical distributions were generated with a top quark mass from 160 GeV to 180 GeV in steps of 1 GeV. Afterwards, data-sets with the expected statistic, at particle level and using a Monte Carlo top-quark mass of 173.1 GeV were created. The selection criteria was applied to obtain the $B_\gamma(m_t, \zeta_{S'_\gamma})$. Finally, the pseudo-theoretical curves were used to perform the fits.

The selection criteria are applied sequentially, considering only the particles inside the detector coverage. On the CLIC 380 GeV scenario:

- **First Step (energy cut):** It has been fixed at 3 GeV. The background reduction will be ~ 76%. The ISR photons rejected will go up to ~ 53%
- **Second step (selection via isolation angle):** It is applied to the remaining photons from first cut. The isolation angle has been fixed on 8º This will reduce the remaining background up to ~ 95% and will reject around 15% of true ISR photons.

On the ILC 1000 GeV scenario:

- **First Step (energy cut):** It has been fixed at 30 GeV. The background reduction will be ~ 99%. The ISR photons rejected will go up to ~ 75%
- **Second step (selection via isolation angle):** It is applied to the remaining photons from first cut. The isolation angle has been fixed on 4º This will reduce the remaining background up to ~ 98% and will reject around 5% of true ISR photons.

The results obtained, considering the corresponding integrated luminosity on each possible stage, are shown in table 29 (CLIC 380 GeV) and table 30 (ILC 1000 GeV).

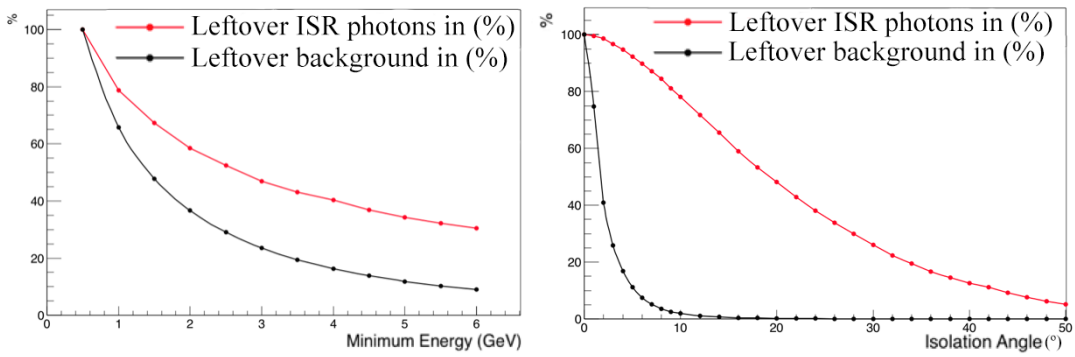

Figure 111: CLIC 380 GeV scans. In red, leftover photons after applying the cut, in black, remaining background. Rigth: Scan over the minimum energy of the photons. Left: Scan over the isolation angles of the photons.

Stage	$\mathcal{L}$ (fb^{-1})	m_t (GeV)	Δm_t (GeV)
1	500	173.141	0.10

Table 29: CLIC 380 GeV results, obtained with the ISR photons selected. The m_t is the mean value of the top-quark mass fitted. The uncertainty or sensitivity is the RMS of all fitted masses.

The $B_\gamma(m_t, \zeta_{S'_\gamma})$ sensitivity decreases as the available energy increases. Notice that the resolution obtained at 380 GeV, with 500 fb^{-1}, is comparable to the value obtained

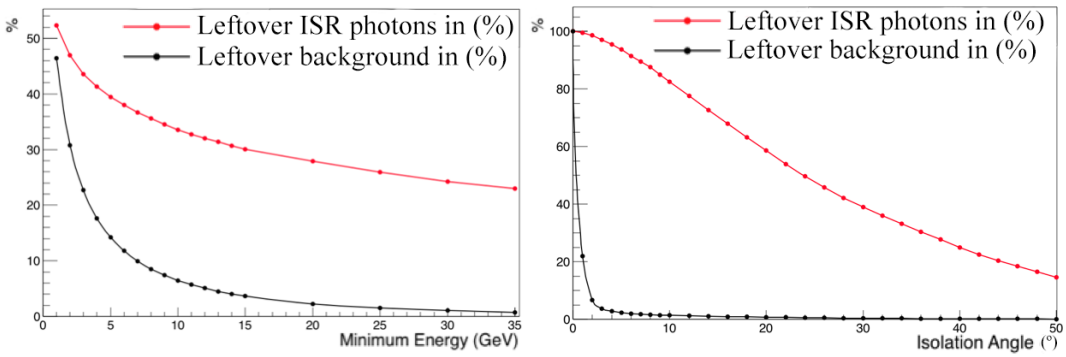

Figure 112: ILC 1000 GeV scans. In red, leftover photons after applying the cut, in black, remaining background. Rigth: Scan over the minimum energy of the photons. Left: Scan over the isolation angles of the photons.

Stage	$\mathcal{L}$ (fb^{-1})	m_t (GeV)	Δm_t (GeV)
3	1000	173.381	0.63
4	3500	173.197	0.38

Table 30: ILC 1000 GeV results, obtained with the ISR photons selected. The m_t is the mean value of the top-quark mass fitted. The uncertainty or sensitivity is the RMS of all fitted masses.

at 500 GeV, using 4000 fb^{-1}. The resolution decreases even more if the interaction energy goes up to 1000 GeV. This happens due to the lessening of the production rates of $e^+e^- \to t\bar{t}$ as the energy grows. In case of unpolarized beams, the cross section of $e^+e^- \to t\bar{t}$ production at 380 GeV is around 520 fb in front 210 fb at 1000 GeV. Moreover, also important is the losses of photons due to the acceptance angle effect, which is bigger at high energies.

9.1.2 *Full Range Running Mass*

One advantage of having access to higher interaction energy ranges is the opportunity to perform the study of the"running of the top-quark mass", extending the range of energies. Despite it has been proved that larger interaction energies are unprofitable for the $B_\gamma(m_t, \zeta_{S'_\gamma})$ sensitivity, the results presented for ILC-1000 GeV are even better than present LHC results. Therefore, the idea of this section was to repeat same study as the one presented on Section 8.4 but at particle level and including these larger range of energy scales.

Same method has been applied to the different interaction energy scenarios. The $B_\gamma(m_t, \zeta_{S'_\gamma})$ distributions were divided in several regions, the divisions strategy depends on the energy range available and the potential resolution on that specific region. For instance, on CLIC - 380 GeV scenario, only one region of 65 GeV was considered, from $\zeta_{min} = 315$ GeV $\rightarrow \zeta_{max} = 380$ GeV. On the other hand, on ILC - 1000 GeV scenario, two regions of 320 GeV were applied; region one: $\zeta_{min} = 320$ GeV $\rightarrow \zeta_{max} = 640$ GeV; region two: $\zeta_{min} = 640$ GeV $\rightarrow \zeta_{max} = 960$ GeV. Individual fits were performed in each region. The scale, to calculate the running mass, is defined as the weighted average of $\zeta_{S'}$ in the selected range. The distributions were constructed at particle level and including the limitation of the detector acceptance angle. In each case, the higher available luminosity was used to calculate the maximum sensitivity achievable. Figure 113 shows the mean mass and the sensitivity of the three interaction energies, compared to the expected top-quark running mass (red) calculated with $m_{t_{OS}} = 173.1$ GeV.

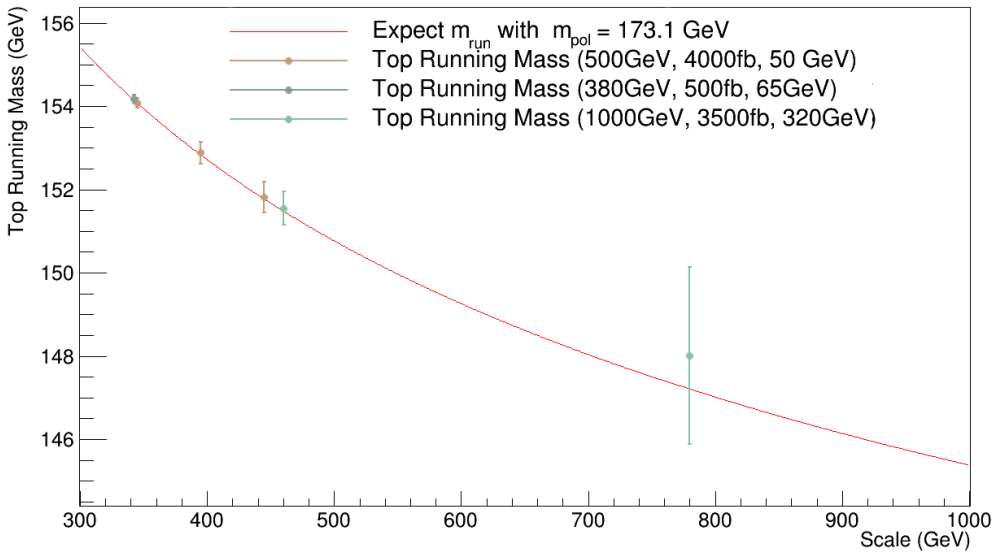

Figure 113: Top-quark running mass obtained considering multiple interaction energies, at particle level. The sensitivity is calculated in the defined $B_\gamma(m_t, \zeta_{S'_\gamma})$ regions.

The results are summarized on table 31. Starting from left column: the interaction energy and the expected luminosity applied; the scale used to calculate the running mass of the top quark; the mean top-quark mass obtained fitting only on the specific region; expected uncertainty obtained with RMS of all fitted masses; distance to the reference value in sigmas ($\sigma = \Delta m_t$). As was expected, the resolution at larger scales is worse compared to the threshold region.

Int. En. (GeV)	Scale S′ (GeV)	Run. m_t (GeV)	Run. Δm_t (GeV)	Sigma
380($500fb^{-1}$)	~342	154.2	0.096	Ref.
500($4000fb^{-1}$)	~345	154.0	0.11	1.8σ
500($4000fb^{-1}$)	~395	152.9	0.26	4.9σ
500($4000fb^{-1}$)	~445	151.8	0.36	6.5σ
1000($3500fb^{-1}$)	~460	151.5	0.41	6.6σ
1000($3500fb^{-1}$)	~780	148.0	2.13	2.9σ

Table 31: $B_\gamma(m_t, \zeta_{S'_\gamma})$ running mass sensitivity on the selected regions, with multiple interaction energies, at particle level. The running m_t is the running mass obtained on the corresponding scale and the running Δm_t is the sensitivity on the selected region.

9.2 *First estimation of Systematic errors - Whizard*

The $B_\gamma(m_t, \zeta_{S'_\gamma})$ sensitivity has been obtained, at particle level, including the limitation of the selection process and the detector acceptance. This section intends to continue increasing the simulation realism to study other sources of uncertainty. To focus only in one energy of interaction the $e^+e^- \rightarrow t\bar{t} + \gamma$ events were generated at 500 GeV. In order to perform a more realistic simulation the Monte Carlo tool Whizard (Section 7.6) was implemented on the generation chain. Whizard is able to compute complete tree-level matrix elements on-line. But most important, it is capable to include the beamsstrahlung and smearing effect, to simulate the interaction in a real bunch crossing process. Moreover, Whizard uses a standard storage format (LCIO - Linear Collider I/O), which allows easier implementation to analyze the output and determine the source of the photons generated.

After the selection process, photons coming from several sources contribute to the $B_\gamma(m_t, \zeta_{S'_\gamma})$ distribution. It is important to perform a distinction between two main sources of distortion: the photons coming from the FSR radiation (they are sensitive to the top-quark mass) and other photons or background photons (it is not expect them to be sensitive to the top-quark mass). The origin of these background photons are multiple, they are photons produced on the beam-beam interaction, photon emissions due to top decay products or π^0 decays. The aim of this section is to study these two contributions a define an strategy to minimize their effects. Figure 114 shows all contribution to the $B_\gamma(m_t, \zeta_{S'_\gamma})$ distribution after the selection criteria. The distribution obtained with the leftover ISR photon is shown in green, it is compared with the MC partonic distribution (black); the contribution of the FSR photons (blue) and the final distribution, including all the photons (red), which becomes larger, on the region of low energy photons, due to the influence of the background photons (purple).

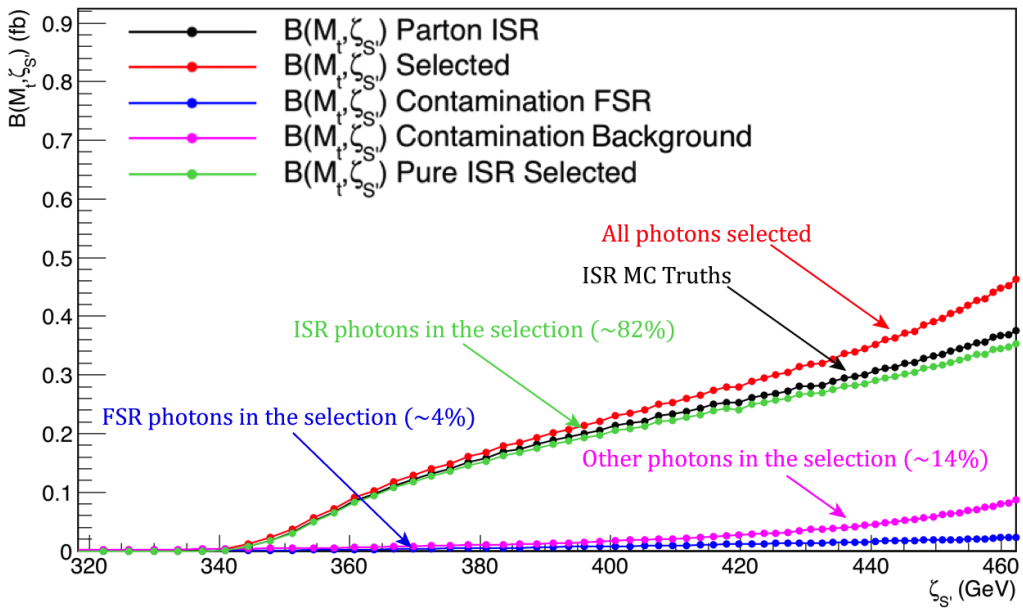

Figure 114: $B_\gamma(m_t, \zeta_{S'_\gamma})$ distribution separated in contributions. Red: All photons selected. Black: Parton level distribution. Green: Remaining ISR photons after applying the selection (84% compare to the parton distribution). Blue: FSR photons selected. Purple: Other photons selected.

9.2.1 *FSR Photon Contamination*

The FSR photon characteristics are very similar to the ISR photons, to determine if it is possible to distinguish them via selection criterions, the scans were repeated, separating the origin of the photon radiated. Figure 115 represents the energy scan, with the ISR photon percentage (black - purity on the sample, blue - total efficiency), the FSR photons (red) and the background contribution (purple). As figure 115 shows, in terms of min-energy cut, the FSR photons are indistinguishable from the rest of the ISR photons.

The isolation angle criterion has been applied to the photons that outlast the energy cut ($E_{min} = 30$ GeV). Figure 116 shows the scan over this cut. Again, the FSR photons seem to be also indistinguishable from the ISR photons. Therefore, considering an isolation angle of 5^o, the contamination from the FSR is around 4% on the final samples.

The FSR photons are irreducible from the ISR photons with the present selection cuts. However, find out a method to get rid of them, would be very costly in terms of $B(m_t, \zeta_{S'})$ sensitivity. On the other hand, FSR photons are also sensitive to the top-quark mass, but, since its emission is very suppressed due to the competition with the emission of the gluon, they are not so common. Considering that a double emis-

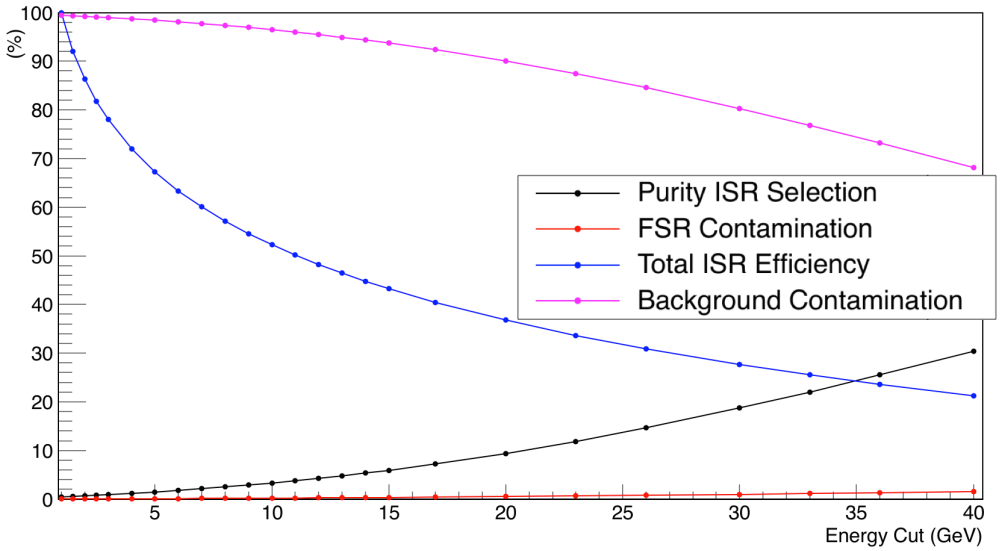

Figure 115: Scan over the minimum energy of the photons accepted (energy cut), at 500 GeV, using Whizard. Blue: the remaining ISR photons on the sample. Purple: the background contamination. Red: the remaining FSR photons on the sample. Black: Purity of the sample.

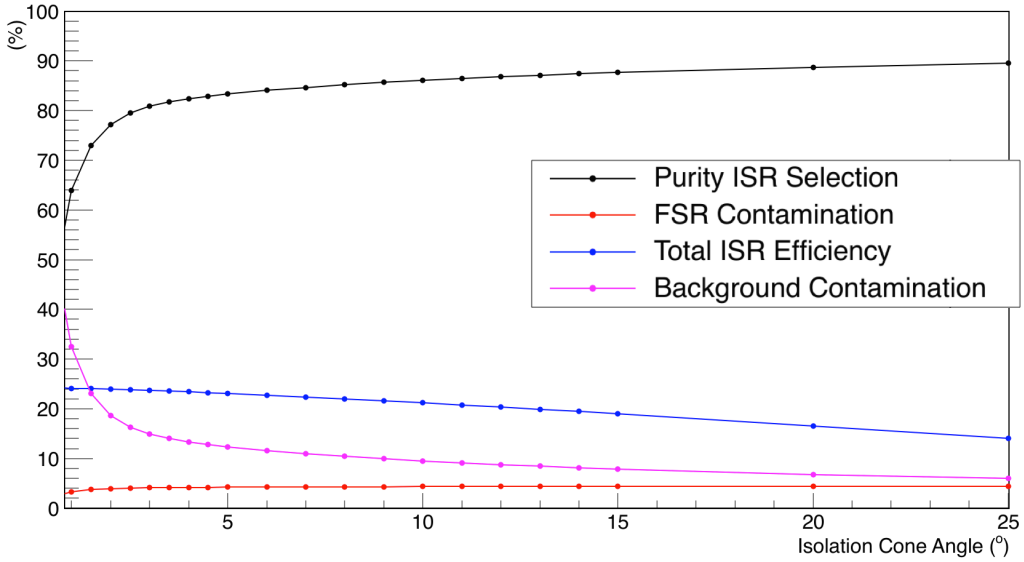

Figure 116: Scan over the isolation angle of the photons, at 500 GeV, using Whizard. Blue: the remaining ISR photons on the sample. Purple: the background contamination. Red: the remaining FSR photons on the sample. Black: Purity of the sample.

sion is very unlikely, and a double emission with high energy (most sensitive part of $B(m_t, \zeta_{S'})$) is even less probable, the strategy followed was to avoid the differentiation between the photons, since the possible effects from the FSR photon will be negligible in front other sources of uncertainty. However, this approach makes necessary to incorporate the FSR into theoretical predictions to extract the top-quark mass.

9.2.2 *Background reduction*

The background photons, passing the selection criteria, modify the shape of the $B_\gamma(m_t, \zeta_{S'_\gamma})$ distribution (Fig. 114). Therefore, to be able to fit the $B_\gamma(m_t, \zeta_{S'_\gamma})$ distribution, at particle level, using a partonic template fit or the theoretical predictions, the background contribution needs to be corrected. Figure 117 shows the background dependence with the top-quark mass, which is very small, moreover, the region of high energy photons, shows a dependency that can be neglected. For this reason and as a first approximation, the bin by bin correction is a valid method to subtract the background contribution, using the Monte Carlo generator.

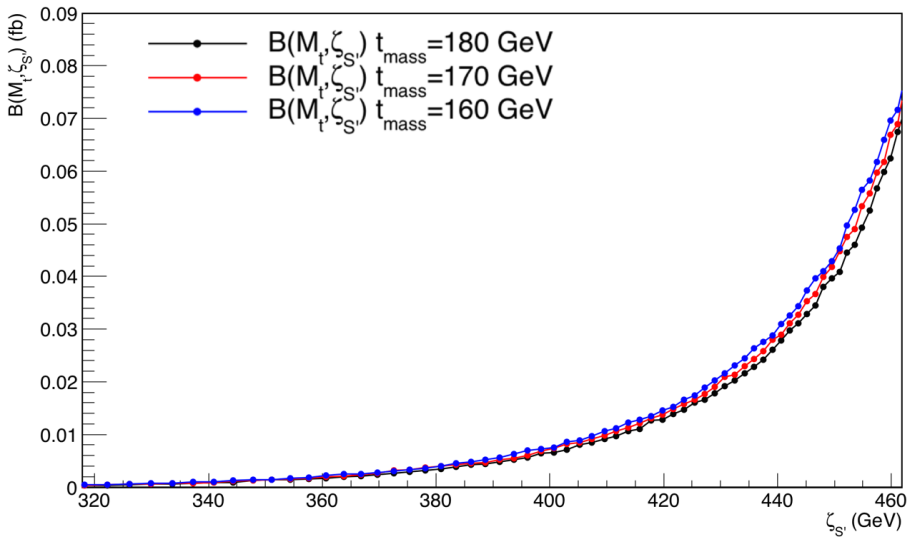

Figure 117: Comparison of the background contribution for different masses to see its dependency with the top-quark mass.

The idea is to use the background distribution calculated with an arbitrary mass (inside the expected range) and then, subtract it to the $B_\gamma(m_t, \zeta_{S'_\gamma})$ distribution. To obtain an estimation of the error remaining after the correction process, a high statistics

sample was generated using an arbitrary Monte Carlo mass of 170 GeV [6]. In order to quantify the primary error due to the background contribution, the $B_\gamma(m_t, \zeta_{S'_\gamma})$ was fitted without any correction, using a partonic template. The upper plots on figure 118 show the results. On the left, the $B_\gamma(m_t, \zeta_{S'_\gamma})$ distribution is compared to the partonic template. The plot on the right shows the best fit obtained, which results on a fitted mass of $m_t = 168.32$ GeV, 1.5 GeV away from the expected value. On the lower plot, the process was repeated with the $B_\gamma(m_t, \zeta_{S'_\gamma})$ **distribution corrected,** resolving in a fitted top-quark mass of $m_t = 170.026$ GeV, **with an error on the estimation of** $\sim$ **30** MeV.

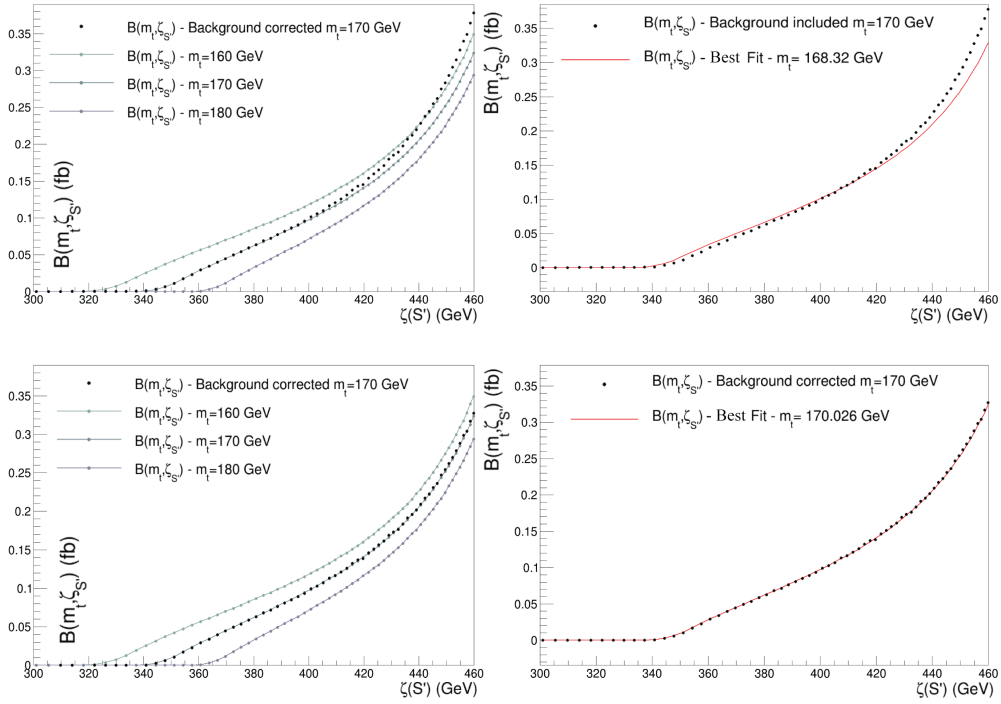

Figure 118: Upper plots: $B_\gamma(m_t, \zeta_{S'_\gamma})$ distribution obtained with the final photons, including the background contribution (Monte Carlo mass - $m_t = 170$ GeV). It has been compared to the partonic distributions (left). The data-set has been fitted with the partonic distributions (right - $m_t = 168.32$ GeV). Lower plots: $B_\gamma(m_t, \zeta_{S'_\gamma})$ distribution obtained with the final photons correcting the background contribution (Monte Carlo mass - $m_t = 170$ GeV). The final mass obatined after the correction was $m_t = 170.026$ GeV (right)

6 The correction should not depends on the top-quark mass used.

9.3 *Luminosity spectrum*

On e^+e^- colliders, the nominal energy is smeared by the beam energy spread and the beamstrahlung, which create an effective interaction energy. This process is not negligible and could be very important to $B(m_t, \zeta_{S'})$, since S' depends directly on the nominal interaction energy. Figure 119 shows the luminosity spectrum and the processes that contribute to it. The region of high energy losses ($x = E'/E_{beam} \sim 0.2$) is dominated by the ISR photon emission. The breamstralung contribution dominates the region of low energy lost ($x = E'/E_{beam} \sim 0.9$). Still, the beamstrahlung, can create a huge number of migrations that will affect the $B_\gamma(m_t, \zeta_{S'_\gamma})$ resolution.

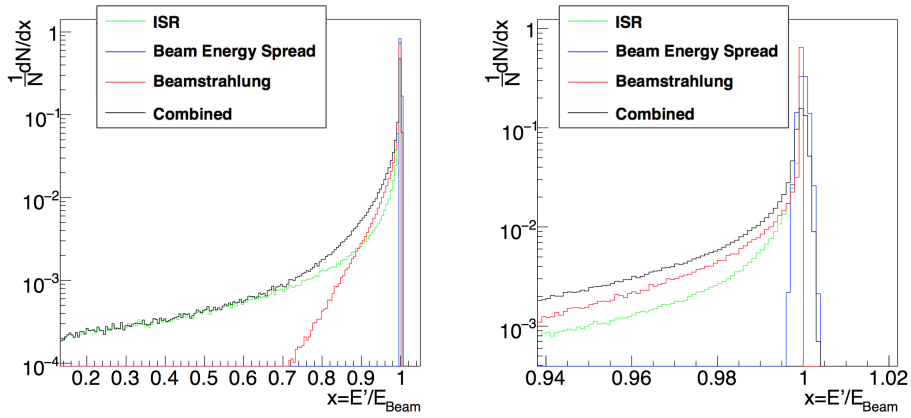

Figure 119: Diferential luminosity spectrum and the different contributions (left). Expanded scale around the peak(left) [107]

It is important to evaluate the impact of the luminosity spectrum on the mass measurement, and also, find out a correction method. First assumption is that the luminosity spectrum is known. In the real experiment, the luminosity spectrum is provided by the reconstruction of the Bhabha events (scattering of electrons), obtaining the effective center of mass energy (Fig. 120 - left). One method to do this is to use the tracker information to reconstruct the angles of the outgoing particles, θ_1 and θ_2 (Fig. 120 - right) and then, use the equation 58. Other option is to take the calorimeter information and reconstruct the energy of the outgoing electrons pair ($\sqrt{S'} = \sqrt{2p_1p_2}$).

$$\frac{\sqrt{S'}}{\sqrt{S}} = \sqrt{\frac{\sin\theta_1 + \sin\theta_1 + \sin\theta_1 + \theta_2}{\sin\theta_1 + \sin\theta_1 - \sin\theta_1 + \theta_2}} \tag{58}$$

To obtain a first estimation of the error propagated to the luminosity spectrum, it has been considered as perfectly known and generated with the Guinea-Pig software package [108]. To correct the $B_\gamma(m_t, \zeta_{S'_\gamma})$ distribution, it is necessary to recover the

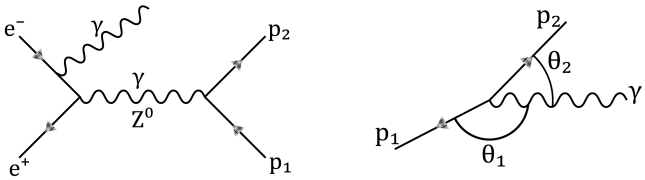

Figure 120: Feyman diagram of the Bhabha interaction, including bremsstrahlung (left). Angular distribution of the scattered electrons (right).

bin by bin migrations produced by the luminosity spectrum. The luminosity spectrum can be used to feed up the Whizard generator, therefore can also be disconnected. Several samples were generated to compare both scenarios, with many top-quark masses. Figure 121 (left) shows the bin by bin comparison for multiple top-quark masses. The study performed demonstrated that the position of the migrations depends on the top-quark mass used, but not the migration itself. Figure 121 (right) shows all distribution piled up and the mean correction.

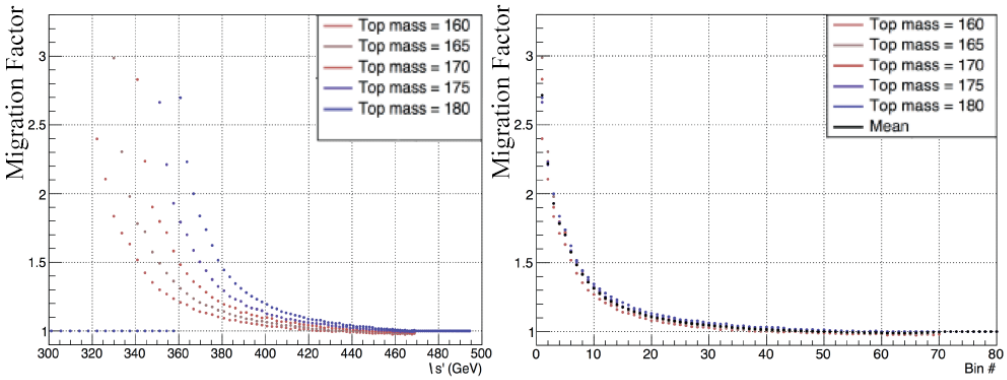

Figure 121: Comparison of the $B_\gamma(m_t, \zeta_{S'_\gamma})$ distribution with the luminosity spectrum included and disconnected, using several top-quark masses (left). Final correction distribution (right).

Analogously to background correction, the luminosity spectrum correction has been applied to a $B_\gamma(m_t, \zeta_{S'_\gamma})$ distribution, generated using an arbitrary Monte Carlo mass of 173.25 GeV [7] and a large number of events. Figure 122 shows the results obtained before and after the correction. On the left, the upper plot compares the distribution after the selection and including the luminosity spectrum, with the partonic template. On the lower plot, the distribution, after the selection, has been corrected. The plots on the

7 The top-quark mass finally used depended on the availability of the samples.

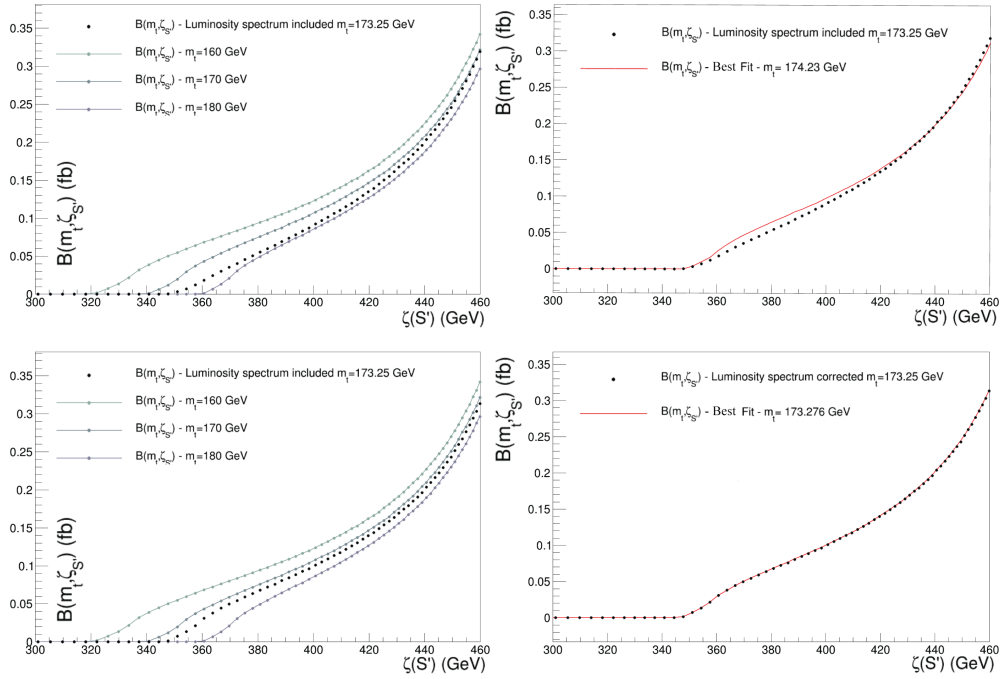

Figure 122: Upper plots: $B_\gamma(m_t, \zeta_{S'_\gamma})$ distribution obtained with the luminosity spectrum included (m $m_t = 173.25$ GeV). It has been compared to the partonic distributions (left). The data-set has been fitted with the partonic distributions (right - $m_t = 174.23$ GeV). Lower plots: $B_\gamma(m_t, \zeta_{S'_\gamma})$ distribution with the migrations due to the luminosity spectrum corrected ($m_t = 173.25$ GeV). The final mass obtained after the correction was $m_t = 173.276$ GeV (right)

right show the best fits obtained using the partonic template. The mass with the non-corrected distribution is around $m_t = 174.23$ GeV, 1 GeV away from the expected value. On the other hand, **after the correction** the resulting mass fitted is $m_t = 173.276$ GeV, with an **error, on the estimation, of ~ 30** MeV. Therefore, it is proved that if the luminosity spectrum is known, the correction can be performed.

9.4 *Summary*

This chapter has studied more deeply the ISR emission, introducing several effects to increase the realism of the simulation. On the first part, the detector acceptance and the selection process have been considered to estimate the $B_\gamma(m_t, \zeta_{S'_\gamma})$ resolution, at particle level. This section proved that although the resolution has worsened, it can reach, on the ILC-500 GeV scenario, around ~ 100 MeV. Afterwards, the $B_\gamma(m_t, \zeta_{S'_\gamma})$ study has been extended to cover the CLIC-380 GeV and ILC-1000 GeV physics programs, result-

ing on an improved $B_\gamma(m_t, \zeta_{S'_\gamma})$ resolutions at lower energies. Moreover, having access to higher interaction energy ranges gives the opportunity to perform the "running of the top-quark mass" study, extending the range of scales. Then, Whizard Monte Carlo tool has been implemented on the generation chain, which allowed to study, in detail, the multiple contributions to the $B_\gamma(m_t, \zeta_{S'_\gamma})$ distribution, after the selection process, such the FSR and the background contamination. **A bin by bin correction method was proposed and implemented to minimize the background contribution effect, resulting in a final deviation of ~ 30 MeV. Finally, the luminosity spectrum contribution was introduce. In this case, the correction was implemented minimizing the error to the level of ~ 30 MeV.**

10

$B(m_t, \zeta_{S'})$: Summary and Future Work

The cross section of the $e^+e^- \to t\bar{t} + \gamma$ (ISR and FSR) and $e^+e^- \to t\bar{t} + g$ (FSR) radiative events are dynamically related with the top-quark mass, since each of them imply a reduction on the phase space of the other processes. **The observable** $B(m_t, \zeta_{S'})$ exploit these relations to be able to **measure the mass of the top-quark in the continuum, studying the energy of the particles radiated via ISR and FSR**.

$B(m_t, \zeta_{S'})$ has been introduced in Chapter 8, defining **independent observables for the ISR photon emission** (Eq. 59) **and the FSR gluon emission** (Eq. 60).

$$S'_\gamma = S\left(1 - \frac{2E_\gamma}{\sqrt{S}}\right),\ B_\gamma(m_t, \zeta_{S'_\gamma}) = \frac{d\sigma_{t\bar{t}\gamma}}{d\zeta_{S'_\gamma}} \to \zeta_{S'_\gamma} = \sqrt{S'_\gamma} \tag{59}$$

$$S'_g = S\left(1 - \frac{2E_g}{\sqrt{S}}\right),\ B_g(m_t, \zeta_{S'_g}) = \frac{d\sigma_{t\bar{t}g}}{d\zeta_{S'_g}} \to \zeta_{S'_g} = \sqrt{S'_g} \tag{60}$$

First study at partonic level has been performed in order to obtain, in both cases, the maximum potential resolution. The physics scenario corresponded to the ILC with an interaction energy of 500 GeV. Both studies were done separately and both resulted in a **resolutions around** ~ 60 MeV**, considering non-polarized beams and an integrated luminosity of** 2600 $\mathbf{fb}^{-1}$. However, the ultimate goal of this study was to find out the maximum resolution, combining both observables. To do this, all ILC-500 GeV luminosity scenario and polarized beams were included ($p_{e^-} = +80\%$, $p_{e^+} = -30\%$), table 32 shows the maximum expected resolutions combining ISR and FSR radiative events.

Stage	$\mathcal{L}$ (fb^{-1})	Δm_t (GeV)
1	500	~ 0.080
2	1000	~ 0.055
3	2600	~ 0.035
4	4000	~ 0.030

Table 32: Combined results ISR/FSR at partonic level. It considers polarized beams ($p_{e^-} = +80\%$, $p_{e^+} = -30\%$) in a possible stages of the ILC.

Furthermore, since the observable $B(m_t, \zeta_{S'})$ does not require a specific interaction energy to be applied, the top-quark pairs used are generated on a range of energy

scales. Therefore, enclosing the energy of the radiated particle, the $t\bar{t}$ production energy (S') will be also enclosed on a scale range. **This allows to study the top-quark mass not only over the production threshold but in the continuum, and therefore, the mass can be defined on a good renormalization system and even being sensitive to its running**. Section 8.4 has studied the sensitivity of $B(m_t, \zeta_{S'})$ to the running of the top-quark mass, table 33 shows the results obtained only with the ISR photon and table 34 the resolution archivable with the FSR gluon.

Scale S'(GeV)	Run. m_t (GeV)	Run. Δm_t (GeV)	Sigma
~ 360	153.7	0.062	Ref.
~ 400	152.7	0.30	3.3σ
~ 440	151.9	0.39	4.5σ
~ 490	150.9	0.24	11.6σ

Table 33: Resulting $B_\gamma(m_t, \zeta_{S'_\gamma})$ running mass sensitivity on the selected regions. The remaining interaction energy is the weighted average of S', the running m_t, is the running mass obtained on the corresponding scale and the running Δm_t is the sensitivity on the selected region.

Scale S'(GeV)	Run. m_t (GeV)	Run. Δm_t (GeV)	Sigma
~ 360	153.5	0.11	Ref.
~ 400	152.7	0.18	4.4σ
~ 440	151.8	0.16	10.4σ
~ 490	150.9	0.077	33.6σ

Table 34: Resulting $B_g(m_t, \zeta_{S'_g})$ running mass sensitivity on the selected regions. The remaining interaction energy is the weighted average of S', the running m_t, is the running mass obtained on the corresponding scale and the running Δm_t is the sensitivity on the selected region.

These estimations are very unrealistic and no detector or particles level effects are included, but shows that the study is worth and the physics potential high.

To approach towards a realistic study, next steps required the inclusion of the hadronization and the basic detector effects. **In Chapter 9, the ISR photon was studied at particle level and, likewise, the influence of the selection process, including some detector and accelerator induced effects.**

The **simulations have been performed at particle level** to include the effects of the selection process and the detector acceptance. The samples have been generated using PYTHIA8, **considering, at first, the ILC program at** 500 GeV**, and then extending the study to CLIC -** 380 GeV **and ILC -** 1000 GeV.

It is expected that majority of photons emitted, by the incident beams, will have a very low polar angle and, probably, will not be detected. Therefore, **the coverage of the forward and backward photon detectors are of crucial importance for this analysis**. To include this limitation on the study, an acceptance cut has to be defined ($\theta_{\mathbf{min}} = 7^o$**, considering the ILD coverage angle** - Tab. 35).

Physic Program	$\theta_{min}(^0)$	ISR lost
CLIC - 380 GeV	7	~ 71%
ILC - 500 GeV	7	~ 75%
ILC - 1000 GeV	7	~ 79%

Table 35: Percentage of ISR lost after the coverage cut, considering the physics program studied.

The most sensitive part of the $B_\gamma(m_t, \zeta_{S'_\gamma})$ distribution correspond to the most energetic photons, accordingly, **a requirement on the photons minimum energy will not affect, significantly, the sensitivity,** but will reduce the background substantially. Moreover, the ISR photon emission happens alone and, usually, only a single photon is emitted. It is not expected to have ISR photons included in a jet of particles, therefore, **the photon isolation angle will be a good criteria to exclude photons generated on a electromagnetic cascade**. To optimize the cut values, a scan was performed considering all physics program studied:

- **First Step (energy cut - Tab. 36):** It is applied to the remaining photons from coverage cut.

Physic Program	Min. Energy (GeV)	ISR lost	Back. Reduction
CLIC - 380 GeV	3	~ 53%	~ 76%
ILC - 500 GeV	10	~ 79%	~ 97%
ILC - 1000 GeV	30	~ 75%	~ 79%

Table 36: Best minimum energy cut selected, considering the physics program studied.

- **Second step (selection via isolation angle - Tab. 37):** It is applied to the remaining photons from first cut.

Physic Program	Isolation angle (^{0})	ISR lost	Back. Reduction
CLIC - 380 GeV	8	~ 15%	~ 95%
ILC - 500 GeV	8	~ 15%	~ 98%
ILC - 1000 GeV	4	~ 5%	~ 98%

Table 37: Best isolation angle cut selected, considering the physics program studied.

The results obtained after the selection process, at 500 GeV **(ILC) are shown in table 39, at** 1000 GeV **(ILC) in table 40 and at** 380 GeV **(CLIC) in table 38**, where $\mathcal{L}$ represents the total accumulated luminosity used, Δm_t represents the resolution obtained, at particle level, only with the ISR photon [1], and "Total $\Delta m_t^{extrapol}$" represents an extrapolation of the total resolution achievable, at particle level, combining ISR and FSR radiative events and polarized beams[2].

Stage	$\mathcal{L}$ (fb^{-1})	Δm_t (GeV)	Total $\Delta m_t^{extrapol}$ (GeV)
1	500	0.10	0.06

Table 38: CLIC 380 GeV expected sensitivities at particle level.

Stage	$\mathcal{L}$ (fb^{-1})	Δm_t (GeV)	Total $\Delta m_t^{extrapol}$ (GeV)
1	500	0.29	0.17
2	1000	0.21	0.12
3	2600	0.12	0.07
4	4000	0.10	0.06

Table 39: ILC 500 GeV expected sensitivities at particle level.

Stage	$\mathcal{L}$ (fb^{-1})	Δm_t (GeV)	Total $\Delta m_t^{extrapol}$ (GeV)
1	1000	0.63	0.36
2	3500	0.38	0.22

Table 40: ILC 1000 GeV expected sensitivities at particle level.

1 Non-polarized beams are considered.
2 Assuming selection efficiencies for the FSR similar to the efficiencies obtained with the ISR.

As expected, the resolution is better as the energy of interaction approaches to the $t\bar{t}$ threshold. However, the study at higher interaction energies allows to explore larger energy ranges to be sensitive to the running of the top-quark mass. Accordingly, **the study of the sensitivity to the running mass has been extended to the full range, at particle level (see Section 9.1.2)**.

Finally, in order to continue increasing the simulation realism and perform the study of systematics, **Whizard was implemented on the generation chain**. Whizard is able to compute complete tree-level matrix elements on-line. But most important, it is capable to include the beamsstrahlung and smearing effects, to simulate the interaction in a real bunch crossing process.

After the selection process, photons coming from several sources contribute to the $B_\gamma(m_t, \zeta_{S'_\gamma})$ distribution. It is important to perform a distinction between two main sources of distortion: the photons coming from the top FSR radiation and background photons:

- **FSR contamination:** The FSR photons **are irreducible from the ISR photons** with the present selection cuts. The contamination from the FSR represents **around** 4% **on the final samples on the ILC -** 500 GeV **scenario**.
- **Background reduction:** The background photons, passing the selection criteria, modify the shape of the $B_\gamma(m_t, \zeta_{S'_\gamma})$ distribution. The **solution is to use a bin by bin subtraction, resolving in an estimation error** $\sim$ 30 MeV.

On e^+e^- colliders, the nominal energy is smeared by the beam energy spread and the beamstrahlung, which creates an **effective interaction energy**. This effect was also studied. **If the luminosity spectrum is known, the bin migration correction can be performed. The estimation error after the correction is** $\sim$ 30 MeV.

The results presented in these chapters motivated the development of a **theoretical implementation of** $B_\gamma(m_t, \zeta_{S'_\gamma})$. It has been performed by A. H. Hoang and V. Mateu. In addition, the FSR radiation has to be included to develop a complete theoretical calculation and estimate completely the theoretical error.

On the other hand, the study of $B_\gamma(m_t, \zeta_{S'_\gamma})$ **has to be extended to a full simulation environment**, where all the effects coming from the machine are considered. These effects have to be studied and corrected via an unfolding process.

The **FSR gluon has to be studied at particle level**, including jet reconstruction and identification of all top decay channels. Finally, the process will be implemented on the full simulation stage. **The ultimate goal is to obtain a combined estimation of the top-quark mass using ISR photon and FSR gluon, in a full-simulation scenario**.

Part IV

Closure

11 Conclusions

The discovery of the Higgs Boson, in 2012, with ATLAS and CMS experiments, at LHC (CERN), was an amazing success performed by the wold wide scientific community. It was the last particle predicted by the Standard model that was observed. The results provided by the LHC determine the next steps to be followed on the development of the next generation of physics accelerators. Several projects are, currently, under discussion. Since LHC has broken the energy of interaction frontier, the goal of new projects will be to explore the precision measurement limits. The International Lineal Collider (ILC) and the Compact Lineal Collider (CLIC) will perform e^+e^- collisions at high energy to take advantage of this clean environment and explore energy ranges from hundreds of GeV to the multi-TeV scale. Other approach followed by SuperKEKB accelerator is to use e^+e^- collisions, at intermediate energies, but with unprecedented luminosities to study the $B\bar{B}$-pair productions processes, with maximum accuracy, to be sensitive to deviations from the SM predictions.

This report entered on this context to perform a tiny contribution on the development of future colliders. On one side, it summarized the work performed on the study of the DEPFET technology, capable to cope the requirements of the new accelerators. Moreover, a new observable has been proposed to measure the mass of the top-quark, in the continuum, using radiative events.

The **DEP**leted **F**ield **E**ffect **T**ransistor (DEPFET) is an active pixel technology, constructed as an all-Silicon structure, with a high granularity matrix, characterized by its very small power consumption and a minimum material budget. These features, and its versatility in terms of design and operation, make DEPFET a strong candidate as a pixel technology for the (ILC), moreover, currently, it is the baseline technology for the Belle II PXD (SuperKEKB). On this context, this thesis has presented some of the studies performed to characterize the current DEPFET prototypes.

- A study of the DEPFET spatial resolution has been performed, resulting in a maximum spatial resolution of ~ 8.5 μm, using the data obtained in the July-2012 test beam campaign. Moreover, since DEPFET technology is capable to reach an unprecedented spatial resolution, the results from distinct test beam campaigns were used to prove that spatial resolution of such devices is limited by the Landau distribution and the δ-electron effects, and even increasing the S/N ratio, reducing the pixel size or the thickness, these will generate a negligible improvement on this parameter [75].

- In order to fulfill all the SuperKEKB requirements, the PXD have to be designed to work with the injection scheme of the corresponding accelerator. For this, DEPFET technology has developed a method to survive to the injected noisy bunches, called *Gated Mode*. The operation and efficiency, of this method, have been successfully tested.

However, the main task assigned during this thesis was to participate on the development of the construction plans for the Belle II PXD. Specifically, the design and implementation of the first sanity check performed over the full assembled modules using a *needle card*. To achieve this, several needle cards were designed for the different DEPFET prototype. Based on the results, a baseline testing protocol was proposed to check the quality of the chips bump bonding and the chips operation performance. **After all development period, the setup, with all the mechanical parts, the electronic boards and the software, was mounted and prepared to be used during the production. Likewise, the two required needle cards and also the test protocol for the sanity check.**

The second part of this report intends to summarize the work performed on the development of a new observable, $B(m_t, \zeta_{S'})$, to measure the mass of the top-quark in the continuum, using radiative events on e^+e^- interactions. This observable has been specially designed for the future high-energy e^+e^- colliders, such ILC or CLIC. It takes advantage that the cross section of the $e^+e^- \rightarrow t\bar{t} + \gamma$ (ISR and FSR) and $e^+e^- \rightarrow t\bar{t} + g$ (FSR) radiative events are dynamically related with the top-quark mass, therefore studying the energy of the particles radiated via ISR and FSR, the mass of the top quark can be inferred.

The calculation of the potential sensitivity of $B(m_t, \zeta_{S'})$ has been done sequentially, starting from the easiest scenario, only considering processes at partonic level and neglecting all possible sources of inefficiencies, to finally move towards a more realistic study.

The first scenarios considered was the ILC with an interaction energy of 500 GeV, at partonic level. The ISR, $B_\gamma(m_t, \zeta_{S'_\gamma})$, and FSR, $B_g(m_t, \zeta_{S'_g})$, were studied independently, resulting in a potential resolution around ~ 60 MeV, considering non-polarized scenario and an integrated luminosity of 2600 fb^{-1}. However, this resolution can be improved if both observables are combined and the polarized beam scenario are included ($p_{e^-} = +80\%$, $p_{e^+} = -30\%$), in this case the **total resolution can reach** ~ 35 MeV**, including** 2600 $\mathbf{fb^{-1}}$**.**

Since the measurement is performed on the continuum, $B(m_t, \zeta_{S'})$ does not depend on a fixed interaction energy, and therefore, the mass can be defined on a good renormalization system and even being sensitive to its running.

The promising results obtained at partonic level motivated to continue towards a more realistic approach, for simplicity, at this step, only the ISR photon was included. The simulations were performed at particle level including the detector coverage effect and the selection efficiencies. Moreover, the study was extended CLIC - 380 GeV and ILC - 1000 GeV. The expected sensitivities are shown in table 41, including an extrapolation of the total resolution achievable, at particle level, combining ISR and FSR radiative events and polarized beams ("Total $\Delta m_t^{\text{extrapol}}$").

Scenario	$\mathcal{L}$ (fb^{-1})	Δm_t (GeV)	Total $\Delta m_t^{\text{extrapol}}$ (GeV)
CLIC - 380 GeV	500	0.10	0.06
ILC - 500 GeV	4000	0.10	0.06
ILC - 1000 GeV	3500	0.38	0.22

Table 41: $B(m_t, \zeta_{S'})$ expected sensitivities at particle level.

Finally, the main systematic error were explored and a method to minimize its effect was proposed: the FSR photon contamination (irreducible $\sim 4\%$), background contamination (estimation error after the correction ~ 30 MeV) and luminosity spectrum deviation (estimation error after the correction ~ 30 MeV).

The results obtained proved that the resolution of $B(m_t, \zeta_{S'})$ are way below the methods currently used in hadron colliders and in the same order of the threshold measurements on the ILC. Moreover, with $B(m_t, \zeta_{S'})$ the top-quark mass can be defined on a good renormalization system and even being sensitive to its running.

12

Resumen

El Modelo Estándar (SM) es el marco teórico más preciso jamas construido, el cual incluye todas las partículas descubiertas y las interacciones entre ellas. Es el resultado de más de 100 años de investigación en física de partículas, empezando por las observaciones de J.J. Thompson de los así llamados "corpusculos", usando un pequeño tubo de rayos catódicos; hasta el reciente descubrimiento del bosón de Higgs, que ha necesitado de la colaboración de miles de científicos de todo el mundo, así como la mayor y más sofisticada máquina jámas construida por el ser humano (el LHC).

La necesidad de entender los fenónemos de la naturaleza es imparable, así como la creación de nuevos aparatos para continuar avanzando. Máquinas como el "International Linear Collider (ILC)" o el "Compact Linear Collider (CLIC)" que serán capaces de generar interacciones e^+e^- a energías desde cientos de GeV hasta la escala de los TeV. Por otro lado, SuperKEKB, que pretende alcanzar la frontera de la luminosidad, para estudiar con máxima precisión los procesos $B\bar{B}$ en interacciones e^+e^-.

El presente trabajo entra en este contexto para hacer una pequeña contribución al desarrollo de estos nuevos proyectos. Por un lado, la participación en el proceso de producción del los detectores de píxeles para Belle II (superKEKB), basados en tecnología DEPFET. Por otro lado, se ha propuesto un nuevo observable para medir la masa del quark top, usando eventos e^+e^- radiativos, en el continuo.

12.1 *Desarrollo del protocolo de control de calidad para los detectores DEPFET.*

DEPFET (**DEP**leted **F**ield **E**ffect **T**ransistor) es una tecnología de píxeles activos, lo que significa que la primera fase de amplificación de la señal se produce internamente. Para conseguir dicha amplificación se usa un transistor de efecto de campo del tipo MOS (MOSFET) integrado en un volumen de Silicio del tipo-n. Esto permite generar señales detectables solamente a partir de la pequeña carga depositada por una partícula incidente. El Capítulo 3 describe el funcionamiento de la tecnología DEPFET e introduce sus modos de operación. Además, las diferentes estrategias de análisis son descritas, junto con los estudios realizados durante la tesis, para analizar algunos parámetros de estos detectores y sus implicaciones.

El primer estudio realizado pretendía encontrar la máxima resolución espacial de las matrices DEPFET en función del *"zero suppression cut"*, concluyendo que, para los prototipos presentados, este valor podía llegar a ~ 8.5 μm. A este nivel, hay ciertos efectos

físicos que empiezan a deteriorar la posición reconstruida. Usando los datos obtenidos con los prototipos DEPFET, estos efectos fueron estudiados para determinar si existe un límite a la resolución espacial que se puede alcanzar con dispositivos que se basan en compartir carga entre píxeles vecinos. En particular, el efecto de los electrones-δ en el caso de incidencia perpendicular (Fig. 123), así como el efecto de la distribución Landau de la carga depositada en el caso de incidencia bajo cierto ángulo (Fig. 124).

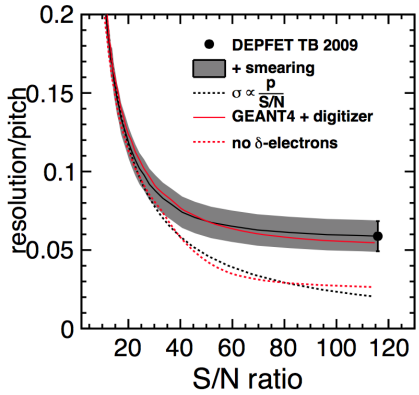

Figure 123: Resolución espacial dividida por el tamaño del pixel en función del ratio señal/ruido (S/R), considerando piones de 120 GeV, con incidencia perpendicular, sobre prototipos DEPFET de 450 µm de grosor (linea sólida en negro), comparando con la simulación de GEANT4 incluyendo electrones-δ (linea sólida en rojo) y sin incluir electrones-δ (linea discontinua en rojo). El comportamiento ideal también se representa (linea discontinua en negro)[75].

En los dos estudios se concluye que **la resolución espacial de este tipo de dispositivos está limitada por estos efectos, por lo que, incluso, mejorando el ratio** S/R**, reduciendo el tamaño de los pixeles o el grosor del sensor, no va a tener un efecto apreciable en la resolución espacial final.** También cabe remarcar que la tecnología DEPFET es capaz de alcanzar este límite de resolución.

El Capítulo 3 ha descrito las características generales de la tecnología DEPFET, enfatizando en su versatilidad en términos de diseño de los pixeles, así como en la flexibilidad a la hora de operar las matrices. Su amplificación interna, la baja contibución al material del detector, su bajo consumo, la alta resolución espacial, son algunas de las características que convierten DEPFET en una candidata perfecta, capaz de cumplir todos los requisitos de los futuros aceleradores e^+e^-. Por esta razón, es un candidato como la tecnología para el detector de pixel (PXD) de ILC, y además es la tecnología que va a utilizarse en el PXD de Belle II en SuperKEKB.

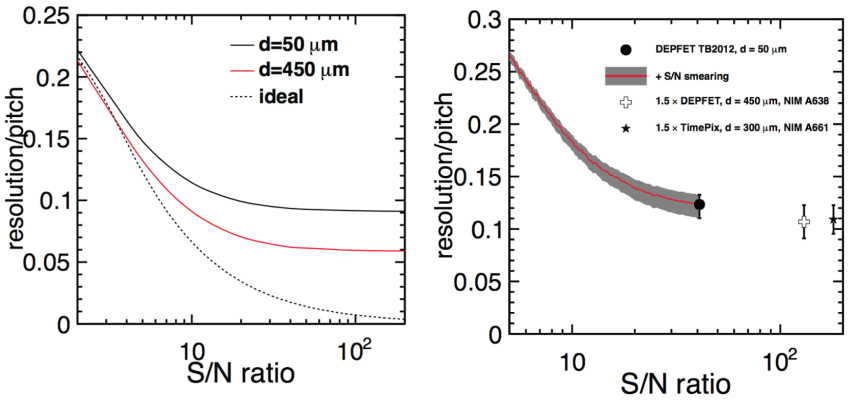

Figure 124: Izquierda: Simulación Monte Carlo de la resolución dividida por el tamaño del pixel en función de ratio S/R. La linea discontinua representa la situación ideal donde la carga se deposita proporcionalmente a la longitud de la trayectoria, la linea sólida incluye las fluctuaciones de Landau, considerando un grosor de Silicio de 50 μm (rojo) y 450 μm (negro). Derecha: La resolución dividida por el tamaño del pixel en función de ratio S/R, obtenida con diferentes dispositivos [75].

En este contexto y para poder cumplir a los requisitos de SuperKEKB, el PXD tiene que ser capaz de adaptarse al esquema de inyección del correspondiente acelerador. Por esto, la tecnología DEPFET ha desarrollado un método para sobrevivir a los nuevos paquetes de partículas inyectados, llamado *Gated Mode*. Otro estudio que se ha realizado cubrió el análisis de este modo de operación para probar su eficiencia en la preservación de la carga y el blindaje de la misma. La figura 125 muestra la región de voltajes donde, este modo de operación, es capaz de preservar la carga.

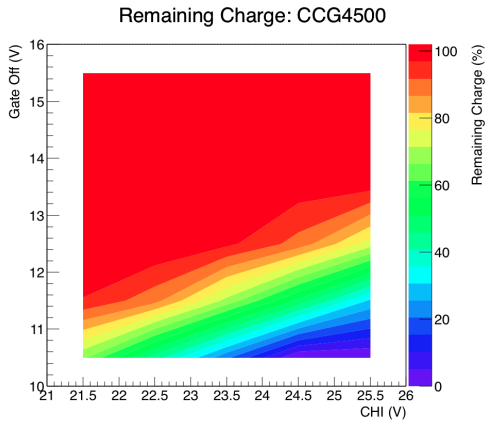

Figure 125: Barrido de los voltages de *Clear* y *Gate* para definir las regiones donde la carga se preserva completamente. El voltaje de *Cleargate* se ha fijado en 4.5 V.

Centrándose en el PXD para Belle II, el Capítulo 4 ha introducido las características de los prototipos DEPFET para este experimento, asimismo, los chips (ASICs) necesarios han sido descritos junto con el sistema de adquisición (DAQ), el sistema mecánico y el sistema de refrigeración. En este escenario, **el trabajo realizado durante esta tesis se centró en el diseño y el desarrollo del test de control de calidad que se aplicará a los módulos DEPFET, completamente ensamblados, usando una tarjeta de agujas**. Este capítulo ha descrito el proceso de producción del PXD de Belle II, para contextualizar este test. Finalmente, el "Boundary-Scan" se introdujo, porque va a ser un paso crucial en el proceso de testeo.

Los módulos del PXD estarán conectados a los componentes externos a través de un cable "kapton", soldado directamente sobre el módulo. En caso que haya algún problema en alguno de los chips, el cable "kapton" dificultaría la sustitución del mismo. La solución propuesta durante la tesis es aplicar el test de control de calidad antes de soldar el cable "kapton" y, para esto, una tarjeta de agujas es necesaria. El desarrollo de este test ha sido resumido en el Capítulo 5. **El primer prototipo fué diseñado para el EMCM y se utilizó para probar que este concepto de test era aplicable (Fig. 126).**

Figure 126: Fotografía de la tarjeta de puntas para el EMCM. El EMCM W17 – 4 esta situado en el "chuck" de la estación de pruebas.

Todas las pruebas sobre el EMCM se realizaron satisfactoriamente, **concluyendo que si el contacto entre las agujas y las conexiones del módulo son suficientemente estables, no hay ningún problema para operar el módulo, incluso para conseguir "links" de alta velocidad. A partir de los resultados obtenidos, se ha propuesto un primer protocolo de testeo.** El objetivo último del protocolo de testeo es comprobar la calidad del "bump bonding" de los chips y el funcionamiento de los mismos. Durante el test, la primera parte sólo incluye la región digital de los chips, donde se aplicará el "Boundary Scan". La segunda parte añadirá la región analógica con el objetivo de leer

los pedestales y con esto, cubrir todos los aspectos básicos de operación de los módulos.

La experiencia obtenida con la tarjeta de agujas del EMCM ha permitido mejorar los prototipos finales de la tarjeta de puntas, aumentando la estabilidad de las conexiones de alta velocidad, la seguridad durante el proceso de testeo y reduciendo el daño infringido en los "pads" de conexión. Como los módulos finales incluyen dos distribuciones de "pads", dos tarjetas de agujas serán necesarias durante la producción (*diseño A* y *diseño B*).

Los prototipos finales de la tarjeta de agujas fueros probados con los módulos PXD9, el protocolo de testeo se aplicó, completamente, con el objetivo de obtener **la imagen de los pedestales**. La figura 127 muestra estos pedestales, concluyendo el proceso de diseño y caracterización de las tarjetas de puntas. Esta imagen **prueba la capacidad de el sistema montado para leer datos y por tanto aplicar completamente el protocolo de testeo propuesto.**

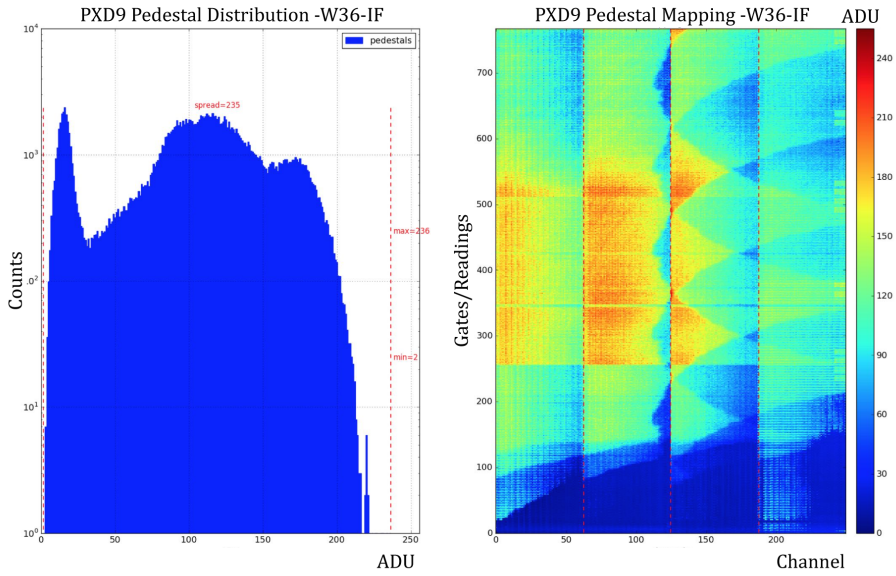

Figure 127: Imagen de los pedestales obtenidos con la tarjeta de agujas tipo A y un módulo IF ("inner-fordward").

Este montaje, con todas las partes mecánicas, las tarjetas electrónicas y todo el software, ha sido ensamblado y preparado para ser usado durante la producción del PXD de Belle II. Asimismo, el *diseño A* y *diseño B* de las tarjetas de agujas y también el protocolo de testeo para el control de calidad (Fig. 128).

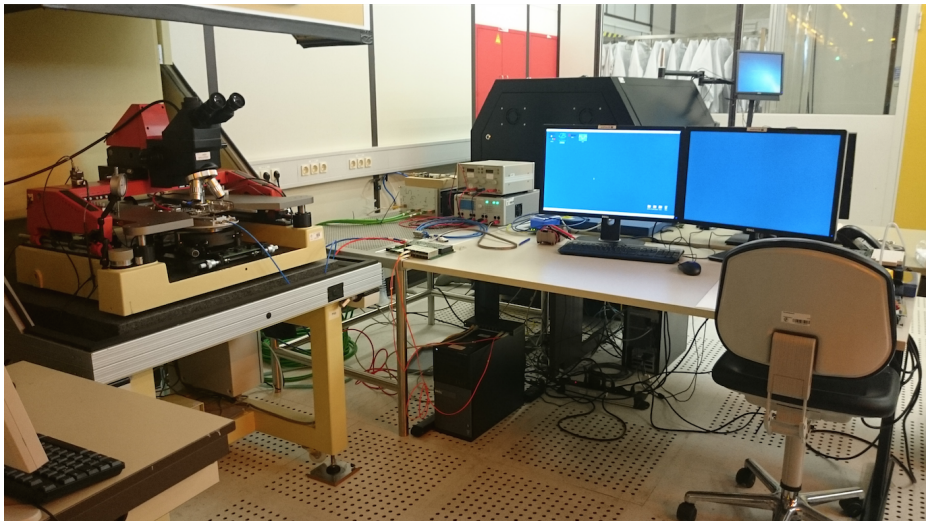

Figure 128: Imagen de montaje usado para hacer los test con las tarjetas de agujas. HLL (Munich).

12.2 *Medida de la masa del top en colisionadores de alta energía* e^+e^-.

La sección eficaz de los eventos radiativos $e^+e^- \to t\bar{t}+\gamma$ (ISR y FSR) y $e^+e^- \to t\bar{t}+g$ (FSR) está dinámicamente relacionada con la masa de quark-top, ya que cada uno de estos procesos implica la reducción del espacio de fase de los otros procesos. El observable $B(m_t, \zeta_{S'})$ usa esta relación para medir la masa del quark-top en el continuo, estudiando la energía de las partículas radiadas vía ISR y FSR.

El el Capítulo 8 se ha introducido $B(m_t, \zeta_{S'})$, definiendo observables independientes para la emisión del fotón ISR (Eq. 61) y la emisión del gluón FSR (Eq. 62).

$$S'_\gamma = S\left(1-\frac{2E_\gamma}{\sqrt{S}}\right),\ B_\gamma(m_t,\zeta_{S'_\gamma}) = \frac{d\sigma_{t\bar{t}\gamma}}{d\zeta_{S'_\gamma}} \to \zeta_{S'_\gamma} = \sqrt{S'_\gamma} \tag{61}$$

$$S'_g = S\left(1-\frac{2E_g}{\sqrt{S}}\right),\ B_g(m_t,\zeta_{S'_g}) = \frac{d\sigma_{t\bar{t}g}}{d\zeta_{S'_g}} \to \zeta_{S'_g} = \sqrt{S'_g} \tag{62}$$

El estudio a nivel partónico se ha realizado para obtener, en los dos observables, la máxima resolución potencial. El escenario de interacción utilizado correspondía al ILC con una energía de 500 GeV. Ambos estudios se realizaron por separado y **en ambos se alcanzó una resolución de** $\sim$ 60 MeV**, considerando haces no-polarizados y una luminosidad integrada de** 2600 $\mathbf{fb}^{-1}$**.** Sin embargo, el máximo potencial se puede alcanzar combinando ambos observables. Con este propósito, se han estudiado todos los escenarios de luminosidad propuestos para el ILC - 500 GeV, además se ha incluido el efecto de usar haces polarizados ($p_{e^-} = +80\%,\ p_{e^+} = -30\%$). En la tabla 42 se resume

los valores obtenido, combinando los eventos radiativos ISR y FSR.

Stage	$\mathcal{L}$ (fb^{-1})	Δm_t (GeV)
1	500	~ 0.080
2	1000	~ 0.055
3	2600	~ 0.035
4	4000	~ 0.030

Table 42: Resultados de la combinación de los eventos radiativos ISR y FSR, a nivel partónico, considerando haces polarizados ($p_{e^-} = +80\%$, $p_{e^+} = -30\%$) en todos los escenarios de luminosidad propuestos para el ILC - 500 GeV.

Una de las principales características del observable $B(m_t, \zeta_{S'})$ es que no necesita de una energía de interacción específica para poderlo aplicar y, por tanto, la pareja $t\bar{t}$ se puede generar en un rango de escalas de energía. Además estos rangos se pueden controlar, ya que acotando el rango de energía de la partícula radiada, la escala de producción queda también acotada. **Esto permite el estudio de la masa del quark-top, no sólo sobre el umbral de producción sino en el continuo y, por tanto, la masa se puede definir en un buen sistema de renormalización e incluso ser sensibles a sus variaciones en función de la escala ("running mass").** En la Sección 8.4 se ha estudiado la sensibilidad de $B(m_t, \zeta_{S'})$ a las variaciones de la masa del quark-top en función de la escala. En la tabla 43 se muestran los resultados obtenidos sólo considerando el fotón ISR y en la tabla 44 se muestra los valores obtenidos con el gluón FSR.

Scale S'(GeV)	Run. m_t (GeV)	Run. Δm_t (GeV)	Sigma
~ 360	153.7	0.062	Ref.
~ 400	152.7	0.30	3.3σ
~ 440	151.9	0.39	4.5σ
~ 490	150.9	0.24	11.6σ

Table 43: Sensibilidad de $B_\gamma(m_t, \zeta_{S'_\gamma})$ en las regiones de escala seleccionadas. La energía remanente, después de la emisión (escala), corresponde a la media ponderada de S'; m_t es la masa en la correspondiente escala y Δm_t representa la sensibilidad alcanzable en esa región.

Los resultados obtenidos a nivel partónico son poco realistas, ya que no se ha considerado ningún efecto debido al detector o por el proceso de selección de las partículas finales. Sin embargo se ha mostrado que el potencial físico del estudio es muy alto.

Scale S'(GeV)	Run. m_t (GeV)	Run. Δm_t (GeV)	Sigma
~ 360	153.5	0.11	Ref.
~ 400	152.7	0.18	4.4σ
~ 440	151.8	0.16	10.4σ
~ 490	150.9	0.077	33.6σ

Table 44: Sensibilidad de $B_g(m_t, \zeta_{S'_g})$ en las regiones de escala seleccionadas. La energá remanente después de le emisión (escala), corresponde a la media ponderada de S', m_t es la masa en la correspondiente escala y Δm_t representa la sensibilidad alcanzable en esa región.

Para acercarse a un estudio más realista, en los siguientes pasos se requiere de la inclusión de los efectos debidos a la hadronización y los efectos básicos del detector. **En el Capítulo 9 el fotón ISR ha sido estudiado a nivel partículas, incluyendo las eficiencias en el proceso de selección y algunos efectos inducidos por el detector o el acelerador.**

Las simulaciones se han realizado a nivel partículas, generando las muestras con PYTHIA8, primero para el programa de física del ILC a 500 GeV**, y después extendiendo el estudio a CLIC -** 380 GeV **y ILC -** 1000 GeV**.**

Se espera que la mayoría de las partículas emitidas por los haces incidentes tendrán un ángulo polar muy bajo y que, probablemente, no se podrán detectar. Por lo tanto, **el ángulo de cobertura del detector de fotones es un parámetro crucial en este análisis**. Para incluir este efecto, un **corte en el ángulo polar de los fotones (corte de cobertura) se ha fijado en $\theta_{min} = 7^o$, considerando el ángulo de cobertura de detector ILD (Tab. 45)**.

Physic Program	$\theta_{min}(^0)$	ISR lost
CLIC - 380 GeV	7	$\sim 71\%$
ILC - 500 GeV	7	$\sim 75\%$
ILC - 1000 GeV	7	$\sim 79\%$

Table 45: Porcentaje de fotones ISR eliminados después de aplicar el ángulo de cobertura en los distintos escenarios estudiados.

La parte más sensible de la distribución $B_\gamma(m_t, \zeta_{S'_\gamma})$ corresponde a la de los fotones más energéticos, por tanto **requerir una energía mínima no tendrá un efecto considerable en la sensibilidad, pero reducirá mucho las partículas de fondo.** Además,

la emisión ISR tiende a suceder aislada y normalmente sólo un fotón energético es emitido a la vez, por lo que, exigir **un ángulo de aislamiento a los fotones es un buen criterio para excluir gran parte de las partículas de fondo que se generan en una cascada electromagnética.** Para estudiar los cortes óptimos, se han realizado barridos de los parámetros seleccionados:

- **Primer corte (Corte en enegías - Tab. 46):** Este corte se aplica a los fotones que han sobrevivido al corte de cobertura.

Physic Program	Min. Energy (GeV)	ISR lost	Back. Reduction
CLIC - 380 GeV	3	~ 53%	~ 76%
ILC - 500 GeV	10	~ 79%	~ 97%
ILC - 1000 GeV	30	~ 75%	~ 79%

Table 46: Corte en energías óptimo en los distintos escenarios estudiados.

- **Segundo corte (Selección por ángulo de aislamiento - Tab. 47):** Este corte se aplica a los fotones que han sobrevivido al primer corte.

Physic Program	Isolation angle (^{0})	ISR lost	Back. Reduction
CLIC - 380 GeV	8	~ 15%	~ 95%
ILC - 500 GeV	8	~ 15%	~ 98%
ILC - 1000 GeV	4	~ 5%	~ 98%

Table 47: Corte en el ángulo de aislamiento óptimo en los distintos escenarios estudiados.

Los resultados obtenidos, después de aplicar el proceso de selección a las muestras generadas, se han resumido en las siguientes tablas: En la tabla 49 se ha considerado el programa de física del ILC-500 GeV**, en la tabla 50 el del ILC-**1000 GeV **y en la table 48 el de CLIC-**380 GeV , donde $\mathcal{L}$ representa la la luminosidad total utilizada, Δm_t es la resolución obtenida, a nivel partículas, sólo considerando el fotón ISR [1], y "Total $\Delta m_t^{\text{extrapol}}$" es la estimación de la resolución total alcanzable, a nivel partículas, combinando los eventos radiativos ISR y FSR y utilizando haces polarizados [2].

Como era de esperar la resolución mejora tal y como la energía de interacción se aproxima al umbral de producción $t\bar{t}$. Sin embargo, el estudio a mayores energías permite ampliar el rango de energías en el cual $B_\gamma(m_t, \zeta_{S'_\gamma})$ es sensible a las variaciones

1 Sin considerar en ningún caso haces polarizados.
2 Asumiendo que las eficiencias de selección para las eventos FSR son similares a las de los eventos ISR.

Stage	$\mathcal{L}$ (fb^{-1})	Δm_t (GeV)	Total $\Delta m_t^{extrapol}$ (GeV)
1	500	0.10	0.06

Table 48: Resolución esperada de $B_\gamma(m_t, \zeta_{S'_\gamma})$ en CLIC-380 GeV, a nivel partículas.

Stage	$\mathcal{L}$ (fb^{-1})	Δm_t (GeV)	Total $\Delta m_t^{extrapol}$ (GeV)
1	500	0.29	0.17
2	1000	0.21	0.12
3	2600	0.12	0.07
4	4000	0.10	0.06

Table 49: Resolución esperada de $B_\gamma(m_t, \zeta_{S'_\gamma})$ en ILC-500 GeV, a nivel partículas

Stage	$\mathcal{L}$ (fb^{-1})	Δm_t (GeV)	Total $\Delta m_t^{extrapol}$ (GeV)
1	1000	0.63	0.36
2	3500	0.38	0.22

Table 50: Resolución esperada de $B_\gamma(m_t, \zeta_{S'_\gamma})$ en ILC-1000 GeV, a nivel partículas

de la masa del quark-top en función de la escala de producción. Este estudio se ha extendido a todo el rango completo, a nivel partículas en la Sección 9.1.2.

Finalmente, para continuar incrementando el realismo de la simulación y poder estudiar los errores sistemáticos, **el simulador Monte Carlo Whizard se implementó en la cadena de producción de las muestras.** Whizard es capaz de calcular elementos de matriz a nivel-árbol on-line, pero lo más importante, es capaz de incluir en las simulaciones, efectos como el "beamsstrahlung" y el "smearing" para generar la interacción real del cruce de dos haces de partículas.

Después de aplicar el proceso de selección, algunos fotones, que provenientes de otras fuentes, contribuyen a la distribución $B_\gamma(m_t, \zeta_{S'_\gamma})$. Es importante realizar una distinción entre las dos fuentes principales de distorsión: los fotones que proceden de radiación FSR y aquellos que son fotones de fondo.

- **Contaminación FSR: Los fotones FSR son indistinguibles de los fotones ISR**, con los criterios aplicados. La contaminación de estos representa **aproximadamente el** 4% **para las muestras finales de ILC-**500 GeV.

- **Reducción de los fotones de fondo:** Los fotones de fondo que superan los criterios de selección influyen en el observable cambiando la forma de la distribución $B_\gamma(m_t, \zeta_{S'_\gamma})$. **La solución encontrada es la eliminación de esta contribución bin a bin, utilizando el Monte Carlo. El error producido después de la corrección es** ~ 30 MeV**, para ILC-**500 GeV**.**

Además, **en colisionadores** e^+e^- la energía nominal no es fija, debido a la anchura de la energía de los haces ("smearing") y el "beamsstrahlung", creando una **energía de interacción efectiva** (espectro de luminosidad). Este efecto también ha sido incluido y estudiado. **Si el espectro de luminosidad es conocido, la migración en los "bins" de la distribución puede corregirse. La estimación del error después de la corrección es de** ~ 30 MeV**, para ILC-**500 GeV**.**

Los resultados presentados en estos capítulos han motivado el desarrollo del **estudio teórico de** $B_\gamma(m_t, \zeta_{S'_\gamma})$, el cual está siendo realizado por A. H. Hoang y V. Mateu. Además, la radiación FSR tiene que ser incluida para desarrollar el cálculo teórico completo y estimar su error.

Por otra parte, **el estudio de** $B_\gamma(m_t, \zeta_{S'_\gamma})$ **ha de ser aplicado en una simulación completa para incluir todos los efectos de detector y acelerador**, y para poder encontrar un método de corrección ("unfolding").

El gluón FSR, $B_g(m_t, \zeta_{S'_g})$**, ha de ser estudiado a nivel de partículas**, incluyendo la reconstruccíon de "jets" y la identificación de los canales de desintegración del $t\bar{t}$. Finalmente, $B_g(m_t, \zeta_{S'_g})$ ha de ser utilizado en una simulación completa. **El objetivo final es obtener una estimación combinada de la sensibilidad a la masa del quark-top, con ISR y FSR, aplicándolo a una simulación completa.**

Part V

Appendices

Appendix A: Standard Model Basic Concepts

A.1 *The QED Gauge Theory*

The QED gauge theory is the easiest example to see how massless gauge bosons are a consequence of the local invariance requirement in a global invariant Lagrangian. Considering the Lagrangian of a free fermion (Eq. 63), which is invariant under global gauge transformations $U = e^{-i\alpha q}$.

$$\mathcal{L}_0 = \bar{\psi}(x)(i\gamma^\mu \partial_\mu - m)\psi(x) \tag{63}$$

The gauge principle requires the invariance in local gauge transformation $U = e^{-i\alpha(x)q}$. In this case, the parameter ($\alpha(x)$) depends on the space-time coordinate and therefore, extra terms will be generated. To get rid off these terms, it is required the redefinition of the derivative and to introduce a "gauge boson field" ($A_\mu(x)$) to cancel them (Eq. 64).

$$\begin{aligned}
&\psi(x) \xrightarrow{U(1)} \psi(x)' = e^{-i\alpha(x)q}\psi(x) \\
&\partial_\mu\psi(x) \xrightarrow{U(1)} \partial_\mu\psi'(x) = e^{-i\alpha(x)q}(\partial_\mu\psi(x) - i\psi(x)\partial_\mu\alpha(x)) \\
&A_\mu(x) \xrightarrow{U(1)} A'_\mu(x) \equiv A_\mu(x) - \frac{1}{e}\partial_\mu\alpha(x) \\
&D_\mu\psi(x) \equiv [\partial_\mu + ieqA_\mu(x)]\psi(x)
\end{aligned} \tag{64}$$

The covariant derivatives transform invariantly under the local gauge transformations. The invariant Lagrangian generates the interaction term between the fermions and a gauge boson (A_μ). However, to define A_μ as propagating field, a gauge invariant kinetic term must be added $F_{\mu\nu} \equiv \partial_\mu A_\nu - \partial_\nu A_\mu$. The final Lagrangian is shown in equation 65.

$$\begin{aligned}
\mathcal{L} &\equiv \bar{\psi}(x)(i\gamma^\mu D_\mu - m)\psi(x) - \frac{1}{4}F^{\mu\nu}F_{\mu\nu} \\
&= \mathcal{L}_0 - eqA_\mu(x)\bar{\psi}(x)\gamma^\mu\psi(x) - \frac{1}{4}F^{\mu\nu}F_{\mu\nu}
\end{aligned} \tag{65}$$

The mass term of the gauge boson does not appear naturally ($\mathcal{L}_m = 1/2m^2A^\mu A_\mu$) and cannot by added by hand because it breaks the local gauge invariance. In the QED case, this situation seems correct, because the gauge boson, the photon (γ), is massless.

A.2 The Goldstone Model

The Goldstone Model postulates that if one arbitrary state is chosen from a bunch of degenerated and continuos possibilities, new massless scalar particles appear in the spectrum of possible degenerate states. Considering a scalar complex field $\phi(x) = 1/\sqrt{2}(\phi_1(x) + i\phi_2(x))$ and the Lagrangian shown in 66.

$$\begin{aligned} &\mathcal{L} = \partial^\mu \phi(x)^* \partial_\mu \phi(x) - V(x), \\ &\text{where } V(x) = \mu^2 |\phi(x)|^2 + \lambda |\phi(x)|^4 \end{aligned} \tag{66}$$

The aim is to obtain the state of minimum energy. In order to do this, the sign of the potential parameters have to be chosen. The parameter λ will be always $\lambda > 0$ to have a $V(x)$ bounded inferiorly. On the other hand, μ^2 can acquire the two signs (Fig. 129).

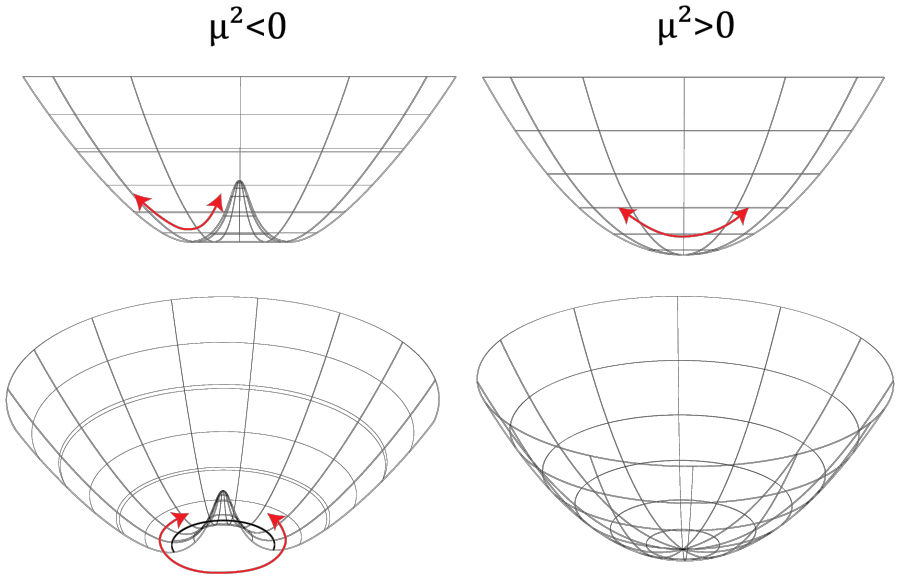

Figure 129: Golstone potentials depending on μ^2 sign. Left, the potential generates a set of states with minimal energy.

- Case $\mu^2 > 0$, the potential has the correct shape to perform perturbation studies (Fig. 129, right). Developing the scalar complex field on the Lagrangian, the minimum of the potential correspond to $\phi = 0$. It describes a massive scalar particles with mass μ (Eq. 67)

$$\mathcal{L} = \frac{1}{2}(\partial_\mu \phi_1)^2 - \mu^2 \phi_1^2 + \frac{1}{2}(\partial_\mu \phi_2)^2 - \mu^2 \phi_2^2 + \text{ interactions} \tag{67}$$

- Case $\mu^2 < 0$, the potential generates a continuum of degenerated minimum values (Fig. 129, left). $\partial V(x)/\partial\phi = -\phi^*|\mu|^2 + 2\lambda\phi^*|\phi|^2$, where $\phi^* = 0$ is the top of the central pic, and $|\phi| = \sqrt{-\mu^2/2\lambda} \equiv v/\sqrt{2}$ are the degenerate states of minimum energy. To be able to apply the perturbative theory, a minimum energy value should be chosen. Using the redefinition $\phi(x) = 1/\sqrt{2}(v + \sigma(x) + i\eta(x))$ and developing the Lagrangian, it is transformed as shown in equation 68.

$$\mathcal{L} = \frac{1}{2}(\partial^\mu \sigma \partial_\mu \sigma + \partial^\mu \eta \partial_\mu \eta) - \lambda v^2 \sigma^2 + \text{ interactions} \tag{68}$$

The Lagrangian 68 describes a massive state $\sigma(x)$ with $m_\sigma = \sqrt{2\lambda v^2}$, while $\eta(x)$ remain massless (Goldstone Particle).

A.3 *The Higgs Model*

The Goldstone method proved its capability to generated mass terms on the Lagrangian. The easiest example, to see how this method will affect to the masses of the gauge boson, is to use it on the $U(1)_{QED}$, even not making any sense, just as an academic exercise. Consider the Lagrangian of equation 69.

$$\begin{gathered}\mathcal{L}_{SSB} = (D^\mu \phi(x))^* (D_\mu \phi(x)) - \mu^2 |\phi(x)|^2 - \lambda |\phi(x)|^4 - \frac{1}{4} F^{\mu\nu} F_{\mu\nu} \\ \text{where } D_\mu \phi(x) = (\partial_\mu + iqA_\mu) \text{ and } F_{\mu\nu} = \partial_\mu A_\nu - \partial_\nu A_\mu\end{gathered} \tag{69}$$

As the Goldstone model says, if $\mu^2 < 0$, the minimum of the potential corresponds to the degenerated value $|\phi| = \sqrt{-\mu^2/2\lambda} \equiv v/\sqrt{2}$. To apply perturbative theory, a minimum of energy is required, therefore, the field has to be redefined as $\phi(x) = 1/\sqrt{2}(v + \sigma(x) + i\eta(x))$ to transform the Lagrangian on the equation 70.

$$\begin{aligned}\mathcal{L}_{SSB} = &\frac{1}{2}\partial_\mu \sigma \partial^\mu \sigma - \frac{1}{2}(2\lambda v^2)\sigma^2 - \frac{1}{4} F^{\mu\nu} F_{\mu\nu} + \frac{q^2 v^2}{2} A_\mu A^\mu + \\ &\frac{1}{2}\partial^\mu \eta \partial_\mu \eta + \frac{1}{2} q v A_\mu \partial^\mu \eta + \text{ interactions}\end{aligned} \tag{70}$$

Via SSB, the gauge boson obtains the mass term ($m_A^2 = q^2 v^2$), also the scalar field ($m_\sigma^2 = 2\lambda v^2$) and the massless goldstone boson appear. But this process also generate

some mixing terms and due to the massless goldstone boson, the problem is not solved completely.

Higgs mechanism proposed to use a more general parametrization $\phi(x) = e^{\frac{i\eta(x)v}{\sqrt{2}}}(v + \sigma(x))$ which $\phi(x) \xrightarrow{\eta(x)<<<1} \phi(x) = 1/\sqrt{2}(v + \sigma(x) + i\eta(x))$ [47], choosing a unitary gauge, the Lagrangian will transform to equation 71

$$\begin{aligned}\mathcal{L}_{SSB} = &\frac{1}{2}\partial_\mu\sigma\partial^\mu\sigma - \frac{1}{2}(2\lambda v^2)\sigma^2 - \frac{1}{4}F^{\mu\nu}F_{\mu\nu} + \frac{q^2v^2}{2}A_\mu A^\mu + \\ &- \lambda v\sigma^3 - \frac{\lambda}{3}\sigma^4 + \text{ interactions}\end{aligned} \tag{71}$$

The Goldstone field disappeared, but the terms corresponding to the gauge boson mass and the scalar field mass remains in the Lagrangian. The Higgs mechanism generated mass to the gauge field. In QED case, it does not make any sense, because having a broken symmetry in the vacuum will purport that vacuum is full of charge and the particles will interact with it. However, this idea will be very important for the $SU(2)_L \otimes U(1)_Y$ gauge symmetry group.

Appendix B: DEPFET Parameters

B.1 *DEPFET: Internal Amplification*

The internal amplification (g_q) is defined with the transistor's current (I_{DS}) as a function of the charge located on the internal gate (Q_{sig}) considering a constant Gate-Source voltage, V_{GS}, (see Fig. 27) and a constant Source-Drain voltage, V_{DS} (Eq. 72).

$$g_q = \left[\frac{\partial I_{DS}}{\partial Q_{sig}}\right]_{V_{GS},V_{DS}} \tag{72}$$

Equation 72 can be developed, noticing that changes on the Gate-Source voltage (V_{GS}) are proportional to the changes produced on internal gate charge (Q_{sig}). Equation 73 shows this relation, where f is the fraction of charge that does not affect the transistor's current due to the parasitic couplings. C_G is the Gate-Channel capacitance and can be written as a function of the transistor parameters, $C_G = WLC_{ox}$, where W is the transistor's width, L is the gate length, $C_{ox} = \frac{\epsilon_{ox}\epsilon_0}{d_{ox}}$ is the oxide capacitance and d_{ox} is the oxide width.

$$\partial V_{GS} = (1-f)\frac{\partial Q_{sig}}{C_G} \tag{73}$$

On the other hand, considering that MOSFET transistors on DEPFET devices operate in the saturation region, the Drain-Source current ($I_{DS_{sat}}$) can be written as equation 74, where μ_p is the hole mobility.

$$I_{DS_{sat}} = I_{DS}(V_{DS_{sat}}) = -\frac{W}{L}\mu_p C_{ox}\frac{V_{DS_{sat}}^2}{2} \tag{74}$$

$$g_{q_{sat}} = (1-f)\sqrt{\frac{-2\mu_p I_{DS_{sat}}}{WL^3 C_{ox}}} \tag{75}$$

In summary, the internal amplification can be defined as a function of the transistor's design parameters (Eq. 76), see Appendix C from Ref. [69]. In the current devices, which use $L = 5$ µm and a $I_{DS} \sim 100$ µA/LSB, the internal gain is about 750 pA/e^-.

$$g_q \propto L^{-3/2},\ W^{-1/2},\ d_{ox}^{1/2},\ I_{DS}^{1/2} \tag{76}$$

Appendix C: Needle Card Design Figures

C.1 *EMCM Prototype*

The special needs of each connection have been considered during the definition of the needle distribution. Several needles are used to connect the Cu pads, since high current will travel through them. Same happens with some Al pads, which require multiple contacts. For the EMCM prototype, 114 needles were used (Fig. 130).

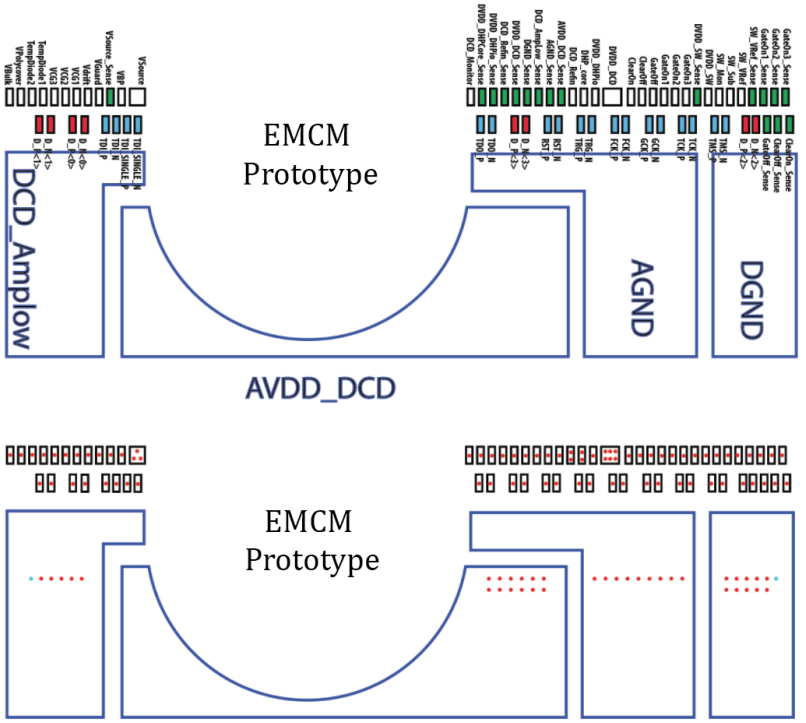

Figure 130: Top: EMCM pad distribution. Bottom: Contact distribution of the needles over the EMCM pad footprint, the red dots represent the place where the needle will perform the touchdown.

Figure 130 - top shows the pad distribution, including the 8 pads for the LVDS high speed lines (red) and the pads related with the JTAG configuration (blue). The rest of the pads are the necessary connections for the power supply (white), and the sense line connections (green). The image on the bottom, shows the defined contact position of the needles (red dots).

The attachment via distribution on the PCB [1] has to be defined according to the needle contact distribution. For this reason, a vision hole (needle windows) will be implemented to be able to control the touchdown process. Figure 131 shows the attachment via distribution on the PCB.

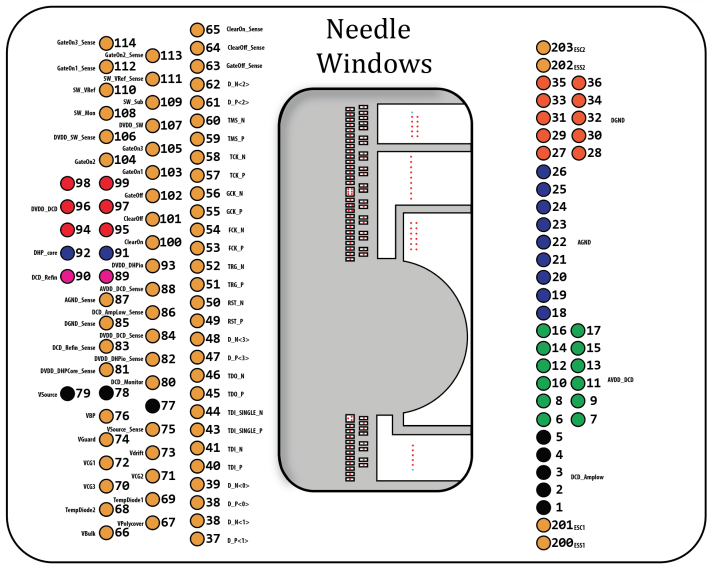

Figure 131: EMCM attachment via distribution on the PCB, the vias are distributed on two regions, keeping a open windows to make visible the tips of the needles.

The PCB was designed routing the required lines, from the connectors to the attachment via distribution, including the required filtering and decoupling region. The size of the PCB was limited by the connectors and the requirement of keeping the high speed lines as short as possible, forcing to move the Infiniband connectors near to the attachment via distribution. Also, two connectors to monitor the voltages were also added. Notice that another window has been implemented on the region where the DEPFET matrix will be located, to avoid covering it. Figure 132 shows the layout of the EMCM needle card PCB [2].

1 Holes that traverse the PCB, used to communicate different layers or, in this case, to assemble the metal needles.

2 The PCB routing and design was performed by Dr. Daniel Esperante.

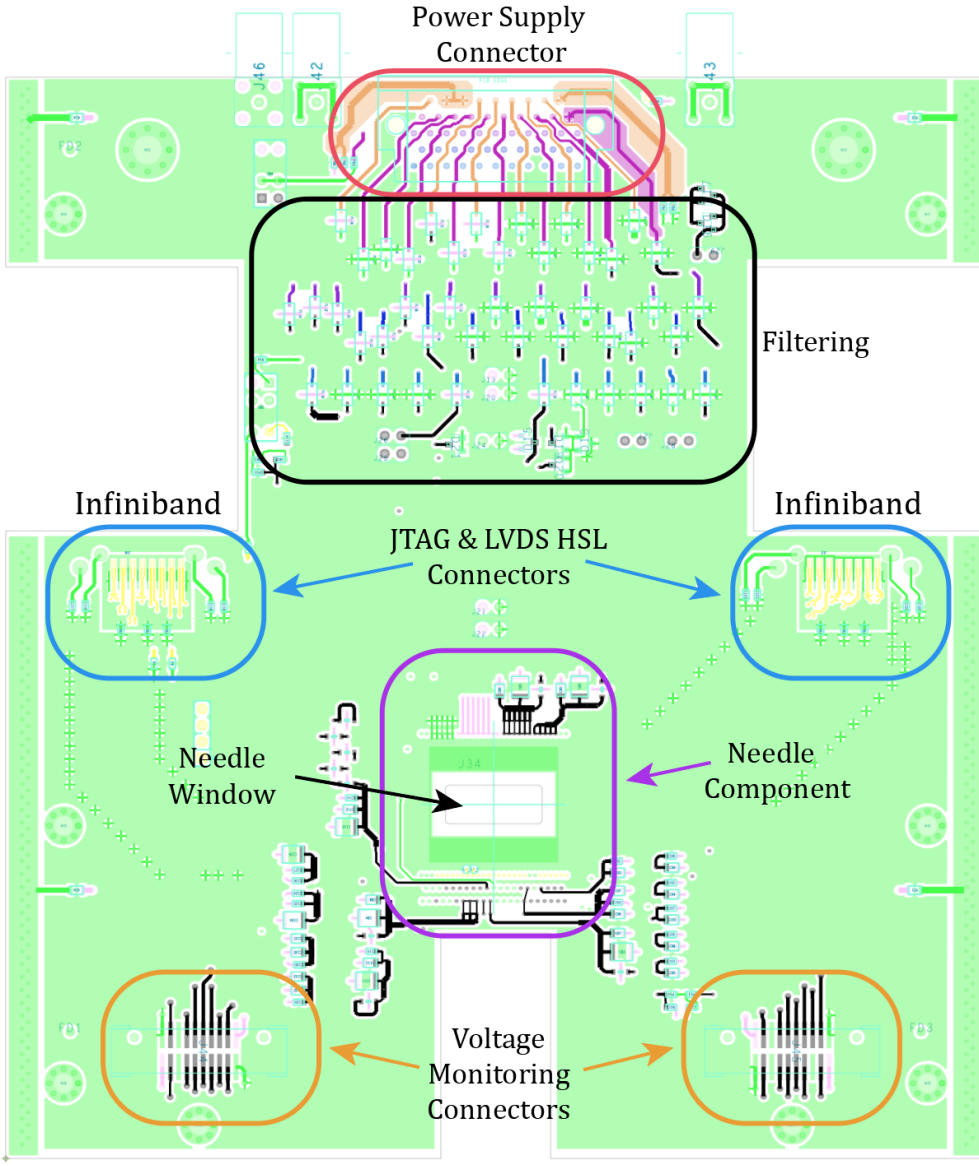

Figure 132: EMCM needle card PCB layout.

C.2 *PXD9 Needle Card*

The needle card prototypes designed for the DEPFET PXD production were based on the EMCM needle card, implementing the corresponding modifications to improve the performance and the stability of the high speed links. The position of the pads has been redesigned and two distinct distributions have been implemented, depending on the prototype. Likewise, two needle cards have been constructed: one for the IF and OB modules (*design A*) and a second for the IB and OF modules (*design B*). Figure 133 and 134 show the pad distribution, including the 8 pads for the LVDS high speed lines (red) and the pads related with the JTAG configuration (blue). The rest of the pads are the necessary connections to the power supply (white), and the sense line connection (green). The image on the bottom, shows the defined contact position of the needles (red dots), in this case the needles contact distribution has been redesigned to minimize the spread of the scratches over the pad surface, replacing a double row distribution to a linear distribution, which allow to perform the needle contact on the corner of the pads.

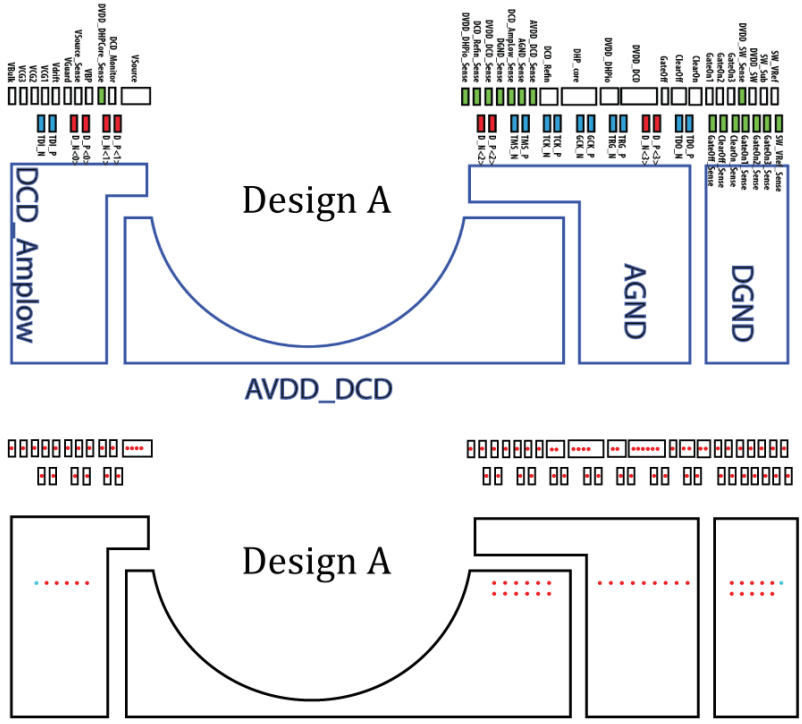

Figure 133: Top: Needles footprint. Bottom: Contact distribution of the needles over the IF-OB pads footprint, the dots represent the place where the needle will perform the touch-down.

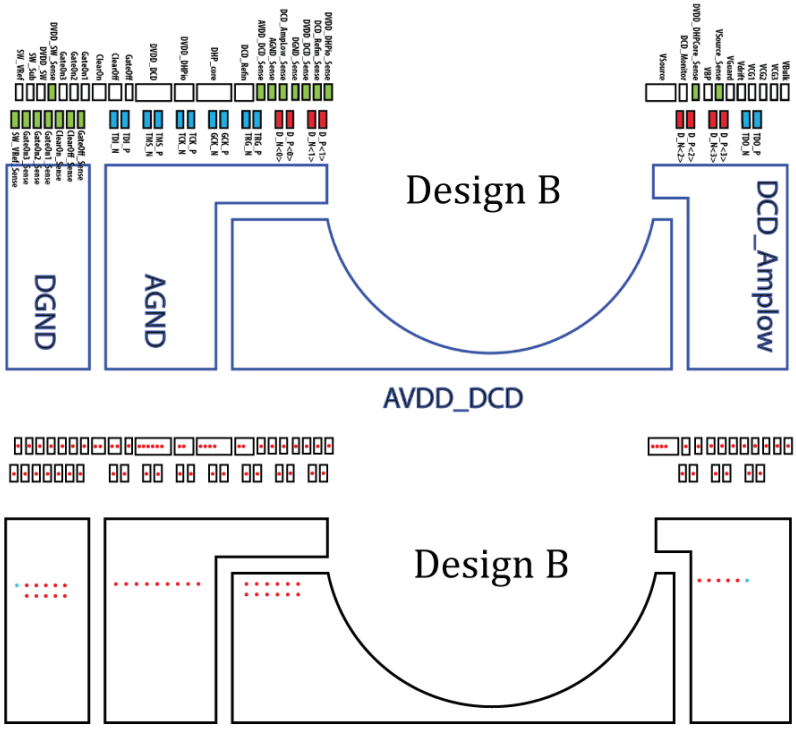

Figure 134: Top: Needle footprint. Bottom: Contact distribution of the needles over the OF-IB pads footprint, the dots represent the place where the needle will perform the touchdown.

Another important modification was the minimization of the length of the HS link needles, for this, the eight attachment vias, corresponding to the HSL, have been moved near to needle window, on the left-side, implementing them as close as possible to the pads. Figure 135 shows the needle components of the design A (top) and design B (bottom). They seem to be specular images, but, they are not, since the order on the pads is different from one design to another.

The PCB design has been modified to accommodate the new DHE connectors, replacing one ifiniband connector with a RJ45, moreover, all bends on the HS link PCB paths have been removed to reduce as much as possible the length of the lines. Finally, the sampling point of the sense lines has been moved before the needle spider. Figure 136 shows the over-layer of the design B. Figure 137 shows the design A PCB layout [3].

3 The PCB routing was performed by Dr. Daniel Esperante.

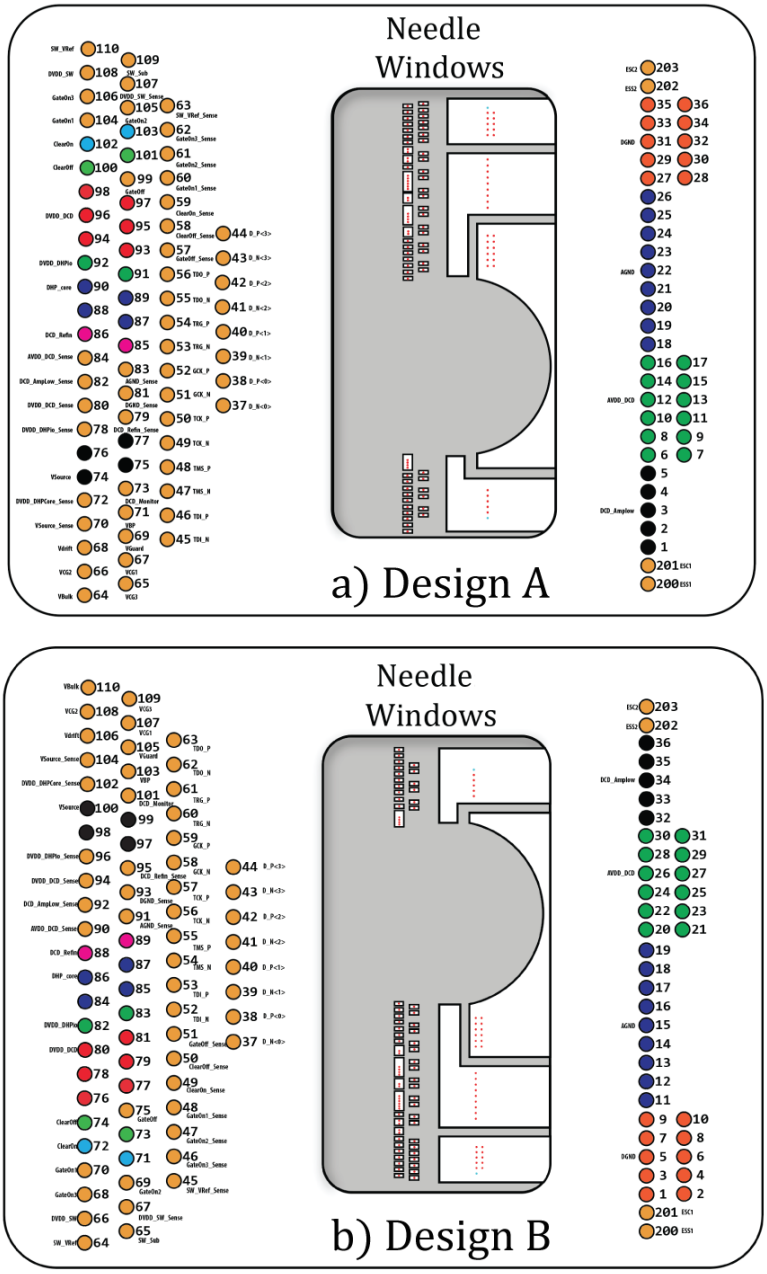

Figure 135: PXD9 needle component.

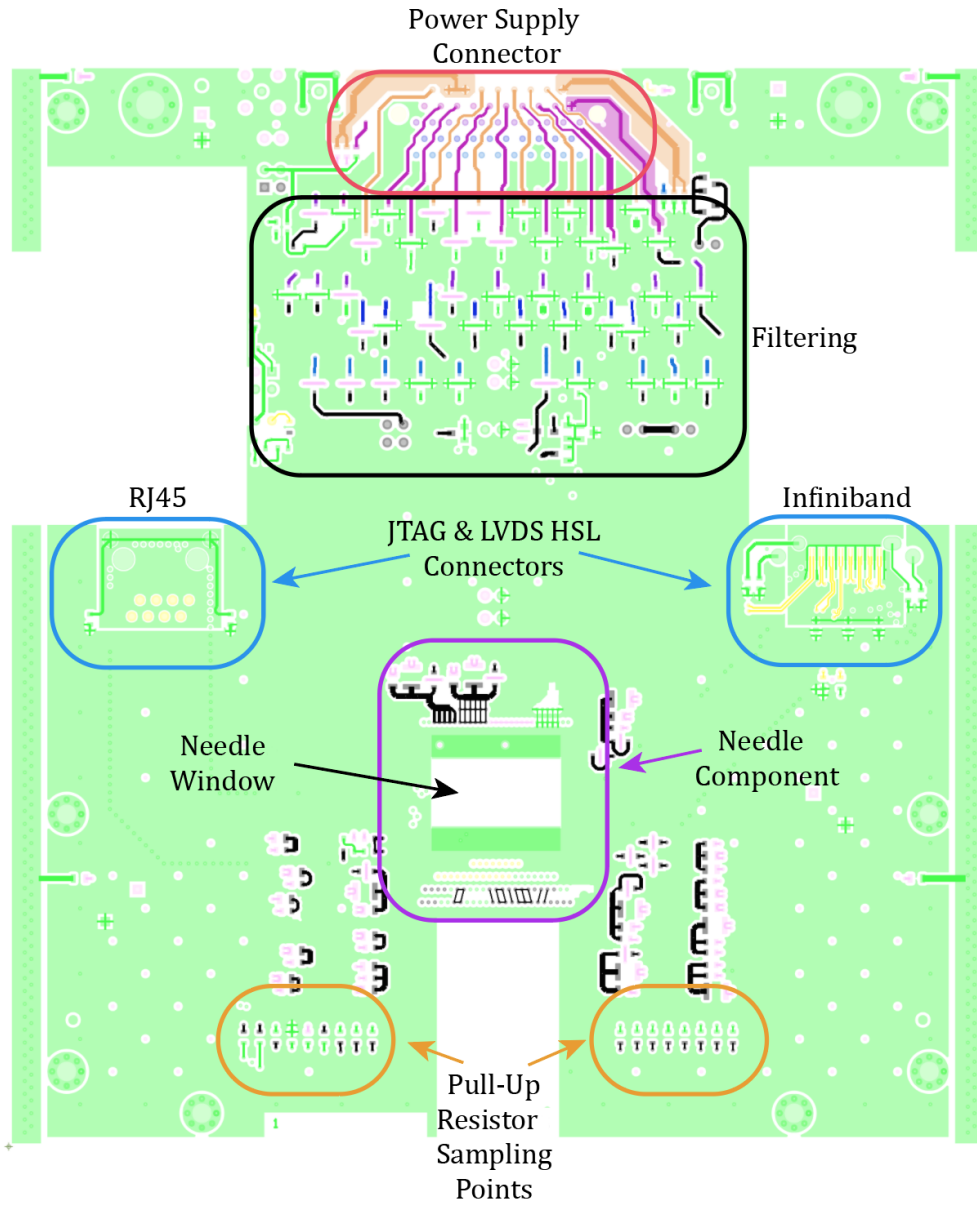

Figure 136: PXD9, design B, needle card PCB layout.

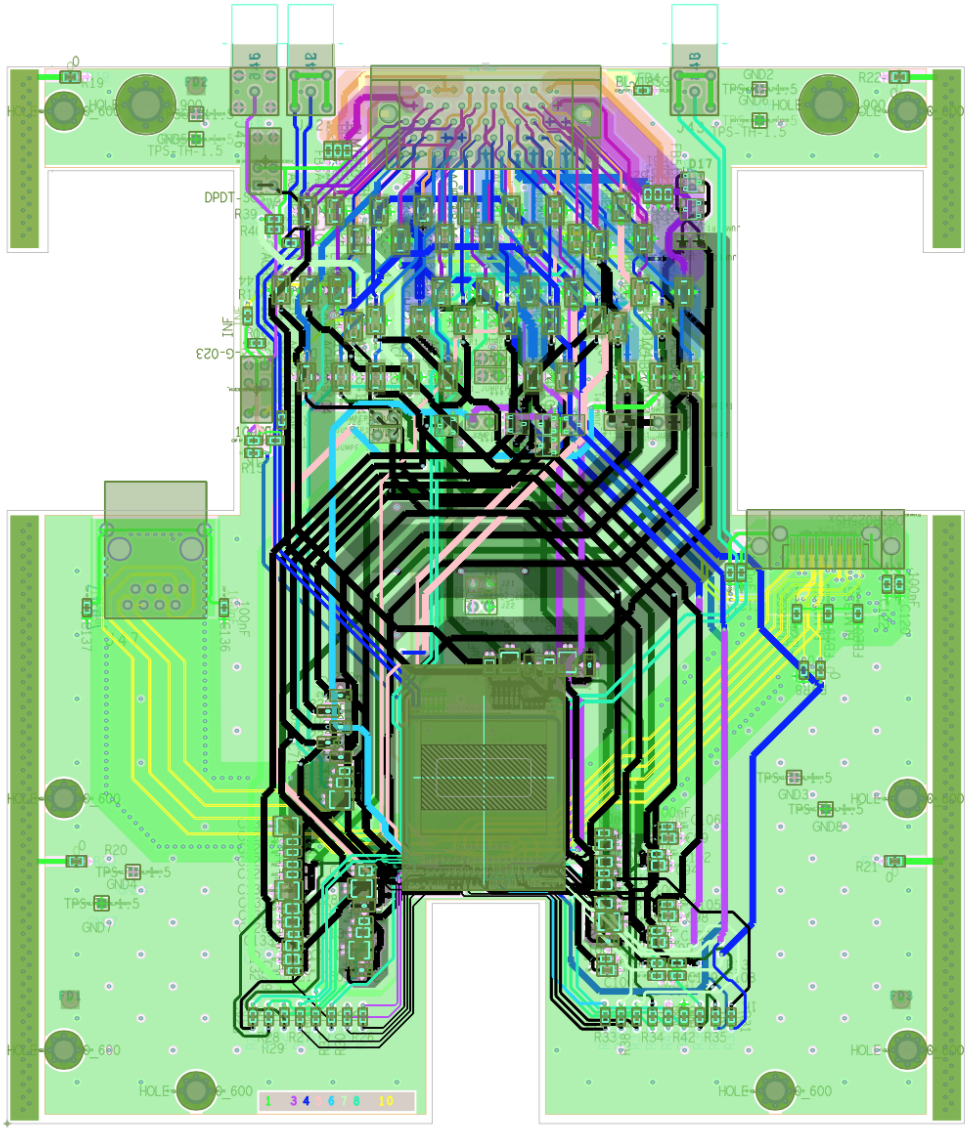

Figure 137: PXD9, design A, needle card PCB layout.

Appendix D: PXD9 Test

D

D.1 *Testing Protocol over PXD9*

The testing protocol was defined, based on the results obtained with the EMCM needle card, to perform a sanity check over the full assembled modules and search for problems on the ASICs (essentially related with the bump-bonding). The PXD9 W36-IF was the first opportunity to fully go over all the steps and prove the capability of the needle card to apply them. This module (in contrast with the EMCM) includes a functional DEPFET matrix, therefore it offered the chance to power up the matrix and obtain matrix data. Hence, this was the ultimate goal, but previously all the testing protocol steps were carried on, the output results are shown in the following list:

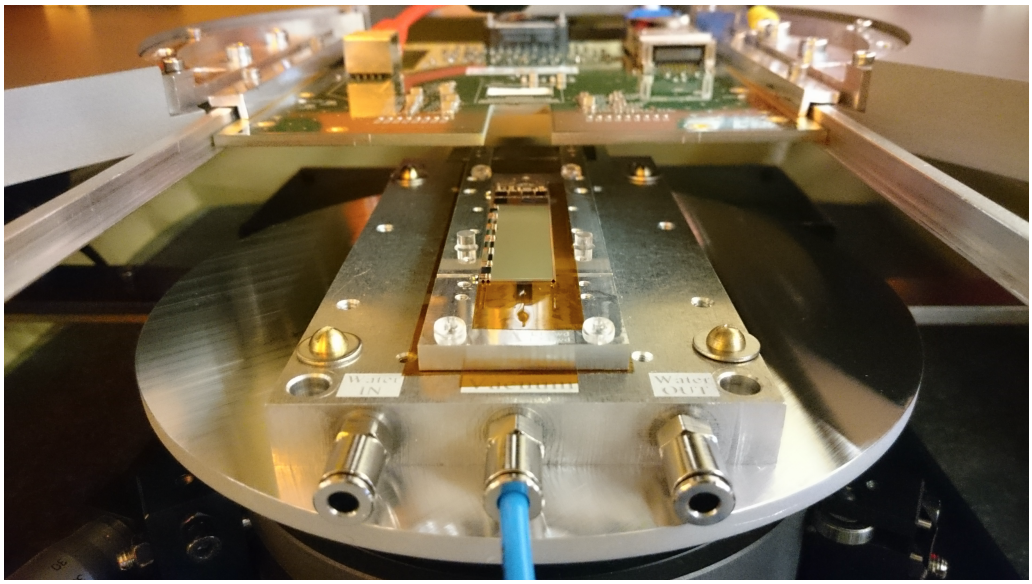

Figure 138: PXD9 W36-IF module on the probe station. Starting from the bottom, circular plate to adapt the probe station chuck to the cooling block, cooling block, module jig and needle card fixed on the corresponding holder.

- **Voltages and Current consumption (digital) and JTAG Chip Configuration:** A first touchdown were performed with an overtravel of 50 µm. Then, the power up sequence was started, step by step, until ASICs digital region was enabled. Since the current consumptions were on the expected range the configuration script

was executed and the current consumption changed as expected, an output example is show on figure 139.

min.	Set Voltage	max.	Reg.	Voltage at Regulator	Voltage at Load	Current	
0 mV	0 mV	0 mV		-13 mV	-8 mV	0 mA	sw-sub
0 mV	1800 mV	2000 mV		2312 mV	1801 mV	15 mA	sw-dvdd
0 mV	0 mV	0 mV		-8 mV	6 mV	0 mA	sw-refin
0 mV	400 mV	500 mV		469 mV	401 mV	-2 mA	dcd-amplow
0 mV	1900 mV	2000 mV		2018 mV	1900 mV	113 mA	dcd-avdd
0 mV	1900 mV	2000 mV		2819 mV	1905 mV	428 mA	dcd-dvdd
0 mV	900 mV	1300 mV		961 mV	902 mV	5 mA	dcd-refin
0 mV	1200 mV	1640 mV		2383 mV	1199 mV	399 mA	dhp-core
0 mV	1800 mV	2000 mV		2549 mV	1799 mV	169 mA	dhp-io

Figure 139: Voltages control table after enabling the digital region of the ASICs. Starting from left, minimum voltage that can be applied, voltage selected, maximum voltage, green - enabled voltage, voltage provided by the PS, voltage applied on the sampling point, current consumption.

- **Boundary-Scan:** The boundary-scan test was applied using the specific boundary scan tool and the breakout board [82]. The results are shown on figure 140, which did not reveal any issue on the digital connection between the ASICs (In this case, the infrastructure and the interconnection tests were performed at the same time).

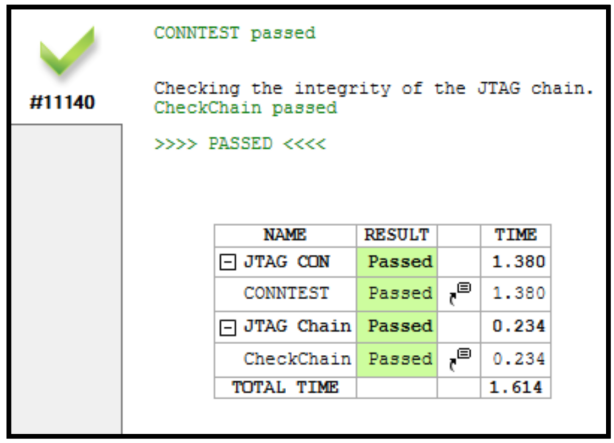

Figure 140: PXD9 W36-IF boundary scan results.

- **High Speed Link Stability:** After disconnecting the breakout board, the data connection can be enabled, the process requires a fine tuning of the connection parameters. Figure 141 shows the indicators, pointing out that the four data connections are stably established.

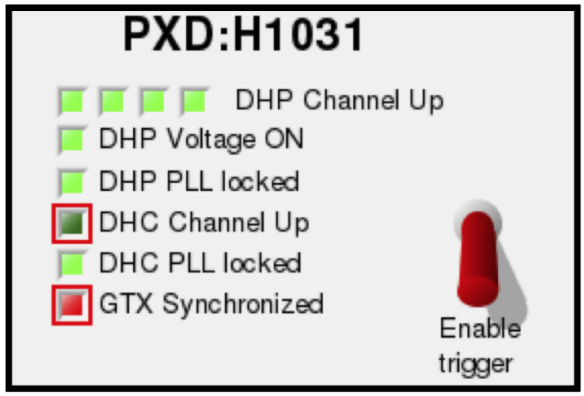

Figure 141: Indicator on the standard control software pointing that the four data connections are stably established

- **Voltages and Current consumption (analog):** The power up sequence was continued, step by step, until analog region of the ASICs was enabled. The changes on the current consumption were on the expected range. An example of the outputs is show on figure 142.

min.	Set Voltage	max.	Reg.	Voltage at Regulator	Voltage at Load	Current	
0 mV	0 mV	0 mV		-13 mV	-8 mV	0 mA	sw-sub
0 mV	1800 mV	2000 mV		2567 mV	1798 mV	7 mA	sw-dvdd
0 mV	0 mV	0 mV		0 mV	-7 mV	0 mA	sw-refin
0 mV	400 mV	500 mV		684 mV	396 mV	-877 mA	dcd-amplow
0 mV	1900 mV	2000 mV		4673 mV	1897 mV	2445 mA	dcd-avdd
0 mV	1900 mV	2000 mV		3326 mV	1899 mV	650 mA	dcd-dvdd
0 mV	900 mV	1300 mV		2858 mV	899 mV	351 mA	dcd-refin
0 mV	1200 mV	1640 mV		2669 mV	1196 mV	416 mA	dhp-core
0 mV	1800 mV	2000 mV		2696 mV	1802 mV	175 mA	dhp-io

Figure 142: Voltages control table after enabling the analog region of the ASICs. Starting from left, minimum voltage that can be applied, voltage selected, maximum voltage, green - enabled voltage, voltage provided by the PS, voltage applied on the sampling point, current consumption.

- **DCD Pedestals and Test Injection Pattern:** When the analog region of the ASICs was enabled, the DCD pedestal (Fig. 143 - default current of the DCD current converters) and the Test Injection Pattern (Fig. 144 - predefined digital pattern used to optimize the delay communication between the DCD and the DHP) can be extracted as a crosscheck over the digital connection between the DCD and DHP and to prove the stability of the data connections.

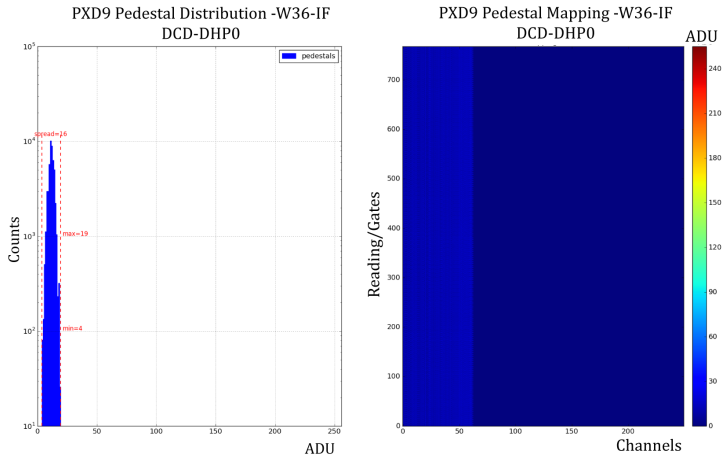

Figure 143: Example of the DCD pedestals only enabling the DCD-DHP pair 0. Left: ADU distribution, right: ADU map.

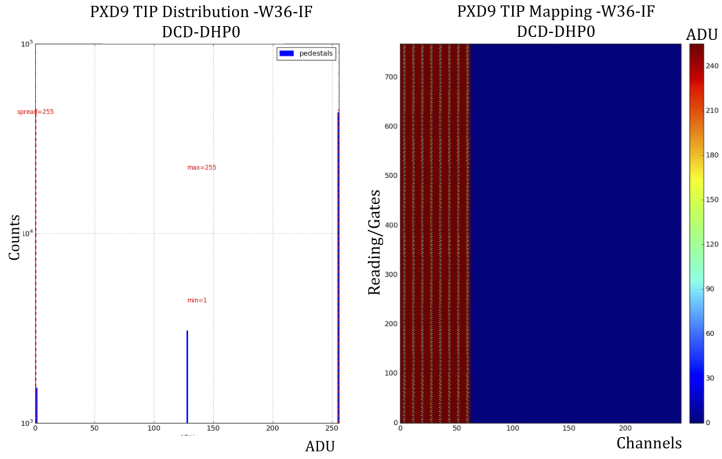

Figure 144: Example of the Test Injection Pattern only enabling the DCD-DHP pair 0. Left: ADU distribution, right: ADU map.

- **Voltages and Current consumption (matrix):** Once the stability of the needle contact and the system were ensured, the process of powering up the DEPFET matrix was carried out, step by step, and checking that no current consumption went out of the expected range. An output example is show on figure145.

min.	Set Voltage	max.	Reg.	Voltage at Regulator	Voltage at Load	Current	
0 mV	0 mV	0 mV		-13 mV	-8 mV	0 mA	sw-sub
0 mV	1800 mV	2000 mV		2567 mV	1798 mV	7 mA	sw-dvdd
0 mV	0 mV	0 mV		0 mV	-7 mV	0 mA	sw-refin
0 mV	400 mV	500 mV		684 mV	396 mV	-877 mA	dcd-amplow
0 mV	1900 mV	2000 mV		4673 mV	1897 mV	2445 mA	dcd-avdd
0 mV	1900 mV	2000 mV		3326 mV	1899 mV	650 mA	dcd-dvdd
0 mV	900 mV	1300 mV		2858 mV	899 mV	351 mA	dcd-refin
0 mV	1200 mV	1640 mV		2669 mV	1196 mV	416 mA	dhp-core
0 mV	1800 mV	2000 mV		2696 mV	1802 mV	175 mA	dhp-io
0 mV	10000 mV	10000 mV		10005 mV	10001 mV	0 mA	bulk
0 mV	20000 mV	22000 mV		20246 mV	19993 mV	24 mA	clear-on
0 mV	5000 mV	20000 mV		4897 mV	5001 mV	-17 mA	clear-off
-4000 mV	-1000 mV	3000 mV		-1214 mV	-1006 mV	-2 mA	gate-on1
-4000 mV	-1000 mV	3000 mV		-1027 mV	-997 mV	-1 mA	gate-on2
-4000 mV	-1000 mV	3000 mV		-1064 mV	-1001 mV	-1 mA	gate-on3
0 mV	3000 mV	6000 mV		3039 mV	2996 mV	10 mA	gate-off
0 mV	6000 mV	7000 mV		7169 mV	5997 mV	30 mA	source
-5000 mV	-500 mV	0 mV		-501 mV	-497 mV	1 mA	ccg1
-5000 mV	-500 mV	0 mV		-492 mV	-508 mV	0 mA	ccg2
-5000 mV	-500 mV	0 mV		-502 mV	-501 mV	1 mA	ccg3
-80000 mV	-70000 mV	0 mV		-70025 mV	-70078 mV	0 mA	hv
-6000 mV	-5000 mV	0 mV		-5005 mV	-5006 mV	0 mA	drift
0 mV	0 mV	0 mV		-14 mV	-16 mV	0 mA	polycover
-6000 mV	-5000 mV	0 mV		-4997 mV	-5004 mV	0 mA	guard

Figure 145: Voltages control table after enabling the DEPFET matrix. Starting from left, minimum voltage that can be applied, voltage selected, maximum voltage, green - enabled voltage, voltage provided by the PS, voltage applied on the sampling point, current consumption.

- **Pedestals:** After a complete the power up sequence, a trigger can be sent to extract the matrix information. Figure 146 presents an image of the pedestal distribution (left) and a pedestals map (right).

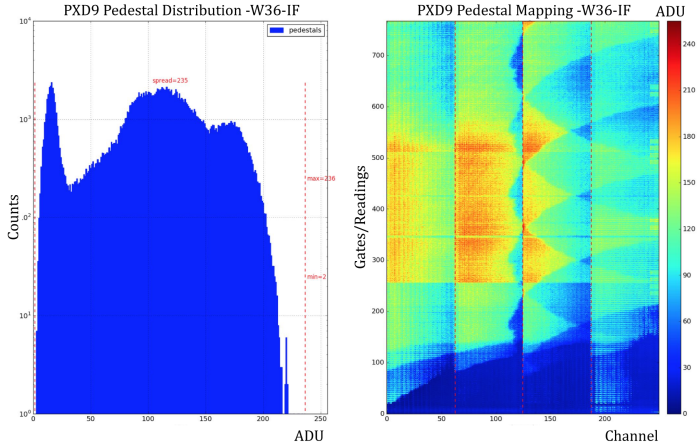

Figure 146: Pedestal distribution (left) and a pedestals map (right).

- **Matrix Response:** To prove the response of the matrix, a laser beam was pointed over the surface. Figure 147 shows the spot on different position of the matrix (saturate region), only extracting data from the DCD-DHP pair 0.

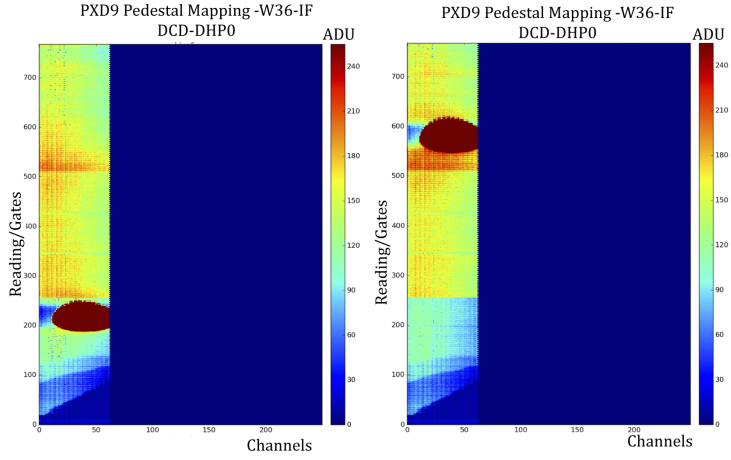

Figure 147: Matrix response, pointing with a laser in different positions, only extracting data from the DCD-DHP pair 0.

D.2 *Other Pictures:*

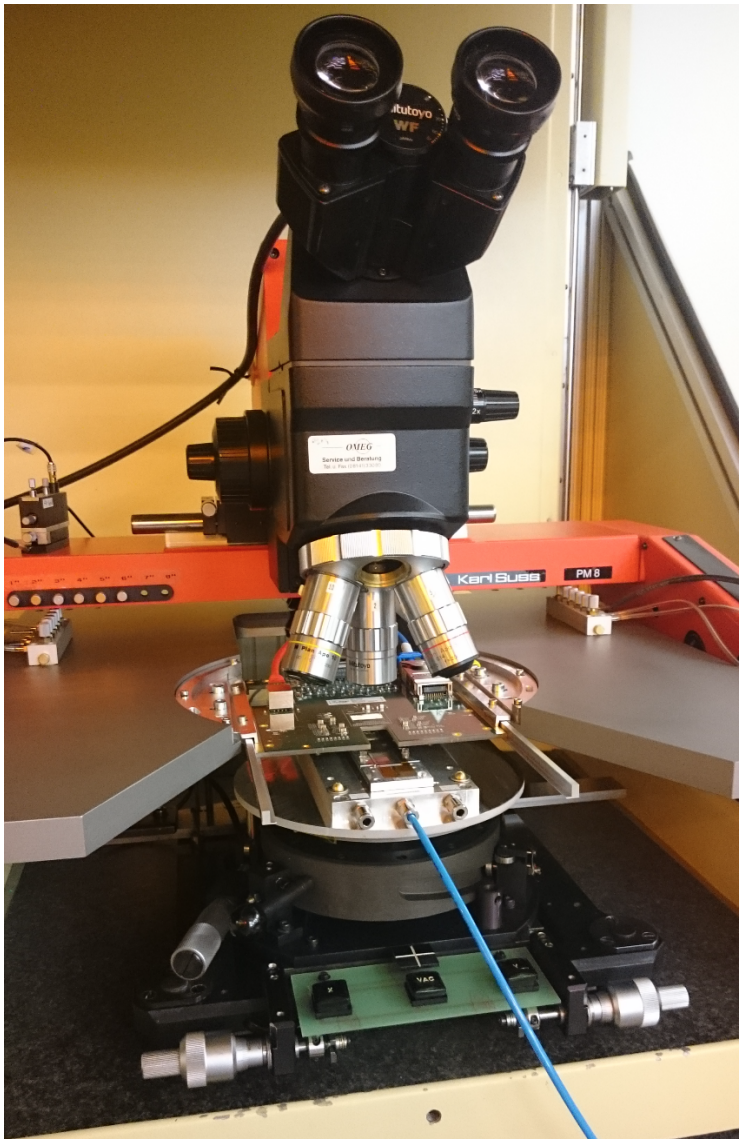

Figure 148: Adapted probe station to hold the needle card and the cooling system, for the sanity check, during the PXD production.

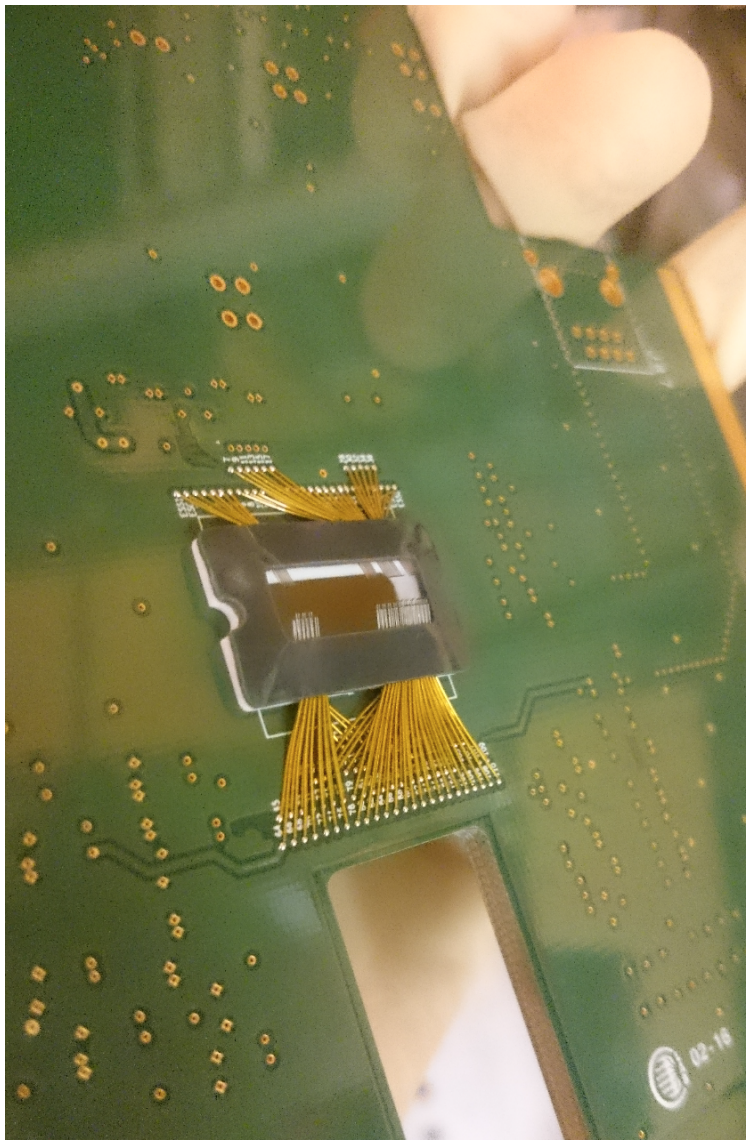

Figure 149: Image of the needles spider. Needle card design A.

Appendix E: $B_\gamma(m_t, \zeta_{S'_\gamma})$ Studies

E.1 *Multiple Final Photons, Selection Strategy*

In case of two photons survive the selection steps, a strategy to proceed has to be defined. In such cases, there are two options: select one of them, as the final candidate, and calculate S', using the equation 52 or consider all the candidates, and use the extended equation instead (Eq. 51). Figure 150 shows the comparison between the different criteria and the $B_\gamma(m_t, \zeta_{S'_\gamma})$ distribution at parton level. The selection criteria tested were; choose the photon with maximum energy (red), choose the most isolated photon (blue). The distribution with multiple photons was also considered (purple). The figure proved that these criteria do not change the $B_\gamma(m_t, \zeta_{S'_\gamma})$ distribution substantially. Therefore, the best option is to apply the criterion which implementation will be easier, in this case, the energy criterion. The differences between the $B_\gamma(m_t, \zeta_{S'_\gamma})$ distribution, at parton level , and the resulting distribution after applying the selection criteria is due to the background photons that cannot be discriminated via the selection cuts.

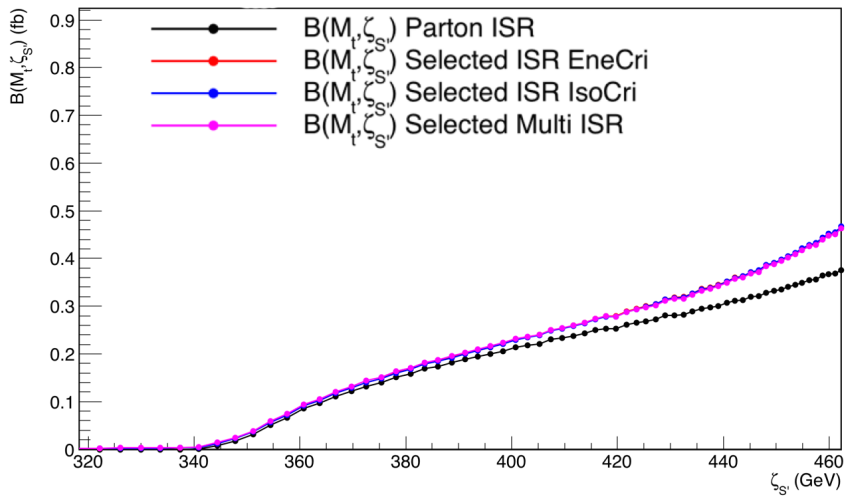

Figure 150: $B_\gamma(m_t, \zeta_{S'_\gamma})$ comparison, using a final selection criteria, in case multiple photos survive to the selection process. Black: $B(m_t, \zeta_{S'})$ in at partonic level. Red: Most energetic photon selected. Blue: Most isolated photon selected. Purple: Multiple photon calculation.

Bibliography

[1] D. Mendeleev. Über die beziehungen der Eigenschaften zu den Atom Gewichten der Elemente. *Zeitschrift für Chemie*, 12:405–406, 1869.

[2] H. Hertz. Über den Einfluss des ultravioletten Lichtes auf die Electrische Entladung. *Annalen der Physik*, 8(267):983–1000, 1887.

[3] A. Einsten. Über einen die Erzeugung und Verwandlung des Lichtes betreffenden heuristischen Gesichtspunkt. *Annalen der Physik*, 17(6):132–148, 1905.

[4] J. J. Thomson. Cathode Rays. *Phil. Mag.*, 44(269), 1897.

[5] R.A. Millikan. The isolation of an Ion, a Precision Measurement of its Charge and a Correction of Stokes's Law. *Science*, 32(822):436–448, 1910.

[6] E. Rutherford. The Scattering of alpha and beta Particles by Matter and the Structure of the atom. *Philosophical Magazine*, 21:669–688, 1911.

[7] H. Yukawa. On the Interaction of Elementary Particles. *Proc. Phys. Math. Soc. Jap.*, 17(48), 1935.

[8] E. Rutherford. Collision of α particles with light atoms. An anomalous effect in nitrogen. *Philosophical Magazine*, 37(222):581–587, 1919.

[9] P. M. S. Blackett. The Ejection of Protons from Nitrogen Nuclei, Photographed by the Wilson Method. *Proc. R. Soc. Lond.*, A107:349–360, 1925.

[10] J. Chadwick. The Existence of a Neutron. *Proc. Roy. Soc.*, A136(692), 1932.

[11] V. F. Heiss. Über Beobachtungen der durchdringenden Strahlung bei sieben Freiballonfahrten. *Physikalische Zeitschrift*, 13:1084–1091, 1912.

[12] W. Kolhörster W. Bothe. Die Natur der Höhenstrahlung. *Naturwissenschaften*, 17:271–273, 1929.

[13] E. Schrödinger. An Undulatory Theory of the Mechanics of Atoms and Molecules. *Phys. Rev.*, 28(6):1049–1070, 1926.

[14] A. Einstein. Zur Elektrodynamik bewegter Körper. *Annalen der Physik*, 17:891–921, 1905.

[15] P. A. M. Dirac. The Quantum Theory of the Electron. *Proceedings of the Royal Society A: Mathematical, Physical and Engineering Sciences*, 117(778):610–614, 1928.

[16] P. A. M. Dirac. A Theory of Electrons and Protons. *Proc. R. Soc. Lond.*, 126(801):360–365, 1930.

[17] C. D. Anderson. The Apparent Existence of Easily Deflectable Positives. *Science*, 76(1967):238–239, 1932.

[18] C. D. Anderson. The Positive Electron. *Phys. Rev.*, 43(6):491–494, 1933.

[19] E. Fermi. Tentativo di una Teoria dei Raggi β. *La Ricerca Scientifica*, 2(12), 1933.

[20] S. H. Neddermeyer and C. D. Anderson. Note on the Nature of Cosmic-Ray Particles. *Phys. Rev.*, 51(884), 1937.

[21] G. P. S. Occhialini C. M. G. Lattes and C. F. Powell. Observations on the Tracks of Slow Mesons in Photographic Emulsions. *Nature*, 160:453–456, 1947.

[22] G. D. Rochester and C. C. Butler. Evidence for the Existence of Unstable Elementary Particles. *Nature*, 160:855–857, 1947.

[23] A. Pais. Some Remarks on the V-Particles. *Phys. Rev.*, 86(5):663–672, 1952.

[24] F. Reines and L. Cowan. Detection of a Free Neutrino. *Phys. Rev.*, 92:830, 1953.

[25] C. N. Yang and R. L. Mills. Conservation of Isotopic Spin and Isotopic Gauge Invariance. *Phys. Rev.*, 96:191–195, 1954.

[26] M. Gell-Mann. The Interpretation of the New Particles as Displaced Charge Multiplets. *Nuov. Cim. Suppl.*, 4(2):848–866, 1956.

[27] M.Gell-Mann. Symmetries of Barions and Mesons. *Phys. Rev.*, 125:1067–1084, 1962.

[28] Y. Ne'eman. Derivation of Strong Interactions from a Gauge Invariance. *Nuclear Physics*, 26:222–229, 1961.

[29] V. E. Barnes et al. Observation of a Hyperon with strangeness minus three. *Phys. Rev.*, 12(8):204–206, 1964.

[30] G. Danby et al. Observation of High-Energy Neutrino Reactions and the Existence of Two Kinds of Neutrinos. *Phys. Rev.*, 9:36–44, 1962.

[31] M. Gell-Mann. A Schematic Model of Barions and Mesons. *Phys. Lett.*, 8(3):214–215, 1964.

[32] M. Y. Han and Y. Nambu. Three-Triplet Model with Double SU(3) Symmetry. *Phys. Rev.*, 139:1006–1010, 1965.

[33] S. L. Glashow. Partial-Symmetries of Weak-Interactions. *Nucl. Phys.*, 22:579–588, 1961.

[34] P. W. Higgs. Broken Symmetries and the Masses of Gauge Bosons. *Phys. Rev. Lett.*, 13:508–509, 1964.

[35] J. Ilipoulos S. L. Glashow and L. Maiani. Weak Interactions with Lepton-Hadron Symmetry. *Phys. Rev.*, 2:1285–1292, 1970.

[36] H. Leutwyler M. Gell-Mann and H. Fritzsch. Advantages of the Color Octet Gluon Picture. *Phys. Lett.*, 47B:365–368, 1973.

[37] S. W. Herb et al. Observation of a Dimuon Resonance at 9.5 GeV in 400 − GeV Proton-Nucleus Collisions. *Phys. Rev. Lett.*, 39:252–255, 1977.

[38] TASSO Collaboration. Evidence for Planar Events in e^+e^- Annihilation at High Energies. *Phys. Lett. B*, 86:243–249, 1979.

[39] PLUTO Collaboration. Evidence for Gluon Bremsstrahlung in e^+e^- Annihilations at High Energies. *Phys. Lett.*, B86(3):418–425, 1979.

[40] C. Rubbia. Experimental Observation of the Intermediate Vector Bosons W^+, W^- and Z^0. *Rev. Mod. Phy.*, 57:699–722, 1985.

[41] D. E. Groom et al. Number of Light Neutrino Types. *Eur. Phys. Jour*, C15(1), 2000.

[42] F. Abe et al. Observation of Top Quark Production in $p\bar{p}$ Collisions with the Collider Detector at Fermilab. *Phys. Rev. Lett.*, 74:2626–2631, 1995.

[43] K. Kodama et al. Observation of tau Neutrino Interactions. *Phys. Lett.*, 504(3):218–224, 2000.

[44] G. Aad et al. Measurement of the Higgs Boson Mass from the $h \to \gamma\gamma$ and $h \to zz^* \to 4l$ channels in $p\bar{p}$ Collisions at center-of-mass energies of 7 and 8 GeV with the ATLAS Detector. *Phys. Rev.*, D90(052004), 2014.

[45] C. Patrignani et al. (Particle Data Group). Review of Particle Physics. *Chin. Phys.*, C40(100001), 2016.

[46] María José Costa Mezquita. *Determination of the b Quark Mass at the M_Z Scale with the Delphi Detector at LEP*. PhD thesis, Universidad de Valencia, January 2003.

[47] A. Pich. The Standard Model of Electroweak Interactions. *arXiv*, 0705.4264, 2012.

[48] The ALEPH. DELPHI. L3. OPAL and SLD Collaborations. Precision Electroweak Measurements on the Z Resonance. *Phys. Rept.*, 427, 2006.

[49] The ATLAS and CMS Collaborations. Combined Measurement of the Higgs Boson Mass in $p\bar{p}$ Collisions at $\sqrt{s} = 7$ and 8 TeV with the ATLAS and CMS Experiment. *Phys. Rev. Lett*, 114(191803), 2015.

[50] Adrián Irles Quiles. *Determination of the Top-Quark Pole Mass using $t\bar{t}$+1-jet Event with ALTAS Detector at the LHC*. PhD thesis, Universidad de Valencia, December 2014.

[51] ILC Community Collaboration. The International Linear Collider. *TDR*, Volume 1: Executive Summary, 2013.

[52] CLIC Collaboration. Updated Baseline for a Staged Compact Linear Collider. *CERN Yellow Report*, CERN-2016-004, 2016.

[53] Belle II Collaboration. Belle II Technical Design Report. *KEK Report*, 2010-1, 2010.

[54] ILC Community Collaboration. The International Linear Collider. *TDR*, Volume 2: Physics, 2013.

[55] Ignacio Garcia Garcia. *Future Linear Colliders: Detectors R&D, Jet Reconstruction and Top Physics Potential*. PhD thesis, Universidad de Valencia, December 2016.

[56] ILC Community Collaboration. The International Linear Collider. *TDR*, Volume 3: Accelerator, 2013.

[57] ILC Community Collaboration. The International Linear Collider. *TDR*, Volume 4: Detectors, 2013.

[58] Erik Adli. *A Study of the Beam Physics in the CLIC Drive Beam Decelerator*. PhD thesis, University of Oslo, October 2009.

[59] CLIC Collaboration. Update Baseline for a Staged CLIC. *CERN Report*, 2016(004), 2016.

[60] CLIC Collaboration. CLIC Conceptual Design Report: Accelerator. *CERN Report*, 2012(007), 2012.

[61] CLIC Collaboration. CLIC Conceptual Design Report: Detector & Physics. *CERN Report*, 2012(003), 2012.

[62] S. Stone. New Physics from Flavour. *36th International Conference on High Energy Physics*, Proceedings, 2012.

[63] Y. Ohnishi et al. Accelerator Design at SuperKEKB. *Prog. Theor. Exp. Phys*, 03A011, 2013.

[64] Eduard Prinker. Testing of the Gated Mode for the Belle II Pixel Detector. Master's thesis, Ludwig-Maximilians-University Munich, August 2015.

[65] Gerhard Lutz. *Semiconductor Radiation Detectors*. Springer, 1999.

[66] J. Kemmer and G. Lutz. New Detector Concepts. *Nucl. Instrum. Meth.*, A253:365–377, 1987.

[67] J. Kemmer et al. Experimental Confirmation of a New Semiconductor Detector Principle. *Nucl. Instrum. Meth.*, A288:92–98, 1990.

[68] Carlos Manuel Marinas Pardo. *DEPFET: A Silicon Pixel Detector for Future Colliders. Fundamentals, Characterization and Performance*. PhD thesis, Universidad de Valencia, April 2011.

[69] Stefan Rummel. *Investigation of DEPFET as Vertex Detector at ILC, Intrinsic properties, radiation hardness and alternative readout schemes*. PhD thesis, Technic-University Munich, September 2009.

[70] H. G. Moser. Progress Detector System in High Energy Physics. *Progress in Particle and Nuclear Physics*, 63:186–237, 2009.

[71] Manuel Tobias Kock. *Development of a test environment for the characterization of the Current Digitizer chip DCD2 and the DEPFET pixel system for the Belle II experiment at SuperKEKB*. PhD thesis, Friedrich-Wilhelms-University Bonn, July 2011.

[72] C. Sandow et al. Clear-performance of Linear DEPFET Devices. *Nucl. Instrum. Meth.*, A 568:176–180, 2006.

[73] M. Boronat. The spatial Resolution of DEPFET Active Pixel Detectors. Master's thesis, University of Valencia, September 2012.

[74] L. Andricek et al. Intrinsic Resolutions of DEPFET Detector Prototypes Measured at Beam Tests. *Nucl. Instrum. Meth.*, A638:24–32, 2011.

[75] M. Boronat et al. Physical Limitations to the Spatial Resolution of Solid-State Detectors. *IEEE Trans. Nucl. Sci.*, 62(1):381–386, 2015.

[76] R. Turchetta. Spatial Resolution of Silicon Micro-Strips Detectors. *Nucl. Instrum. Meth.*, A335:44–58, 1992.

[77] H. Bichsel. Straggling in Thin Silicon Detectors. *Rev. Mod. Phys.*, 60(3):663–699, 1988.

[78] Benjamin Schwenker. *Development and Validation of a Model for the response of the Belle II Vertex Detector*. PhD thesis, Georg-August-Universitat Gottingen, May 2014.

[79] DEPFET Collaboration. *The PXD Whitebook*. DEPFET coll., 2012.

[80] A. Oyanguren. Air Cooling for Vertex Detectors. *Proceedings*, LCWS11, 2011.

[81] DEPFET Collaboration. DEPFET Active Pixel Detectors for a Future epem Collider. *Tra. on Nucl. Sci.*, 6(1), 2010.

[82] Philipp Leitl. JTAG Boundary-Scan of theBelle II Pixel Vertex Detector. Master's thesis, Ludwig-Maximilians-University Munich, December 2015.

[83] Kenneth P. Parker. *The Boundary-Scan Handbook*. Springer, 2003.

[84] G.'t Hooft and M. Veltman. Regularization and Renormalization of Gauge Fields. *Nucl. Phys.*, B44:189–213, 1972.

[85] J.A.M. Vermaseren T. van Ritbergen and S.A. Larin. The Four-loop β-function in Quantum Chromodynamics. *Phys. Lett.*, B400:379–384, 1997.

[86] S.A. Larin J.A.M. Vermaseren and T. van Ritbergen. The Four-loop Quark Mass Anomalous Dimension and the Invariant Quark Mass. *Phys. Lett.*, B405:327–333, 1997.

[87] A.S. Kronfeld. The Perturbative Pole Mass in QCD. *FERMILAB-PUB-98*, 139-T, 1998.

[88] I.I. Bigi et al. The Pole Mass of the Heavy Quark. Perturbation Theory and Beyond. *Phys. Rev.*, D50:2234–2246, 1994.

[89] N. Gray et al. Three-loop Relation of Quark $\bar{m}s$ and Pole Masses. *Z. Phys.*, 48(4):673–679, 1990.

[90] W. J. Stirling R.K. Ellis and B.R. Webber. QCD and Collider Physics. *Cambridge monograph on particle physics, nuclear physics and cosmology*, 8, 1996.

[91] T.D. Lee and M. Nauenberg. Degenerate Systems and Mass Singularities. *Phys. Rev.*, B133:1549–1562, 1964.

[92] Stefan Hoche. Introduction to Parton-Shower Event Generators. *SLAC-PUB*, 16160, 2015.

[93] M. Vos M. Boronat and I. Garcia. A New Jet Reconstruction Algorithm for Lepton Colliders. *Nucl. Phys.*, B273:2749–2751, 2016.

[94] JADE Collaboration. Experimental Investigation of the Energy Dependence of the Strong Coupling Strength. *Phys. Lett.*, B213:235–241, 1988.

[95] S. Catani et al. New Clustering Algorithm for Multijet Cross Sections in e^+e^- Annihilation. *Phys. Lett.*, B269:432–438, 1991.

[96] S. Catani et al. The k^- Perpendicular Clustering Algorithm for Jets in Deep Inelastic Scattering and Hadron Collisions. *Phys. Lett.*, B285:291–299, 1992.

[97] M. Vos M. Boronat and I. Garcia. A Robust Jet Reconstruction Algorithm for High-Energy Lepton Colliders. *Phys. Lett.*, B750:95–99, 2015.

[98] T. Sjostrand et al. A Brief Introduction to PYTHIA 8.1. *Comput. Phys. Commun.*, 178:852–867, 2008.

[99] W. Kilian et al. WHIZARD: Simulating Multi-Particle Processes at LHC and ILC. *Eur. Phys. J.*, C71:1742, 2011.

[100] M.S. Amjad et al. A Precise Characterisation of the Top Quark electro-weak Vertices at the ILC. *Eur. Phys. J.*, C75(512), 2015.

[101] N. Mirman. Measurements of the Top Quark Mass at ATLAS and CMS. *CMS*, CR-2015(306), 2015.

[102] S. Alioli et al. A new Observable to Measure the Top Quark Mass at Hadron Colliders. *Eur. Phys. J.*, C73(2438), 2013.

[103] Howard E. Haber. Higgs/EWSB Working Group Summary. LCWS13, 2013.

[104] I. Antcheva et al. Root - A C++ Framework for Petabyte Data Storage, Statistical Analysis and Visualization. *Comp. Phys. Com.*, 180(12):2499–2512, 2009.

[105] B. Schmidt et al. CRunDec: a C++ Package for Running and Decoupling of the Strong Coupling and Quark Masses. *Comp. Phys. Com.*, 183:1845–1848, 2012.

[106] J. Brau. ILC Running Scenarios. PAC Meeting, 2015.

[107] A. P. Sailer. Studies on the Measurement of Differential Luminosity using Bhabha events at the International Linear Collider. *Diplomarbeit*, 2013.

[108] K. Yokoya. Beam-Beam Interaction in Linear Colliders. *AIP Conf. Proc.*, 592:185–204, 2001.

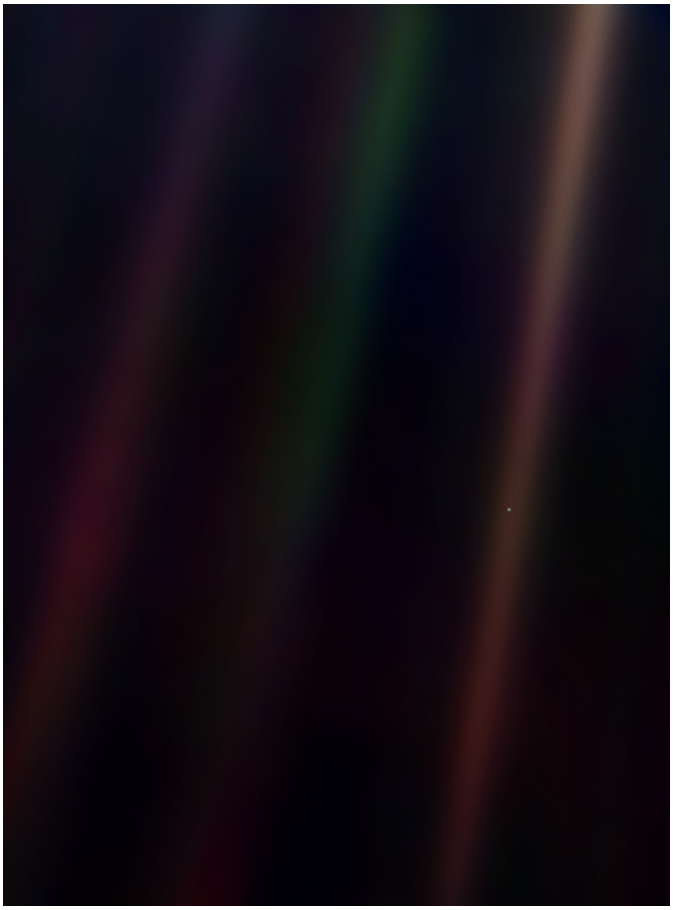

Pale Blue Dot

We succeeded in taking that picture, and, if you look at it, you see a dot. That is here. That is home. That is us. On it, everyone you ever heard of, every human being who ever lived, lived out their lives. The aggregate of all our joys and sufferings, thousands of confident religions, ideologies and economic doctrines, every hunter and forager, every hero and coward, every creator and destroyer of civilizations, every king and peasant, every young couple in love, every hopeful child, every mother and father, every inventor and explorer, every teacher of morals, every corrupt politician, every superstar, every supreme leader, every saint and sinner in the history of our species, lived there, on a mote of dust, suspended in a sunbeam.

— Carl Sagan, speech at Cornell University, October 13, 1994